Structural Tectonic Evolution of the Buffels River shear zone, Namaqua Sector, Namaqua-Natal Metamorphic Province, South Africa

by

YASMEEN FORTUNE

2913828

A thesis submitted in fulfilment of the requirements for the degree of Magister Scientiae in the Department of Earth Sciences, University of the Western Cape

Supervisors:
Prof Russell Bailie
Prof Jan van Bever Donker
Dr Paul Macey

Keywords

Namaqua-Natal Metamorphic Province
Bushmanland Subprovince
Okiep terrane
Garies terrane
Buffels River shear zone
Structural geology
Steep structure

Abstract

The Buffels River shear zone is located in north-western Namaqualand within the Bushmanland Subprovince, approximately 50 km south of the town of Springbok in the Namaqua Metamorphic Province in South Africa. The Buffels River shear zone has an overall ENE-WSW orientation and spans approximately 95 kilometres from the West Coast belt to the Bushmanland plateau in the east where it is further masked by Cenozoic cover. The trace of the supracrustal belt is defined by a steep NNW-dipping, 4 km-wide zone consisting of mainly sheared supracrustal sequences and streaky augen gneiss which have a regionally consistent ENE-WSW trend of about 260°. The rocks of the supracrustal belt occur as sheet-like bodies generally concordant to the regional gneissic foliation and are bordered on either side by a wall-rock of less deformed coarse-grained augen gneiss which has the same penetrative foliation trend as the supracrustal belt.

The shear zone was previously described by most authors as the contact between the Okiep and Garies terranes in the north and south respectively, but other authors disagree with this, stating that the contact between these two terranes is not the Buffels River shear zone but rather lies further south of the Buffels River shear zone. Thus the extent and relationship of the Buffels River shear zone with the adjacent terranes, namely the Okiep and Garies terranes, have been poorly defined in the past with various authors defining the shear zone differently due to lack of structural and geochronological data. This study addresses defining the tectonic evolution of the Buffels River shear zone by making use of geological mapping, petrography, geochemistry, geochronology and isotope analysis.

The Buffels River shear zone is host to granitic orthogneisses of the ~1210 Ma Mesklip Gneiss, leucocratic gneisses of the 1204 ± 4 Ma Rooiplatklip Gneiss, as well as metamorphosed supracrustal rocks, namely, garnet-biotite semi-pelitic gneiss (1222 ± 25 Ma - 1171 ± 21 Ma) and the grey biotite gneisses of the Kamiesberg Subgroup (1138 ± 22 Ma - 1113 ± 22 Ma) and 1168 ± 9 Ma amphibolite lenses of the Oorkraal Suite. The Buffels River shear zone formed during D_3 deformation and its age can be constrained between ~1138 Ma and ~1005 Ma using the youngest detrital zircon age of the volcaniclastic rocks of the grey biotite gneiss and the end of the D_3 deformation respectively.

In this study it has been proven that the Buffels River shear zone does not represent a terrane boundary as the Mesklip Gneiss outcrops on either side of the shear zone and their geologic, geochemical and geochronological histories on either side of the shear zone are identical. Rather, the Buffels River shear zone developed by preferential shearing along a supracrustal belt and represents a steeply dipping, well-foliated, ENE-WSW-trending "steep structure". This structure has undergone largely coaxial shortening strain and developed between a dome and basin structure situated north and south of the Buffels River shear zone respectively.

There are three scenarios that likely best describe the evolution of the BRSZ: (1) the BRSZ represents a pre-existing terrane boundary where it is thought that the two tectonic domains were accreted prior to the ~1.2 Ga magmatism of the Namaquan Orogeny, and that the present day Buffels River shear zone, formed during D_3 deformation, represents a reactivated shear zone along a pre-existing terrane boundary, or (2) the Buffels River shear zone formed during

D_3 deformation, with age constraints between ~1138 Ma and ~1005 Ma, and no terrane boundary exists at the Buffels River shear zone itself but is rather located further south of the shear zone or does not exist at all, or (3) that both of these statements are true and that the BRSZ represents a reactivated shear zone located at the contact between the Okiep and Garies terranes which was then reactivated between ~1138 Ma and ~1005 Ma.

Based on the findings of this study the most likely scenario to represent the evolution of the Buffels River shear zone is that the development of the Buffels River shear zone initiated preferentially along a supracrustal belt between ~1138 Ma and ~1005 Ma, during the D_3 deformational phase, forming what is known as a "steep structure" and it does not represent a terrane boundary between the Okiep and Garies terranes.

UNIVERSITY of the
WESTERN CAPE

Declaration

I declare that *Structural Tectonic Evolution of the Buffels River shear zone, Namaqua Sector, Namaqua-Natal Metamorphic Province, South Africa* is my own work, that it has not been submitted for any degree or examination in any other university, and that all the sources I have used or quoted have been indicated and acknowledged by complete references.

Full name....Yasmeen Fortune........................... Date....23/02/2023.............................

Signed...

Dedication

To my son, Lance Ernest Fortune, everything I am and strive to be is because of you.

Table of contents

UNIVERSITY *of the*

WESTERN CAPE

Chapter 1: Introduction

1.1 Major overview

The Buffels River shear zone is located in the Mesoproterozoic Namaqua Metamorphic Province (NMP) which is a vast area of complicated geology comprising of an igneous and metamorphic history with ages between 1000 and 1200 Ma (Hartnady et al., 1985). Metamorphic rocks of the Namaqua Metamorphic Province were first recognised in the 1950s by Nicolaysen and Burger (1965) through minerals which preserved metamorphic activity dating back to ~1000 Ma (Eglington, 2006).

The Namaqua Metamorphic Province, which is a mid- to late-Proterozoic orogenic belt, extends along the south and southwest boundary of the Kaapvaal Craton (Yuhara, et al., 2002). The orogenic belt is a structurally controlled belt consisting of metasedimentary and meta-igneous rocks which have experienced metamorphism ranging from greenschist to granulite facies (Waters, 1986, 1988, 1989, 1990; Robb et al., 1999; Andreoli et al., 2006; Moen and Toogood, 2007). The Namaqua Metamorphic Province can be subdivided into various tectonostratiphic terranes which have amalgamated during the 1.2-1.0 Ga Namaquan Orogeny namely the Kheis, Gordonia, Bushmanland and Richtersveld Subprovinces from east to west respectively (Hartnady et al, 1985, Thomas et al, 1994a, Moen and Toogood, 2007, Macey et al, 2011).

1.2 Overall setting

The study area, known as the Buffels River shear zone (Fig. 1), is located in north-western Namaqualand within the Bushmanland Subprovince, approximately 50 km south of the town of Springbok in the Namaqua Metamorphic Province in South Africa. It has been described as the boundary between the Okiep and Garies terranes of the Bushmanland Subprovince (McClung, 2006). The Bushmanland Subprovince consists of mainly granitic orthogneisses and metamorphosed supracrustal rocks (Yuhara, et al., 2002). The supracrustal rocks are defined by five main lithologies, biotite augen gneisses, leucocratic gneisses, amphibolites, biotite gneiss and garnetiferous quartzofeldspathic and biotite-sillimanite gneiss (Yuhara, et al., 2002). The metamorphic rocks in the Bushmanland Subprovince have undergone metamorphic conditions ranging from upper amphibolite to upper granulite facies (Waters, 1986, 1990; Thomas et, 1994).

1.3 Problem statement

The Bushmanland Subprovince has been divided by workers (Hartnady et al., 1985; Joubert, 1986; Moore, 1989; Thomas et al., 1994; Eglington, 2006; McClung, 2006) into two terranes of which the BRSZ is said to be the boundary between the Garies and Okiep terranes. Other workers (Raith et al., 2003; Clifford and Barton 2012), however, have said that the Bushmanland Subprovince is not a Subprovince but rather one domain (Bushmanland Domain) with a shear zone that crosscuts it and does not define the contact between the Okiep and Garies terrane. Thus, the BRSZ's structural evolution is poorly understood and various workers in the area have given different significance to the BRSZ. Waters (1986, 1988, 1989) describes the Bushmanland terrane as being divided into three metamorphic zones from north to south. The high-grade rocks of the Bushmanland Subprovinceof the Namaqua Metamorphic Province have three distinct metamorphic zones; a central zone of upper-granulite facies, with lower-

1

granulite and upper amphibolite facies zones to the north and south of the central zone (Fig. 1; Waters, 1986).
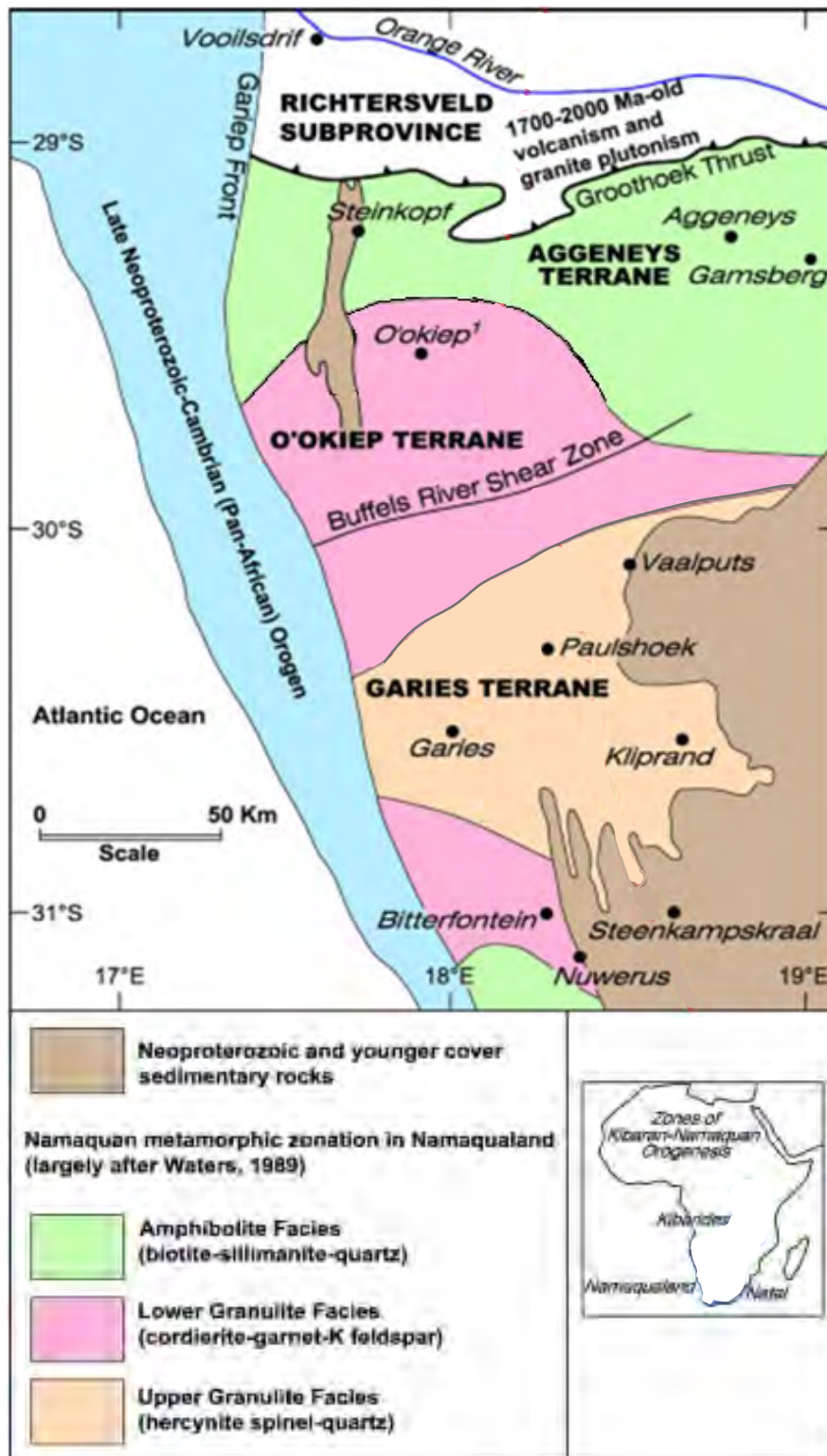

Figure 1 Simplified geological map showing the Bushmanland Subprovince and constituent terranes (Aggeneys, Okiep and Garies), with their relevant metamorphic facies. This map shows the BRSZ as located within the Okiep terrane as a shear zone and not as a boundary as argued by other workers. Adapted from Clifford and Barton (2012).

2

They report that the Namaqua Metamorphic Province displays an E-W-trending metamorphic zonation (Raith et al, 2003). McClung (2006) refers to the Bushmanland Subprovince as an amphibolite- to granulite-facies zone which is subdivided into distinct units, namely the Aggeneys terrane (north) and the Garies terrane (south) which is separated by the Buffels River-Putsberg shear zone. McClung (2006) describes the Bushmanland Subprovince as composed of variably thick metavolcano-sedimentary successions. He further refers to Moore (1989) as illustrating that the Aggeneys and Garies terranes display comparable lithostratigraphic units and suggests that they may have been deposited in contiguous geographical areas. Eglington (2006) defines the Bushmanland Subprovince based on research obtained from Hartnady et al. (1985) and Thomas et al. (1994) which states that the Bushmanland Subprovince is divided into three distinct terranes namely the Aggeneys, Okiep and Garies terranes of which the BRSZ is defined as the boundary between the Okiep and Garies terranes. Petterson (2008) follows the Thomas et al. (1994) subdivision of the Namaqua Sector of the Namaqua Metamorphic Province in having no Bushmanland Subprovince but rather six terranes and Subprovinces divided due to their age constraints and change in regional fabric in moving from east to west in the Namaqua Sector. These six terranes are the Kaaien, Areachap, Kakamas (constituting the eastern part) and the Bushmanland and Garies terranes and the Richtersveld Subprovince constituting the western part. According to Petterson (2008) the BRSZ separates the Bushmanland terrane (north) from the Garies terrane (south). Petterson (2008) further suggests that the Bushmanland Terrane be further subdivided due to the northern part of the terrane showing early Paleoproterozoic to Achaean model ages and can clearly be differentiated from the Mesoproterozoic southern part.

In the Garies terrane of the Bushmanland Subprovince Nd T_{DM} model ages indicate a juvenile influence due to it being younger than the Nd T_{DM} dates for the Aggeneys and Okiep terranes of the Bushmanland Subprovince (Eglington, 2006; Clifford and Barton, 2012). Due to its nature and having model ages which are marginally older than the emplacement ages this would indicate a considerable juvenile contribution to the development of the crust in this area (Eglington, 2006). Therefore, Eglington (2006) has concluded that there is little indication for a substantial contribution of any older crustal material as the juvenile crust formed during two major periods at ~1.4 to ~2.2 Ga. There is evidence for substantial reworking of Paleoproterozoic lithosphere within the Aggeneys and Okiep terranes but this is less evident within the Garies terrane (Eglington, 2006).

The aim of the study is to determine whether the BRSZ represents a terrane boundary between the Okiep and Garies terranes or if it is simply a structural feature located in the Bushmanland Subprovince. The objectives are to produce a geological map, delineating subareas within the study area and characterising folds and their significance to the evolution of the BRSZ. Lithological descriptions including petrographic analysis of the units along the BRSZ will be done in order to determine the nature, origin and characteristics of the rocks. Structural analysis, geochemistry, isotope geochemistry and geochronology of the specific lithologies in and around the BRSZ will demonstrate the general tectonic evolution of the region. Geochronology and isotopic analysis contribute to determining an age estimate and approximate timing of shear zone development as the age of the supracrustals in the study area are poorly constrained.

Chapter 2: Geological setting

2.1 Regional geology

The Namaqua-Natal Metamorphic Province (NNMP) spans the southern and western border of the Kaapvaal Craton situated in South Africa and is defined as a tectono-stratigraphic province (Cornell et al., 2006). The rocks of the NNMP are host to igneous and metamorphic rocks formed during the Namaquan Orogeny (~1.2-1.0 Ga) and outcrops are comprehensively found in the Northern Cape, Western Cape and KwaZulu-Natal provinces (Cornell et al., 2006).

The NNMP can be subdivided into the Natal Sector and the Namaqua Sector each separated by Phanerozoic cover (Petterson, 2008). The Namaqua Sector comprises three main lithostratigraphic components: (1) late Paleoproterozoic rocks (~2000 Ma) that have been reworked, (2) juvenile supracrustal successions and plutons which formed during the Namaquan Wilson Cycle (~1600-1200 Ma) and amassed during collision caused by deformation and metamorphic events, and (3) large granitoids which formed between 1200 and 1000 Ma syn- and post-tectonically which also includes mafic to ultramafic intrusions occurring on a small scale (Cornell, et al., 2006).

The Namaqua Sector can be divided into four Subprovinces, which are, from east to west, the Kheis, Gordonia, Richtersveld and Bushmanland Subprovinces (McClung, 2006). These Subprovinces are then further subdivided into tectono-stratigraphic terranes which are areas bounded by shear zones with similar lithostratigraphy and structural features (Joubert, 1984, 1986). Here the metamorphic grade can range from greenschist facies to amphibolite facies and granulite facies (McClung, 2006).

The Kheis Subprovince (Fig. 2), which is located along the eastern extent of the Namaqua Metamorphic Province (NMP) is composed of mainly phyllites, quartzites and amphibolites of ages between 1600 and 1900 Ma which are said to have been deformed between 1100 and 1300 Ma (SACS, 1980; Moen, 1999; van Niekerk, 2006). The Gordonia Subprovince is positioned between the Kheis Subprovince (eastern boundary) and the Bushmanland-Richtersveld Subprovinces (western boundary) (Geringer, 1979; Cornell et al., 1990).

The Gordonia Subprovince is further subdivided into an eastern and western terrane, namely the Areachap and Kakamas terranes (McClung, 2006). The Areachap terrane is characterised by a Mesoproterozoic (1300-1600 Ma) juvenile bimodal volcanic arc and related sedimentary rocks whereas the Kakamas terrane is composed of numerous syn- to post-collisional S-type granites which intruded a thin package of quartzites and calc-silicate rocks during the Namaquan Orogeny (1020-1220 Ma) (Barton, 1983).

The Richtersveld and Bushmanland Subprovinces constitute the western NMP (Fig. 2) located in the north and south with respect to the western NMP (McClung, 2006). The Richtersveld Subprovince has undergone greenschist facies metamorphism and comprises mafic to felsic lavas, ignimbrites and additional volcanic rocks of Paleoproterozoic age (1700-2000 Ma) that are interbedded with numerous sedimentary rocks (Reid, 1977). During the time of a continental volcanic arc complex these sedimentary rocks were then syn- to post-tectonically intruded by calc-alkaline I-type granitoids (Reid, 1977).

The Bushmanland Subprovince has undergone amphibolite to granulite facies metamorphism and is dominated by Paleoproterozoic (~1800 to 2000 Ma) supracrustal rocks (Aggeneys

4

Sequence) and gneissic granitoid intrusions (Gladkop Suite) further intruded by ~1200 Ma pre- to syn-tectonic gneissic granitoids (Little Namaqualand Suite) and ~1030 to ~1060 Ma plutons (Spektakel Suite) late- to post-tectonically (Schmitz et al., 2004). The Paleoproterozoic supracrustal rocks consist of metasedimentary rocks dominated by schists, quartzites, sillimanite-bearing rocks, amphibolites and rare iron formations (Petterson, 2008). Controversy surrounds the subdivision of the Bushmanland Subprovinces. According to Eglington (2006), the Bushmanland Subprovince is subdivided into three terranes, namely the Aggeneys, Okiep and Garies terranes. The boundary between the Aggeneys and Okiep terranes is poorly defined whereas the BRSZ defines the boundary between the Okiep and Garies terrane (Eglington, 2006).
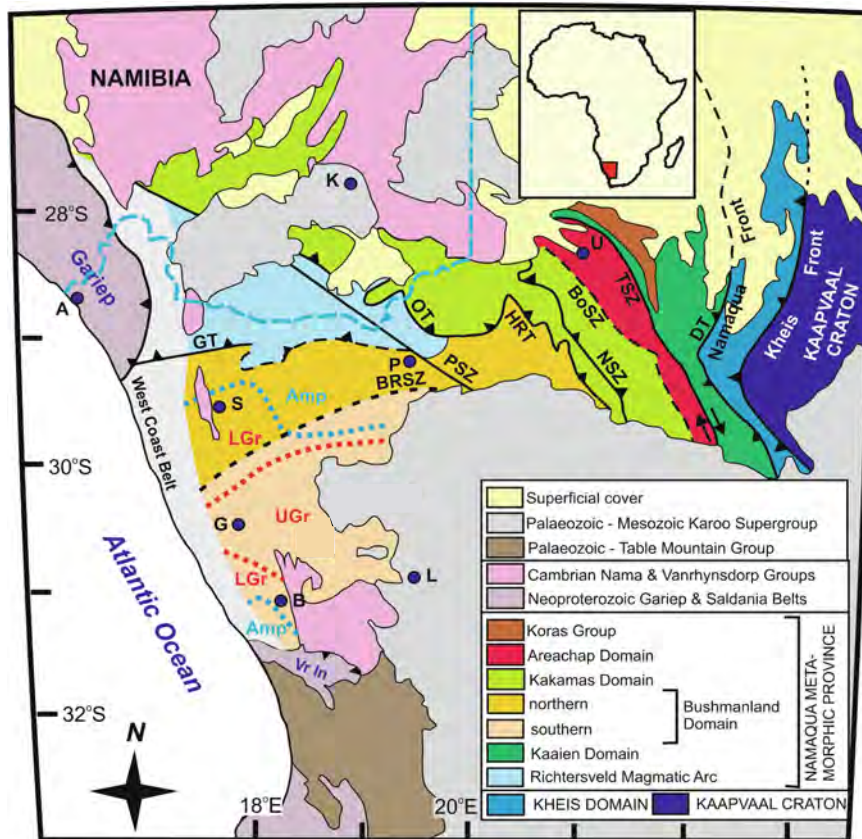
Figure 2 The Namaqua Metamorphic Province and its tectonostratigraphic subdivisions modified after Hartnady et al. (1985); Joubert (1986) and Bailie et al. (2019). Abbreviations: Towns: A – Alexander Bay, B – Bitterfontein, G – Garies, K - Karasburg, L – Loeriesfontein, P – Pofadder, S – Springbok, U – Upington; Metamorphic grade indicators: Amp – amphibolite, LGr – lower granulite, UGr – upper granulite; structural features – BoSZ – Boven Rugzeer Shear Zone, BRSZ – Buffels River Shear Zone, DT – Dabep Thrust, GT – Groothoek Thrust, HRT – Hartbees River Thrust, NSZ – Neusspruit Shear Zone, OT – Onseepkans Thrust, PSZ – Pofadder Shear Zone, TSZ – Trooilapspan Shear Zone, Vr In – Vanrhynsdorp Inlier.

2.2 Local geology

The BRSZ (Fig. 2 & 3) has an ENE-WSW orientation of which the eastern extent of the shear zone is poorly defined (Petterson, 2008). The BRSZ consists of a supracrustal succession which is defined by three main lithologies; biotite gneiss and garnetiferous quartzofeldspathic biotite-sillimanite gneiss and commonly occurs with lenses and small bands of amphibolite-throughout the supracrustal sequence (McStay, 1991; Moore, 1989). The supracrustal rocks of

5

the BRSZ belong to the Kamiesberg Group of which the biotite gneisses are considered the basal unit of the supracrustal succession (Table 1 & Fig. 3). The Mesklip and Rooiplatklip Gneisses, of the ~1.2 Ga Little Namaqualand Suite gneisses, are mesocratic augen gneiss and leucocratic gneiss respectively and are the basement rocks which underlie the supracrustal succession.

The metamorphic rocks in the Bushmanland Subprovince have undergone metamorphism ranging from upper amphibolite to upper granulite facies (Yuhara et al., 2002). Zones A, B and C (Appendix A1) characterise the metamorphic sequence of the Bushmanland Subprovince of which zone C is the highest–grade zone, upper granulite metamorphic facies (quartz-hercynite: Waters, 1991; osumilite: Nowicki et al., 1995) (central part), with the metamorphic grade decreasing moving to the north and south of the central area. Zone C displays an estimated temperature of 800-870°C and a pressure of 0.4-0.7 GPa (Zelt, 1980; Waters, 1986, 1989; Nowicki et al., 1995). Lower granulite facies (biotite-sillimanite-muscovite) and the upper granulite facies (garnet-cordierite-K-feldspar) represent zones B and A respectively (Waters, 1986, 1989). Zone B exhibits a temperature of 750-820°C and pressure of 0.3-0.65 GPa (Waters, 1989; Raith and Harley, 1998) whereas zone A displays a temperature of 650-700°C and a pressure range of 0.35-0.45 GPa (Waters, 1989). Pan-African age greenschist to amphibolite facies metamorphism partly overprints these metamorphic rocks in particular along the west coast adjacent to the Bushmanland Subprovince (Waters et al., 1986). Sediments of the Nama Group (late Precambrian to early Palaeozoic) unconformably overlay these rocks (Waters et al., 1986). The area has undergone very little retrograde metamorphism therefore peak metamorphism is preserved in the textures and mineralogy (McStay, 1991). According to McStay (1991) the regional late shears which formed during later tectonic events (D_4) do not constitute terrane boundaries unless they have formed along previous tectonic zones which were reactivated between terranes of different lithostratigraphy, structure and metamorphic facies.

2.3 Structural geology

At least four phases of deformation have been identified as having occurred during the Namaquan Orogeny. The first phase of deformation, D_1 constitutes original bedding in the supracrustal rocks and well-developed compositional banding in the pelites and grey biotite gneisses are thought to represent this fabric but has not been identified in the field as they have been overprinted by multiple folding and metamorphic events (McStay, 1991). The second phase of deformation [D_{2-3}/M_{2-4}] is the most intense. D_2 can be divided into two (McClung, 2006), namely D_{2a} and D_{2b} and was referred to as the "O'okiepian Episode" (Clifford et al., 2004) (1180-1210 Ma). D_{2a} is considered to be the age of emplacement of the Little Namaqualand Suite constituting an early granitic intrusion and is associated with amphibolite- to granulite-facies metamorphism (M_2, 530-800°C, 2.8-6 kbar; Rozendaal, 1975; Lipson, 1978, 1990; Ryan et al., 1986; Moore, 1989; Hoffmann, 1993), whereas D_{2b} is characterised by later structures (Raith and Meisel, 2001; Colliston and Schoch, 2002).

D_3, the third phase of deformation, referred to as the "Klondikean Episode" (1020-1040 Ma) (Clifford et al., 2004) is also divided into two events (D_{3a} and D_{3b}). D_{3a} constitutes large-scale open, asymmetrical folds that are associated with retrograde upper amphibolite- to granulite-facies metamorphism (M_3, 580-660°C, 5.8± 0.5 kbar; Raith and Harley, 1988) (Clifford et al., 2004). D_{3b} soon followed and was associated with late retrograde metamorphism (M_4) and

monoclinal folds with steep limbs (Clifford et al, 2004). D_4 is the last phase of deformation and is characterised by shear zones, fractures and faults (Colliston and Schoch, 2002).

Table 1 Lithostratigraphy of the rocks along the BRSZ and surrounding areas (after Thomas et al., 2001).

| **COVER**			
Era	*Period*	*Formation*	*Lithological description*
Cenozoic	Quaternary		Braided ephemeral channel alluvium
			Sheetwash sandy colluvium
IGNEOUS ROCKS			
Group	*Subgroup*	*Formation*	*Lithological description*
Koperberg Suite			Meso- to melanocratic unfoliated to weakly foliated metadiorite, porphyritic and medium- to coarse-grained
Korridor Suite		Kweekfontein granite	Fine- to medium-grained equigranular aplitic granite
Oorkraal Suite			Amphibolite, two pyroxene granulite
Little Namaqualand suite		Rooiplatklip Gneiss	Fine- to medium-grained leucogranitic gneiss
		Mesklip Gneiss	Coarse-grained mesocratic augen gneiss
METAMORPHIC ROCKS OF SEDIMENTARY ORIGIN			
Group	*Subgroup*	*Formation*	*Lithological description*
Bushmanland group			Garnetiferous quartzofeldspathic biotie-sillimanite gneiss, quartzite; minor calc-silicate rocks and conglomerate
	Kamiesberg	Hunboom Gneiss	Biotite gneiss, quartzite, lenses of calc-silicate rocks and amphibolite
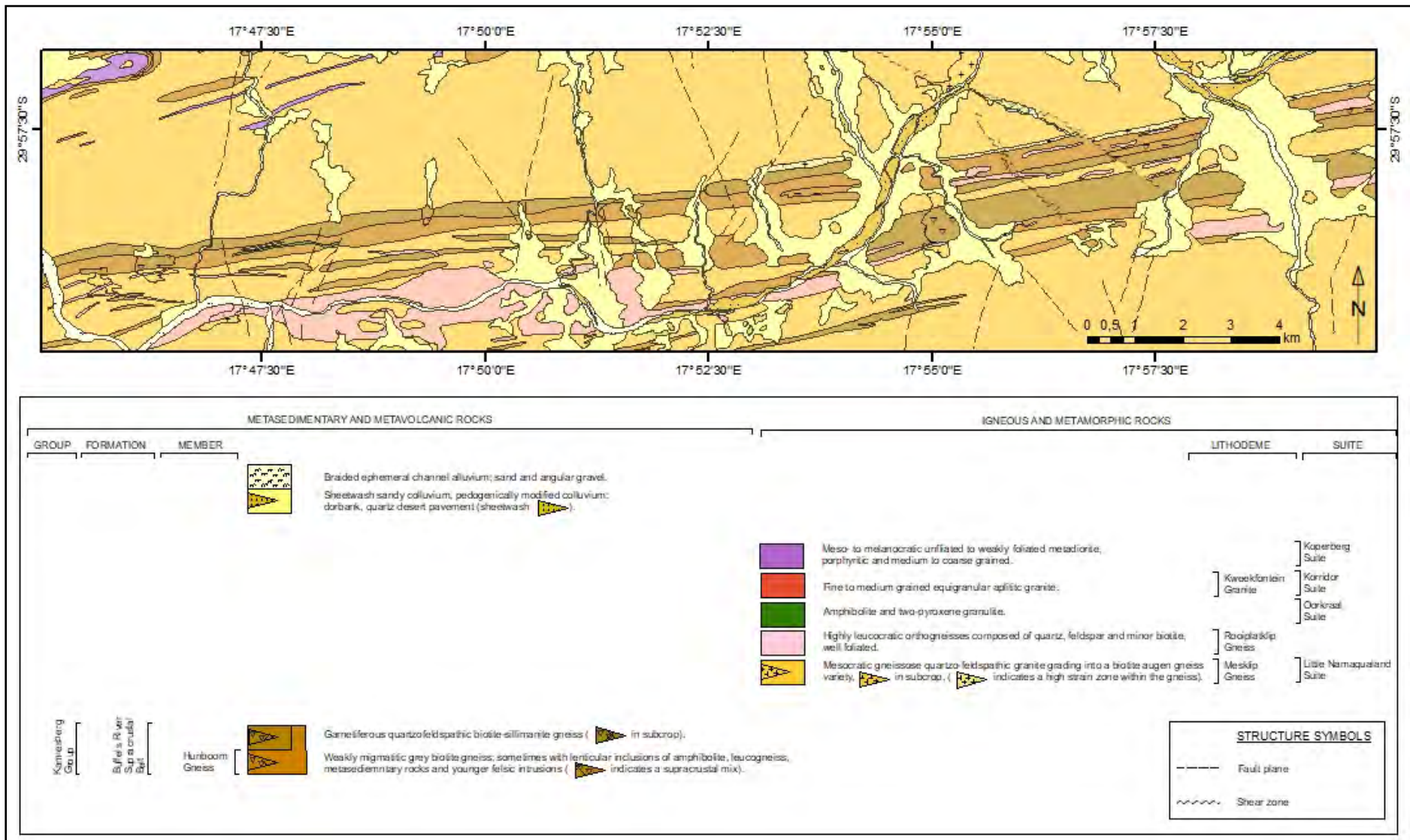
Figure 3 Geological map of the rocks found in the Buffels River shear zone and surrounding rocks (Adapted from Abrahams et al., 2020).

http://etd.uwc.ac.za/

Chapter 3: Methodology

3.1 Fieldwork

The purpose of the fieldwork is to obtain the regional trend of the shear zone, to determine the composition of the rocks within and adjacent to the shear zone and to sample them for whole-rock geochemistry including isotope analysis and geochronology. This includes foliation and lineation measurements which were taken along four main traverses, one traversing E-W, one NW-SE and two traversing N-S in relation to the BRSZ. Grain size, mineral lineation, foliation, percentage of minerals, GPS coordinates, structural measurements and mineralogy were recorded in the field at each waypoint. Shear orientations of shear bands identified in the field were measured to determine the sense of shear (dextral or sinistral). Lithological descriptions and structural features were recorded at all waypoints along each of the four traverses. All structural measurements were taken using a Freiberger compass, recording dip and dip direction of each structural feature. Stereographic projection, Flinn and rose diagrams of these structural features were analysed using GEOrient 9.5.1 (Holcombe, 2017) and OpenStereo 2.0 software (Grohmann et al., 2017).

3.2 Map compilation

A hand drawn draft map of the BRSZ area was traced from two adjacent 1:50 000 map sheets (2917DD Mesklip and 3017BB Kamieskroon) as the BRSZ area borders the bottom of the former map sheet and top of the latter map sheet, respectively. The hand drawn map was then scanned and uploaded into ArcMap and four corresponding corners on the BRSZ area were geo-referenced (WGS 1984) and all major and minor roads were digitized. Waypoints were added using GPS coordinates and lithologies were digitized according to the data collected in the field and associated historical geological maps for comparison. Structural and geological data was also collated from sheets mapped by previous workers (Marais et al., 2001; De Beer, 2010; Agenbacht, 2007; Macey et al., 2011; Abrahams et al., 2020; Groenewald and Macey, 2020).

3.3 Petrography and geochemistry

Thin sections for petrographic descriptions were cut at the University of the Western Cape (UWC). 70 samples were taken from the field representing the rock types found along the BRSZ for whole-rock major and trace element analysis and geochronology (Appendix, Table B1 & B2). Due to the large grain size of the augen gneiss locally large samples were taken and weathered material was removed in the field. The samples for geochemistry were split, crushed and milled to powder at the UWC and analysed for major and trace elements at Stellenbosch University at the Central Analytical Facilities (CAF). Trace elements in samples were detected by Inductively Coupled Plasma-Mass Spectrometry (ICP-MS) analysis. Major elements for all samples were determined by XRF (X-ray Fluorescence) Spectrometry on glass beads prepared from 0.2 g samples followed by a lithium metaborate/tetraborate fusion and dilute nitric acid digestion. Loss on ignition (LOI) was calculated by weight difference after ignition to 1000 degrees Celsius. A 1:10 ratio of sample-to-flux (lithium tetraborate) was mixed using the

1

powdered whole-rock samples with the lithium tetraborate. Thirty-two USGS and GSJ standard reference samples were used for calibration of the instrument. Inductively Coupled Plasma-Mass Spectrometry (ICP-MS) was used to determine trace and rare earth element (REE) abundances and followed the same technique as that of whole-rock analyses but with a separate 0.5 g split digested in Aqua Regia. Using replicate analyses of international rock standards, the precision and accuracy of the results were assessed and are 2-5% (1σ) for most elements. Most trace element detection limits are 0.1 ppm except for Th and Co (0.2 ppm), Sr (0.5 ppm), Sc and Zn (1 ppm), and V (8 ppm). Detection limits for most REE are less than or equal to 0.05 ppm excluding La and Ce (0.1 ppm), and Nd (0.3 ppm).

3.4 Geochronology

All U-Pb age data were obtained by laser ablation-single collector-magnetic sector field-inductively coupled plasma-mass spectrometry (LA-SF-ICP-MS) using a Thermo Finnigan Element2 mass spectrometer coupled to an ASI Resolution S155 excimer laser ablation system (Frei and Gerdes, 2009) at the Central Analytical Facilities (CAF), Stellenbosch University (SU). All age data presented here were obtained by single spot analyses with spot diameter of 20 µm and a crater depth of approximately 15-20 µm. Frei and Gerdes (2009) describe the methods used for analysis and data processing. For quality control, the 91500 (Wiedenbeck et al. 1995), (Slama et al. 2008) and M127 (Nasdala et al. 2008; Mattison, 2010) zircon reference materials were analysed, and the results were consistently in excellent agreement with the published ID-TIMS ages. The calculation of concordia ages and the plotting of concordia diagrams were executed using Isoplot/Ex 3.0 (Ludwig, 2003). Unfortunately the metamorphic rims on zircons could not be analysed as the LA-ICP-MS dating technique does not allow spots of <20 µm to be analysed.

3.5 Isotope geochemistry

Rb-Sr and Sm-Nd isotope analysis was implemented on a PESCIIEX Elan 6000 ICP-MS at the University of Cape Town (UCT) following dissolution and dilution with 5% HNO_3 containing an internal standard, with concentrations determined in duplicate for each sample. In order to maintain accuracy and precision the international standard BHVO-2 was analysed with every batch of samples.

Based on the measured $^{86}Sr/^{88}Sr$ and $^{146}Nd/^{144}Nd$ ratios the background compositions were measured and the instrumental mass fractionation was corrected using the exponential law and fractionation factors. For the assessment of instrument tuning and constancy, the Sr solution of the NIST SRM987 Sr isotope standard and the Nd solution of the JNdi-1 Nd isotope standard were analysed twice preceding any sample and after every fifth sample. The external, measured 2σ reproducibility of the SRM987 and JNdi-1 standards were determined on the average $^{87}Sr/^{86}Sr$ and $^{143}Nd/^{144}Nd$ ratios, respectively. The $^{87}Sr/^{88}Sr$ data were reported and normalized to 0.710255 and the $^{143}Nd/^{144}Nd$ data normalized to 0.512115. The initial $^{87}Sr/^{88}Sr$ and $^{143}Nd/^{144}Nd$ ratios were calculated using decay constants of 1.42 x 10^{-11} y^{-1} (Steiger and Jager, 1977) and 6.554 x 10^{-12} y^{-1} (Begemann et al., 2001), respectively.

As described by Míková and Denková (2007) the samples were subjected to HF and HNO₃ acid digestion. The separation of Sr and Nd isotopes were carried out by chromatographic

2

techniques, after the technique described by Pin and Zalduegui (1997) and Pin et al. (1994). All isotope analyses were performed on a Nu Instruments NuPlasma HR in the Department of Geological Sciences, University of Cape Town (UCT). Sr is analysed as a 200 ppb 0.2% HNO_3 solution. The NIST SRM987 reference standard was used. A normalising value of 0.710255 for $^{87}Sr/^{86}Sr$ was used. The average $^{87}Sr/^{86}Sr$ values for the SRM987 standard for these analyses is 0.71083±11 (n = 11). The international rock standard BHVO-2 gave a value of 0.703490±15 relative to a value of 0.703479±20 reported by Weis et al. (2006). The long-term UCT average is 0.703487±32 (n = 28). All Sr isotope data is corrected for Rb interference using the measured signal for ^{85}Rb and the natural $^{85}Rb/^{87}Rb$ ratio. Instrumental mass fractionation is corrected using the exponential law and a $^{86}Sr/^{88}Sr$ value of 0.1194.

Nd isotopes are analysed as 50 ppb 2% HNO_3 solutions using a Nu Instruments DSN-100 desolvating nebuliser. JNdi-1 is used as a reference standard, with a $^{143}Nd/^{144}Nd$ normalizing value of 0.512115±7 using the methods of Tanaka et al. (2000). The average $^{143}Nd/^{144}Nd$ ratio for the JNdi-1 reference for these analyses is 0.512074±22 (n = 11). For the same standard Tanaka et al. (2000) reported a value of 0.512115±7. The BVHO-2 standard was used giving values of 0.512981±10, relative to a value of 0.512984±11 reported by Weis et al. (2006). All Nd isotope data is corrected for Sm and Ce interference using the measured signal for ^{147}Sm and ^{140}Ce, and the natural Sm and Ce isotope abundances. Instrumental mass fractionation is corrected using the exponential law and a $^{146}Nd/^{144}Nd$ value of 0.7219.
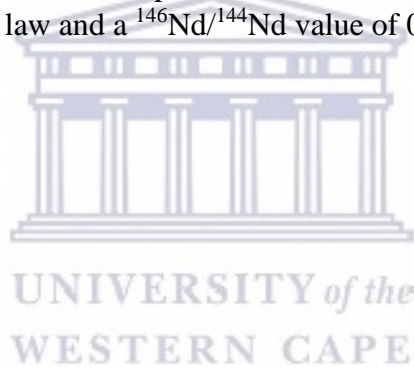
Chapter 4: Lithological descriptions

4.1 Introduction

This chapter aims to describe the rock types identified in the BRSZ based on field and petrographic descriptions as well as their contact relationships. Lithologies are described in chronological order.

4.1.1   Mesklip Gneiss

Good exposures of the Mesklip Gneiss can be found on the farm Mesklip (GPS 29 49.611 S, 17 51.571 E). It is by far the most dominant lithology in the mapped area, and extends to all adjoining sheets to the north, west and south. The name, Mesklip Gneiss was given to the rocks by Marais et al. (2001) and Agenbacht (2007) on the 2917 Springbok and 2918 Pofadder sheets.

The Mesklip Gneiss of the Little Namaqualand Suite has a leucocratic to biotite-bearing variety, with pink to light brown-weathering, well foliated, porphyritic and medium- to coarse-grained (Fig. 4). The augen are coarse-grained and ovoid in shape with biotite defining the overall planar fabric which envelops the K-feldspar augen. The size of the augen varies from 0.8 cm to 1.5 cm in length but larger grain sizes have been observed in areas of less strain. Outcrops typically weather to rounded boulders and convex domes. Rafts of amphibolite bands are commonly found within the Mesklip Gneiss having an overall trend similar to that of the regional foliation, and having sharp contact relationships. The strain across the Mesklip Gneiss varies and it appears streakier within the BRSZ. This streakiness usually sees an increase in biotite content. Minimal amounts of epidote are found within N-S-trending joints. Outcrop-scale discrete shear zones within the BRSZ display both a sinistral and dextral sense of movement and crosscut the Mesklip Gneiss. These shear zones are also recognised by the development of crenulation cleavage.

This gneiss is composed of 35% quartz, 27% orthoclase, 18% plagioclase, 10% biotite, 7% garnet, 3% myrmekite. The quartz crystals occur as anhedral and large (3 mm) sized crystals (Fig. 5). They display first order grey-white interference colours with undulose extinction. Quartz also has curved lobate boundaries that are sutured and this suggests recrystallization. Orthoclase, when viewed in crossed polars, displays perthitic textures where the streaks of the light grey mineral have been exsolved. The feldspars are also elongated subparallel to the biotite foliation. Plagioclase is subhedral and displays deformation twinning. Plagioclase grain size ranges from 0.9 mm to 2 mm in length. Biotite is subhedral to euhedral and the foliation is defined by the biotite and it wraps around the augen which are made up of quartz and orthoclase. Quartz, plagioclase and biotite are also typically intergrown and indicative of a symplectitic texture. Biotite reaches widths ranging from 0.2 mm to 2.1 mm. The presence of garnet indicates this was an S-type peraluminous granite. Fractures across the garnet are perpendicular to the overall foliation which are indicative of a compressional regime, as is the foliation wrapping around the augen. The garnets present are anhedral and range in length from 2 mm to 4 mm. Myrmekite is typically formed along the boundaries of orthoclase and have widths ranging from 0.2 mm to 1 mm.
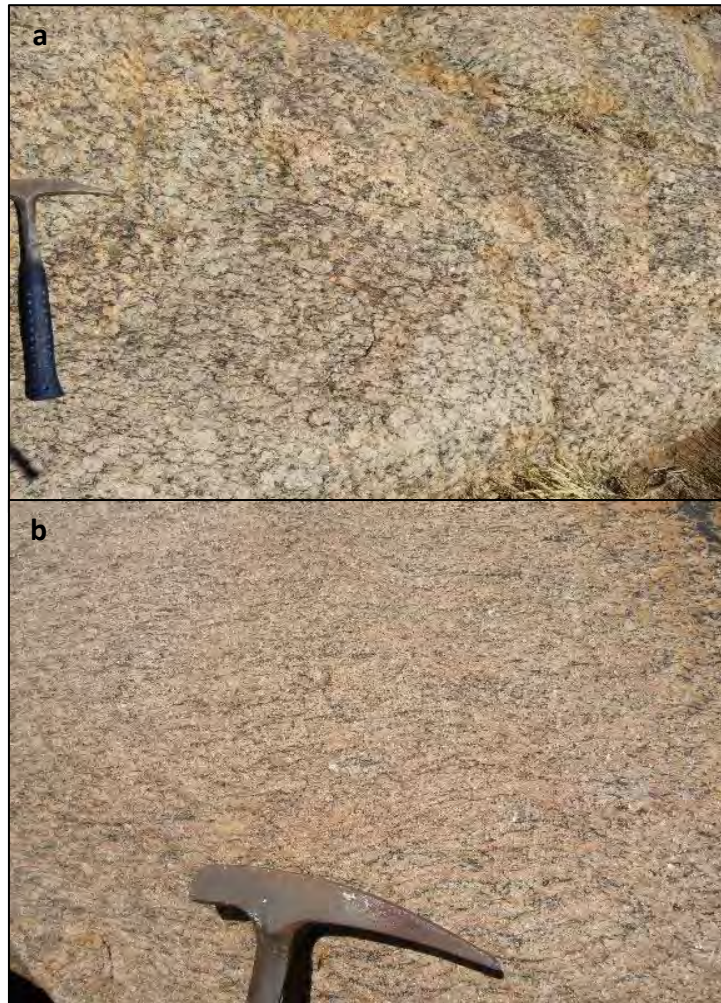
Figure 4 (a) Biotite augen gneiss of the Mesklip Gneiss and **(b)** a close-up of the typical texture of moderately to strongly foliated, rather leucocratic equigranular phase of the Mesklip Gneiss with thin foliates of biotite.
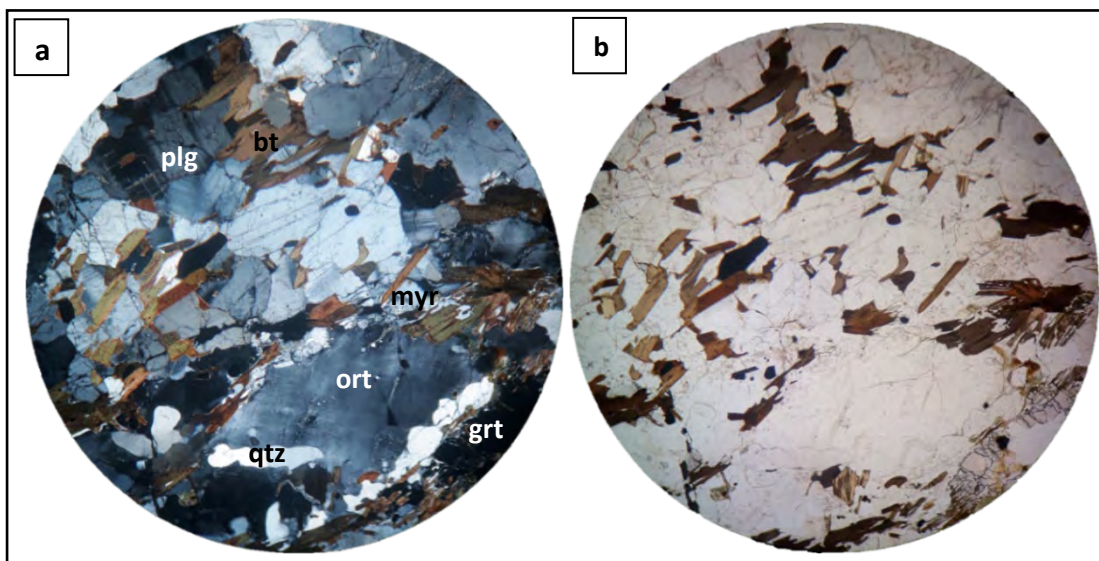
Figure 5 Microphotograph of a well-foliated Mesklip Gneiss in crossed and plane polarisation ((a) and (b) respectively). The biotite clearly defines a foliation and wraps around the augen made up of aggregates of quartz and orthoclase. (plg = plagioclase, qtz = quartz, myr = myrmekite, ort = orthoclase, bt = biotite and grt = garnet), (FOV=5 mm).

5

4.1.2 Rooiplatklip Gneiss (Leucocratic gneiss)

The leucocratic gneiss intruded parallel to the regional foliation as sheet-like bodies. These rocks are gneissic and have also been subjected to the same stress that the Mesklip Gneiss has been subject to in the BRSZ. These sheet-like intrusions range in size from metres to hundreds of metres in length. Outcrops were fairly weathered to a pale pink colour and pale-grey on a fresh surface. Its texture is porphyritic, ranging from medium- to coarse-grained and pegmatitic in some places. Biotite delineates a well-foliated rock with an overall ENE-WSW orientation and locally, in areas of higher strain, aggregates of coarser grained quartz and feldspar define a streaky-like texture, but this is a lesser occurrence. This also locally gives rise to a kind of compositional banding. Mafic xenoliths ranging in sizes from centimetres to metres are found within the leucocratic gneiss all of which have an ENE-WSW orientation. There are two main sets of joints which crosscut the leucocratic gneiss which are N-S- and E-W-orientated.

This gneiss is composed of 45% orthoclase, 30% quartz, 20% plagioclase, 2% microcline, 1% myrmekite, 1% chlorite and 1% biotite (Fig. 7). Orthoclase has undergone sericitic alteration to a degree indicating partial alteration and also displays perthitic intergrowths in some instances. The crystals are subhedral and display poikiloblastic textures with inclusions of quartz. The quartz inclusions range in size from 0.5 mm to 6 mm in diameter. Quartz crystal size ranges from 0.2 mm to 8 mm in diameter and commonly display undulose extinction. Plagioclase is typically twinned and ranges from 1 mm to 5.5 mm along the long axis. Chlorite is seen replacing biotite, indicating either the occurrence of a retrograde reaction or deuteric alteration. The biotite is generally 0.2 mm in length with one occurrence of it being 5 mm in length. Overall the rock displays abundant fracturing, sericitic alteration and the minor occurrence of symplectite textures.

4.1.3 Amphibolite

The melanocratic, well-foliated hornblende-bearing amphibolite dyke has a dark grey to black weathered surface but on a fresh surface reveals a dark green colour. The amphibolite tends to be quite resistant to weathering which produces upright blocky structures which trend ENE-WSW (Fig. 8a & b). This rock is composed of hornblende, biotite, clinopyroxene, with quartz, plagioclase and orthoclase as minor constituents, all in decreasing abundance. Furthermore, it is slightly porphyritic and fine- to medium-grained. These dykes vary in width from 10 cm to 1.3 m, but in length can trend for kilometres. It is boudinaged for kilometres from east to west across the BRSZ and commonly intruded by the Mesklip and Rooiplatklip Gneisses. They can also be slightly folded and cross-cut and displaced by N-S-trending joints.
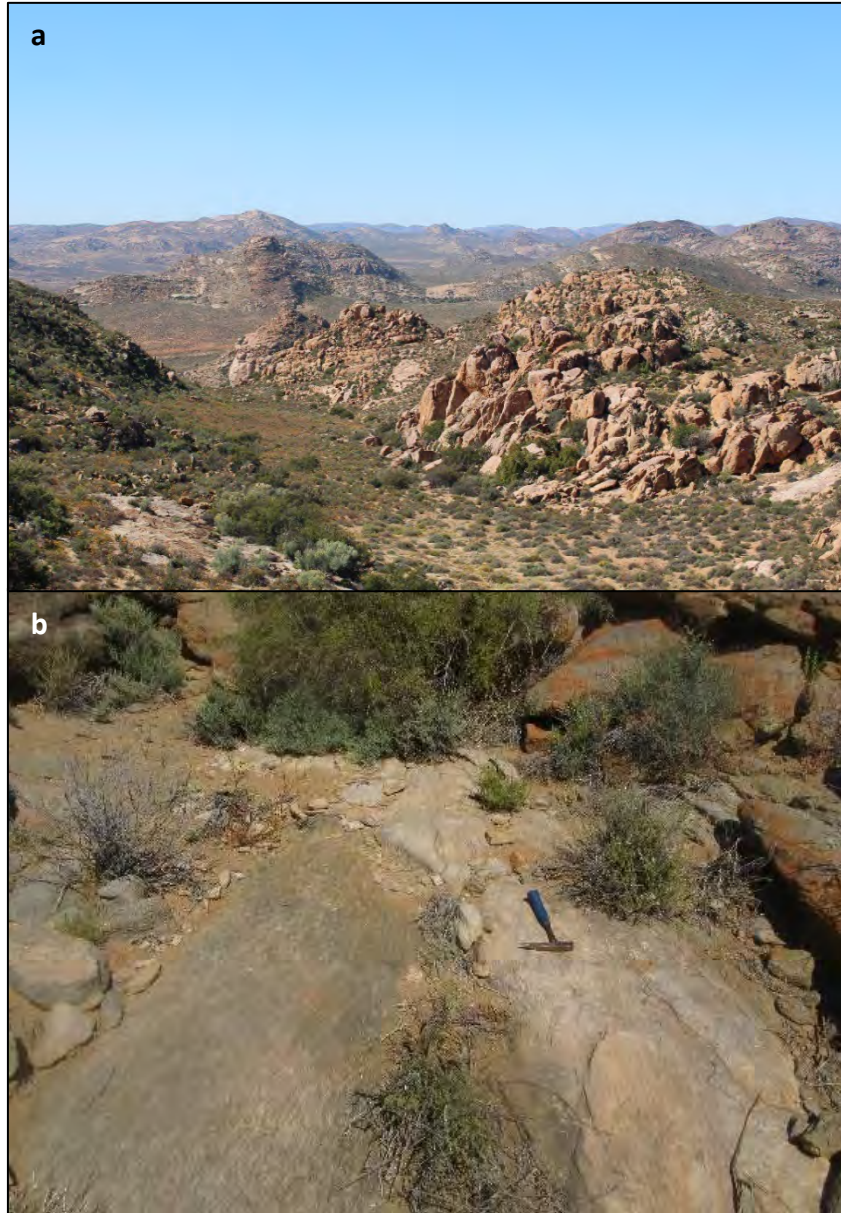
Figure 6 (a) The leucocratic gneiss is highly strained and well-foliated and outcrops are hundreds of metres long. **(b)** Sheet of pinkish Rooiplatklip Gneiss (right) intrudes across the foliation in the Mesklip Gneiss (left).

This amphibolite is composed of 50% hornblende, 25% plagioclase, 10% clinopyroxene, 7% orthoclase, 5% quartz and 3% opaque minerals with accessory amounts of zircon (Fig. 9c & d). Hornblende tends to be second order yellow and green and commonly contains inclusions of subhedral plagioclase. Hornblende has good cleavage and ranges in size from 0.2 mm to 2 mm. Hornblende is also replaced by clinopyroxene in some instances which is an indication of the onset of granulite facies metamorphism (Harlov, 2012). Plagioclase is subhedral with deformation twinning and crystal sizes ranging from 0.3 mm to 1 mm in length. Clinopyroxene has violet to pinkish yellow interference colours and ranges in size from 0.2 mm to 1 mm. Orthoclase is also present with a length ranging from 0.2 mm to 1.1 mm. Quartz is 0.2 mm to 1.1 mm in length and displays grain boundary migration. The amphibolite has a polygonal granoblastic texture with compositional banding, suggesting incomplete recrystallization.

7

Figure 7 Microphotograph of the Rooiplatklip Gneiss in crossed and plane polarisation ((**a**) and (**b**) respectively). Orthoclase is seen undergoing sericitic alteration and typical symplectite textures (development of myremekite). (qtz = quartz, ort = orthoclase, plg = plagioclase, mcr = microcline, myr = myremekite and bt = biotite), (FOV = 5 mm).

4.1.4 Hunboom Gneiss
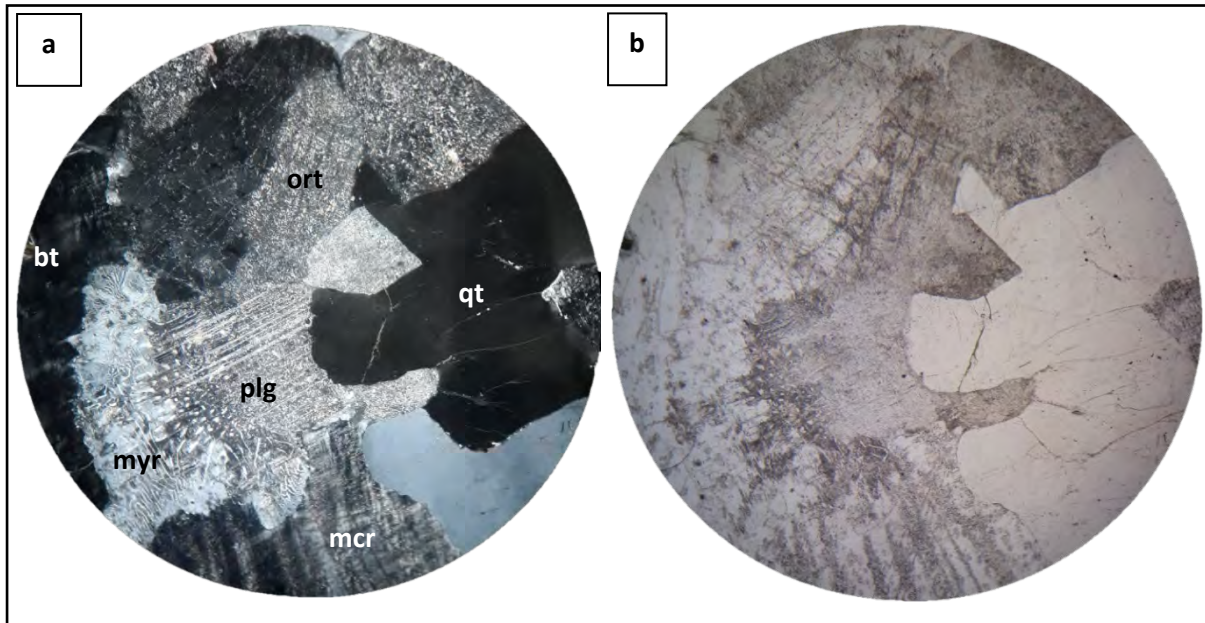
The Hunboom Gneiss is a biotite gneiss that is well exposed along the mountainous area in the south-easternmost portion of the BRSZ on the farm *Die Draai* (29.9532 S, 17.9899 E). The Hunboom Gneiss for the most part is a fine- to medium-grained, mesocratic dark grey porphyritic rock that comprises quartz, orthoclase, plagioclase, biotite, and hornblende (Fig. 10a & b.). It is a locally banded rock which resembles the Steinkopf Gneiss but lacks the latter's characteristic migmatitic character.

It is well-foliated and a flecky migmatitic texture has been observed in some instances. Melanocratic and leucocratic zones are typical of the Hunboom Gneiss with the distinct banding commonly displaying ptygmatic structures. It is also commonly intruded by weakly foliated quartzofeldspathic pink gneisses (Rooiplatklip Gneiss) of medium- to locally coarse-grained equigranular texture trending E-W. It has thicknesses ranging from 100-400 metres. Typically, it contains lenticular inclusions of amphibolite, leucogneiss, metasedimentary rocks and younger felsic intrusions with an overall trend following the regional tectonic fabric. This rock type weathers to a dark grey to greenish colour. Lenses of the Hunboom Gneiss are also commonly found within the Mesklip Gneiss with an E-W orientation.

This gneiss is composed of 30% quartz, 25% orthoclase, 20% plagioclase, 15% biotite, 7% microcline and 3% myrmekite with accessory amounts of opaque minerals (Fig. 11). Quartz is anhedral and has a diameter ranging from 0.2 mm to 2.5 mm commonly displaying undulose extinction. Orthoclase is anhedral with crystal sizes ranging between 1 mm and 2.5 mm. Poikiloblastic textures are also observed. Orthoclase has also undergone sericitic alteration. Plagioclase is anhedral with deformation twinning and ranges in size from 0.1 mm to 2.7 mm in diameter. Biotite is euhedral and ranges in size from 0.2 mm to 2.5 mm. Microcline and

8

myrmekite intergrowths are not as common as the rest of the minerals but are present at sizes ranging between 0.9 mm to 5.5 mm and 1mm for the myrmekite intergrowths respectively. Overall the biotite defines a foliation (well-foliated) and forms dark bands as seen in Figure 11a and 11b.
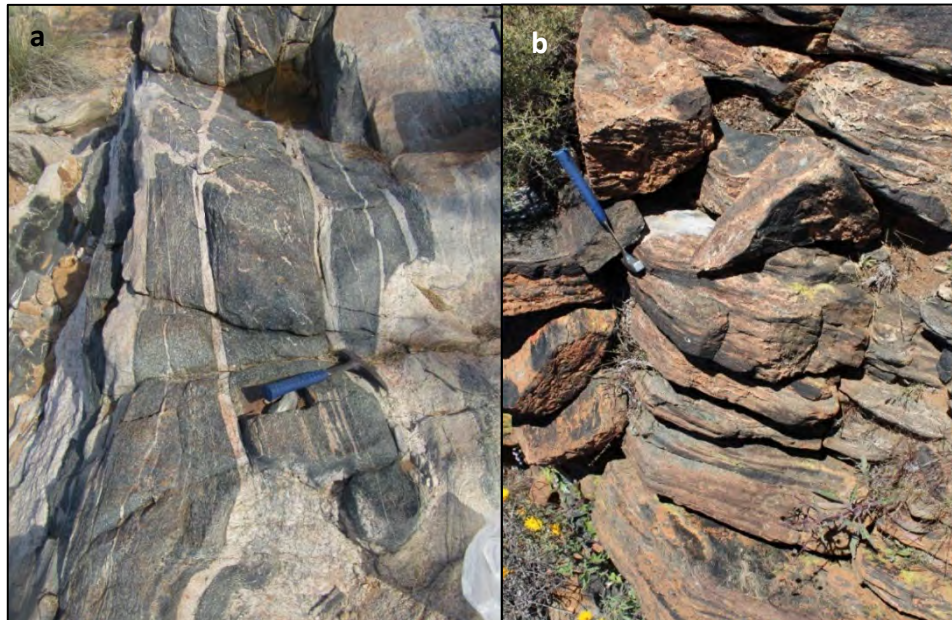
Figure 8 (a) Amphibolite rafts intruded by the Rooiplatklip Gneiss. **(b)** Brown weathering of the upright and blocky weathered amphibolite.
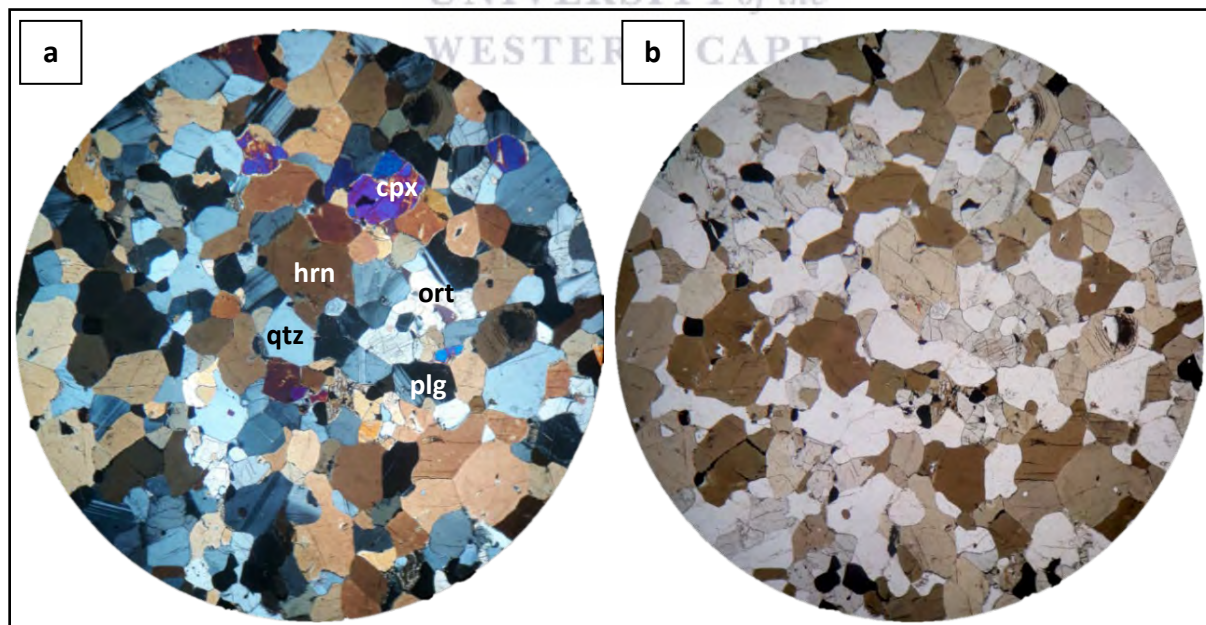
Figure 9 Microphotograph of the amphibolite in crossed and plane polarisation (**(c)** and **(d)** respectively). The abundance of quartz in this amphibolite gives the impression that it could be a para-amphibolite. (hrn = hornblende, plg = plagioclase, cpx = clinopyroxene, ort = orthoclase and qtz = quartz), (FOV = 5 mm).

9
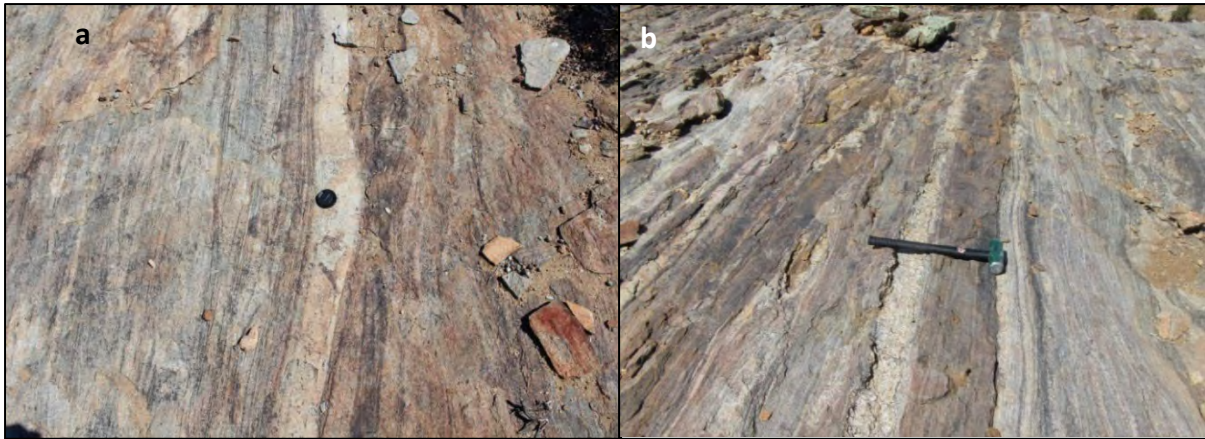
Figure 10 (a) and **(b)** The Hunboom Gneiss is a locally banded rock which resembles the Steinkopf Gneiss, but lacks the latter's characteristic migmatitic character.

4.1.5 Garnetiferous quartzofeldspathic biotite-sillimanite gneiss

The garnetiferous quartzofeldspathic biotite-sillimanite gneiss is a heterogeneous banded grey gneiss package of interlayered (1-7 m thick) metapsammitic gneiss found within the BRSZ (Fig. 12). It weathers to a medium grey-pinkish to orange colour with red garnet spots. The semi-pelite gneiss is fine- to medium-grained and consists of plagioclase, biotite, garnet, alkali feldspar, quartz and cordierite. The close relationship between the biotite and garnet delineates a well-defined ENE-WSW-trending foliation. This banded gneiss also commonly has small scale boudin-shaped inclusions of amphibolite and sillimanite-feldspar rock. It is closely associated with the intrusion of the Mesklip Gneiss.
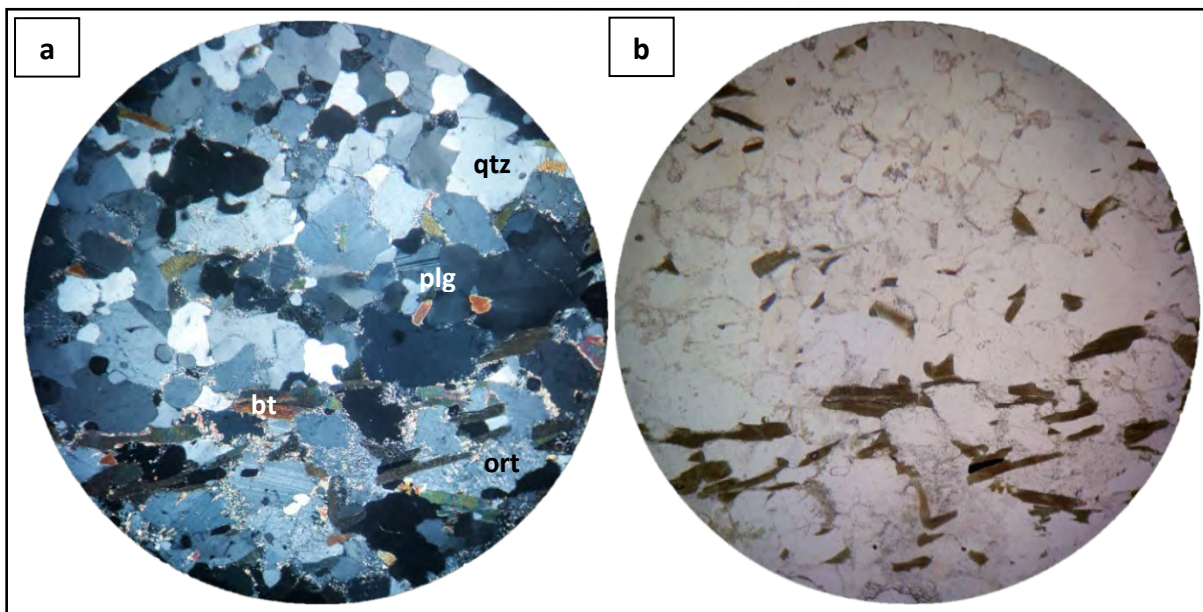
Figure 11 The Hunboom Gneiss in crossed and plane polarisation ((**a**) and **(b)** respectively). A medium-grained banded and foliated gneiss is seen in the microphotograph. Biotite can clearly be seen defining a foliation which is typical of the Hunboom Gneiss. (qtz = quartz, ort = orthoclase, plg = plagioclase and bt = biotite). (FOV = 5 mm)

10

Figure 12 *(a)* typical pale-pinkish weathering pattern of the Garnet biotite semi-pelite of the Buffels River shear zone. **(b)** and **(c)** aggregates of small garnets with biotite are observed defining the overall foliation of the rock. Light and dark coloured bands are typical of the semi-pelite.

Contacts between these two rock types are always sharp. This garnetiferous quartzofeldspathic biotite-sillimanite gneiss is composed of 25% plagioclase, 22% biotite, 20% garnet, 13% orthoclase, 10% quartz, 8% cordierite and 2% myrmekite (Fig. 13). Plagioclase ranges in size from 0.2 mm to 4.2 mm. It displays deformation twinning and has twins that taper off at the edges. Biotite ranges in size from 0.05 mm to 4 mm and is typically associated with garnet and locally occurs as inclusions within the garnet indicating the garnet grew synchronous or later. The biotite within the garnet is oblique to the overall foliation and therefore suggests that it is an earlier generation of biotite. The biotite is also well-foliated. Garnet is anhedral and ranges in size from 2 mm to 7 mm. Orthoclase ranges in size from 1 mm to 2.5 mm and displays sericitic alteration. Quartz commonly displays grain boundary migration and subgrain rotation (also evident in plagioclase) indicating incomplete recrystallization of the deformed crystal under high temperatures. Quartz ranges in size from 1 mm to 2.5 mm.

11

Figure 13 Microphotographs of the Garnet biotite semi-pelite in crossed and plane polarisation ((a) and (b) respectively (FOV=5 mm). Here garnet and biotite can clearly be seen defining the foliation. It can be observed that felsic and mafic bands are present at microscopic scale as well. (plg =plagioclase, qtz =quartz, ort = orthoclase, bt=biotite and grt=garnet)
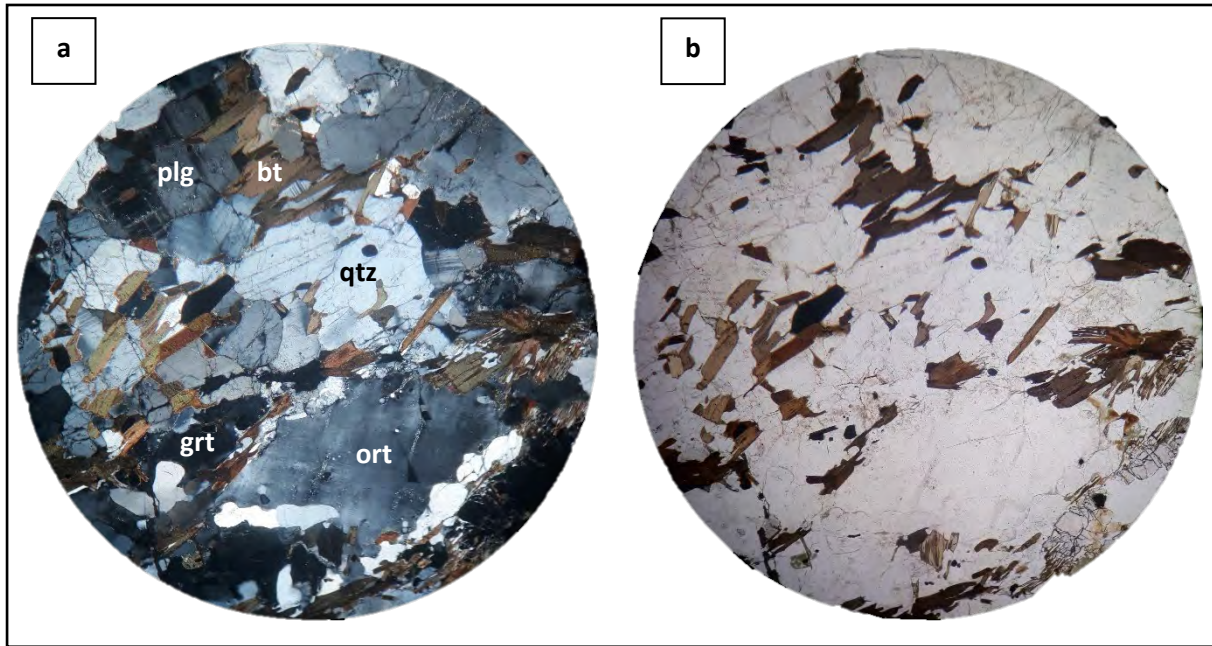
Chapter 5: Whole-rock geochemistry

5.1 Introduction

This chapter is divided into felsic magmatic rocks, mafic magmatic rocks and paragneisses. Along and surrounding the BRSZ fifty-six samples were collected and analysed. A variety of plots were then generated to characterize and classify the various lithologies found within the BRSZ.

5.2 Felsic magmatic rocks

5.2.1   Biotite and Leucocratic Augen gneiss

The granites of the Mesklip Gneiss have average SiO_2 values ranging between 68.5%-75.2%, validating its felsic nature and can be classified into the alkali-granitic to granitic field on the total alkalis vs. silica (TAS) diagram (Cox et al., 1979 adapted by Wilson, 1989) (Fig. 14a). For the construction of the QAPF diagram the CIPW norm (after Cross, Iddings, Pirsson and Washington) was utilized to calculate normative mineral percentages for quartz, alkali-feldspar and plagioclase and the Mesklip Gneiss plots within the monzogranite field (Fig. 14b).

Furthermore, the alumina saturation index (Fig. 15a) dictates the various influences the molecular proportions of Al_2O_3, Na_2O, K_2O and CaO have on the overall composition of the rock type where four subdivisions form independently of silica saturation (Barton and Young, 2002). Figure 15a indicates that the Mesklip Gneiss borders the metaluminous and weakly peraluminous boundary but is characterised by an overall weakly peraluminous nature ((ASI) Al/(Ca-3.33*P)+Na+K) molar= 1.00-1.25).

When the FeO composition is represented on a FeO_{TOT} /(FeO_{TOT}+MgO) vs. SiO_2 plot (after Frost et al., 2001) it displays two significant differences in the FeO enrichment against overall SiO_2 content which is subsequently divided into two fields, the "ferroan' and the "magnesian". Here the Mesklip Gneiss clearly plots within the "magnesian" field (Fig. 15b). Further classifying the Mesklip Gneiss with the modified alkali-lime index (MALI) vs. SiO_2 plot (after Frost et al., 2001), it has a MALI index = 2.2-9.1, of which the Mesklip Gneiss shows a range in composition ranging from alkali-calcic to calc-alkalic (Fig. 15c). In the K_2O vs. SiO_2 wt.% diagram (after Peccerilo and Taylor, 1976) the K_2O varies between 2.2-8.3 wt.% indicating that the rocks are highly potassic and falls on average within the high-K calc-alkaline series to shoshonite series (Fig. 15d).

Here Harker diagrams, used to simplify and condense large datasets of analytical data, rationalize the negative and positive relationships between major and trace elements against SiO_2. In the diagram (Appendix A, Fig. A2) SiO_2 is plotted against nine major element oxides, namely Al_2O_3, CaO, K_2O, MgO, Na_2O, P_2O_5, TiO_2, FeO_{TOT} and MnO. There is a weak negative correlation between SiO_2 and all the other major oxides except K_2O, which shows a weak positive correlation. For the Harker diagrams where SiO_2 is plotted against the trace elements (Appendix A, Fig. A3) a positive relationship can be seen for SiO_2 with Th and Rb and a negative relationship associated with Hf and V.
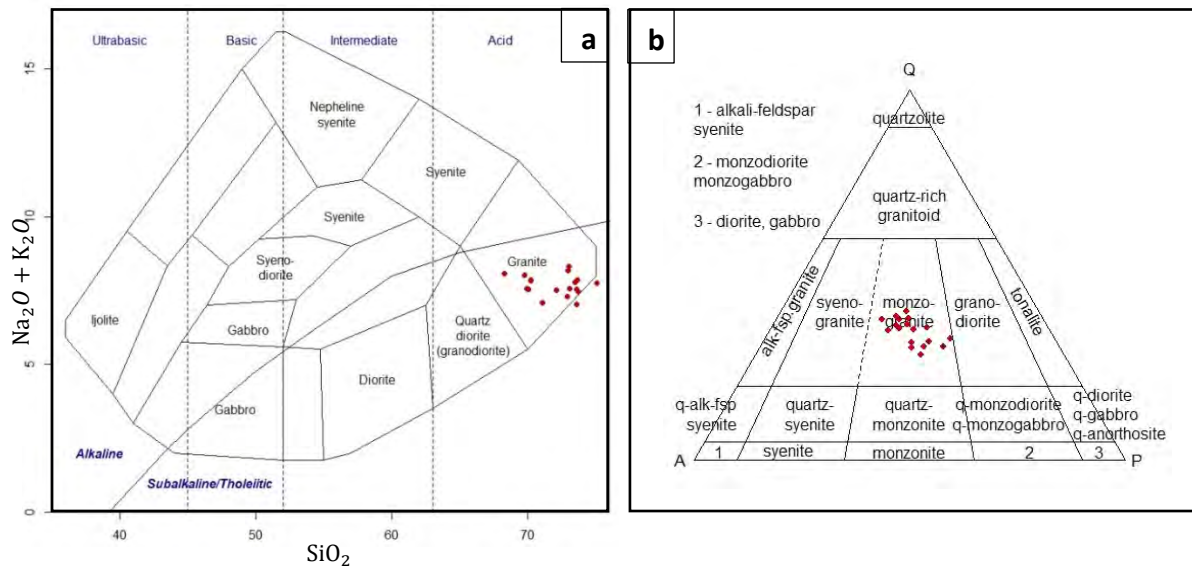
13

Figure 14 (a) TAS plutonic diagram (after Cox et al., 1979) classifying the felsic magmatic rocks of the Mesklip Gneiss in the Buffels River shear zone, and **(b)** the monzogranitic classification of the Mesklip Gneiss is represented in the QAPF diagram utilizing the CIPW norm (after Streckeisen, 1974).

In the maficity plots (Appendix A, Fig. A4) the element variation diagrams are represented by Fe + Mg vs. element atomic values where Ca, Mg, P and Ti exhibit positive correlations when compared to the negative trends exhibited by K and Si. Other element variation comparisons such as Al and Na have positively trending yet scattered correlations. For maficity plots against trace elements (Appendix A, Fig. A5), Hf, La, Nb and Zr, exhibit strong positive correlations. The other trace elements have poor correlations and variable relationships when plotted against maficity and a large amount of scattered data.

The rare earth element (REE) diagram is normalised to the primitive mantle values (after McDonough and Sun, 1995) (Fig. 16a). Overall the REE pattern is moderately negatively sloping ($[La/Yb]_{PM} = 8.24$) with a negative Eu anomaly that ranges between 0.4 and 2.2. The light REE (LREE) have a moderate steep slope with $[La/Sm]_{PM}$ values ranging 2.86 from to 10.48 with an average of 4.62. The heavy REE (HREE) are characterised by a slight negative to flat trend, with $[Gd/Lu]_{PM}$ values ranging from 1.24 to 5.11 with an average value of 2.42.

The Mesklip Gneiss has been normalised to the primitive mantle values of Sun and McDonough (1989) in the form of a multi-element trace element plot called a spider diagram. It is shown here with a gradual decrease in elemental concentration from left to right of Cs to Lu respectively (incompatible to compatible elements) indicating a slightly negative trend (Fig. 16b) but with intermittent peaks and troughs which represent enrichments and depletions of certain elements throughout the diagram. Overall there is a slight enrichment of the Large-ion Lithophile Elements (LILE) over the High Field Strength Elements (HFSE). Depletions are represented by the LIL element Ba, and the HFS elements Nb, P and Ti, whereas enrichments are typified by LIL elements Cs, K, Pb and Rb, and HFS elements Th, La, Nd and Zr.

14
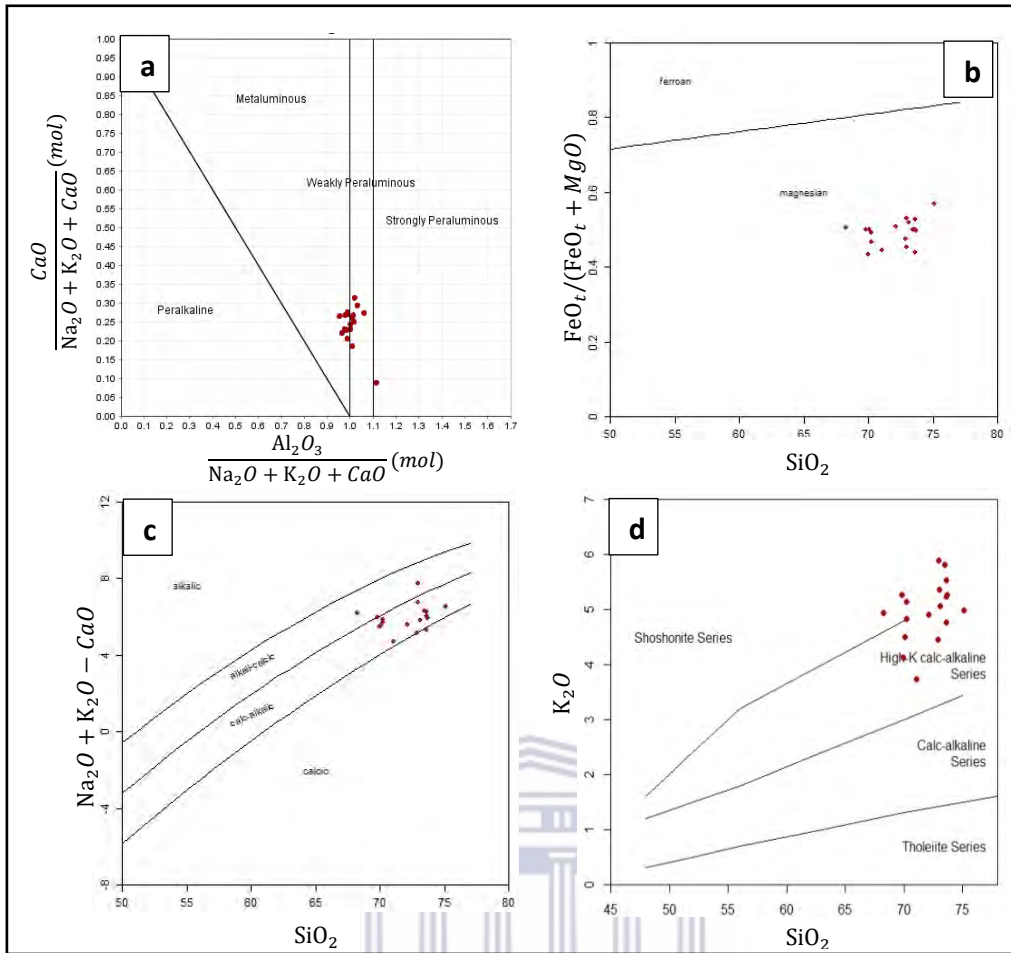
Figure 15 (a) C/NKC vs. A/NKC plot of the alumina saturation in the Mesklip Gneiss by Barton and Young (2002). **(b)** FeO composition is represented on a $FeO_{TOT}/(FeO_{TOT}+Mgo)$ vs. SiO_2 plot (Frost et al., 2001). (**c**) Modified alkali lime index of $Na_2O + K_2O - CaO$ vs. weight percent SiO_2. **(d)** K_2O vs. SiO_2 diagram by Peccerillo and Taylor (1976).
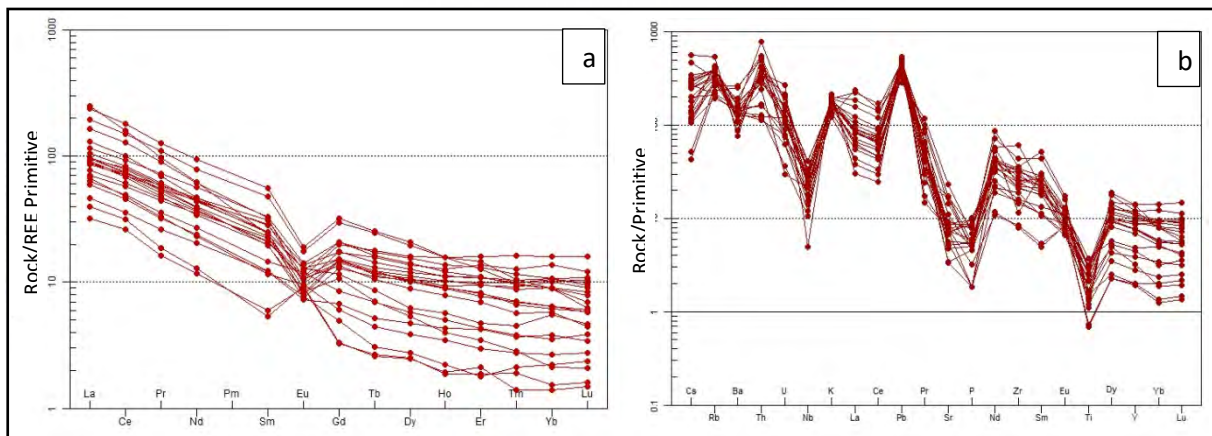
Figure 16 (a) REE Primitive mantle normalised plot normalized to the values of McDonough and Sun (1995) and **(b)** Primitive Mantle-normalised multi-element diagram of Sun and McDonough (1989) of the Mesklip Gneiss of the Buffels River shear zone.

5.2.2 Leucogneiss

The granites of the Rooiplatklip Gneiss have average SiO_2 values ranging between 68.7%-77.5 wt.%, validating its felsic nature and can be classified into the alkali-granitic to granitic field

15

(Fig. 17a) on the TAS diagram (Cox et al., 1979). The CIPW norm was utilized to calculate normative mineral percentages in the QAPF diagram, for quartz, alkali-feldspar and plagioclase respectively. The Rooiplatklip Gneiss plots within the monzogranite field (Fig. 17b). The alumina saturation index (Fig. 18a) reflects that the Rooiplatklip Gneiss is characterised as having an overall weakly peraluminous nature ((ASI) (Al/(Ca-3.33*P+Na+K) molar = 1.16-1.37). In the $FeO_{TOT}/(FeO_{TOT}+Mgo)$ vs. SiO_2 plot (Frost et al., 2001) the Rooiplatklip Gneiss clearly plots within the "magnesian" field (Fig. 18b). Further classifying the Rooiplatklip Gneiss using the MALI vs. SiO_2 plot, where it has a MALI index= 4.21-8.70. This indicates that the Rooiplatklip Gneiss shows a range in composition plotting in the fields ranging from alkali-calcic to calc-alkalic (Fig. 18c). In the K_2O vs. SiO_2 wt.% diagram (Fig. 18d) the K_2O content varies between 3.48-6.72 wt.% indicating the rocks are highly potassic and falls on average within the high-K calc-alkaline series to shoshonite series.

In the Harker diagrams (Appendix A, Fig. A6) there is a weak negative correlation between SiO_2 and MgO, TiO_2, FeO and CaO while Al_2O_3, K_2O, Na_2O and P_2O_5 are generally scattered with no trend. The slope of the negatively correlating major elements are quite steep. For the Harker diagrams where SiO_2 is plotted against the trace elements (Rb, Sr, Y, Zr, Ba, La, Co, Hf, Nd and V) a somewhat positive relationship can be seen with Rb and a steeply negative sloping relationship is associated with all other trace elements (Appendix A, Fig. A7).

In the maficity plots (Appendix A, Fig. A8) the element variation diagrams for the Rooiplatklip Gneiss are represented by Fe+Mg vs. element atomic values where Ca, Mg, P and Ti exhibit positive correlations, whereas Al, K, and Na exhibit relatively flat to variably scattered plots. Si is the only major element to exhibit a negative trend against Fe+Mg. For maficity plots against the trace elements (Appendix A, Fig. A9), Sr, Zr and Ba exhibits strong positive correlations and La, Ce, Sm, Nd, and Hf have fairly positive correlations with similar patterns. Rb is the only trace element that has a negative correlation with Fe+Mg.

The REE diagram is normalised to the primitive mantle values of McDonough and Sun (1995) (Fig. 19a). Overall the REE pattern is moderately negatively sloping (average $[La/Yb]_{PM}$ = 34.5), with mostly negative Eu anomalies and three positive Eu anomalies that ranges between 0.48 and 2.17. The LREE have a moderately steep negative slope with $[La/Sm]_{PM}$ values ranging from 4.04 to 8.03 with an average of 5.16. When compared to that of the HREE they are represented by a slight negative pattern to flat trend, with $[Gd/Lu]_{PM}$ values ranging from 0.98 to 7.42 with an average value of 3.51.

The Rooiplatklip Gneiss has been normalised to the primitive mantle values of Sun and McDonough (1989). It has a gradual decrease in elemental concentration from left to right (incompatible to compatible elements) and showing a slightly negative to flat trend (Fig. 19b) but with intermittent peaks and troughs which represent enrichments and depletions. Overall there is a slight enrichment of the LILE over the HFSE. Depletions are represented by the LIL elements Ba, U and Eu, and the HFS elements Nb, P, Zr and Ti, whereas enrichments are typified by LIL elements Cs, K, Pb and Rb, and HFS elements Th, La and Nd.

16

**Figure 17 (a)** TAS plutonic diagram (after Cox et al., 1979) classifying the felsic magmatic rocks of the Rooiplatklip Gneiss in the Buffels River shear zone, and **(b)** the monzogranitic classification of the Rooiplatklip Gneiss is represented in the QAPF diagram utilizing the CIPW norm (after Streckeisen, 1974).

17
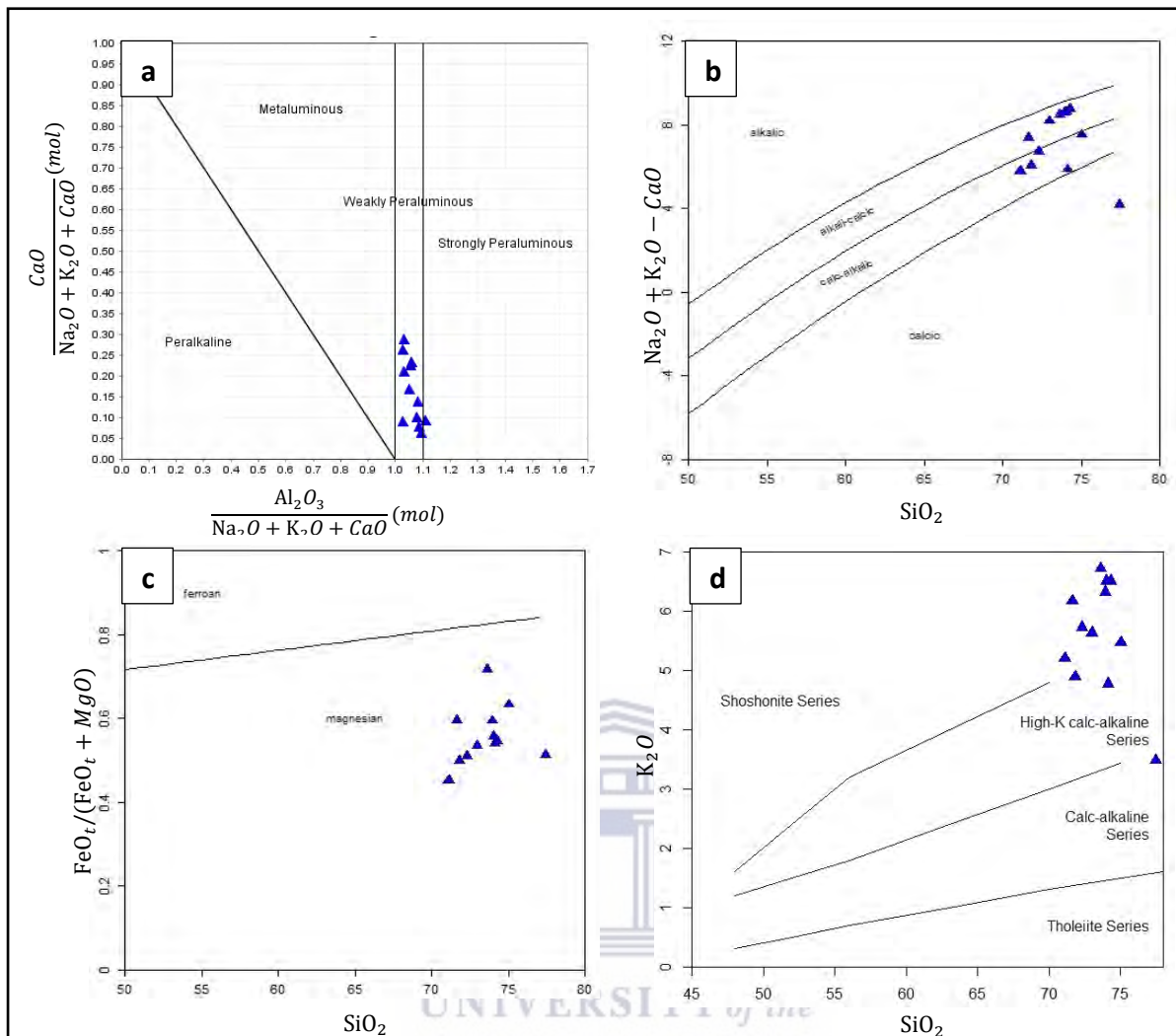
Figure 18 (a) C/NK vs. A/NK plot of the alumina saturation in the Rooiplatklip Gneiss by Barton and Young (2002). **(b)** FeO composition is represented on a FeO$_{TOT}$/(FeO$_{TOT}$+Mgo) vs. SiO$_2$ plot (Frost et al., 2001). **(c)** Modified alkali lime index of $Na_2O + K_2O - CaO$ vs. weight percent SiO_2). **(d)** K_2O vs SiO_2 diagram by Peccerillo and Taylor (1976).

Figure 19 (a) REE Primitive mantle normalised using the values of McDonough and Sun (1995) and **(b)** Primitive Mantle-normalised multi-element diagram of Sun and McDonough (1989) of the Rooiplatklip Gneiss of the Buffels River shear zone.

18

5.3 Mafic magmatic rocks

5.3.1   Mafic rocks

The mafic magmatic rocks of the Oorkraal Suite have SiO_2 values ranging between 44.86% and 59.82% (basic to intermediate), validating its mafic nature and can be classified into three fields, namely gabbro, syeno-diorite and diorite (Fig. 20a) on the TAS plutonic diagram (after Cox et al., 1979). In the K_2O vs. SiO_2 wt.% diagram (Fig. 20b) the K_2O varies between 3.48-6.72 wt.% indicating the rocks are highly potassic and falls on average within the high-K calc-alkaline to shoshonite series.

In the binary major element plot (Appendix A, Fig. A10) MgO is plotted against nine major oxides, namely Al_2O_3, CaO, K_2O, Na_2O, P_2O_5, SiO_2, TiO_2, FeO_{TOT} and MnO. There is a strong negative correlation between MgO and SiO_2. There is a positive correlation between MgO and the following oxides; CaO, TiO_2, FeO_{TOT} and MnO. For the binary trace element plots where MgO is plotted against the trace elements (Rb, Sr, Y, Zr, Ba, La, Co, Hf, Nd and V) the only discernible relationship can be seen between MgO and V, as well as Zr, both displaying an increase in content as MgO increase (Appendix A, Fig. A11). These two trends seem to become steeper approaching the higher MgO content samples.

The CIPW norm was utilized to calculate normative mineral percentages of the QAPF diagram, for quartz, alkali-feldspar and plagioclase respectively. The Oorkraal Suite samples 004B, 013B, 013C, 041A, and 041B plot within the quartz monzodiorite field and sample 026B plots within the quartz syenite field (Appendix A, Fig. A12-a). Furthermore, two IUGS classification ternary diagrams for mafic rocks were generated that plot plagioclase, pyroxene and hornblende and plagioclase, pyroxene and olivine respectively, to further classify the rest of the mafic rocks (Appendix A, Fig. A12-b & A12-c). Sample 014D is classified as a plagioclase-bearing hornblende norite on the plagioclase, pyroxene and hornblende ternary diagram (Appendix A, Fig. A12-c) and samples 008C, 008C1 and 013F plot in the olivine gabbronorite field, sample 020C plots within the gabbronorite field, with samples 011C, 035B and 035C plot within the leuco-gabbro field (Appendix A, Fig. A12-b).

Overall the REE pattern (Fig. 21a) has a moderate to steep negative slope (average $[La/Yb]_{PM}$ =25.17) with a negative Eu anomaly that ranges between 0.73 and 1.01. The LREE have a moderately steep slope with $[La/Sm]_{PM}$ values ranging from 1.20 to 4.96 with an average of 3.08. The HREE are characterised by a slightly negatively sloping to flat trend, with $[Gd/Lu]_{PM}$ values ranging from 1.17 to 11.18 with an average value of 3.51.

The Oorkraal Suite rocks have been normalised to primitive mantle values of Sun and McDonough (1989). There is a gradual decrease in elemental concentration from incompatible to compatible elements indicating a slightly negative to flat trend (Fig. 21b). Overall there is a slight enrichment of the LILE over the HFSE. There is scattered trend particularly in the LILE and LREE suggesting a degree of remobilization and element mobility. Depletions are represented by the LIL element Rb, and HFS elements Nb and Zr, whereas enrichments are typified by the LIL elements K and Pb, and the HFS element Nd.
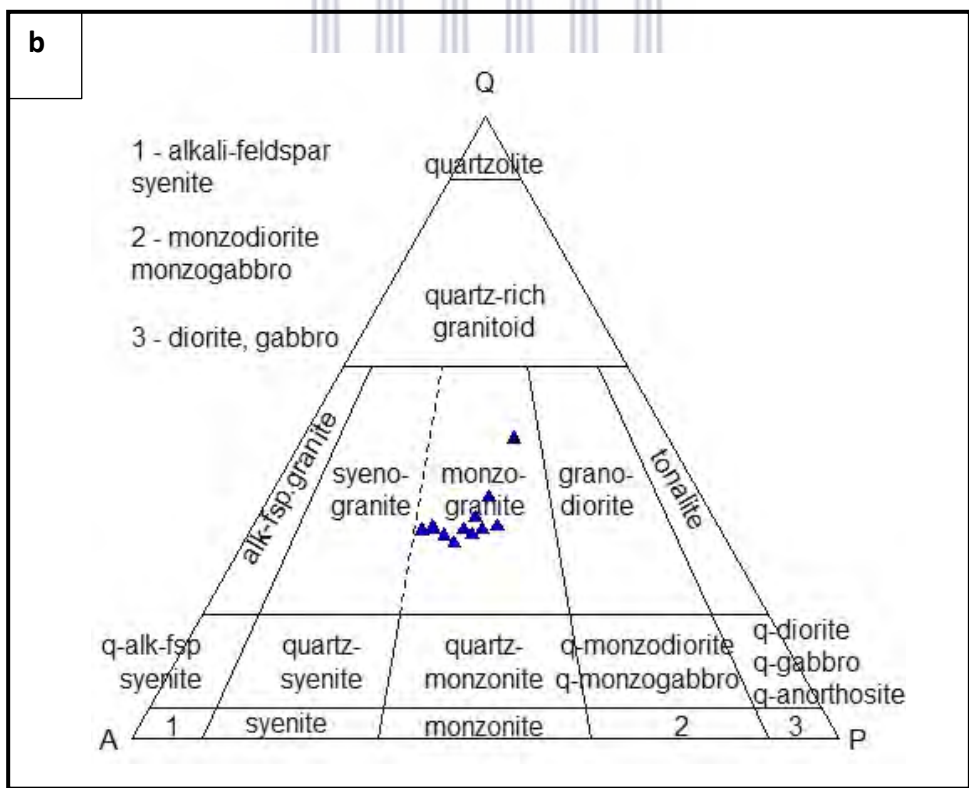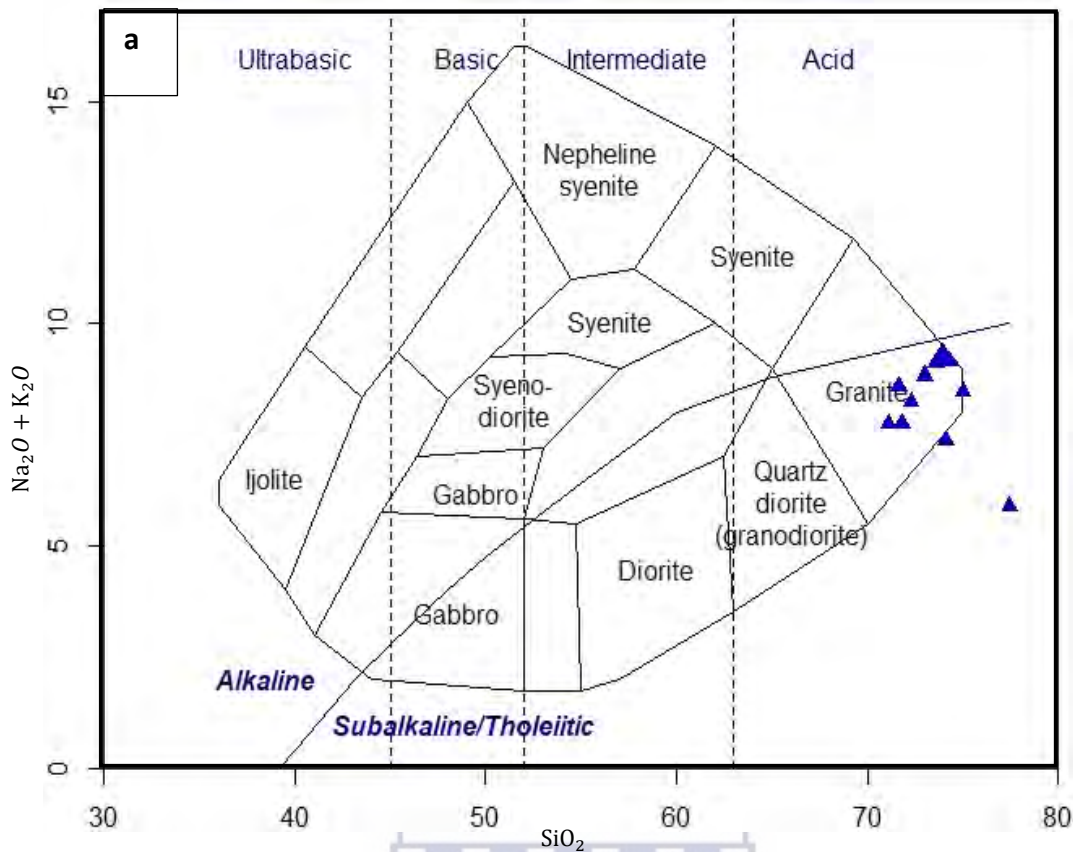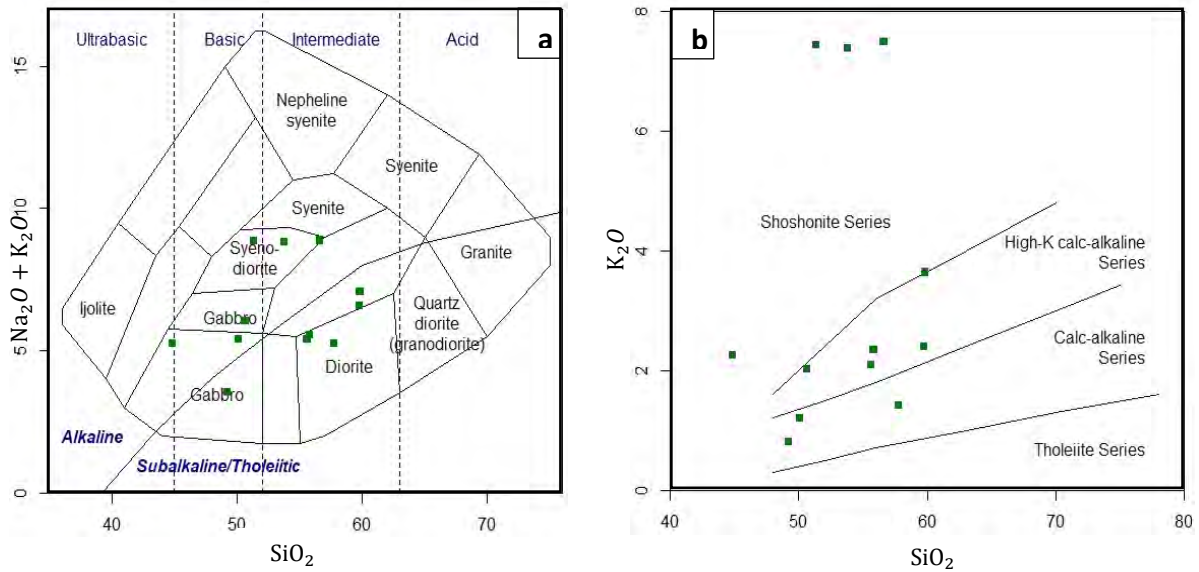
Figure 20 (a) TAS plutonic diagram (after Cox et al., 1979) classifying the mafic magmatic rocks of Oorkraal Suite rocks in the Buffels River shear zone. **(b)** K_2O $vs.$ SiO_2 diagram by Peccerillo and Taylor (1976).
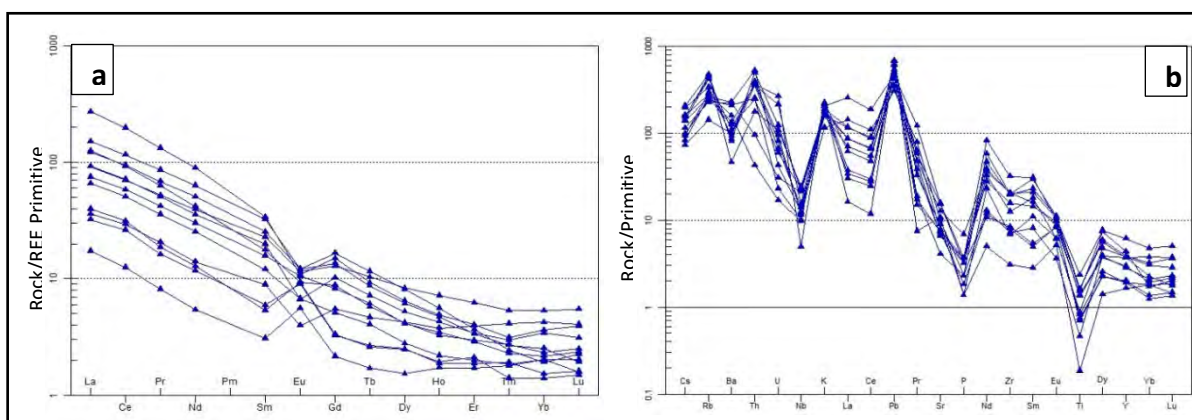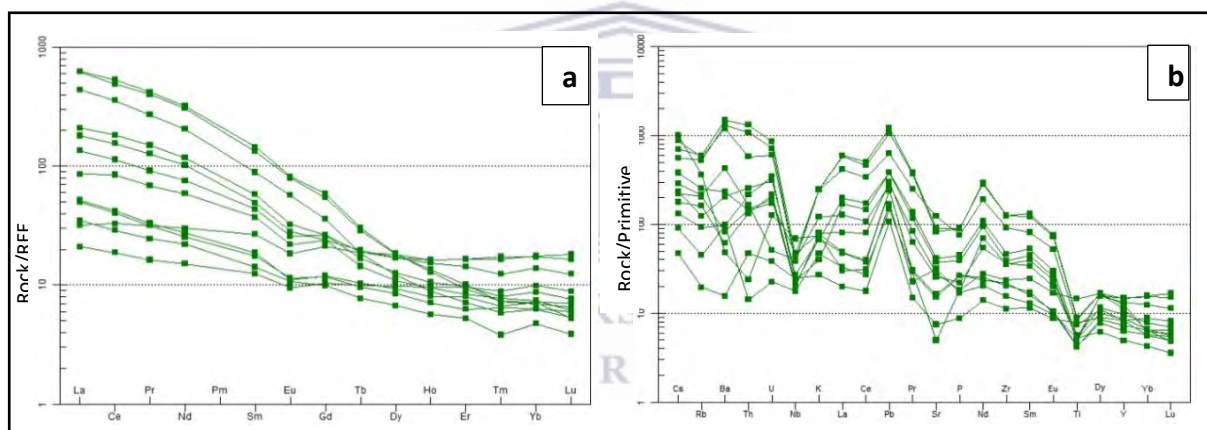

Figure 21 (a) REE Primitive mantle normalised values of McDonough and Sun (1995) and **(b)** Primitive Mantle-normalised multi-element diagram of Sun and McDonough (1989) of the Oorkraal Suite rocks in the Buffels River shear zone.

5.4 Paragneisses

5.4.1 Biotite gneiss

The biotite gneisses of the BRSZ are closely associated with the metapelitic and metapsammitic gneisses. They are commonly seen interbanded with the metasedimentary sequence and their origins have been broadly theorized in the past. According to Moore (1989) two main opinions exist pointing to a sedimentary, broadly arkosic origin (von Backstrom, 1964; Kroner, 1968; Paizes, 1975; Jack, 1980; Moore, 1989) and an opposing intrusive igneous origin (McCarthy, 1976; Lipson, 1978; SACS, 1980; Lipson, 1990). Moore (1989) challenges this approach to explore the origins of the biotite gneisses as extrusive acid volcanic rocks. Here the same approach will be used where various geochemical diagrams will be utilized to characterize the biotite gneisses of the BRSZ.

The supracrustals of the Hunboom Gneiss have average SiO_2 values ranging between 66.16-73.64%, validating its felsic nature and can be classified into the alkali-granitic to granitic field

20

(Fig. 22a) on the TAS diagram (after Cox et al., 1979). The streaky grey biotite gneisses of the Hunboom Gneiss have high concentrations of Al_2O_3 (13.25-15.47%), Fe_2O_3 (2.37-6.93%), Na_2O (2.82-4.80%), and K_2O (2.14-5.76%), and relatively low concentrations of TiO_2 (0.27-0.85%), CaO (1.10-2.81%) and MgO (0.36-2.40%).
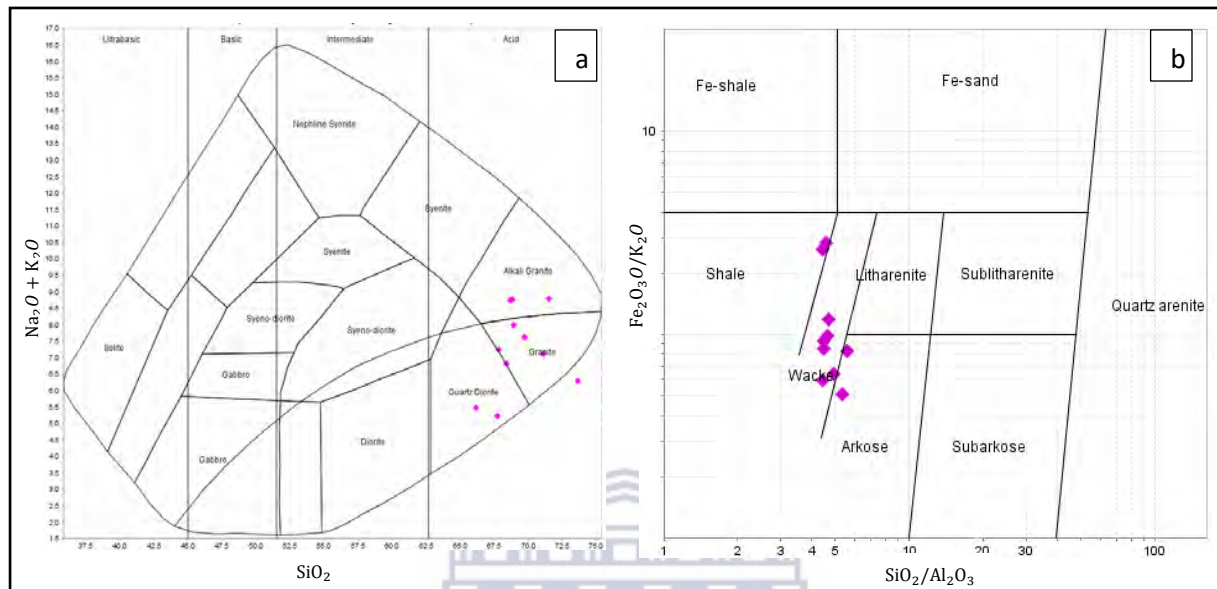
Figure 22 (a) TAS plutonic diagram (after Cox et al., 1979) classifying the rocks of Hunboom Gneiss in the Buffels River shear zone. **(b)** Herron (1988) classification diagram of log (Fe_2O_3/K_2O) *vs.* log (SiO_2/Al_2O_3) classifying the rocks mostly as wackes.
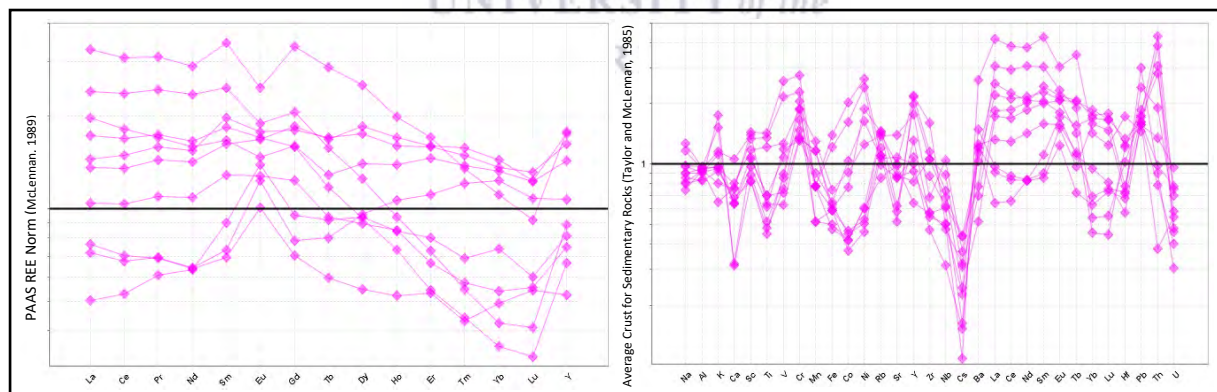
Figure 23 (a) PAAS REE normalised values after McLennan (1989) and **(b)** Average crustal values for multi-element diagram after Taylor and McLennan (1995) for the Hunboom Gneiss rocks of the Buffels River shear zone.

The Herron (1988) classification diagram of log (Fe_2O_3/K_2O) vs. log (SiO_2/Al_2O_3) is used to classify the Hunboom Gneiss based on its distinction between quartz-rich high-ratio sandstones and clay-rich, low ratio shales (Herron, 1988). In Figure 22b it can be seen that the majority of the Hunboom Gneiss samples plot within the wacke field with four samples plotting outside this field, namely samples 028C1 and 024C plotting within the arkose field and samples 012A and 012B plotting within the shale field.

21

The REE diagram is normalised to the Post-Archean Australian Shale norm (PAAS; after McLennan, 1989) (Fig. 23a). Overall the REE pattern is moderately negatively sloping (average $[La/Yb]_{PM}$ =2.16) with six samples having a negative Eu anomaly that ranges between 0.72 and 1.62, with the rest of the samples having a steep positive Eu anomaly. The LREE has a flat trend with $[La/Sm]_{PM}$ values ranging from 0.56 to 1.18 with an average of 0.91. When compared to that of the HREE they are represented by a moderately negative pattern, with $[Gd/Lu]_{PM}$ values ranging from 0.73 to 5.00 with an average value of 2.35.

The streaky biotite gneisses of the Hunboom Gneiss have been normalised to average crustal values of Taylor and McLennan (1985) (Fig. 23b). The major element Al is slightly depleted, with Ca and Ti displaying moderate depletions whereas K has a moderate positive anomaly. With regard to the LIL elements, Rb, Pb and Ba have positive anomalies as compared to Cs and Sr which display relatively strong depletions. Nd is the only HFSE that has a prominent positive anomaly whereas Ce is slightly depleted and Zr, Hf and Nb are moderately depleted. The HFSE Hf and U display prominent negative anomalies. Sc, V, Ni and Co have strong positive anomalies and Mn has a strong negative anomaly.

5.4.2 Garnetiferous quartzofeldspathic biotite-sillimanite gneiss

The supracrustals of the Kamiesberg Subgroup rocks have SiO_2 values ranging between 58.48 and 64.08% (acidic), validating their intermediate nature (Fig. 24a). The garnetiferous quartzofeldspathic biotite-sillimanite gneiss of the Kamiesberg Subgroup has high concentrations of Al_2O_3 (16.1-17.11%), Fe_2O_3 (6.61-8.96%), MgO (1.89-4.29%) and K_2O (3.07-4.57%), along with relatively low concentrations of Na_2O (0.79-3.64%), TiO_2 (0.86-1.22%) and CaO (0.83-2.28%).

The Herron (1988) classification diagram of log (SiO_2/Al_2O_3) vs. log (Fe_2O_3/K_2O) is used to classify the Kamiesberg Subgroup rocks based on their distinction between quartz-rich high-ratio sandstones and clay-rich, low ratio shales (Herron, 1988). In Figure 24b it can be seen that all three rock samples of the Kamiesberg Subgroup plot within the shale field.

The REE diagram is normalised to the PAAS REE values (McLennan, 1989) (Fig. 25a). Overall the REE pattern is relatively flat to slightly negatively sloping (average $[La/Yb]_{PM}$ =1.28) with one sample having a negative Eu anomaly. The Eu anomaly values range between 0.76 and 1.13. The LREE have a flat trend with $[La/Sm]_{PM}$ values ranging from 0.68 to 0.98 with an average of 0.88. When compared to that of the HREE two samples continue as a relatively flat pattern and one sample is represented by a prominent negative pattern, with $[Gd/Lu]_{PM}$ values ranging from 1.11 to 3.26 with an average value of 1.85.

The garnetiferous quartzofeldspathic biotite-sillimanite gneiss of the Kamiesberg Subgroup has been normalised to average crustal values of Taylor and McLennan (1985) (Fig. 25b). The major element Na is slightly depleted, with Mn and Ca moderately to prominently depleted respectively. K shows a slightly positive anomaly whereas Al is strongly enriched. With regard to the LIL elements, Ba displays a positive anomaly compared to Rb and Pb which are slightly depleted and Cs and Sr have moderate negative anomalies. All the HFSE have negative anomalies, where Ce tends to have a rather flat to negative trend, Zr and Hf are slightly depleted and U and Th are moderately depleted when compared to the prominent negative anomaly displayed by Ti. Sc, V, Ni and Co have strong positive anomalies.
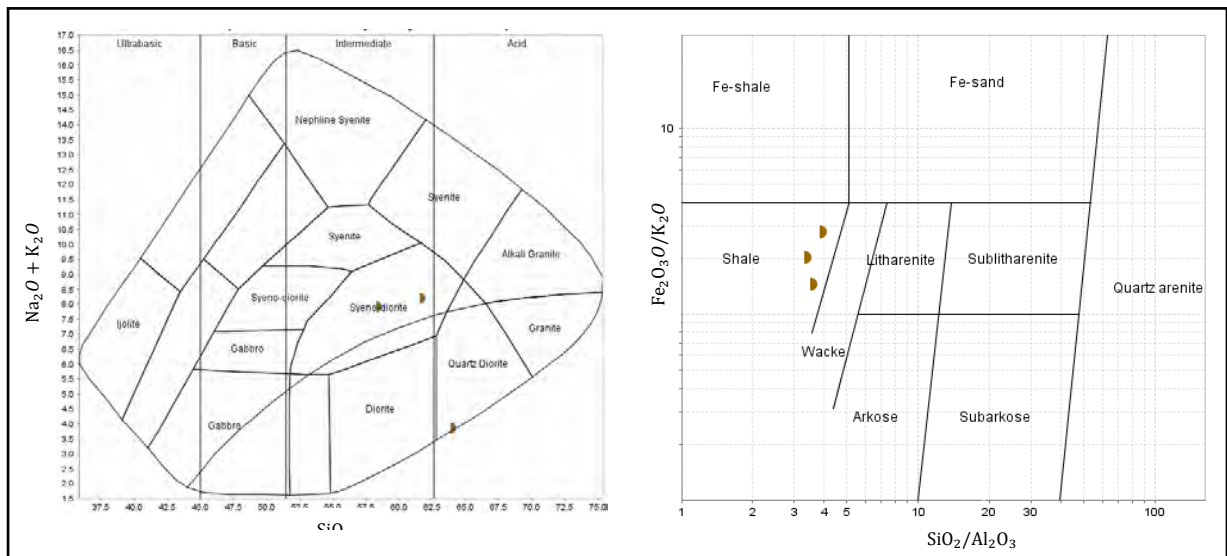
Figure 24 (a) TAS plutonic diagram (after Cox et al., 1979) classifying the rocks of Kamiesberg Subgroup rocks in the Buffels River shear zone. **(b)** Herron (1988) classification diagram of log (SiO$_2$/Al$_2$O$_3$) vs. log (Fe$_2$O$_3$/K$_2$O) classifying the rocks as shale.
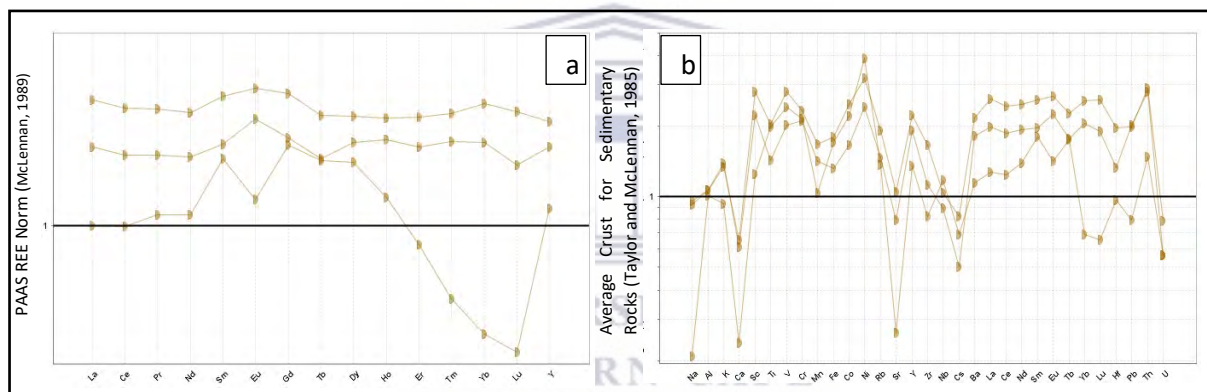
Figure 25 (a) REE plot normalized to the PAAS values of McLennan (1989) and **(b)** Multi-element normalized to average crustal values using the values of Taylor and McLennan (1995) for the Kamiesberg Subgroup rocks of the Buffels River shear zone.

23

Chapter 6: Geochronology

6.1 Introduction

A total of eight samples were submitted for analyses, of which seven yielded reliable results, namely three of the Mesklip Gneiss, one Rooiplatklip Gneiss, one garnet-biotite semi-pelitic gneiss and two Hunboom Gneiss samples and will be discussed in detail in this chapter. Data with a concordance of between 95-102% was used for the analyses of all samples in determining the concordia ages and discordant data were used when determining the upper intercept ages (2 sigma level of uncertainty applied to all analyses). Data tables are inserted at the end of each sample description. A table with locations of sample points as well as a sample location map are given in the Appendix (Table B2 and Fig. A13). In addition to this, each of these geochronology descriptions will include their analysed Sr−Rb and Sm−Nd isotopes and calculated isotopic ratios, of which age dates used in the calculations below are taken from the geochronological age data obtained in this study. The εNd(t) function is also calculated and described for each sample. Isotopic concentrations and calculations as well as the εNd(t) vs. age plot for each sample are presented in Table B3 and Figure A14 respectively, in the Appendix.

6.2 Magmatic rocks

6.2.1   Mesklip Gneiss: Sample 034D

Sample 034D is a porphyroclastic, medium- to coarse-grained streaky augen gneiss collected at a road cut exposure along the N7 (29 $^\circ$ 53.133' S, 17 $^\circ$ 52.400' E). Forty spots were analysed on 19 zircons. The zircons are subhedral to rounded, with flat to round terminations, possibly abraded due to physical grinding during sample preparation as seen in Figure 26 (e.g. spot 034D-25). The zircons are approximately 100-250 μm in size (Fig. 26). Overall the CL images of these zircons exhibit cores with bright luminescence (spots 034D-06, 034D-13, 034D-18, 034D-30, 034D-32 and 034D-39), surrounded by dark overgrowths or rims. Internally, the cores are mostly unzoned but some display convoluted zonation (spot 034D-25) and indistinct oscillatory zoning (e.g. spot 034D-15). Analyses 034D-05, 034D-10, 034D-11 and 034D-12 are metamict.

Sample 034D provided 26 concordant dates from a total of 40 analyses (Table 2). Of the 26 analyses, 15 were from rim regions, and 11 were from core regions. The remaining results were discordant. One inherited age and three prominent age populations were observed from the U-Pb Concordia plot (Fig. 27). The analyses show that one zircon, which has a bright zoned core (spot 034D-39), yields a ^{206}Pb/^{238}U inheritance age of 1880 ± 44 Ma (Fig. 27). The U value for this bright zoned core is 234 ppm with a Th/U of 0.59. The predominant age grouping is observed between 1254 Ma and 1202 Ma (Fig. 27, Table 2) and typical characteristics of zircons from this age grouping are bright, as well as disrupted and convoluted zoned cores with thick dark overgrowths or rims (Fig. 26; spots 034D-13, 034D-18, 034D-30 & 034D-32). Uranium values for the bright cores range between 81 and 446 ppm with Th/U of between 0.55 and 0.75. The U values for the dark overgrowth rims of this population yield values ranging between 295 and 875 ppm with Th/U of between 0.38 and 0.50. This population has a calculated ^{206}Pb/^{238}U concordia age of 1224 ± 5 Ma (MSWD = 1.07) and, based on the above characteristics, is considered the crystallization age of this sample (Fig. 27).

24
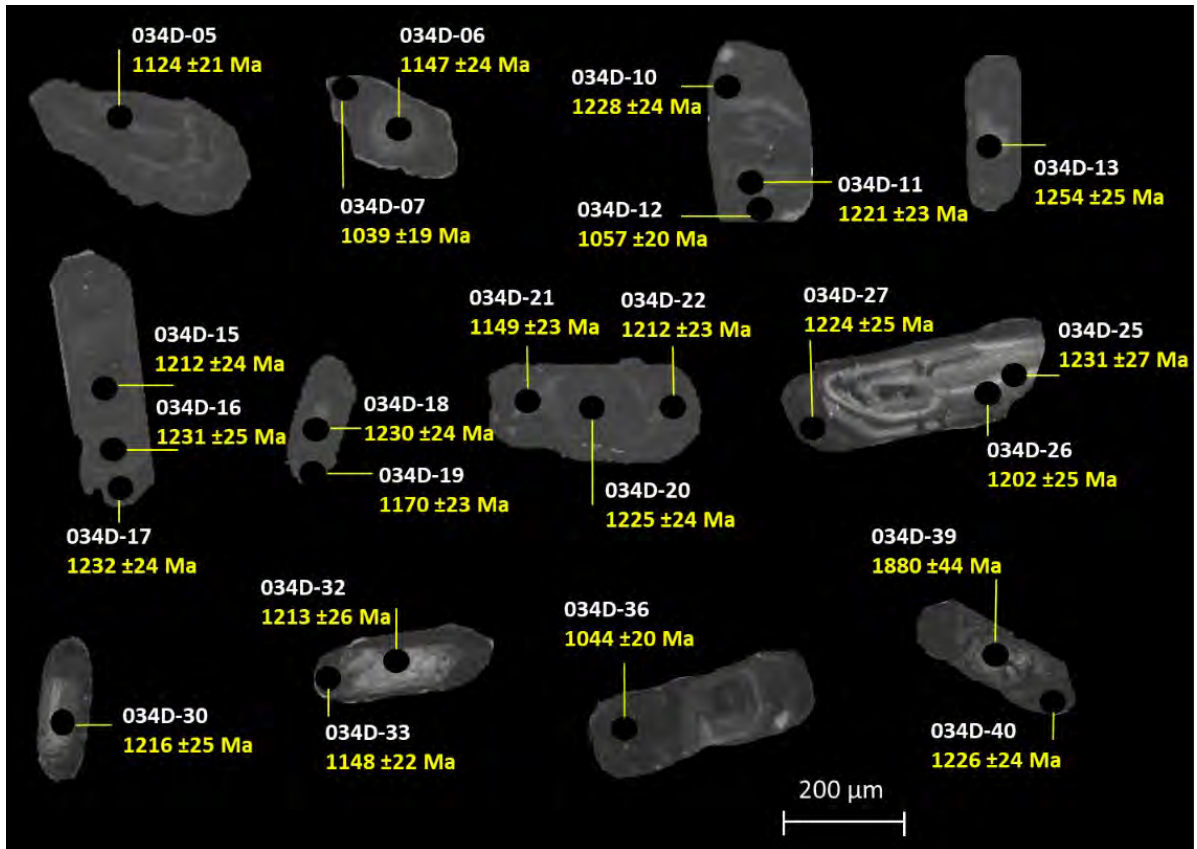
Figure 26 CL images of zircons collected from sample 034D. Each spot, represented by a black circle, has been labelled with the analyses/spot number and the calculated $^{206}Pb/^{238}U$ ages.
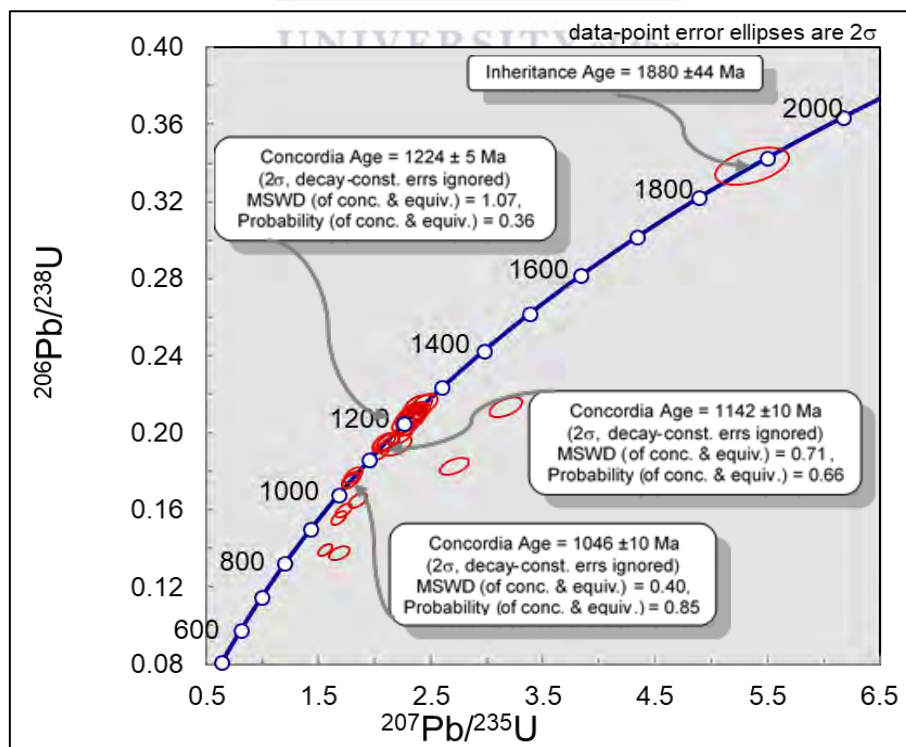
Figure 27 U-Pb concordia plot of sample 034D displaying minor discordance. The concordia plot for near-concordant analyses is used to calculate weighted mean $^{206}Pb/^{238}U$ ages of the three concordant ages in sample 034D. Confidence limits for the error ellipses are expressed as 2σ.

Two concordant age groupings are considered to represent a metamorphic overprint with $^{206}Pb/^{238}U$ concordia ages of 1142 ± 10 Ma (MSWD= 0.71) and 1046 ± 10 Ma (MSWD= 0.40), respectively. The older metamorphic age population is represented by spot 034D-06, which is characterised by a bright unzoned core (U = 153 ppm, Th/U = 0.56; Table 2), along with analyses 034D-21 and 034D-33 characterised by dark, thick overgrowths (Fig. 26) with U values of 284 ppm and 655 ppm respectively, with Th/U of 0.37 and 0.35 respectively. The younger metamorphic age population (spots 034D-07, 034D-12 and 034D-36) are all characterized by dark, thick unzoned rims (Fig. 26). The U values for this population ranges between 534 and 871 ppm with Th/U of between 0.11 and 0.18.

6.2.1. (a)   Isotope geochemistry

The streaky augen gneiss has a low Sm/Nd ratio of 0.1718 (Appendix B, Table B4). The $^{143}Nd/^{144}Nd$ value is moderate (0.5116) with a corresponding and relatively strongly negative epsilon $\varepsilon Nd_{(i)}$ value of -5.70 calculated from the 1224 ± 5 Ma emplacement age of this gneiss (Appendix B, Table B4). The streaky augen gneiss has a Rb/Sr ratio of 2.424, yields a $^{87}Rb/^{86}Sr$ ratio of 6.4390. In addition, the initial Sr ($^{87}Sr/^{86}Sr_{(i)}$) is 0.7390 and the epsilon $Sr_{(t)}$ value for today is 509 (Appendix B, Table B4). Calculated T_{CHUR} and T_{DM} ages are 1.69 Ga and 2.14 Ga respectively (Appendix Table B4; Figure A14).

6.2.2   Mesklip Gneiss: Sample 033A1

Sample 033A1 is a porphyroclastic, coarse-grained biotite augen gneiss (29° 58' 31.8" S, 17° 53' 58.09" E). Forty-two spots analyses were done on 24 zircons. One distinct population can be identified in this sample, namely a subhedral and prismatic one with sub-rounded to blunt terminations and irregular fracturing. The zircons are approximately 100-300 μm in size (Fig. 28). Spherical and acicular inclusions are also prevalent (spots 033A1-02 and 033A1-27). The CL images revealed an internal structure consisting of a relatively bright core (e.g. spots 033A1-02 and 033A1-13; which represents low U and Th) surrounded by a darker rim. Two zircons have thick concentric overgrowths with dark CL cores (spots 033A1-09 and 033A1-32). The spherical and acicular inclusions are randomly oriented, and disrupts the original zonation. Analyses 033A1-03 and 033A1-04 (analysed on the same core region; Fig. 28) are both characterised by bright, weakly zoned cores with cracks crosscutting the zircon but with vastly different $^{206}Pb/^{238}U$ ages (Fig. 28; 1795 ± 37 Ma & 1180 ± 26 Ma respectively). The difference in age may be due to potential Pb loss due to the presence of the cracks.

Table 2 U-Th-Pb isotopic compositions of zircon grains extracted from sample 034D of the Mesklip Gneiss located to the north of the BRSZ.

	Spot number	U [ppm][a]	Pb [ppm][a]	$^{206}Pb/^{204}Pb$	Th/U[a]	RATIOS $^{207}Pb/^{235}U$[b]	2 σ[d]	$^{206}Pb/^{238}U$[b]	2 σ[d]	rho[c]	$^{207}Pb/^{206}Pb$[e]	2 σ[d]	AGES [Ma] $^{207}Pb/^{235}U$	2 σ	$^{206}Pb/^{238}U$	2 σ	$^{207}Pb/^{206}Pb$	2 σ	Conc. %	Region	Luminescence	Description
Analyses used	034D-01	87	19	479	0.72	2.382	0.103	0.2141	0.0045	0.48	0.0807	0.0031	1237	54	1251	26	1214	75	103	rim	bright	overgrowth rim
	034D-03	426	86	116457	0.38	2.285	0.080	0.2029	0.0039	0.55	0.0817	0.0024	1208	42	1191	23	1237	58	96	rim	dark	thick metamorphic rim
	034D-05	516	98	3465	0.16	2.052	0.070	0.1904	0.0036	0.56	0.0782	0.0022	1133	39	1124	21	1151	56	98	core	bright	fragment of metamict zircon
	034D-06	153	30	4041	0.56	2.093	0.094	0.1947	0.0041	0.47	0.0780	0.0031	1147	52	1147	24	1147	79	100	rim	bright	unzoned core
	034D-07	871	152	205402	0.18	1.785	0.059	0.1749	0.0033	0.57	0.0740	0.0020	1040	34	1039	19	1042	55	100	rim	dark	thick metamorphic rim
	034D-10	295	62	1277	0.50	2.335	0.087	0.2099	0.0041	0.52	0.0807	0.0026	1223	46	1228	24	1213	62	101	rim	dark	overgrowth rim
	034D-11	773	161	4946	0.47	2.361	0.080	0.2086	0.0039	0.56	0.0821	0.0023	1231	42	1221	23	1248	55	98	rim	dark	metamict zircon
	034D-12	534	95	128123	0.11	1.814	0.066	0.1781	0.0034	0.53	0.0739	0.0023	1051	38	1057	20	1038	63	102	rim	dark	thin metamorphic rim
	034D-13	284	61	82101	0.61	2.439	0.097	0.2148	0.0043	0.50	0.0824	0.0028	1254	50	1254	25	1254	67	100	core	bright	unzoned core
	034D-15	258	53	71939	0.31	2.303	0.086	0.2068	0.0040	0.52	0.0808	0.0026	1213	45	1212	24	1215	63	100	core	dark	faint oscillatory zoning
	034D-16	511	108	5981	0.60	2.348	0.097	0.2103	0.0043	0.49	0.0810	0.0029	1227	51	1231	25	1220	71	101	rim	medium bright	zoned, overgrowth rim
	034D-17	301	63	96003	0.44	2.379	0.094	0.2107	0.0040	0.48	0.0819	0.0028	1236	49	1232	24	1243	68	99	rim	dark	zoned, overgrowth rim
	034D-18	446	94	1356	0.55	2.362	0.089	0.2103	0.0041	0.52	0.0815	0.0026	1231	46	1230	24	1233	63	100	core	bright	unzoned core
	034D-19	712	142	3063	0.38	2.234	0.083	0.1990	0.0039	0.52	0.0814	0.0026	1192	44	1170	23	1231	62	95	rim	dark	metamorphic rim
	034D-20	742	155	3921	0.96	2.366	0.085	0.2093	0.0040	0.54	0.0820	0.0025	1232	44	1225	24	1245	59	98	core	dark	sector zoning
	034D-21	284	55	74751	0.37	2.116	0.082	0.1952	0.0039	0.51	0.0786	0.0026	1154	45	1149	23	1163	66	99	rim	dark	thick metamorphic rim
	034D-22	875	181	6593	0.41	2.339	0.081	0.2069	0.0039	0.55	0.0820	0.0024	1224	42	1212	23	1245	56	97	rim	dark	overgrowth rim
	034D-25	81	17	4824	0.75	2.350	0.113	0.2105	0.0046	0.45	0.0810	0.0035	1227	59	1231	27	1220	84	101	core	bright	convolute zonation
	034D-26	98	20	941	0.59	2.280	0.103	0.2050	0.0043	0.47	0.0807	0.0032	1206	54	1202	25	1214	78	99	core	bright	convolute zonation
	034D-27	678	142	2423	0.37	2.337	0.096	0.2091	0.0042	0.49	0.0811	0.0029	1224	50	1224	25	1223	70	100	rim	dark	thick metamorphic rim
	034D-30	197	41	2119	0.61	2.305	0.100	0.2077	0.0043	0.48	0.0805	0.0031	1214	52	1216	25	1209	75	101	core	bright	zoned core
	034D-32	116	24	1165	0.63	2.324	0.107	0.2071	0.0044	0.46	0.0814	0.0033	1220	56	1213	26	1231	80	99	core	bright	unzoned core
	034D-33	655	128	3477	0.35	2.089	0.078	0.1949	0.0038	0.52	0.0777	0.0025	1145	43	1148	22	1140	63	101	rim	dark	thin metamorphic rim
	034D-36	808	142	191826	0.16	1.792	0.069	0.1759	0.0034	0.50	0.0739	0.0025	1043	40	1044	20	1039	67	101	rim	dark	thick metamorphic rim
	034D-39	234	79	5939	0.59	5.361	0.270	0.3386	0.0079	0.46	0.1149	0.0051	1879	95	1880	44	1878	80	100	core	bright	zoned core
	034D-40	652	137	301288	0.47	2.360	0.099	0.2095	0.0041	0.47	0.0817	0.0030	1231	51	1226	24	1239	72	99	rim	dark	overgrowth rim
Analyses not used	034D-02	1826	254	1926	0.18	1.561	0.051	0.1392	0.0026	0.57	0.0814	0.0022	955	31	840	16	1231	53	68			
	034D-08	1001	138	856	0.30	1.686	0.077	0.1377	0.0029	0.47	0.0888	0.0036	1003	46	832	18	1400	77	59			
	034D-09	1790	279	2612	0.24	1.676	0.055	0.1560	0.0029	0.57	0.0779	0.0021	1000	33	934	17	1145	54	82			
	034D-14	839	134	7249	0.42	1.720	0.058	0.1597	0.0030	0.56	0.0781	0.0022	1016	34	955	18	1150	55	83			
	034D-24	975	161	3206	0.31	1.847	0.066	0.1648	0.0032	0.54	0.0813	0.0025	1062	38	983	19	1229	59	80			
	034D-35	694	134	1712	0.45	2.179	0.118	0.1938	0.0045	0.42	0.0815	0.0040	1174	64	1142	26	1234	96	93			
	034D-37	455	83	427	0.49	2.709	0.103	0.1829	0.0036	0.51	0.1074	0.0035	1331	51	1083	21	1756	60	62			
	034D-38	521	111	531	0.46	3.167	0.121	0.2135	0.0042	0.51	0.1076	0.0035	1449	55	1247	24	1759	60	71			

[a] U and Pb concentrations and Th/U ratios are calculated relative to GJ-1 reference zircon

[b] Corrected for background and within-run Pb/U fractionation and normalised to reference zircon GJ-1 (ID-TIMS values/measured value); $^{207}Pb/^{235}U$ calculated using $(^{207}Pb/^{206}Pb)/(^{238}U/^{206}Pb * 1/137.88)$

[c] Rho is the error correlation defined as the quotient of the propagated errors of the $^{206}Pb/^{238}U$ and the $^{207}/^{235}U$ ratio

[d] Quadratic addition of within-run errors (2 SD) and daily reproducibility of GJ-1 (2 SD)

[e] Corrected for mass-bias by normalising to GJ-1 reference zircon (~0.6 per atomic mass unit) and common Pb using the model Pb composition of Stacey & Kramers (1975)

███ Grey highlighted analyses represent rims and overgrowths that are likely related to metamorphism

Figure 28 CL images of zircons collected from sample 033A1. Each spot, represented by a black circle, has been labelled with the analyses/spot number and the calculated ^{206}Pb/^{238}U ages.

Of the 42 analyses 20 provided concordant results. Five analyses on inherited faintly zoned to unzoned, medium dark to bright cores yielded a ^{206}Pb/^{238}U concordia age of 1811 ± 12 Ma and have U values between 87 ppm and 487 ppm and Th/U values ranging between 039 and 0.95. Another seven analyses on inherited faintly zoned, fairly bright cores gave a ^{206}Pb/^{238}U concordia age of 1741 ± 11 Ma (MSWD = 0.45) with U values of between 53 and 502ppm and Th/U ranging between 0.40 and 0.88. Two more analyses are determined to be inherited with ^{206}Pb/^{238}U ages of 1420 ± 29 Ma (faintly zoned, dark core) and 1382 ± 28 Ma (thick, dark rim; Fig. 29; Table 3). A ^{206}Pb/^{238}U concordant age of 1205 ± 9 Ma (MSWD = 0.34) was calculated for 6 analyses from fairly dark to bright, thick magmatic overgrowths on core regions, with U values ranging between 134 and 919 ppm and Th/U ranging between 0.15 and 0.47. This is interpreted to be the crystallisation age of this rock (Fig. 29 & Table 3).

6.2.2. (a)   Isotope geochemistry

The biotite augen gneiss has a low Sm/Nd ratio of 0.1623 (Appendix B, Table B4). The ^{143}Nd/^{144}Nd value is moderate (0.51150) with a corresponding and relatively strongly negative

epsilon $\text{ENd}_{(t)}$ value of -6.78 calculated from the 1205 ± 7 Ma emplacement age of this gneiss (Appendix, Table B4). The biotite augen gneiss has a Rb/Sr ratio of 1.7003, which yields a $^{87}\text{Rb}/^{86}\text{Sr}$ ratio of 4.5166. In addition, the initial Sr ($^{87}\text{Sr}/^{86}\text{Sr}_{(i)}$) is 0.73880 and the epsilon $\text{Sr}_{(t)}$ value for today is 498 (Appendix B, Table B4). Calculated T_{CHUR} and T_{DM} ages are 1.73 Ga and 2.15 Ga respectively (Appendix, Table B4 & Figure A14).

Figure 29 U-Pb concordia plot of sample 033A1 displaying minor discordance. The concordia plot for near-concordant analyses is used to calculate weighted mean $^{206}\text{Pb}/^{238}\text{U}$ ages of the three concordant ages in sample 033A1. Confidence limits for the error ellipses are expressed as 2σ.

6.2.3 Mesklip Gneiss: Sample 019A

Sample 019A is a porphyroclastic, medium- to coarse-grained leucocratic augen gneiss (30° 0' 22.68" S, 17° 49' 16.5" E). There is a total of 11 zircons which were analysed (Table 4), and these zircons range in size between 170 μm and 300 μm. The zircon morphology in this sample (Fig. 30) displays prismatic euhedral to subhedral, stubby shapes and irregular fracturing (e.g. spot 019A-10). The CL images revealed simple concentric oscillatory zoned internal structure which are typical of magmatic rocks.

Of the total of 23 analyses that were analysed, 8 provided concordant ages, 4 of them yielded meaningless numbers and the remainder were discordant (Table 4). The discordia plot (Fig. 31a), which utilises all the discordant and concordant data together, yields a discordia best fit regression line with an upper intercept age of 1204 ± 22 Ma and a lower intercept of -2 ± 84

29

Ma indicating recent Pb loss. This indicates that the zircons are all of the same age population that was affected by the same event. Combining the 8 concordant ages yields a precise concordia age of 1204 ± 8 Ma (Fig. 31b) and is interpreted to be the crystallization age of this rock. There are a total of 6 bright-CL cores (U content ranging between 82 ppm and 202 ppm; Table 4) and 2 bright-CL overgrowths (U values of 215 ppm and 317 ppm respectively). The cores and overgrowths have Th/U ranging from 0.41-0.69 representative of a magmatic origin.
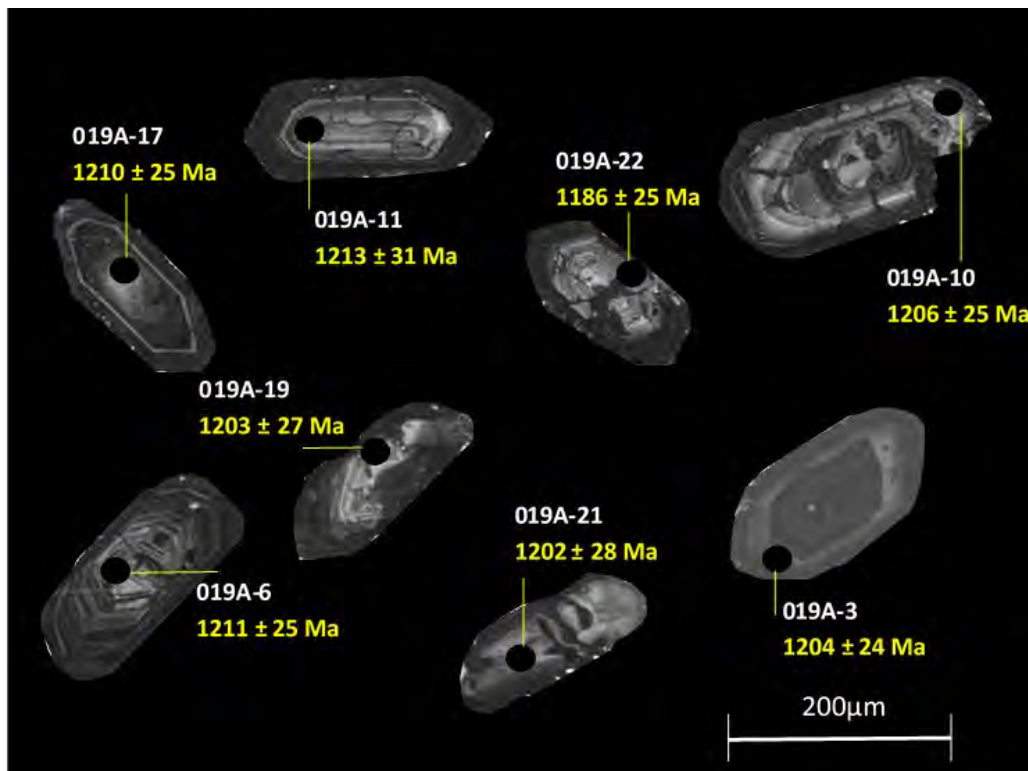
Figure 30 CL images of zircons collected from sample 019A. Each spot, represented by a black circle, has been labelled with the analyses/spot number and the calculated ^{206}Pb/^{238}U ages.

6.2.3. (a)   Isotope geochemistry

The leucocratic augen gneiss has a low Sm/Nd ratio of 0.1680 (Appendix B, Table B4). The ^{143}Nd/^{144}Nd value is moderate (0.51170) with a corresponding and relatively strongly negative epsilon ƐNd(t) value of -3.23 calculated from the 1204 ± 8 Ma emplacement age of this gneiss (Appendix B, Table B4). The leucocratic augen gneiss has a Rb/Sr ratio of 0.3791, which yields a ^{87}Rb/^{86}Sr ratio of 1.0070. In addition, the initial Sr (^{87}Sr/^{86}Sr$_{(i)}$) is 0.70650 and the epsilon Sr$_{(t)}$value for today is 49 (Appendix B, Table B4). Calculated T$_{CHUR}$ and T$_{DM}$ ages are 1.46 Ga and 1.93 Ga respectively (Appendix, Table B4 & Figure A14).
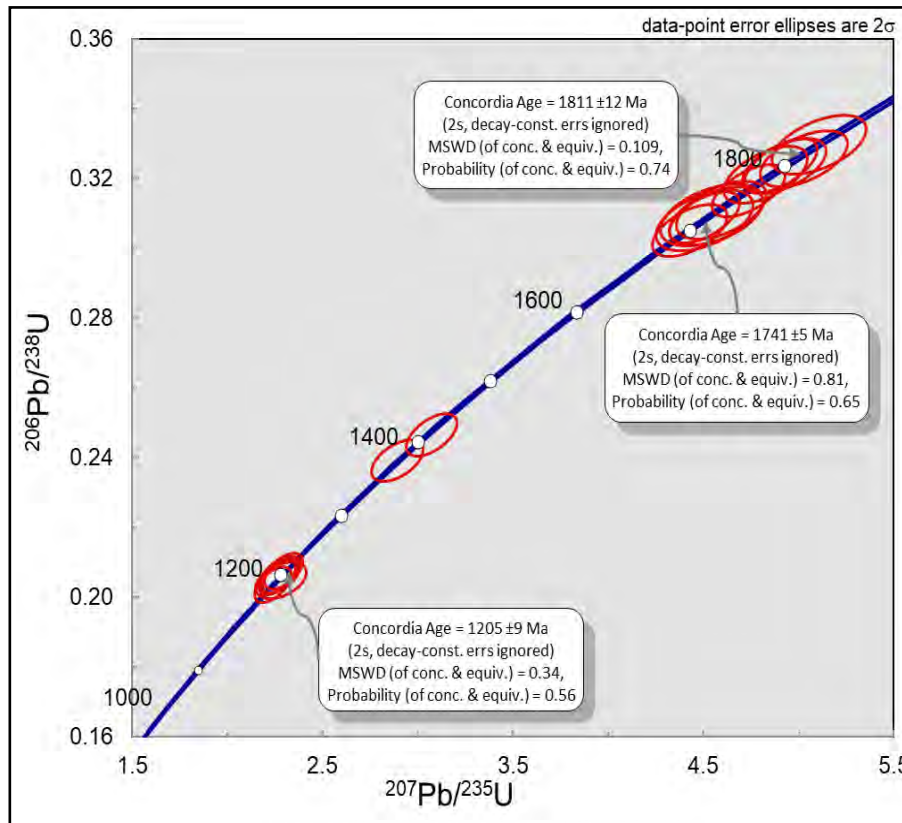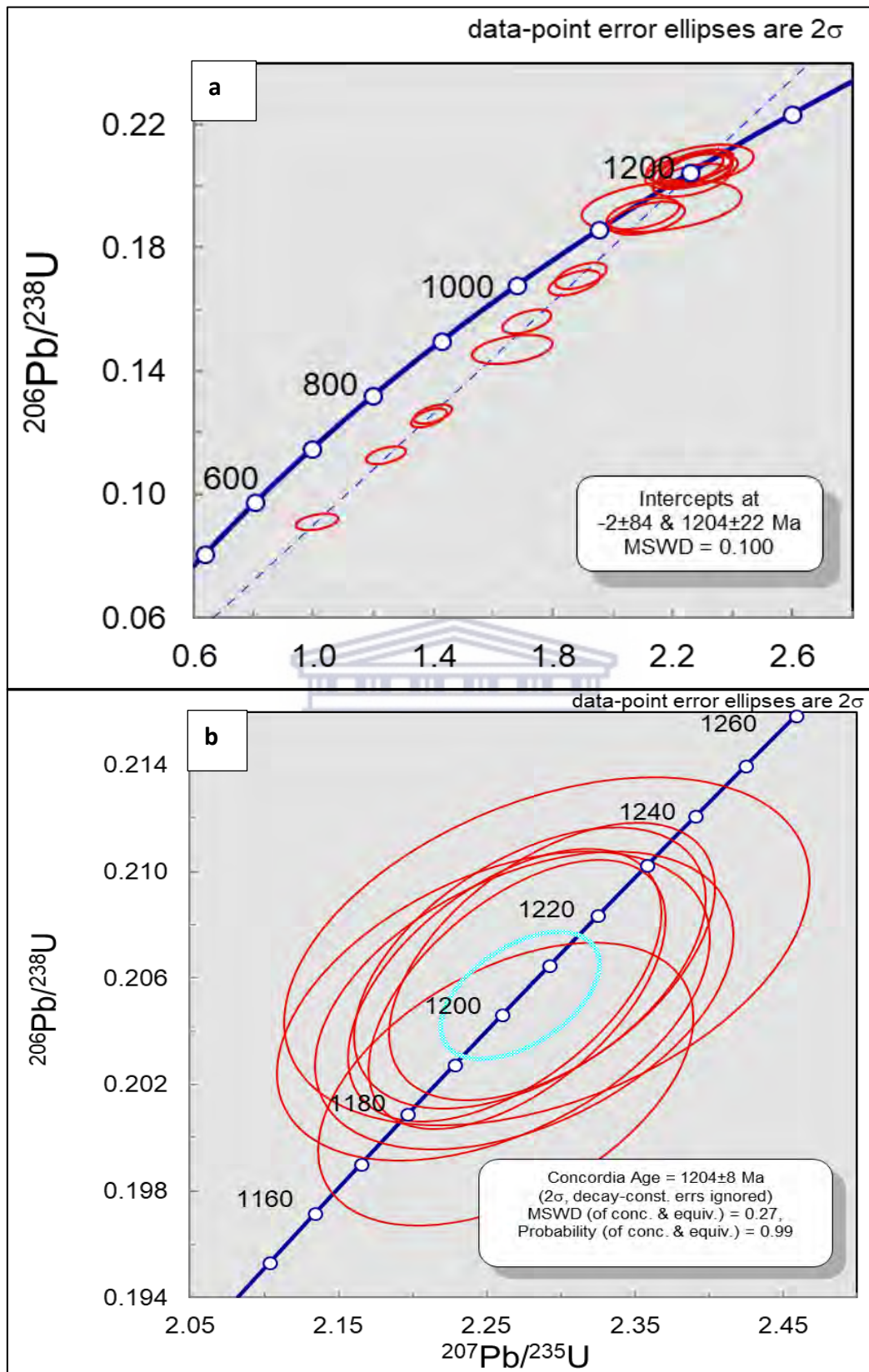
Figure 31 (a) U-Pb concordia plot of sample 019A displaying minor discordance, where a discordia line (dotted line) is fitted through the discordant zircons back to the concordia curve and gave an upper intercept age of 1204 ± 22 Ma and lower intercept age of -2 ± 84 Ma. The concordia plot for near-concordant analyses is used to calculate a weighted mean [206]Pb/[238]U age for sample 019A. Confidence limits for the error ellipses are expressed as 2σ; **(b)** U-Pb concordia plot of sample 019A. The concordia plot for near-concordant analyses is used to calculate a weighted mean [206]Pb/[238]U age for sample 019A. Confidence limits for the error ellipses are expressed as 2σ.

31

Table 6 U-Th-Pb isotopic compositions of zircon grains extracted from sample 033A1 of the Mesklip Gneiss located along the northern boundary of the BRSZ.

Spot number	U [ppm][a]	Pb [ppm][a]	$^{206}Pb/^{204}Pb$	Th/U[a]	RATIOS $^{207}Pb/^{235}U$[b]	2σ[d]	$^{206}Pb/^{238}U$[b]	2σ[d]	rho[c]	$^{207}Pb/^{206}Pb$[e]	2σ[d]	AGES [Ma] $^{207}Pb/^{235}U$	2σ	$^{206}Pb/^{238}U$	2σ	$^{207}Pb/^{206}Pb$	2σ	Conc. %	Region	Luminescence	Description
Analyses used																					
033A1-02	397	82	131170	0.26	2.280	0.089	0.2065	0.0043	0.53	0.0801	0.0026	1206	47	1210	25	1199	65	101	core	bright	overgrowth on core
033A1-03	87	28	2097	0.95	4.825	0.180	0.3211	0.0067	0.56	0.1090	0.0034	1789	67	1795	37	1783	56	101	core	med bright	thick zonation/ prismatic shape
033A1-07	182	45	19237	0.36	3.074	0.110	0.2465	0.0050	0.57	0.0904	0.0027	1426	51	1420	29	1435	56	99	core	med dark	faintly zoned core with geometrically irregular surfaces;fractured
033A1-08	487	158	7771	0.39	4.904	0.157	0.3238	0.0063	0.61	0.1099	0.0028	1803	58	1808	35	1797	46	101	core	bright	faintly zoned core
033A1-10	290	60	5824	0.26	2.294	0.083	0.2075	0.0042	0.56	0.0802	0.0024	1211	44	1215	24	1202	59	101	core	med dark	overgrowth on core; unzoned highly fractured
033A1-12	357	73	14406	0.33	2.263	0.079	0.2057	0.0041	0.57	0.0798	0.0023	1201	42	1206	24	1192	56	101	core	bright	overgrowth on core; unzoned core
033A1-13	64	20	31856	0.80	4.595	0.192	0.3111	0.0068	0.52	0.1071	0.0038	1748	73	1746	38	1751	65	100	core	bright	faintly zoned core with thin overgrowth /whole zircon is abraded
033A1-15	357	113	12033	0.41	4.739	0.156	0.3166	0.0062	0.60	0.1086	0.0029	1774	59	1773	35	1776	48	100	core	bright	unzoned core
033A1-21	134	27	50286	0.47	2.282	0.109	0.2049	0.0042	0.43	0.0808	0.0035	1207	58	1202	25	1215	85	99	core	bright	overgrowth on core; highly fractured unzoned core
033A1-23	44	14	416	0.59	4.507	0.209	0.3081	0.0071	0.49	0.1061	0.0043	1732	80	1731	40	1733	74	100	core	dark	zoned and fractured core with acicualr inclusions
033A1-24	502	155	60733	0.40	4.508	0.151	0.3089	0.0060	0.58	0.1058	0.0029	1732	58	1735	34	1729	50	100	core	dark	dark area of overgrowth on core
033A1-25	472	96	2022	0.15	2.239	0.079	0.2036	0.0042	0.58	0.0798	0.0023	1193	42	1194	24	1192	57	100	core	bright	overgrowth on core; rounded core with fractures
033A1-26	919	190	9967	0.26	2.279	0.077	0.2062	0.0040	0.58	0.0801	0.0022	1206	41	1209	24	1200	55	101	core	dark	thick overgrowth on core
033A1-27	162	49	6485	0.53	4.428	0.161	0.3052	0.0061	0.55	0.1052	0.0032	1718	62	1717	35	1719	56	100	core	bright	unzoned core
033A1-29	53	16	26720	0.63	4.543	0.221	0.3097	0.0072	0.48	0.1064	0.0045	1739	85	1739	41	1738	78	100	core	bright	faintly zoned core
033A1-30	64	20	32085	0.88	4.567	0.202	0.3094	0.0068	0.50	0.1071	0.0041	1743	77	1738	38	1750	70	99	core	med bright	thick zonation pattern and contains acic;iular inclusions
033A1-31	106	35	2152	0.49	5.109	0.203	0.3296	0.0069	0.53	0.1124	0.0038	1838	73	1837	39	1839	61	100	core	dark	thick overgrowth on core
033A1-32	224	73	2145	0.48	4.925	0.179	0.3237	0.0065	0.55	0.1103	0.0033	1806	66	1808	36	1805	55	100	core	dark	thick overgrowth on core
033A1-34	141	46	1299	0.55	5.027	0.188	0.3258	0.0066	0.54	0.1119	0.0035	1824	68	1818	37	1831	57	99	core	med dark	overgrowth on core
033A1-35	711	170	2261	0.23	2.892	0.110	0.2392	0.0048	0.53	0.0877	0.0028	1380	53	1382	28	1376	62	100	rim	dark	thick rim
Analyses not used																					
033A1-01	40	11	18020	0.52	4.532	0.222	0.2823	0.0068	0.49	0.1164	0.0050	1737	85	1603	39	1902	77	84			
033A1-04	249	50	3472	0.36	2.222	0.104	0.2009	0.0045	0.47	0.0802	0.0033	1188	56	1180	26	1203	82	98			
033A1-05	375	106	167387	0.53	4.203	0.143	0.2828	0.0056	0.58	0.1078	0.0030	1675	57	1605	32	1762	51	91			
033A1-06	531	114	8395	0.39	2.691	0.108	0.2143	0.0045	0.53	0.0911	0.0031	1326	53	1252	26	1448	65	86			
033A1-09	209	36	404	1.08	2.368	0.146	0.1744	0.0046	0.43	0.0985	0.0055	1233	76	1036	27	1596	104	65			
033A1-11	128	23	1516	0.53	2.030	0.099	0.1837	0.0041	0.46	0.0801	0.0035	1126	55	1087	25	1200	86	91			
033A1-14	78	17	27154	0.73	2.908	0.269	0.2147	0.0076	0.38	0.0983	0.0084	1384	128	1254	45	1592	160	79			
033A1-18	413	121	35848	0.27	4.496	0.177	0.2927	0.0062	0.54	0.1114	0.0037	1730	68	1655	35	1823	60	91			
033A1-19	53	15	23983	0.56	4.258	0.277	0.2861	0.0085	0.46	0.1079	0.0062	1685	110	1622	48	1765	106	92			
033A1-22	120	27	1007	0.48	3.309	0.136	0.2256	0.0047	0.50	0.1064	0.0038	1483	61	1311	27	1738	65	75			
033A1-36	540	154	3487	0.24	4.205	0.164	0.2859	0.0059	0.53	0.1067	0.0035	1675	65	1621	33	1743	61	93			
033A1-16	0	0	57.05									0									
033A1-17	0	0	47.02		0.112	119.270	0.7203		-1.8534	2.13	4.2576	-114.8575	295	704			239				
033A1-20	0	0	11.63		0.411	-164.794	0.0000						-859	2832			-330				
033A1-28	0	0	79.00		0.100	83.361	0.6866		-1.2479	1.10	2.2030	-88.2688	376	627			167				
033A1-33	0	0	26.95									0									
033A1-37	55	11	315.84	1.58	2.289	0.184	0.2068	0.0047	0.28	0.0803	0.0062	1209	97	1212	27	1204	152	101	CL image missing	CL image missing	
033A1-38	381	79	44806.17	0.48	2.274	0.088	0.2063	0.0041	0.51	0.0799	0.0027	1204	47	1209	24	1196	66	101	CL image missing	CL image missing	
033A1-39	213	44	2547	0.40	2.288	0.090	0.2071	0.0042	0.52	0.0801	0.0027	1209	48	1213	25	1200	66	101	CL image missing	CL image missing	
033A1-40	0	0	248.44		0.283	-72.372	0.0000						-1404	2032			-145				
033A1-41	441	142	4209.11	0.41	4.839	0.180	0.3212	0.0064	0.54	0.1093	0.0034	1792	67	1796	36	1787	57	100	CL image missing	CL image missing	
033A1-42	123	40	1487.91	0.54	4.952	0.199	0.3245	0.0067	0.52	0.1107	0.0038	1811	73	1812	38	1810	62	100	CL image missing	CL image missing	

[a] U and Pb concentrations and Th/U ratios are calculated relative to GJ-1 reference zircon

[b] Corrected for background and within-run Pb/U fractionation and normalised to reference zircon GJ-1 (ID-TIMS values/measured value); $^{207}Pb/^{235}U$ calculated using $(^{207}Pb/^{206}Pb)/(^{238}U/^{206}Pb * 1/137.88)$

[c] Rho is the error correlation defined as the quotient of the propagated errors of the $^{206}Pb/^{238}U$ and the $^{207}Pb/^{235}U$ ratio

[d] Quadratic addition of within-run errors (2 SD) and daily reproducibility of GJ-1 (2 SD)

 Grey highlighted analyses represent rims and overgrowths that are likely related to metamorphism

Table 4 U-Th-Pb isotopic compositions of zircon grains extracted from sample 019A of the Mesklip Gneiss located south of the BRSZ.

	Spot number	U [ppm][a]	Pb [ppm][a]	Th/U meas	$^{207}Pb/^{235}U$[b]	2σ[d]	$^{206}Pb/^{238}U$[b]	2σ[d]	rho[c]	$^{207}Pb/^{206}Pb$[e]	2σ[d]	$^{207}Pb/^{235}U$	2σ	$^{206}Pb/^{238}U$	2σ	$^{207}Pb/^{206}Pb$	2σ	%	Region	Luminescence	Description
					RATIOS							AGES [Ma]						Conc.			
Analyses used	019A-3	317	65	0.50	2.271	0.082	0.2054	0.0041	0.56	0.0802	0.0024	1203	43	1204	24	1201	59	100	rim	bright	bright overgrowth rim
	019A-6	202	42	0.62	2.294	0.090	0.2066	0.0043	0.53	0.0805	0.0027	1211	47	1211	25	1210	66	100	core	bright	bright concentrically zoned core
	019A-10	215	44	0.46	2.262	0.086	0.2057	0.0042	0.53	0.0797	0.0026	1201	46	1206	25	1191	64	101	rim	bright	bright overgrowth rim
	019A-11	170	35	0.60	2.291	0.145	0.2070	0.0053	0.41	0.0803	0.0046	1209	77	1213	31	1203	114	101	core	bright	bright core
	019A-17	168	35	0.41	2.279	0.097	0.2064	0.0043	0.49	0.0801	0.0030	1206	51	1210	25	1199	73	101	core	bright	bright faintly zoned core
	019A-19	112	23	0.69	2.275	0.115	0.2052	0.0046	0.44	0.0804	0.0037	1205	61	1203	27	1208	90	100	core	bright	bright faintly zoned core
	019A-21	82	17	0.69	2.255	0.119	0.2050	0.0047	0.44	0.0798	0.0038	1198	63	1202	28	1192	94	101	core	bright	bright unzoned core
	019A-22	147	30	0.68	2.263	0.103	0.2020	0.0043	0.47	0.0813	0.0033	1201	55	1186	25	1227	79	97	core	bright	bright zoned and fractured core
Analyses not used	019A-1	1346	170	0.32	1.398	0.054	0.1261	0.0026	0.53	0.0804	0.0026	888	34	766	16	1207	64	63	core	dark	dark faintly zoned core
	019A-2	643	110	0.19	1.893	0.071	0.1710	0.0035	0.54	0.0803	0.0025	1078	41	1017	21	1204	62	84	rim	dark	dark thin rim
	019A-4	212	40	0.45	2.113	0.103	0.1897	0.0043	0.46	0.0808	0.0035	1153	56	1120	25	1217	85	92	core	bright	bright zoned core
	019A-8	1172	146	0.32	1.385	0.049	0.1249	0.0025	0.56	0.0804	0.0024	883	31	759	15	1207	58	63	rim	dark	dark overgrowth rim
	019A-9	885	130	0.60	1.664	0.109	0.1470	0.0038	0.40	0.0821	0.0049	995	65	884	23	1248	118	71	rim	dark	dark overgrowth rim
	019A-12	2092	236	0.26	1.243	0.054	0.1128	0.0024	0.49	0.0799	0.0031	820	36	689	15	1196	76	58	rim	bright	dark zoned overgrowth rim
	019A-13	67	13	0.60	2.163	0.218	0.1934	0.0069	0.35	0.0811	0.0076	1169	118	1140	41	1224	185	93	core	bright	bright zoned core
	019A-14	169	32	0.46	2.103	0.099	0.1910	0.0042	0.47	0.0799	0.0033	1150	54	1127	25	1194	82	94	core	bright	bright zoned core
	019A-16	1179	199	0.10	1.871	0.070	0.1686	0.0034	0.54	0.0805	0.0025	1071	40	1004	20	1209	62	83	rim	dark	dark overgrowth rim
	019A-20	1152	180	0.33	1.714	0.067	0.1560	0.0032	0.52	0.0797	0.0027	1014	40	934	19	1189	66	79	rim	dark	thick dark overgrowth rim
	019A-23	1260	115	0.41	1.011	0.057	0.0912	0.0021	0.41	0.0804	0.0041	710	40	563	13	1207	101	47	rim	dark	thick dark overgrowth rim

[a]U and Pb concentrations and Th/U ratios are calculated relative to GJ-1 reference zircon

[b]Corrected for background and within-run Pb/U fractionation and normalised to reference zircon GJ-1 (ID-TIMS values/measured value); $^{207}Pb/^{235}U$ calculated using $(^{207}Pb/^{206}Pb)/(^{238}U/^{206}Pb * 1/137.88)$

[c]Rho is the error correlation defined as the quotient of the propagated errors of the $^{206}Pb/^{238}U$ and the $^{207}Pb/^{235}U$ ratio

[d]Quadratic addition of within-run errors (2 SD) and daily reproducibility of GJ-1 (2 SD)

[e]Corrected for mass-bias by normalising to GJ-1 reference zircon (~0.6 per atomic mass unit) and common Pb using the model Pb composition of Stacey & Kramers (1975)

6.2.4   Rooiplatklip Gneiss: Sample 004C

Sample 004C is a well-foliated, equigranular to weakly porphyroblastic, medium- to coarse-grained leucogranitic gneiss (29° 59' 52.8" S, 17° 50' 24.9" E). A total of 38 core and rim analyses were done on 18 zircons (Table 8). Zircons from this sample range in size from 70-250 μm. Overall the zircons are subhedral with sharp to sub-rounded terminations with a prismatic habit (Fig. 32). Two populations are identified based on internal structure (CL imaging): 1) 60% of the zircons in this sample have bright concentrically zoned cores with thin dark rims (e.g. spots 004C-7 and 004C-32), and 2) the remaining 40% of the zircons display dark faintly zoned to unzoned cores with thick darker rims (e.g. spots 004C-11 and 004C-24).

Of the 38 analyses, 37 gave concordant dates. Two age populations were observed from the U-Pb concordia plot (Fig. 33). The older age population is represented by four analyses (spots 004C-3, 004C-23, 004C-29 and 004C-37) of bright, faintly zoned to unzoned cores suggesting an inherited age with a weighted mean $^{206}Pb/^{238}U$ age of 1340 ± 12 Ma (MSWD = 1.5). The U values for these analyses range between 103 ppm and 357 ppm and Th/U values range between 0.62 and 1.02. The two age populations correlate to the CL image populations to a certain extent, where the older population is characterised by dark, faintly zoned to unzoned cores with thick darker rims but a few CL images of zircons from the younger population also have these characteristics such as spot 004C-11.
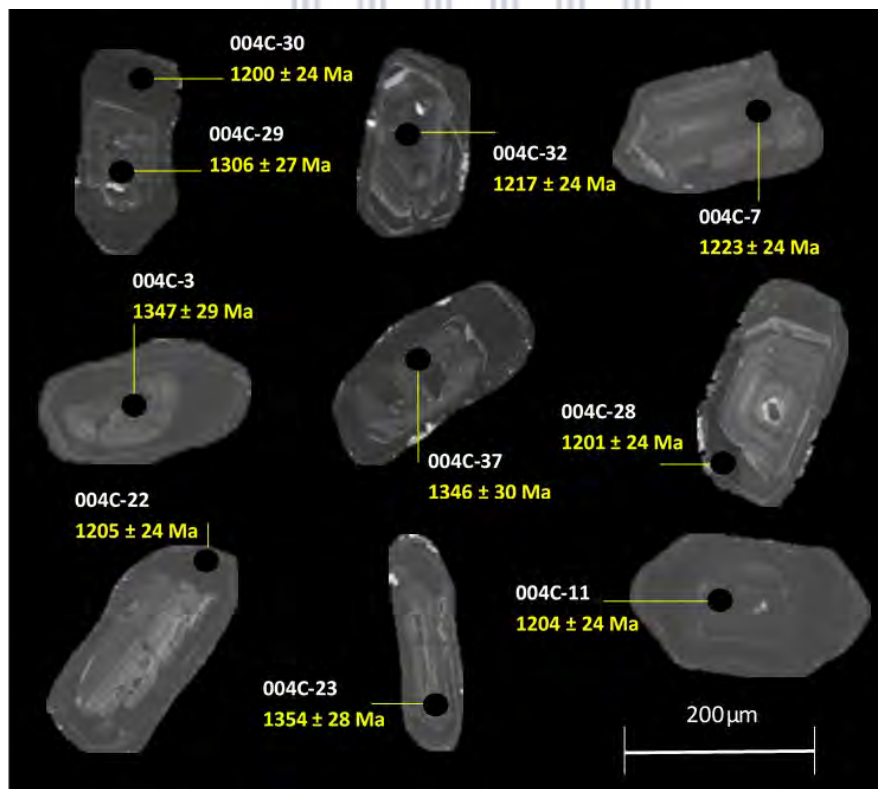
Figure 32 CL images of zircons collected from sample 004C. Each spot, represented by a black circle, has been labelled with the analyses/spot number and the calculated $^{206}Pb/^{238}U$ ages.

34

The younger age population is represented by 33 analyses (9 core regions and 24 overgrowth rims) which yield a weighted mean $^{206}Pb/^{238}U$ age of 1204 ± 4 Ma (Fig. 33; MSWD = 0.28). This age population is considered to be the age of the leucogranitic gneiss crystallization.

6.3.4. (a)   Isotope geochemistry

The leucogranitic gneiss has a low Sm/Nd ratio of 0.167 (Appendix B, Table B4). The $^{143}Nd/^{144}Nd$ value is moderate (0.51170) with a corresponding and moderately to weakly negative epsilon $\epsilon Nd_{(t)}$ value of -2.76 calculated from the 1204 ± 4 Ma emplacement age of this gneiss (Appendix B, Table B4). The leucogranitic gneiss has a Rb/Sr ratio of 0.4271, yields a $^{87}Rb/^{86}Sr$ ratio of 1.13470, and an initial Sr ($^{87}Sr/^{86}Sr_{(i)}$) of 0.7091, with the epsilon Sr(t) value for today being 84 (Appendix B, Table B4). Calculated T_{CHUR} and T_{DM} ages are 1.42 Ga and 1.90 Ga respectively (Appendix, Table B4 & Figure A14).
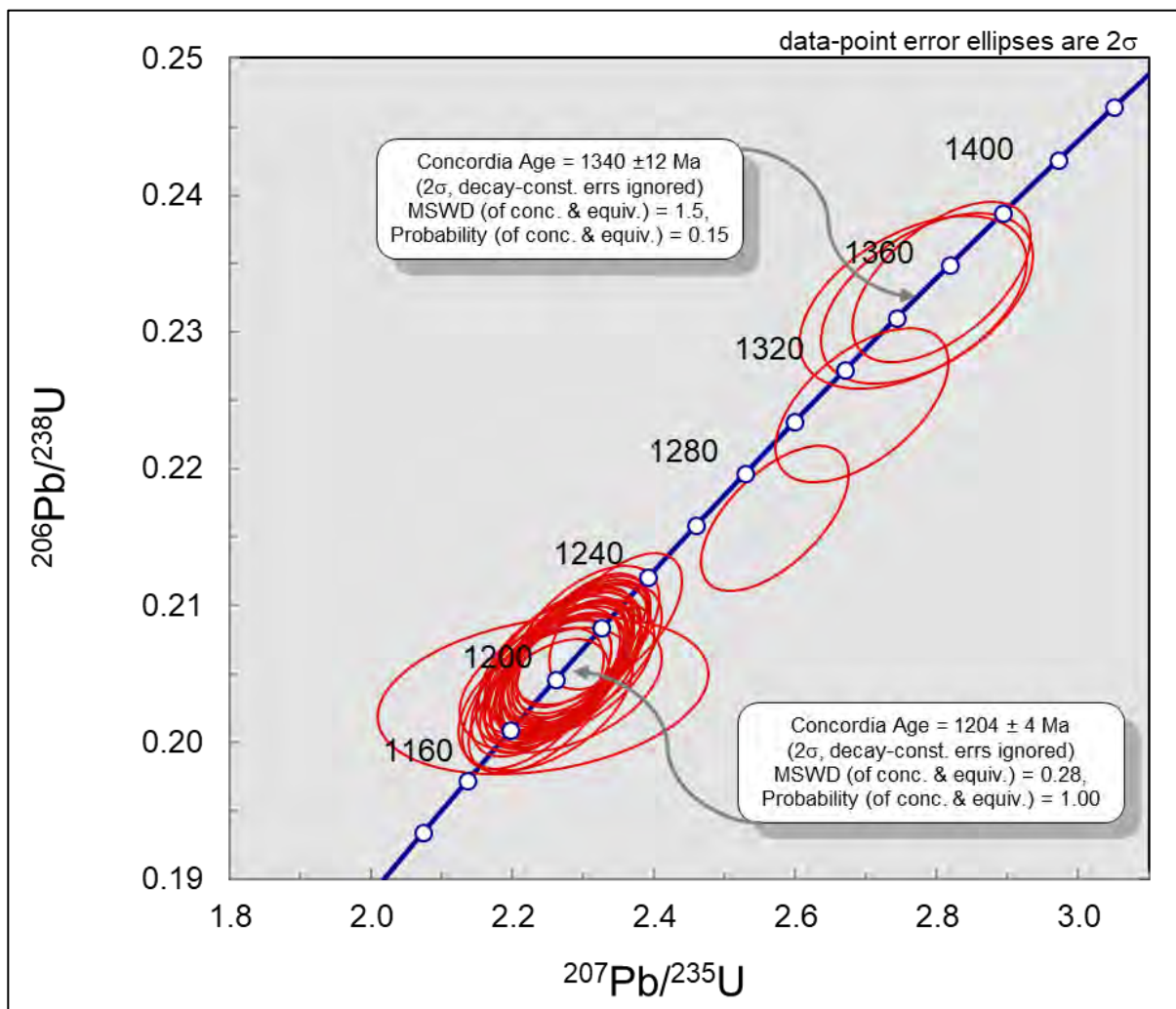
Figure 33 U-Pb concordia plot of sample 004C displaying minor discordance. The concordia plot for near-concordant analyses is used to calculate weighted mean $^{206}Pb/^{238}U$ ages of the two concordant ages in sample 004C. Confidence limits for the error ellipses are expressed as 2σ.

Table 4 U-Th-Pb isotopic compositions of zircon grains extracted from sample 004C of the Rooiplatklip Gneiss located within the BRSZ.

|	Spot number	U [ppm][a]	Pb [ppm][a]	Th/U meas[b]	RATIOS 207Pb/235U[b]	2 σ[d]	206Pb/238U[b]	2 σ[d]	rho[c]	207Pb/206Pb[e]	2 σ[d]	AGES [Ma] 207Pb/235U	2 σ	206Pb/238U	2 σ	207Pb/206Pb	2 σ	Conc. %	Region	Luminescence	Description
Analyses used	004C-01	142	29	1.11	2.261	0.083	0.2050	0.0043	0.56	0.0800	0.0024	1200	44	1202	25	1197	60	100	core	bright	convoluted
	004C-02	211	44	0.47	2.293	0.082	0.2068	0.0041	0.56	0.0804	0.0024	1210	43	1212	24	1207	59	100	rim	bright	overgrowth rim
	004C-03	103	24	0.64	2.785	0.122	0.2324	0.0051	0.50	0.0869	0.0033	1352	59	1347	29	1359	74	99	core	bright	faintly zoned, resorbed core
	004C-04	707	144	0.21	2.246	0.076	0.2041	0.0039	0.57	0.0798	0.0022	1196	40	1197	23	1192	54	100	rim	dark	overgrowth rim
	004C-05	204	42	0.69	2.239	0.081	0.2040	0.0041	0.56	0.0796	0.0024	1193	43	1197	24	1187	59	101	core	bright	faintly zoned, resorbed core
	004C-06	637	131	0.15	2.271	0.073	0.2056	0.0040	0.60	0.0801	0.0021	1203	39	1205	23	1200	51	100	rim	dark	thick overgrowth rim
	004C-07	469	98	1.31	2.345	0.077	0.2088	0.0041	0.59	0.0814	0.0022	1226	40	1223	24	1232	52	99	core	bright	zoned core
	004C-08	797	165	0.21	2.281	0.073	0.2065	0.0040	0.61	0.0801	0.0020	1206	39	1210	23	1200	50	101	rim	dark	overgrowth rim
	004C-09	171	35	1.02	2.228	0.082	0.2032	0.0042	0.56	0.0795	0.0024	1190	44	1192	25	1185	60	101	core	bright	faintly zoned, resorbed core
	004C-10	601	123	0.25	2.267	0.075	0.2054	0.0040	0.59	0.0801	0.0021	1202	40	1204	24	1198	53	100	rim	dark	thick overgrowth rim
	004C-11	243	50	0.73	2.273	0.080	0.2053	0.0041	0.56	0.0803	0.0023	1204	42	1204	24	1205	57	100	core	dark	faintly zoned, resorbed core
	004C-12	725	149	0.13	2.276	0.075	0.2054	0.0040	0.59	0.0804	0.0021	1205	40	1204	23	1206	52	100	rim	dark	thick overgrowth rim
	004C-13	713	148	0.21	2.297	0.075	0.2074	0.0040	0.59	0.0803	0.0021	1211	40	1215	24	1205	52	101	rim	dark	thick overgrowth rim
	004C-15	502	103	0.19	2.265	0.079	0.2045	0.0040	0.57	0.0803	0.0023	1201	41	1199	24	1205	56	100	rim	dark	thin overgrowth rim
	004C-16	210	43	0.61	2.262	0.090	0.2056	0.0041	0.51	0.0798	0.0027	1200	48	1205	24	1191	67	101	rim	dark	thin overgrowth rim
	004C-17	209	43	0.66	2.287	0.085	0.2064	0.0042	0.55	0.0803	0.0025	1208	45	1210	25	1205	61	100	rim	bright	thick overgrowth rim
	004C-18	207	42	0.77	2.267	0.117	0.2042	0.0041	0.39	0.0805	0.0038	1202	62	1198	24	1209	93	99	rim	bright	thick overgrowth rim
	004C-19	958	198	0.16	2.299	0.077	0.2068	0.0040	0.58	0.0807	0.0022	1212	40	1212	24	1213	53	100	rim	dark	thick overgrowth rim
	004C-20	953	196	0.17	2.278	0.076	0.2060	0.0040	0.58	0.0802	0.0022	1205	40	1208	24	1202	54	100	rim	dark	thick overgrowth rim
	004C-21	66	13	0.55	2.242	0.191	0.2035	0.0047	0.27	0.0799	0.0065	1194	102	1194	28	1195	161	100	core	bright	resorbed core
	004C-22	823	169	0.18	2.275	0.078	0.2055	0.0040	0.57	0.0803	0.0022	1205	41	1205	24	1205	55	100	rim	dark	thick overgrowth rim
	004C-23	271	63	0.62	2.805	0.103	0.2336	0.0048	0.56	0.0871	0.0026	1357	50	1354	28	1362	58	99	core	bright	faintly zoned
	004C-24	578	120	0.64	2.297	0.079	0.2071	0.0041	0.57	0.0804	0.0023	1211	42	1213	24	1207	56	101	core	dark	faintly zoned, resorbed core
	004C-25	601	123	0.24	2.287	0.092	0.2054	0.0041	0.49	0.0807	0.0028	1208	49	1204	24	1215	69	99	rim	dark	overgrowth rim
	004C-26	116	23	0.57	2.246	0.101	0.2032	0.0042	0.46	0.0802	0.0032	1195	54	1192	25	1201	79	99	rim	bright	zoned, resorbed core
	004C-27	667	135	0.18	2.236	0.080	0.2026	0.0040	0.55	0.0800	0.0024	1192	43	1189	24	1198	59	99	rim	dark	overgrowth rim
	004C-28	460	94	0.15	2.249	0.083	0.2048	0.0041	0.54	0.0796	0.0025	1196	44	1201	24	1188	61	101	rim	dark	overgrowth rim
	004C-29	357	80	0.85	2.693	0.100	0.2246	0.0046	0.56	0.0869	0.0027	1326	49	1306	27	1359	59	96	core	bright	faintly zoned, resorbed core
	004C-30	782	160	0.15	2.259	0.080	0.2045	0.0041	0.56	0.0801	0.0024	1200	43	1200	24	1200	58	100	rim	dark	thick overgrowth rim
	004C-31	687	141	0.15	2.264	0.081	0.2050	0.0041	0.55	0.0801	0.0024	1201	43	1202	24	1200	59	100	rim	dark	thick overgrowth rim
	004C-32	540	112	0.94	2.303	0.085	0.2078	0.0042	0.54	0.0804	0.0025	1213	45	1217	24	1206	61	101	core	dark	zoned core
	004C-33	285	59	0.61	2.273	0.089	0.2061	0.0042	0.52	0.0800	0.0027	1204	47	1208	25	1197	66	101	rim	bright	overgrowth rim
	004C-34	618	128	0.82	2.289	0.084	0.2064	0.0042	0.55	0.0804	0.0025	1209	45	1210	24	1207	61	100	core	bright	resorbed core
	004C-35	659	136	0.19	2.270	0.090	0.2060	0.0041	0.50	0.0799	0.0027	1203	48	1207	24	1195	68	101	rim	dark	thick overgrowth rim
	004C-36	766	158	0.14	2.304	0.087	0.2065	0.0041	0.53	0.0809	0.0026	1214	46	1210	24	1220	63	99	rim	dark	thick overgrowth rim
	004C-37	161	37	1.02	2.766	0.131	0.2322	0.0052	0.47	0.0864	0.0036	1346	64	1346	30	1347	81	100	core	bright	faintly zoned
	004C-38	816	167	0.16	2.278	0.085	0.2052	0.0041	0.54	0.0805	0.0025	1205	45	1203	24	1210	62	99	rim	dark	thick overgrowth rim
Analyses not used	004C-14	812	176	0.68	2.570	0.085	0.2164	0.0043	0.60	0.0862	0.0023	1292	43	1263	25	1342	51	94	core	dark	unzoned

[a]U and Pb concentrations and Th/U ratios are calculated relative to GJ-1 reference zircon

[b]Corrected for background and within-run Pb/U fractionation and normalised to reference zircon GJ-1 (ID-TIMS values/measured value); 207Pb/235U calculated using (207Pb/206Pb)/(238U/206Pb * 1/137.88)

[c]Rho is the error correlation defined as the quotient of the propagated errors of the 206Pb/238U and the 207Pb/235U ratio

[d]Quadratic addition of within-run errors (2 SD) and daily reproducibility of GJ-1 (2 SD)

[e]Corrected for mass-bias by normalising to GJ-1 reference zircon (~0.6 per atomic mass unit) and common Pb using the model Pb composition of Stacey & Kramers (1975)

6.3 Supracrustal rocks

6.3.1   Hunboom Gneiss: Sample 037

The Hunboom Gneiss is a migmatitic, fine- to medium-grained, mesocratic grey biotite gneiss (29° 59' 36.24" S, 17° 52' 26.62" E). Zircons of this sample are detrital and have the typical rounded terminations present in detrital zircons. A total of 44 zircons were available with a total of 89 analyses done on core and rim regions. At least two main populations are present in the sample and are classified based on their differences in morphology and internal CL (cathodoluminescence) imaging. Eleven zircons (30%) are present as subhedral, thin and elongate grains, approximately 200-420 µm in size, with pyramidal to sub-rounded terminations (e.g. spots 037-41 & 037-56; Fig. 34). The remaining thirty-three zircons (70%) are present as subhedral to stubby zircon prisms, approximately 180-400 µm in size, with sub-rounded to rounded terminations with core regions commonly containing inclusions (e.g. spots 037-23 and 037-70).

Internally, the first population is characterised by bright, concentrically zoned cores (Fig. 34; e.g. spot 037-56) surrounded by dark CL overgrowths. These zircons tend to have less bright cores when compared to that of the second population, with U values typically ranging between 82 and 375 ppm (Table 5) and Th/U ranging between 0.37 and 0.99. The dark, unzoned overgrowth rims of this population have U values ranging between 261 and 448 ppm (Th/U ranges between 0.31 and 0.60). The second zircon population has bright, unzoned cores (Fig. 34; e.g., spots 037-25 & 037-70) that typically display evidence of magmatic resorption (e.g. spots 037-43 & 037-54). Another recognisable feature is metamictization (e.g., spots 037-74 & 037-55) and acicular to stubby rounded inclusions (spots 037-74 & 037-23). The bright, unzoned cores have U values ranging between 30 and 305 ppm and Th/U ranging between 0.33 and 0.9, whereas the dark, unzoned overgrowth rims have U values ranging between 107 and 993 ppm with Th/U ranging between 0.02 and 0.58. Only one analysis of the second population (spot 037-47) has a low Th/U of 0.02 which could indicate a later metamorphic event (Table 5).

Thirty-nine of these 89 analyses provided concordant dates, 15 were discordant and 35 analyses on metamict grains yielded meaningless values. Of the concordant analyses, 28 were on the core regions and the rest on rims. This sample has a source region with $^{206}Pb/^{238}U$ ages dating at 1841 ± 35 Ma, 1799 ± 37 Ma and 1740 ± 36 Ma with a spread of ages along concordia from ~1290 Ma to ~1140 Ma with the most number of analyses having ages around ~1190 Ma (Fig. 35, 36a & 36b). The youngest detrital zircon (spot 037-46) yielded a $^{206}Pb/^{238}U$ age of 1138 ± 22 Ma and is characterised by a dark CL, unzoned core with a U value of 649 ppm and a Th/U of 0.43 (Fig. 34 & Table 5). Analysis 037-47 has a $^{206}Pb/^{238}U$ age of 1131 ± 22 Ma and is characterised by a dark rim with a U value of 993 ppm and a low Th/U of 0.02 typical of a metamorphic origin. Both ages represent the maximum and minimum ages of deposition for this sample respectively.
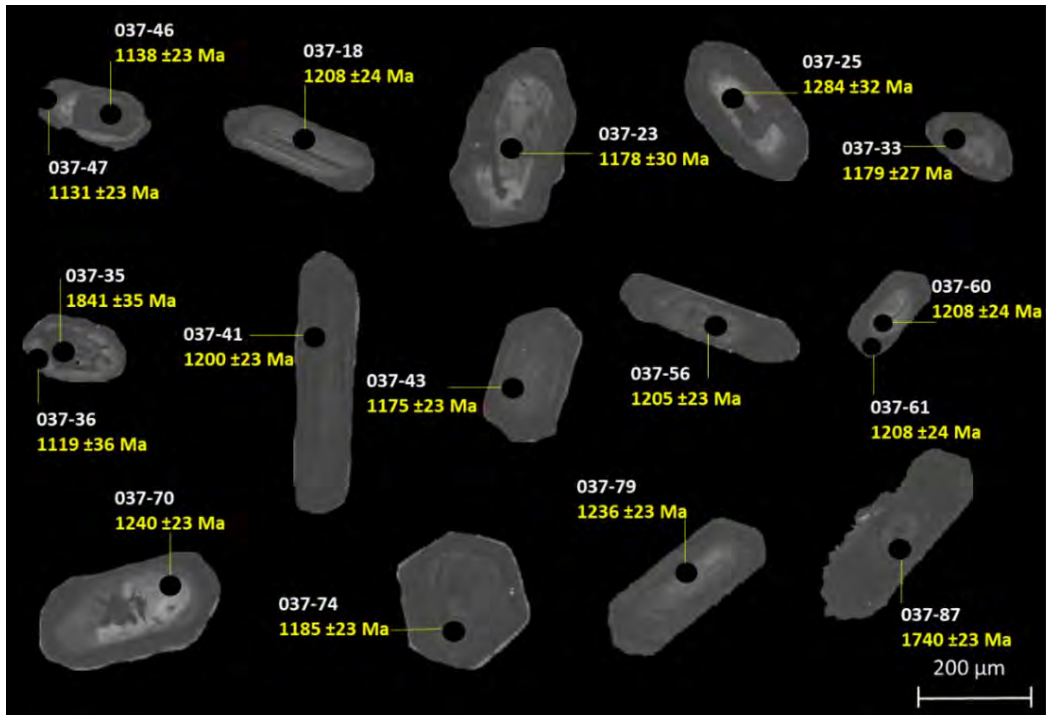
Figure 34 CL images of zircons collected from sample 037. Each spot, represented by a black circle, has been labelled with the analyses/spot number and the calculated $^{206}Pb/^{238}U$ ages.
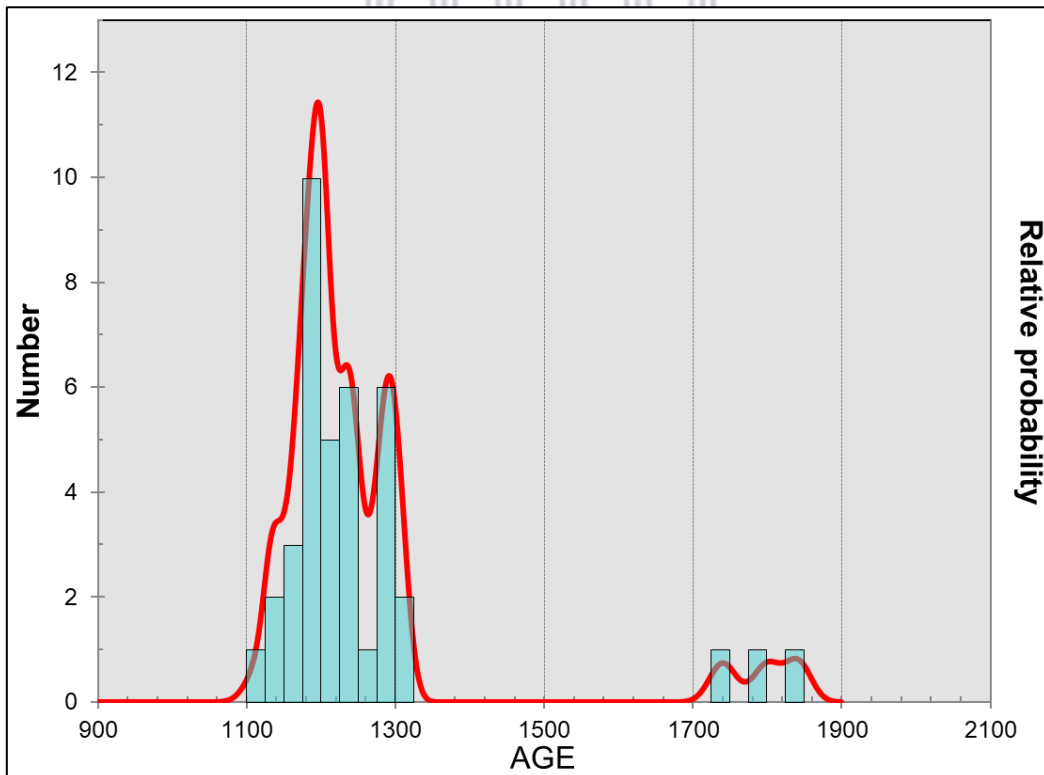
Figure 35 Probability density diagram for the $^{206}Pb/^{238}U$ zircon ages of sample 037.

6.3.1. (a)   Isotope geochemistry

The grey biotite gneiss has a low Sm/Nd ratio of 0.2063 (Appendix B, Table B4). The $^{143}Nd/^{144}Nd$ value is moderate (0.51190) with a corresponding and relatively strongly negative epsilon $\epsilon Nd_{(i)}$ value of -5.86 calculated from the 1138 ± 22 Ma maximum detrital age of this gneiss (Appendix B, Table B4). The grey biotite gneiss has a Rb/Sr ratio of 3.3708, yields a $^{87}Rb/^{86}Sr$ ratio of 8.9537 with an initial Sr ($^{87}Sr/^{86}Sr_{(i)}$) of 0.71890 and epsilon Sr(t) value for today of 222 (Appendix B, Table B4). Calculated T_{CHUR} and T_{PM} ages are 1.65 Ga and 2.20 Ga respectively (Appendix, Table B4 & Figure A14).
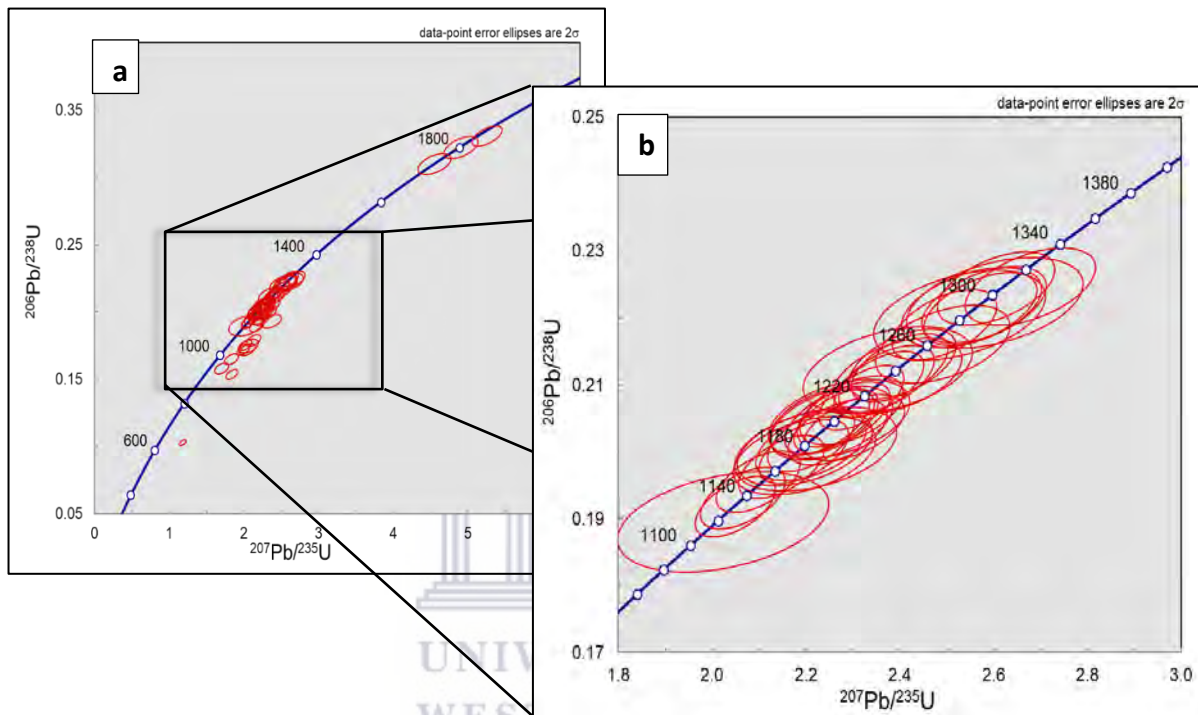
Figure 36 (a) U-Pb concordia plot of all analyses for sample 037 displaying minor discordance, **(b)** Enlarged Concordia plot of younger concordant analyses.

6.3.2   Hunboom Gneiss: Sample 038A

Sample 038A is a migmatitic, fine- to medium-grained, mesocratic grey biotite gneiss (29° 58' 8.4" S, 17° 51' 8.71" E). This sample yielded 60 zircons on which 85 analyses were performed on core and rim regions. The sample contains a distinct population of zircons with subhedral to anhedral prismatic shapes that vary between stubby and elongate with rounded to abraded edges or blunt terminations. They range in size between approximately 200 and 410 μm (Fig. 37). Minor fractures are present in some grains, as seen in analysis 038A-14. The CL images in Figure 37 show largely metamict zircons with poorly defined internal structures (e.g. spot 038A-73), with most commonly having spherical and acicular inclusions (e.g. spot 038A-01). Zircons with unzoned cores of dark CL luminosity are observed in analyses 038A-02, 038A-32, 038A-33 and 038A-49. By contrast, zircons with faintly zoned, bright cores are also observed for analyses 038A-14, 038A-38, 038A-50, 038A-74 and 038A-81. Oscillatory zoning is not particularly pronounced but can be seen in analyses 038A-09 and 038A-15. Analysis 038A-12 displays sector zoning.

39

Table 5 U-Th-Pb isotopic compositions of zircon grains extracted from sample 037 of the Hunboom Gneiss located in the BRSZ.

	Spot number	U [ppm][a]	Pb [ppm][a]	206Pb/204Pb	Th/U[a]	207Pb/235U[b]	2σ[d]	206Pb/238U[b]	2σ[d]	rho[c]	207Pb/206Pb[e]	2σ[d]	207Pb/235U	2σ	206Pb/238U	2σ	207Pb/206Pb	2σ	%	Region	Luminescence	Description
						RATIOS							AGES [Ma]						Conc.			
Analyses used	037-04	684	142	3806	0.31	2.318	0.074	0.2081	0.0039	0.60	0.0808	0.0021	1218	39	1219	23	1217	50	100	rim	dark	overgrowth rim
	037-07	63	14	649	0.89	2.491	0.117	0.2161	0.0047	0.47	0.0836	0.0035	1270	60	1261	28	1284	81	98	core	bright	zoned
	037-11	484	103	9437	0.31	2.400	0.084	0.2126	0.0041	0.56	0.0819	0.0024	1243	43	1243	24	1243	57	100	rim	dark	overgrowth rim
	037-14	319	63	85747	0.65	2.148	0.075	0.1977	0.0038	0.56	0.0788	0.0023	1164	41	1163	23	1167	57	100	rim	medium dark	overgrowth rim
	037-16	270	55	655	0.25	2.254	0.107	0.2043	0.0045	0.46	0.0800	0.0034	1198	57	1198	26	1198	83	100	core	medium bright	zoned
	037-18	162	34	506	0.91	2.298	0.090	0.2062	0.0042	0.52	0.0808	0.0027	1212	48	1208	24	1217	66	99	core	brght	zoned
	037-19	199	40	3103	0.99	2.267	0.086	0.2030	0.0041	0.53	0.0810	0.0026	1202	46	1191	24	1222	64	98	core	bright	zoned
	037-21	676	218	2917	0.19	4.905	0.186	0.3220	0.0066	0.54	0.1105	0.0035	1803	68	1799	37	1807	58	100	core	dark	unzoned
	037-22	107	24	1025	0.58	2.580	0.109	0.2220	0.0046	0.50	0.0843	0.0031	1295	55	1292	27	1299	71	99	rim	dark	overgrowth rim
	037-23	104	21	366	0.86	2.221	0.141	0.2004	0.0051	0.40	0.0804	0.0047	1188	76	1178	30	1206	115	98	core	bright	unzoned, metamict
	037-25	53	12	440	1.06	2.528	0.149	0.2205	0.0055	0.42	0.0832	0.0045	1280	76	1284	32	1273	105	101	core	bright	unzoned, metamict
	037-27	447	94	5631	0.60	2.355	0.078	0.2101	0.0040	0.58	0.0813	0.0022	1229	41	1229	24	1229	53	100	rim	medium dark	overgrowth rim
	037-29	558	125	1242	0.35	2.679	0.113	0.2247	0.0047	0.50	0.0865	0.0032	1323	56	1307	27	1349	71	97	core	dark	unzoned, metamict
	037-31	55	11	15271	1.30	2.271	0.123	0.2049	0.0048	0.43	0.0804	0.0039	1203	65	1201	28	1206	97	100	core	bright	unzoned
	037-33	194	39	596	0.88	2.197	0.117	0.2006	0.0046	0.43	0.0795	0.0038	1180	63	1179	27	1183	95	100	core	bright	unzoned
	037-34	753	147	9174	0.28	2.098	0.073	0.1955	0.0038	0.56	0.0778	0.0022	1148	40	1151	22	1142	57	101	rim	dark	overgrowth rim
	037-35	449	149	5948	0.97	5.251	0.166	0.3306	0.0063	0.60	0.1152	0.0029	1861	59	1841	35	1883	46	98	core	dark	unzoned
	037-36	115	22	1374	0.49	2.024	0.184	0.1896	0.0061	0.36	0.0774	0.0066	1124	102	1119	36	1132	169	99	rim	bright	overgrowth rim
	037-37	752	154	209647	0.04	2.265	0.074	0.2046	0.0039	0.58	0.0803	0.0021	1201	39	1200	23	1204	52	100	core	dark	unzoned
	037-39	680	145	1189	1.21	2.407	0.093	0.2131	0.0043	0.52	0.0819	0.0027	1245	48	1245	25	1243	65	100	core	dark	unzoned, metamict
	037-41	582	119	162169	0.70	2.245	0.074	0.2045	0.0039	0.58	0.0796	0.0022	1195	40	1200	23	1188	54	101	core	dark	zoned
	037-43	278	56	1434	0.21	2.195	0.078	0.2000	0.0039	0.55	0.0796	0.0024	1180	42	1175	23	1187	59	99	core	medium bright	unzoned
	037-45	200	44	76474	0.31	2.496	0.092	0.2190	0.0043	0.54	0.0827	0.0026	1271	47	1277	23	1261	61	101	rim	medium dark	overgrowth rim
	037-46	649	125	11027	0.43	2.065	0.074	0.1931	0.0038	0.55	0.0776	0.0023	1137	41	1138	23	1136	60	100	core	dark	unzoned
	037-47	993	191	2815	0.02	2.049	0.070	0.1918	0.0037	0.56	0.0775	0.0022	1132	39	1131	23	1134	56	100	rim	dark	metamorphic rim
	037-52	173	35	2218	0.68	2.235	0.091	0.2046	0.0042	0.50	0.0792	0.0028	1192	49	1200	23	1178	70	102	core	medium bright	unzoned
	037-54	305	61	83614	0.33	2.211	0.097	0.2009	0.0042	0.48	0.0798	0.0031	1185	52	1180	23	1193	76	99	rim	bright	ovegrowth rim
	037-56	375	77	105269	0.37	2.281	0.081	0.2056	0.0040	0.55	0.0805	0.0024	1206	43	1205	23	1208	58	100	core	bright	zoned
	037-58	211	47	63663	0.72	2.572	0.099	0.2214	0.0044	0.52	0.0843	0.0028	1293	50	1289	23	1298	64	99	core	bright	zoned
	037-60	73	16	22157	0.76	2.553	0.123	0.2216	0.0049	0.46	0.0836	0.0036	1287	62	1290	23	1283	83	101	core	bright	faintly zoned
	037-64	366	77	2041	0.67	2.372	0.083	0.2109	0.0041	0.55	0.0816	0.0024	1234	43	1234	23	1235	57	100	core	bright	zoned
	037-68	33	7	249	1.99	2.603	0.154	0.2223	0.0055	0.42	0.0849	0.0046	1301	77	1294	23	1314	104	98	core	bright	unzoned, zircon ls abraded
	037-70	30	6	1780	0.74	2.375	0.148	0.2122	0.0053	0.40	0.0812	0.0046	1235	77	1240	23	1226	112	101	core	bright	unzoned, metamict
	037-73	112	22	770	0.92	2.197	0.124	0.1994	0.0047	0.42	0.0799	0.0041	1180	66	1172	23	1195	101	98	core	bright	unzoned, zircon ls abraded
	037-74	738	149	203415	0.05	2.210	0.076	0.2017	0.0039	0.56	0.0795	0.0023	1184	41	1185	23	1184	56	100	core	dark	metamict core
	037-76	222	50	3479	0.48	2.606	0.102	0.2244	0.0045	0.52	0.0842	0.0028	1302	51	1305	23	1298	65	101	core	bright	unzoned
	037-78	261	53	1202	0.34	2.302	0.088	0.2036	0.0040	0.52	0.0820	0.0027	1213	46	1195	23	1245	64	96	rim	medium bright	overgrowth rim
	037-79	82	17	23690	0.57	2.396	0.112	0.2114	0.0046	0.46	0.0822	0.0034	1241	58	1236	23	1250	81	99	core	bright	unzoned
	037-87	224	69	13060	0.21	4.548	0.182	0.3099	0.0064	0.52	0.1065	0.0036	1740	69	1740	23	1740	63	100	core	medium bright	zoned
Analyses not used	037-01	591	118	19616	0.35	2.317	0.095	0.1995	0.0041	0.50	0.0842	0.0030	1217	50	1173	24	1298	69	90			
	037-02	620	121	163877	0.19	2.237	0.082	0.1945	0.0038	0.54	0.0834	0.0026	1193	44	1146	23	1279	60	90			
	037-06	447	78	2709	0.43	3.784	0.108	0.1745	0.0040	0.44	0.0856	0.0040	1135	60	1037	24	1329	91	78			
	037-08	528	100	8562	0.25	2.169	0.079	0.1896	0.0037	0.54	0.0830	0.0025	1171	43	1119	22	1269	60	88			
	037-09	596	104	3178	0.48	2.023	0.065	0.1753	0.0033	0.59	0.0837	0.0022	1123	36	1041	20	1286	51	81			
	037-10	431	74	1459	0.47	2.040	0.087	0.1720	0.0036	0.49	0.0860	0.0032	1129	48	1023	21	1339	71	76			
	037-13	413	71	96541	0.47	1.997	0.072	0.1721	0.0034	0.55	0.0841	0.0025	1114	40	1024	20	1296	58	79			
	037-20	1186	195	5373	0.29	1.830	0.076	0.1647	0.0034	0.50	0.0806	0.0029	1056	44	983	20	1211	71	81			
	037-26	1320	136	1382	0.09	1.180	0.038	0.1029	0.0019	0.59	0.0832	0.0022	791	25	631	12	1273	51	50			
	037-48	201	41	1352	0.53	2.356	0.102	0.2050	0.0043	0.49	0.0834	0.0031	1229	53	1202	25	1278	73	94			
	037-50	133	21	869	1.51	1.703	0.077	0.1578	0.0033	0.47	0.0783	0.0031	1010	46	945	20	1153	79	82			
	037-66	308	59	1154	1.15	2.364	0.111	0.1929	0.0042	0.47	0.0889	0.0037	1232	58	1137	25	1402	80	81			
	037-71	167	33	3030	0.44	2.193	0.107	0.1957	0.0043	0.45	0.0813	0.0035	1179	58	1152	25	1228	86	94			
	037-82	310	55	1527	0.48	2.124	0.078	0.1787	0.0035	0.53	0.0862	0.0027	1157	43	1060	21	1343	60	79			
	037-84	768	118	1077	0.16	1.834	0.065	0.1534	0.0030	0.55	0.0867	0.0026	1058	37	920	18	1354	57	68			

[a]U and Pb concentrations and Th/U ratios are calculated relative to GJ-1 reference zircon

[b]Corrected for background and within-run Pb/U fractionation and normalised to reference zircon GJ-1 (ID-TIMS values/measured value); 207Pb/235U calculated using (207Pb/206Pb)/(238U/206Pb * 1/137.88)

[c]Rho is the error correlation defined as the quotient of the propagated errors of the 206Pb/238U and the 207Pb/235U ratio

[d]Quadratic addition of within-run errors (2 SD) and daily reproducibility of GJ-1 (2 SD)

[e]Corrected for mass-bias by normalising to GJ-1 reference zircon (~0.6 per atomic mass unit) and common Pb using the model Pb composition of Stacey & Kramers (1975)

Grey highlighted analyses represent rims and overgrowths that are likely related to metamorphism

The age data is displayed in the probability density distribution diagram and the U-Pb Concordia plot in Figures 38, 39a and 39b. Fifty-three analyses provided concordant dates with the most number of analyses having ages around ~1190 Ma and ~1200 Ma (Table 6a & 6b and Figs. 38, 39a & 39b). Figures 39a and 39b show that the detrital grains have ages of around ~1850 Ma (n=3), and at 1658 ± 33 Ma (n=1) along with a spread of $^{206}Pb/^{238}U$ ages along concordia from ~1270 Ma to ~1113 Ma with the youngest detrital grain dated at 1113 ± 22 Ma (spot 038A-48) characterised by a bright, unzoned core (U = 234 ppm; Th/U = 0.42). A metamorphic age of 1061 ± 21 Ma is obtained from spot 038A-12, which is characterised by a bright, overgrowth (U = 123 ppm; Th/U = 0.61). The youngest age and the youngest metamorphic age represent the maximum and minimum ages of deposition for this sample respectively.

6.3.2. (a)   Isotope geochemistry

The grey biotite gneiss has a low Sm/Nd ratio of 0.1886 (Appendix B, Table B4). The $^{143}Nd/^{144}Nd$ value is moderate (0.51170) with a corresponding and relatively strongly negative epsilon $\epsilon Nd_{(t)}$ value of -4.78 calculated from the 1113 ± 22 Ma maximum detrital age of this gneiss (Appendix B, Table B4). The grey biotite gneiss has a Rb/Sr ratio of 1.3457, yields a $^{87}Rb/^{86}Sr$ ratio of 3.5747 with an initial Sr ($^{87}Sr/^{86}Sr_{(i)}$) of 0.72070 and an epsilon $Sr_{(t)}$value for today of 247 (Appendix B, Table B4). Calculated T_{CHUR} and T_{DM} ages are 1.66 Ga and 2.15 Ga respectively (Appendix, Table B4 & Figure A14).

Figure 37 CL images of zircons collected from sample 038A. Each spot, represented by a black circle, has been labelled with the analyses/spot number and the calculated $^{206}Pb/^{238}U$ ages.

41
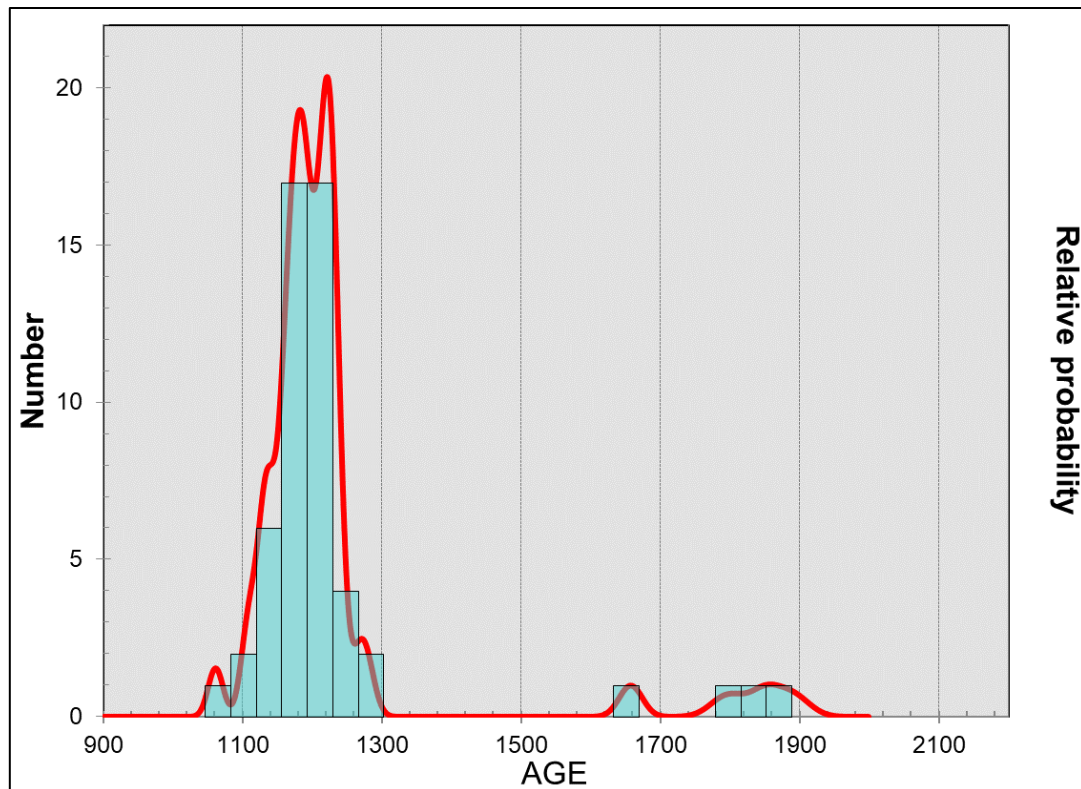
Figure 38 Probability density diagram for the zircon ^{206}Pb/^{238}U ages of sample 038A.

6.3.3 Garnetiferous quartzofeldspathic biotite-sillimanite gneiss: Sample 036A

Sample 036A is a heterogeneous migmatitic package of interlayered garnetiferous quartzofeldspathic biotite-sillimanite gneiss that was sampled at the *Ybeep Farm* (29° 58' 3.36" S, 17° 58' 42.71" E). The results for sample 036A yielded 38 analyses from a total of 23 zircons. One distinct zircon population can be identified based on grain shape with grain sizes ranging between 70 and 230 μm (Fig. 40), with sub-rounded to rounded shapes typical of metamorphic resorption (i.e., the overall grain shape as seen for spots 036A-16, 036A-29 & 036A-39) as well as core regions which display magmatic resorption of the grain with a later overgrowth (core regions labelled 036A-08 and 036A-26). Of the 38 analyses, 33 gave concordant dates (Table 7). As observed on the probability density distribution and U-Pb Concordia diagrams (Fig. 41a & 41b) four prominent peaks can be observed with the highest peak around ~1210 Ma.

These two diagrams show the detrital grains have ages of inheritance at 1539 ± 36 Ma and 1502 ± 38 Ma and a spread of ^{206}Pb/^{238}U ages along concordia from ~1426 Ma to ~1162 Ma and a noteworthy amount of grains (N = 9) with ages around ~1300 Ma. The youngest detrital grain dates at 1222 ± 25 Ma (spot 036A-36) and is characterised by a bright, zoned core (U = 174 ppm; Th/U = 0.46). There is also a metamorphic age of 1171 ± 21 Ma (spot 036A-32) which is characterised by a medium bright, unzoned overgrowth (U = 247 ppm; Th/U = 0.03). The youngest age and the youngest metamorphic age represents the maximum and minimum ages of deposition for this sample, respectively.

42

Figure 39 (a) U-Pb concordia plot of the spread of all analyses data of sample 038A displaying minor discordance; **(b)** Enlarged Concordia plot of younger concordant analyses.

Figure 40 CL images of selected zircons collected from sample 036A. Each spot, represented by a black circle, has been labelled with the analyses/spot number and the calculated $^{206}Pb/^{238}U$ ages.
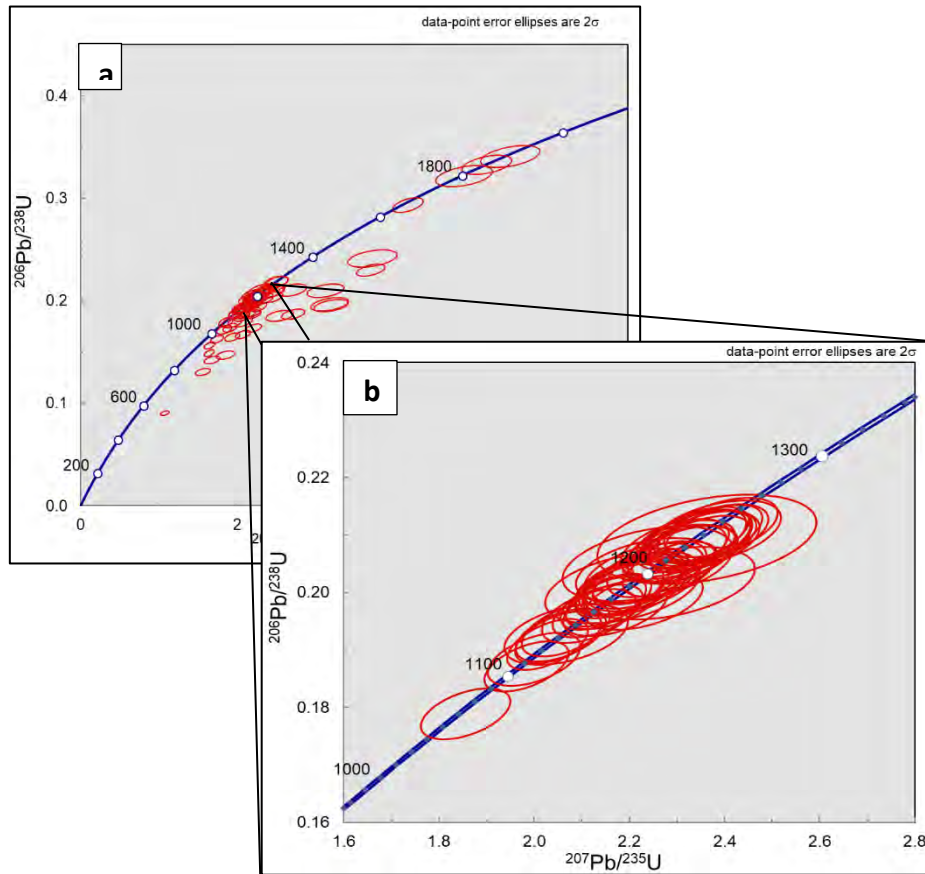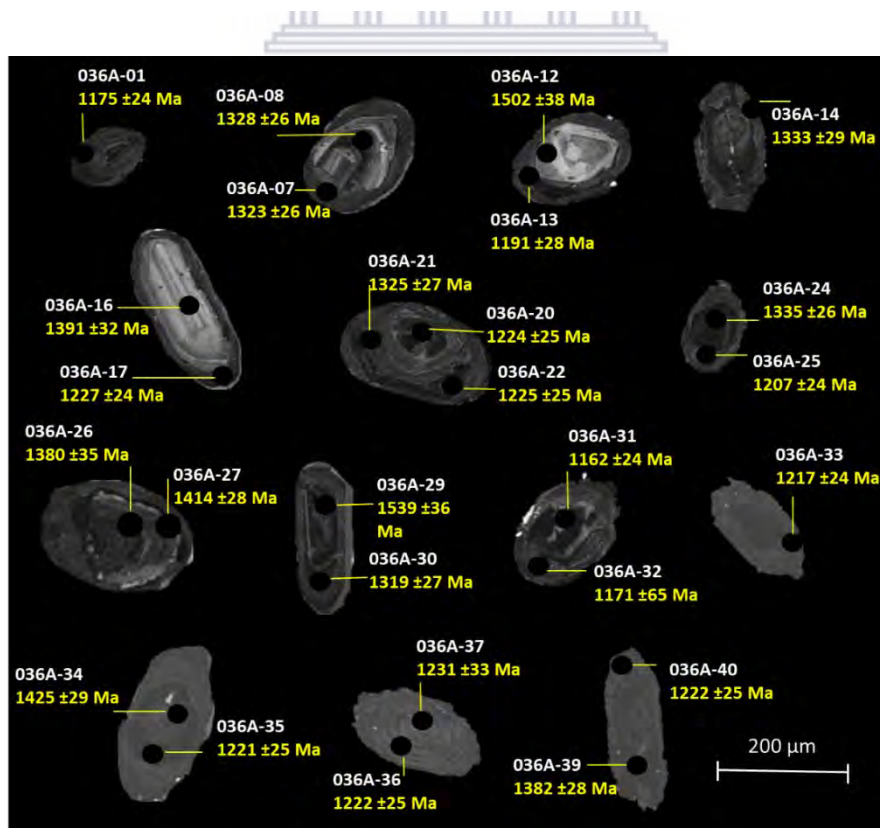
43

Table 6 (a) U-Th-Pb isotopic compositions of zircon grains extracted from sample 038A of the Hunboom Gneiss located within the BRSZ.

Spot number	U [ppm][a]	Pb [ppm][a]	206Pb/204Pb	Th/U[a]	207Pb/235U[b]	2σ[d]	206Pb/238U[b]	2σ[d]	rho[c]	207Pb/206Pb[e]	2σ[d]	207Pb/235U	2σ	206Pb/238U	2σ	207Pb/206Pb	2σ	%	Region	Luminescence	Description
038-01	185	36	49242	0.41	2.056	0.077	0.1926	0.0038	0.52	0.0774	0.0025	1134	43	1135	22	1132	64	100	rim	med bright	overgrowth rim, abraded zircon
038-02	180	36	39529	0.33	2.183	0.080	0.2007	0.0039	0.53	0.0789	0.0025	1176	43	1179	23	1169	62	101	core	dark	unzoned
038-03	297	59	2313	0.44	2.144	0.073	0.1981	0.0038	0.55	0.0785	0.0022	1163	40	1165	22	1160	57	100	rim	med dark	overgrowth rim
038-05	299	60	1509	0.94	2.179	0.076	0.2002	0.0038	0.55	0.0789	0.0023	1174	41	1177	22	1170	58	101	core	med bright	unzoned
038-06	97	19	26789	0.61	2.200	0.093	0.2011	0.0041	0.49	0.0793	0.0029	1181	50	1181	24	1180	73	100	rim	bright	overgrowth rim
038-08	41	8	734	1.35	2.185	0.132	0.2007	0.0050	0.41	0.0790	0.0044	1176	71	1179	29	1171	109	101	core	dark	zoned
038-09	168	35	542	0.73	2.238	0.146	0.2050	0.0053	0.40	0.0792	0.0047	1193	78	1202	31	1177	118	102	rim	bright	zoned overgrowth
038-10	317	93	128371	0.49	4.188	0.158	0.2932	0.0059	0.53	0.1036	0.0033	1672	63	1658	33	1690	59	98	core	med dark	faintly zoned
038-12	123	22	1800	0.61	1.856	0.077	0.1789	0.0036	0.49	0.0752	0.0027	1065	44	1061	21	1075	73	99	rim	bright	zoned overgrowth rim, abraded zircon
038-14	70	14	847	0.88	2.230	0.103	0.2033	0.0043	0.46	0.0796	0.0033	1191	55	1193	25	1186	81	101	core	bright	unzoned core, fractured, abraded zircon
038-17	369	73	3983	0.40	2.156	0.074	0.1986	0.0038	0.55	0.0787	0.0022	1167	40	1168	22	1165	56	100	rim	dark	overgrowth rim
038-18	178	35	1324	0.74	2.166	0.081	0.1984	0.0039	0.52	0.0792	0.0025	1170	44	1167	23	1176	63	99	rim	med bright	overgrowth rim
038-19	135	27	37480	0.61	2.228	0.098	0.2019	0.0042	0.47	0.0800	0.0031	1190	52	1186	25	1197	76	99	core	dark	unzoned core
038-22	56	11	1552	0.67	2.067	0.106	0.1927	0.0043	0.43	0.0778	0.0036	1138	58	1136	25	1142	92	99	rim	bright	zoned rim, abraded zircon
038-23	16	3	167	1.33	2.362	0.188	0.2092	0.0063	0.38	0.0819	0.0060	1231	98	1225	37	1243	145	99	core	bright	unzoned core, abraded zircon
038-24	252	49	1113	0.39	2.050	0.074	0.1922	0.0037	0.53	0.0774	0.0024	1132	41	1133	22	1130	61	100	rim	med dark	overgrowth rim, abraded zircon
038-26	347	71	1427	0.20	2.285	0.080	0.2040	0.0039	0.54	0.0812	0.0024	1208	42	1197	23	1227	58	98	rim	med bright	overgrowth rim, abraded zircon
038-30	243	47	64564	0.25	2.066	0.076	0.1934	0.0037	0.53	0.0775	0.0024	1138	42	1140	22	1133	62	101	core	bright	zoned, abraded zircon
038-31	425	81	17025	0.40	2.028	0.069	0.1910	0.0036	0.55	0.0770	0.0022	1125	38	1127	21	1122	57	100	rim	med bright	overgrowth rim
038-32	490	103	141190	0.11	2.348	0.079	0.2094	0.0039	0.56	0.0813	0.0023	1227	41	1226	23	1230	55	100	rim	bright	bright overgrowth rim
038-34	323	64	4129	0.48	2.133	0.077	0.1968	0.0038	0.53	0.0786	0.0024	1160	42	1158	22	1163	61	100	rim	med bright	overgrowth rim, abraded zircon
038-35	354	69	95342	0.32	2.115	0.081	0.1959	0.0038	0.51	0.0783	0.0026	1154	44	1153	23	1154	65	100	rim	med bright	overgrowth rim, abraded zircon
038-37	334	68	5326	0.47	2.257	0.085	0.2040	0.0040	0.52	0.0802	0.0026	1199	45	1197	23	1203	63	100	rim	med dark	overgrowth rim
038-38	137	27	1519	0.73	2.211	0.090	0.2009	0.0040	0.49	0.0798	0.0028	1185	48	1180	24	1193	70	99	core	bright	faintly zoned
038-44	413	87	47288	0.44	2.378	0.083	0.2104	0.0040	0.54	0.0820	0.0024	1236	43	1231	23	1245	58	99	rim	med dark	overgrowth rim
038-45	282	57	1736	0.46	2.223	0.082	0.2029	0.0039	0.53	0.0795	0.0025	1188	44	1191	23	1184	62	101	rim	med dark	overgrowth rim
038-46	48	16	387	0.84	5.496	0.308	0.3407	0.0088	0.46	0.1170	0.0058	1900	##	1890	49	1911	89	99	core	bright	zoned, abraded zircon
038-47	40	13	2655	0.57	4.905	0.298	0.3216	0.0086	0.44	0.1106	0.0060	1803	##	1797	48	1810	99	99	core	bright	zoned, abraded zircon
038-48	234	44	1262	0.42	2.000	0.080	0.1884	0.0037	0.50	0.0770	0.0027	1115	44	1113	22	1121	69	99	core	med bright	unzoned, abraded zircon, youngest detrital age
038-49	363	68	3730	0.41	1.984	0.072	0.1871	0.0036	0.53	0.0769	0.0024	1110	40	1106	21	1119	62	99	rim	dark	overgrowth rim
038-50	57	11	730	0.76	2.284	0.147	0.2017	0.0052	0.42	0.0821	0.0048	1207	78	1184	30	1249	115	95	rim	bright	unzoned, abraded zircon
038-52	372	75	52802	0.51	2.221	0.081	0.2019	0.0039	0.52	0.0798	0.0025	1188	43	1185	23	1192	61	99	rim	med dark	overgrowth rim
038-53	102	22	30601	0.55	2.513	0.117	0.2183	0.0047	0.46	0.0835	0.0035	1276	59	1273	27	1281	81	99	core	med bright	faintly zoned
038-56	165	34	2899	0.41	2.340	0.095	0.2094	0.0042	0.49	0.0811	0.0029	1224	50	1225	24	1223	69	100	core	med bright	faintly zoned, abraded zircon
038-59	202	42	58092	0.39	2.353	0.093	0.2091	0.0041	0.50	0.0816	0.0028	1229	48	1224	24	1237	67	99	rim	dark	thick overgrowth rim
038-60	179	38	4228	0.31	2.381	0.112	0.2105	0.0045	0.45	0.0820	0.0034	1237	58	1231	26	1246	82	99	rim	dark	thick dark overgrowth rim
038-61	382	80	109298	0.31	2.347	0.087	0.2084	0.0040	0.52	0.0817	0.0026	1227	46	1220	24	1238	62	99	core	med bright	unzoned core
038-62	255	53	72336	0.48	2.295	0.089	0.2068	0.0041	0.51	0.0805	0.0027	1211	47	1212	24	1209	66	100	rim	dark	thick overgrowth rim, abraded zircon
038-63	357	72	37954	0.34	2.201	0.088	0.2011	0.0040	0.50	0.0794	0.0027	1181	47	1181	23	1182	68	100	rim	dark	abraded zircon
038-65	193	38	6824	0.45	2.171	0.090	0.1973	0.0040	0.49	0.0798	0.0029	1172	48	1161	23	1192	71	97	core	med bright	unzoned, abraded zircon
038-66	203	42	57555	0.49	2.312	0.094	0.2066	0.0041	0.49	0.0812	0.0029	1216	49	1211	24	1225	70	99	core	med dark	unzoned core
038-68	31	10	982	0.54	5.197	0.261	0.3324	0.0078	0.47	0.1134	0.0050	1852	93	1850	43	1855	80	100	core	bright	unzoned
038-69	1122	236	9160	0.14	2.346	0.086	0.2100	0.0040	0.52	0.0810	0.0025	1226	45	1229	24	1222	61	101	rim	dark	thin overgrowth rim
038-71	208	43	1305	0.45	2.307	0.094	0.2075	0.0041	0.49	0.0807	0.0029	1215	49	1215	24	1213	70	100	rim	med dark	overgrowth rim
038-72	357	74	101265	0.44	2.314	0.089	0.2067	0.0040	0.50	0.0812	0.0027	1217	47	1211	24	1226	65	99	core	dark	zoned core, abraded zircon
038-76	260	55	75468	0.36	2.392	0.097	0.2113	0.0042	0.49	0.0821	0.0029	1240	51	1236	25	1248	70	99	rim	med dark	overgrowth rim, abraded zircon
038-79	334	70	4837	0.45	2.377	0.095	0.2103	0.0041	0.49	0.0820	0.0028	1236	49	1230	24	1245	68	99	rim	dark	overgrowth rim, abraded zircon
038-80	293	61	1596	0.41	2.296	0.093	0.2078	0.0041	0.49	0.0801	0.0028	1211	49	1217	24	1200	70	101	rim	med bright	overgrowth rim
038-81	119	25	1980	0.78	2.344	0.107	0.2089	0.0044	0.46	0.0814	0.0033	1226	56	1223	26	1230	80	99	core	bright	bright faintly zoned core
038-82	490	103	140706	0.39	2.343	0.094	0.2094	0.0041	0.49	0.0812	0.0028	1225	49	1225	24	1225	69	100	rim	med bright	overgrowth rim
038-84	160	32	2064	0.45	2.230	0.101	0.1985	0.0041	0.46	0.0815	0.0033	1191	54	1167	24	1233	79	95	core	bright	zoned
038-85	111	24	2698	0.54	2.497	0.126	0.2181	0.0048	0.44	0.0831	0.0038	1271	64	1272	28	1270	88	100	rim	med bright	overgrowth rim
038-86	192	39	30915	0.42	2.235	0.121	0.2039	0.0046	0.42	0.0795	0.0039	1192	64	1196	27	1185	97	101	core	med bright	unzoned core

(Analyses used)

[a] U and Pb concentrations and Th/U ratios are calculated relative to GJ-1 reference zircon

[b] Corrected for background and within-run Pb/U fractionation and normalised to reference zircon GJ-1 (ID-TIMS values/measured value); 207Pb/235U calculated using (207Pb/206Pb)/(238U/206Pb * 1/137.88)

[c] Rho is the error correlation defined as the quotient of the propagated errors of the 206Pb/238U and the 207Pb/235U ratio

[d] Quadratic addition of within-run errors (2 SD) and daily reproducibility of GJ-1 (2 SD)

[e] Corrected for mass-bias by normalising to GJ-1 reference zircon (~0.6 per atomic mass unit) and common Pb using the model Pb composition of Stacey & Kramers (1975)

44

Table 6 (b) U-Th-Pb isotopic compositions of zircon grains extracted from sample 038A of the Hunboom Gneiss located within the BRSZ.

	Spot number	U [ppm][a]	Pb [ppm][a]	206Pb/204Pb	Th/U[a]	RATIOS 207Pb/235U[b]	2 σ[d]	206Pb/238U[b]	2 σ[d]	rho[c]	207Pb/206Pb[e]	2 σ[d]	AGES [Ma] 207Pb/235U	2 σ	206Pb/238U	2 σ	207Pb/206Pb	2 σ	Conc. %
	038-04	66	13	444	0.84	3.183	0.195	0.1963	0.0053	0.44	0.1176	0.0065	1453	89	1156	31	1920	99	60
	038-07	331	55	764	0.44	2.077	0.079	0.1671	0.0033	0.52	0.0902	0.0029	1141	43	996	20	1429	62	70
	038-13	274	51	1658	0.23	2.154	0.075	0.1872	0.0036	0.55	0.0835	0.0024	1166	41	1106	21	1280	57	86
	038-15	833	124	7794	0.75	1.642	0.053	0.1490	0.0028	0.58	0.0800	0.0021	987	32	895	17	1196	52	75
	038-16	253	37	541	0.42	1.851	0.099	0.1470	0.0034	0.43	0.0913	0.0044	1064	57	884	21	1453	92	61
	038-20	361	68	93255	0.45	2.055	0.094	0.1874	0.0040	0.46	0.0796	0.0032	1134	52	1107	24	1186	80	93
	038-21	205	33	698	0.43	1.744	0.066	0.1623	0.0032	0.52	0.0779	0.0025	1025	39	969	19	1145	65	85
	038-25	211	39	900	0.45	2.066	0.081	0.1841	0.0037	0.51	0.0814	0.0028	1138	45	1089	22	1231	67	88
	038-27	412	74	4451	0.41	2.040	0.127	0.1795	0.0045	0.40	0.0824	0.0047	1129	70	1064	27	1256	112	85
	038-28	206	36	401	0.33	2.210	0.086	0.1731	0.0034	0.51	0.0926	0.0031	1184	46	1029	20	1480	63	70
	038-29	1483	232	138442	0.11	1.648	0.056	0.1562	0.0029	0.55	0.0765	0.0022	989	34	936	18	1108	56	84
	038-36	159	31	667	0.42	3.205	0.177	0.1955	0.0049	0.45	0.1189	0.0059	1458	81	1151	29	1940	88	59
	038-39	3537	320	427	0.07	1.078	0.045	0.0906	0.0018	0.49	0.0863	0.0031	743	31	559	11	1346	70	42
	038-40	202	36	49779	0.49	1.932	0.104	0.1789	0.0041	0.42	0.0783	0.0038	1092	59	1061	24	1155	97	92
	038-41	184	42	502	0.62	3.713	0.152	0.2299	0.0048	0.51	0.1172	0.0041	1574	64	1334	28	1913	63	70
	038-42	276	56	704	0.24	2.438	0.123	0.2034	0.0046	0.45	0.0869	0.0039	1254	63	1194	27	1359	87	88
	038-43	77	19	675	0.57	3.731	0.255	0.2413	0.0070	0.42	0.1121	0.0070	1578	##	1394	40	1834	112	76
	038-51	487	96	4705	0.29	2.231	0.080	0.1972	0.0038	0.53	0.0821	0.0025	1191	43	1160	22	1248	59	93
	038-54	491	84	115821	0.13	1.836	0.079	0.1715	0.0035	0.48	0.0776	0.0029	1058	45	1021	21	1137	75	90
	038-55	405	76	903	0.44	2.718	0.123	0.1866	0.0040	0.47	0.1057	0.0042	1334	61	1103	24	1726	73	64
	038-57	696	135	5038	0.25	2.280	0.080	0.1941	0.0037	0.54	0.0852	0.0025	1206	42	1143	22	1320	57	87
	038-58	673	127	2513	0.22	2.213	0.079	0.1886	0.0036	0.53	0.0851	0.0026	1185	42	1114	21	1318	58	84
	038-64	246	50	1868	0.34	2.287	0.089	0.2015	0.0040	0.51	0.0823	0.0028	1208	47	1184	23	1253	66	94
	038-67	689	90	1125	0.58	1.565	0.077	0.1304	0.0028	0.44	0.0871	0.0038	957	47	790	17	1362	85	58
	038-70	245	51	384	0.40	2.700	0.152	0.2103	0.0050	0.43	0.0931	0.0047	1329	75	1230	29	1491	96	83
	038-73	132	24	411	0.61	2.544	0.144	0.1853	0.0045	0.43	0.0996	0.0051	1285	73	1096	26	1616	95	68
	038-74	124	18	1344	0.34	1.685	0.082	0.1424	0.0031	0.44	0.0858	0.0037	1003	49	858	18	1334	84	64
	038-75	315	52	1284	0.27	1.943	0.078	0.1644	0.0033	0.50	0.0857	0.0030	1096	44	981	19	1331	67	74
	038-77	470	88	1877	0.46	2.207	0.085	0.1865	0.0036	0.50	0.0858	0.0029	1183	46	1102	21	1334	64	83
	038-78	70	15	19987	0.74	3.134	0.191	0.2096	0.0054	0.42	0.1084	0.0060	1441	88	1227	32	1773	101	69
	038-83	87	18	24970	0.62	2.433	0.148	0.2093	0.0051	0.40	0.0843	0.0047	1252	76	1225	30	1300	108	94
	038-87	1291	224	2638	0.10	1.910	0.075	0.1735	0.0034	0.50	0.0798	0.0027	1085	43	1032	20	1193	67	86

Analyses not used

[a]U and Pb concentrations and Th/U ratios are calculated relative to GJ-1 reference zircon

[b]Corrected for background and within-run Pb/U fractionation and normalised to reference zircon GJ-1 (ID-TIMS values/measured value); 207Pb/235U calculated using (207Pb/206Pb)/(

[c]Rho is the error correlation defined as the quotient of the propagated errors of the 206Pb/238U and the 207/235U ratio

[d]Quadratic addition of within-run errors (2 SD) and daily reproducibility of GJ-1 (2 SD)

[e]Corrected for mass-bias by normalising to GJ-1 reference zircon (~0.6 per atomic mass unit) and common Pb using the model Pb composition of Stacey & Kramers (1975)
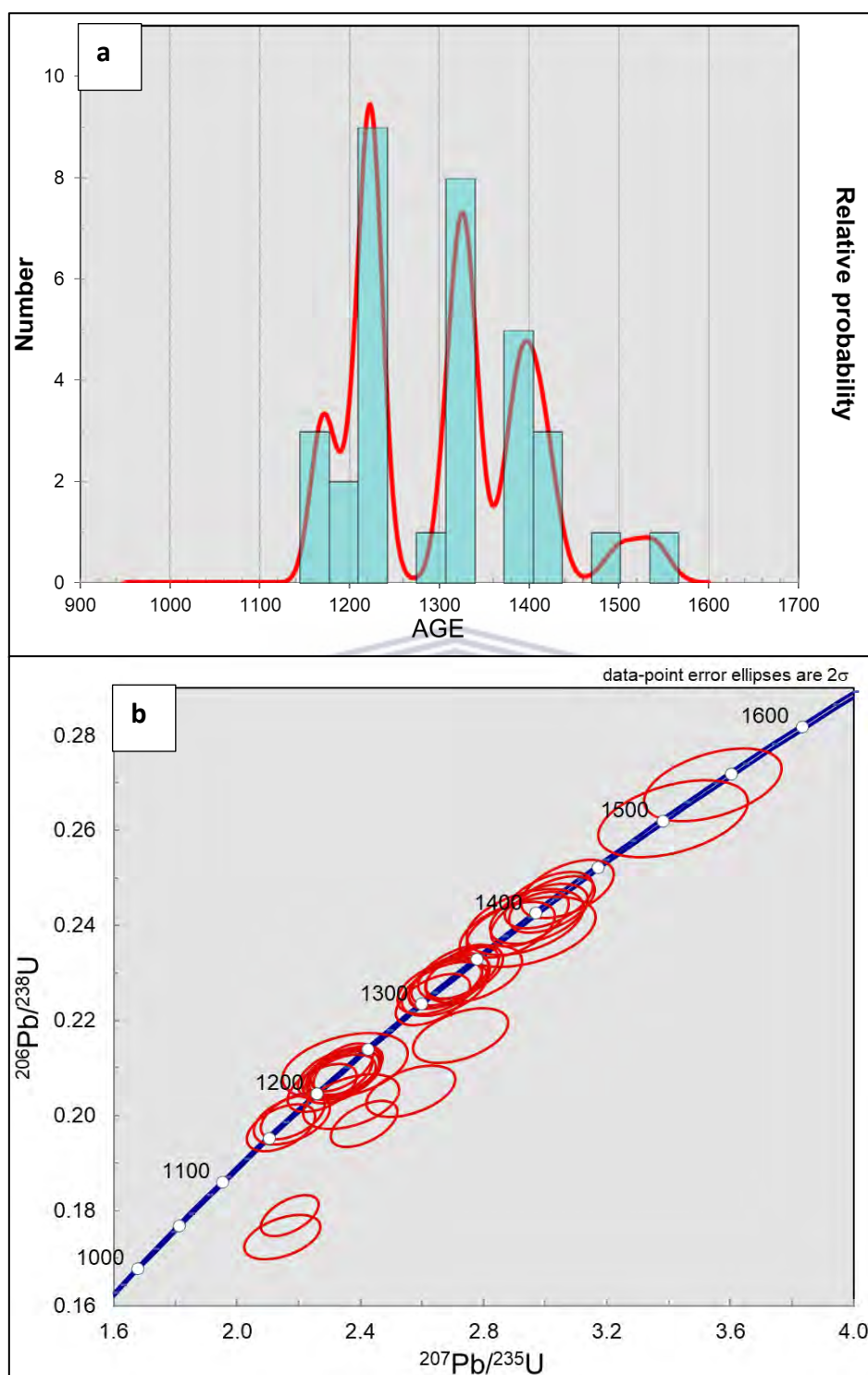
Figure 41 (a) Probability density diagram for the $^{206}Pb/^{238}U$ zircon ages of sample 036A**;** concordance values of between 90-102% were utilized for the analyses with the highest probability bars (9 analyses) plotting at ~1215 Ma, **(b)** U-Pb concordia plot of sample 036A displaying minor discordance as well as concordant ages for the two main metamorphic events from this sample. The Wetherill Concordia plot for near-concordant analyses is used to display the variable distribution of ages in this sample. Confidence limits for the error ellipses are expressed as 2σ.

46

6.3.3. (a)   Isotope geochemistry

The garnetiferous quartzofeldspathic biotite-sillimanite gneiss has a fairly high Sm/Nd ratio of 0.2255 (Appendix- B, Table B4). The ^{143}Nd/^{144}Nd value is moderate (0.51190) with a corresponding and relatively strongly negative epsilon ϵNd$_{(t)}$ value of -4.44 calculated from the 1222 ± 25 Ma maximum age of deposition of this gneiss (Appendix B, Table B4). The garnet-biotite semi-pelitic gneiss has a Rb/Sr ratio of 1.631, yields a ^{87}Rb/^{86}Sr ratio of 4.33450 and an initial Sr (^{87}Sr/^{86}Sr$_{(i)}$) of 0.7213 with an epsilon Sr$_{(t)}$ value for today of 258 (Appendix B, Table B4). Calculated T$_{CHUR}$ and T$_{DM}$ ages are 1.79 Ga and 2.39 Ga respectively (Appendix, Table B4 & Figure A14).

Table 7 U-Th-Pb isotopic compositions of zircon grains extracted from sample 036A of the garnetiferous quartzofeldspathic biotite-sillimanite gneiss located in the BRSZ.

	Spot number	U [ppm]a	Pb [ppm]a	206Pb/204Pb	Th/Ua	RATIOS 207Pb/235Ub	2σd	206Pb/238Ub	2σd	rhoc	207Pb/206Pbe	2σd	AGES [Ma] 207Pb/235U	2σ	206Pb/238U	2σ	207Pb/206Pb	2σ	Conc. %	Region	Luminescence	Description
Analyses used	036A-01	237	47	3392	0.02	2.180	0.085	0.1999	0.0040	0.51	0.0791	0.0027	1175	46	1175	24	1175	67	100	rim	dark	thin metamorphic rim
	036A-02	362	87	3642	0.45	2.949	0.103	0.2413	0.0047	0.55	0.0886	0.0026	1395	49	1394	27	1396	56	100	core	medium dark	zoned, abraded core
	036A-07	218	50	5701	0.42	2.675	0.097	0.2279	0.0045	0.54	0.0852	0.0026	1322	48	1323	26	1319	59	100	core	medium dark	core overgrowth
	036A-08	198	45	62187	0.30	2.689	0.102	0.2287	0.0045	0.52	0.0853	0.0028	1325	50	1322	26	1322	63	100	core	medium dark	zoned, abraded core
	036A-09	268	60	36919	1.10	2.635	0.098	0.2245	0.0044	0.53	0.0851	0.0027	1310	49	1306	26	1319	61	99	core	medium dark	abraded core
	036A-10	371	78	106954	0.01	2.341	0.082	0.2102	0.0041	0.55	0.0808	0.0024	1225	43	1230	24	1217	58	101	rim	dark	thin metamorphic rim
	036A-11	118	29	1417	0.20	2.979	0.129	0.2425	0.0051	0.49	0.0891	0.0034	1402	61	1399	30	1407	73	99	core	bright	fragment
	036A-12	32	8	850	0.20	3.413	0.198	0.2624	0.0066	0.43	0.0943	0.0049	1507	88	1502	38	1515	99	99	core	bright	bright resorbed core
	036A-13	154	31	3670	0.04	2.370	0.127	0.2030	0.0047	0.43	0.0847	0.0041	1233	66	1191	28	1308	94	91	rim	dark	thick metamorphic rim
	036A-14	218	50	3863	0.20	2.767	0.128	0.2297	0.0050	0.47	0.0874	0.0036	1347	62	1333	29	1368	78	97	rim	medium bright	magmatic resorption of core; fracture through centre
	036A-15	165	38	52125	0.20	2.725	0.113	0.2302	0.0047	0.50	0.0859	0.0031	1335	56	1336	27	1335	70	100	core	medium bright	abraded core with overgrowth rim
	036A-16	44	11	985	0.96	2.934	0.155	0.2407	0.0056	0.44	0.0884	0.0042	1391	74	1391	32	1391	91	100	core	bright	zoned core
	036A-17	274	57	1410	0.05	2.359	0.092	0.2096	0.0042	0.51	0.0816	0.0027	1230	48	1227	24	1237	65	99	rim	dark	dark metamorphic rim
	036A-18	189	46	2592	0.91	3.022	0.114	0.2445	0.0048	0.52	0.0897	0.0029	1413	53	1410	26	1418	61	99	core	bright	convolute zonation; abraded core
	036A-20	384	80	5630	0.50	2.350	0.095	0.2092	0.0042	0.50	0.0815	0.0028	1227	49	1224	25	1233	68	99	core	dark	resorbed core
	036A-21	163	37	50913	0.46	2.688	0.107	0.2282	0.0046	0.51	0.0855	0.0029	1325	53	1325	27	1326	67	100	core	medium bright	concentric zonation
	036A-22	282	59	3337	0.17	2.345	0.099	0.2093	0.0043	0.49	0.0813	0.0030	1226	52	1225	25	1228	72	100	core	medium dark	core overgrowth
	036A-24	894	206	17786	0.37	2.731	0.097	0.2301	0.0044	0.54	0.0861	0.0026	1337	47	1335	26	1340	57	100	core	dark	zoned, abraded core
	036A-25	236	49	66747	0.03	2.275	0.092	0.2058	0.0041	0.50	0.0802	0.0028	1205	49	1207	24	1201	69	100	rim	dark	thick overgrowth rim
	036A-26	348	83	114142	0.40	2.942	0.179	0.2386	0.0060	0.42	0.0894	0.0050	1393	85	1380	35	1413	106	98	core	dark	zoned, abraded core
	036A-27	283	69	4084	0.50	3.012	0.117	0.2453	0.0049	0.51	0.0890	0.0030	1411	55	1414	28	1405	64	101	core	medium dark	zoned, abraded core
	036A-29	144	39	1247	0.18	3.542	0.182	0.2696	0.0062	0.45	0.0953	0.0044	1537	79	1539	36	1534	87	100	core	dark	unzoned, abraded core
	036A-30	336	76	5791	0.18	2.658	0.112	0.2270	0.0046	0.49	0.0849	0.0031	1317	55	1319	27	1314	71	100	rim	dark	thick metamorphic rim
	036A-31	680	134	33058	0.38	2.142	0.090	0.1975	0.0040	0.49	0.0787	0.0029	1163	49	1162	24	1164	73	100	core	dark	local recrystalisation
	036A-32	247	49	3809	0.03	2.177	0.101	0.1992	0.0042	0.46	0.0793	0.0033	1174	54	1171	25	1179	81	99	rim	dark	rim around local recrystalized core
	036A-33	330	69	2396	0.02	2.333	0.095	0.2078	0.0042	0.49	0.0814	0.0029	1222	50	1217	24	1232	69	99	rim	medium dark	thick rim
	036A-34	321	80	109301	0.48	3.072	0.122	0.2477	0.0050	0.50	0.0900	0.0031	1426	57	1426	26	1425	66	100	core	dark	unzoned core
	036A-35	307	64	87819	0.01	2.346	0.098	0.2085	0.0042	0.49	0.0816	0.0030	1226	51	1221	25	1236	72	99	rim	medium bright	thick faint zonation on overgrowth rim
	036A-36	174	36	5591	0.46	2.336	0.102	0.2087	0.0045	0.47	0.0812	0.0031	1223	54	1222	25	1227	76	100	core	bright	concentric zonation
	036A-37	217	46	2069	0.44	2.350	0.166	0.2104	0.0057	0.38	0.0810	0.0053	1228	87	1231	33	1221	128	101	core	bright	concentric zonation
	036A-38	306	69	1946	0.45	2.673	0.114	0.2267	0.0046	0.48	0.0856	0.0032	1321	56	1317	27	1328	72	99	core	dark	local recrystalized core
	036A-39	373	89	3273	0.62	2.887	0.117	0.2391	0.0048	0.49	0.0876	0.0031	1379	56	1382	26	1373	68	101	core	dark	convolute zonation
	036A-40	347	72	2491	0.01	2.319	0.098	0.2088	0.0043	0.48	0.0806	0.0030	1218	52	1222	25	1210	73	101	rim	medium dark	thick metamorphic rim
Analyses not used	036A-03	469	84	1950	0.05	2.171	0.078	0.1790	0.0035	0.54	0.0880	0.0026	1172	42	1062	21	1382	58	77			
	036A-06	817	162	1355	0.82	2.412	0.089	0.1983	0.0039	0.53	0.0882	0.0028	1246	46	1166	23	1387	60	84			
	036A-19	257	53	72258	0.14	2.565	0.118	0.2051	0.0044	0.47	0.0907	0.0037	1291	59	1203	26	1440	77	83			
	036A-23	320	69	1097	0.06	2.725	0.126	0.2168	0.0047	0.47	0.0912	0.0037	1335	62	1265	27	1450	78	87			
	036A-28	416	73	583	0.02	2.146	0.101	0.1745	0.0038	0.46	0.0892	0.0037	1164	55	1037	22	1408	80	74			

aU and Pb concentrations and Th/U ratios are calculated relative to GJ-1 reference zircon

bCorrected for background and within-run Pb/U fractionation and normalised to reference zircon GJ-1 (ID-TIMS values/measured value); 207Pb/235U calculated using (207Pb/206Pb)/(238U/206Pb * 1/137.88)

cRho is the error correlation defined as the quotient of the propagated errors of the 206Pb/238U and the 207Pb/235U ratio

dQuadratic addition of within-run errors (2 SD) and daily reproducibility of GJ-1 (2 SD)

eCorrected for mass-bias by normalising to GJ-1 reference zircon (~0.6 per atomic mass unit) and common Pb using the model Pb composition of Stacey & Kramers (1975)

Grey highlighted analyses represent rims and overgrowths that are likely related to metamorphism

Chapter 7: Structural geology

7.1 Preface

This chapter aims to determine the structural evolution of the BRSZ while taking into account the multiphase deformational history of the study area as well as factors controlling shear zone formation and the role it plays in acting as a possible terrane boundary between the Okiep and Garies terranes respectively. According to Howell (1993) there are a number of factors to consider when investigating possible terrane boundaries such as the BRSZ, namely:

1. The preservation of distinctive incompatible geologic histories and age data on either side of the terrane boundary
2. Whether the lithologies on either side of the terrane boundary are genetically related or not
3. The presence of a shear zone or fault system along the contact between two terranes

Here the structural data collected and presented aim to provide a tectonic analysis that explains the kinematic and dynamic history of the BRSZ and its configuration in relation to the Okiep and Garies terranes respectively. This will be done through the description and graphical representation of the various folding events, and shear zone development.

In order to accurately describe the multiphase deformational history of the BRSZ and its relationship with the adjacent terranes, a form line structure map was produced to include the megastructures found to the north and south of the BRSZ (Fig. 42) which includes the geological map produced for this study area. This area is then subdivided into three subareas based on contrasting structural patterns from one subarea to the next and described briefly based on regional structural features.

The three subareas are named:

1. Subarea1: Springbok Antiform
2. Subarea 2: Buffels River shear zone
3. Subarea 3: Rooifontein Synform

The convention used to describe the deformation phases as well as planar and linear features will follow the four-fold subdivision of the deformation in the western Namaqua Metamorphic Province as originally recorded and described by Joubert (1971, 1986).

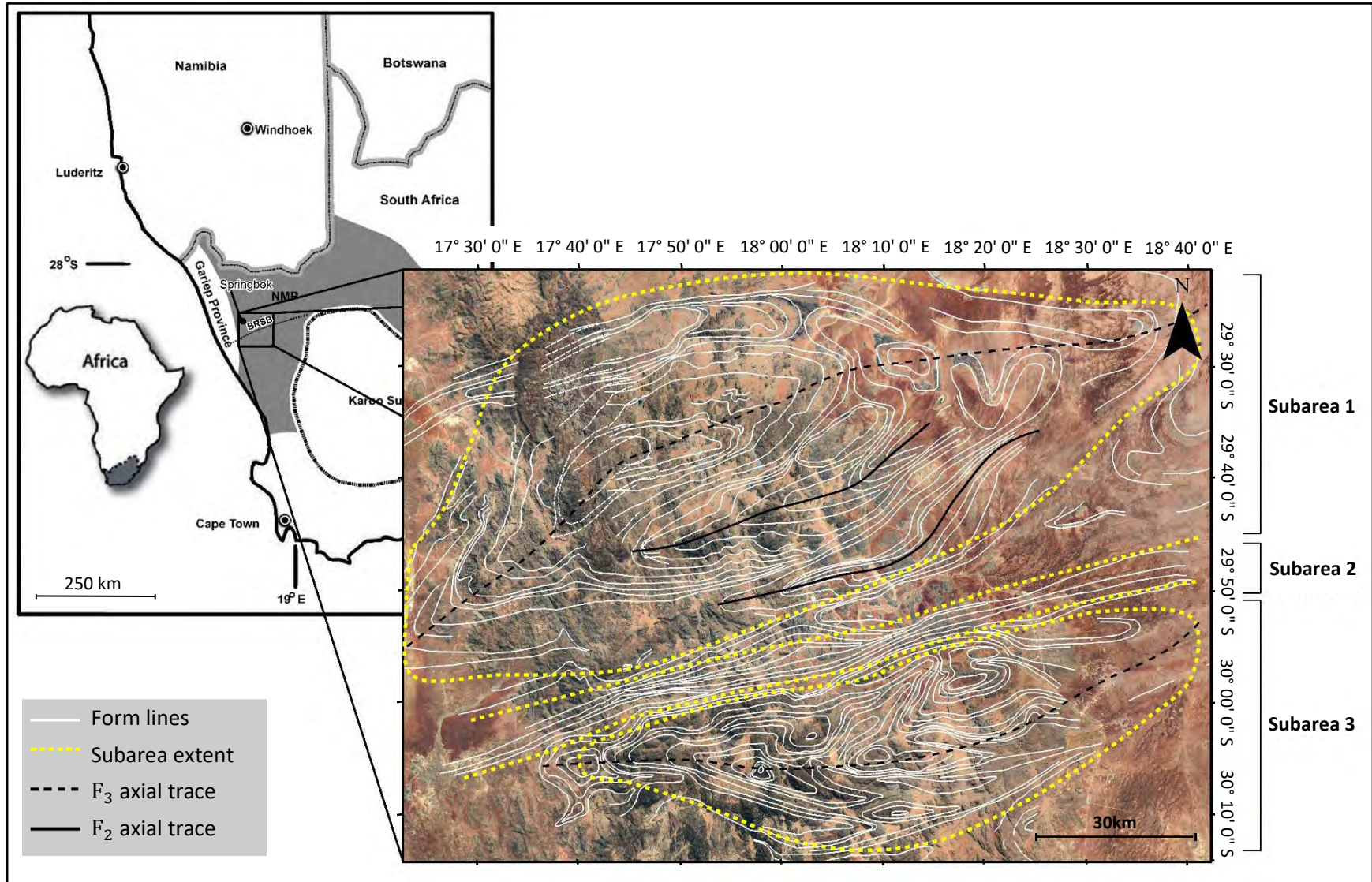**Figure 42** The BRSZ is located approximately 50 kilometres south of the town of Springbok in the Namaqua Metamorphic Province in South Africa with an overall ENE-WSW orientation. The enlarged aerial view image of the BRSZ illustrates the form line interpretation based on structural features found north, south and within the BRSZ. The subareas are labelled 1, 2 and 3 from north to south respectively.

49

Listed below are the conventions used to denote the fabrics identified in the field:

- Deformation phases: D_n, D_{n+1}, D_{n+2}.
- Fold phases: F_n, F_{n+1}, F_{n+2}.
- Planar fabric: S_n, S_{n+1}, S_{n+2}.
    - Two main S fabrics were defined during this study namely: $S_{2/3}$ and S_3
- Linear Fabric: L_n, L_{n+1}.

All structural elements are described and illustrated on equal-area stereographic projections where planar fabrics are recorded as dip and dip direction and linear fabrics as trend and plunge. A combination of stereonet software is utilized for this study, namely GEOrient 9.5.1 (Holcombe, 2017) and OpenStereo 2.0b (Grohmann et al., 2017).

7.2 Introduction

The BRSZ spans approximately 95 kilometres from the West Coast belt to the Bushmanland plateau in the east where it is overlain by Cenozoic cover. The trace of the supracrustal belt is defined by a steep NNW-dipping, 4 km wide zone consisting of mainly sheared supracrustal sequences and streaky augen gneiss which have a regionally consistent ENE-WSW trend of about 260° (Fig. 42). The rocks of the supracrustal belt occur as sheet-like bodies generally concordant to the regional gneissic foliation and are bordered on either side by a wall rock of less deformed coarse-grained Mesklip Gneiss of the Little Namaqualand Suite which has the same penetrative foliation as the supracrustal belt. This study will focus on the well exposed, 24 km long portion of the BRSZ and the megascale dome and basin structures situated north and south of the belt respectively (Appendix A, Fig. A15).

7.2.1   First deformational event- D_1

The study area has been greatly reworked through metamorphism and deformation, therefore any pre-existing sedimentary bedding has been transposed and S_0 and S_1 cannot be identified in the field. The first and most prominent phase of deformation which can be identified in the field is denoted as S_2 and is characterised by a broadly ENE-WSW-trending gneissic foliation (Fig. 43). This developed during the recrystallization of the surrounding igneous and sedimentary rocks during high-grade metamorphism. D_1 structures are mostly associated with this regional penetrative feature (S_2) through tight, small centimetre-scale rootless intrafolial folds (Fig. 43) and are considered to be the first generation of folds (F_1) during D_1 (Joubert, 1971, 1986).
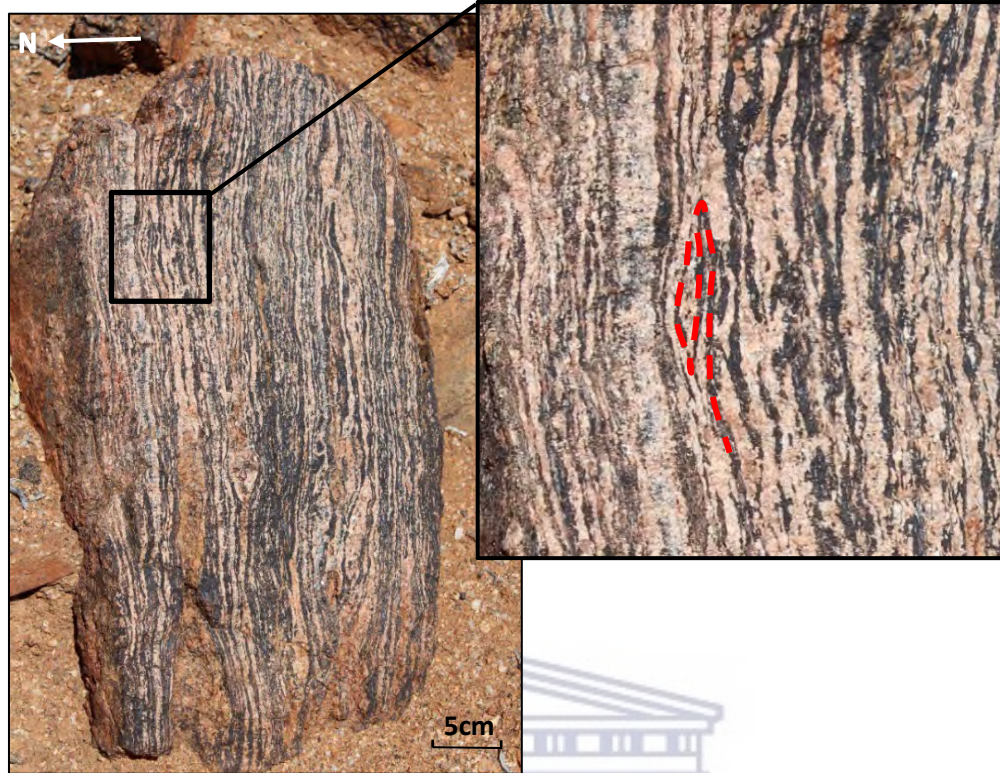
Figure 43 Centimetre-scale, tight intrafolial folds (F_1; red dashed line) representative of the presence of D_1 in the foliated metapsammitic gneiss with an ENE-WSW trend (GPS 29.9629 S; 17.9526 E).

7.2.2 Second deformation event- D_2

The second deformation event, denoted as D_2, is characterised by mesoscale ENE-WSW-trending isoclinal folds (F_2) with an axial plane dipping NNW (Fig. 44a & 44b) which produced a generally ENE-WSW-trending penetrative S_2 foliation and an L_2 stretching lineation within the supracrustal belt (Fig. 44c, d & f). The fold vergence of these isoclinal folds can be determined by z-, s- and m-folds observed in the field with round to sharp hinge zones and long limbs that are parallel to each other (Fig. 44a). These F_2 folds are commonly intrafolial and indicate that this penetrative fabric developed during an isoclinal folding event. The S_2 foliation is a regionally penetrative gneissic fabric that is observed in all lithologies within the shear zone/supracrustal belt (Fig. 44c & d). This fabric is dipping moderately to steeply within the bounds of the shear zone with dip angles ranging between 55° and 85° both to the NNW and SSE whereas to the north and south of the shear zone dip angles gradationally become shallower and range between 35° and 65°. The S_2 fabric is also co-planar in relation to the gneissic banding found within the F_2 isoclinal fold limbs. Locally the L_2 mineral elongation lineations are not easily identifiable due to the smooth weathering patterns of the surrounding gneisses but can be identified in the supracrustal rocks, amphibolites and grey gneisses (Fig. 44f) as shallowly-plunging to the east, elongation lineations with an orientation largely trending ENE. The pelitic rocks are commonly boudinaged and outcrop as isolated rafts within both the streaky augen gneiss and the leucogneiss (Fig. 44e). These bodies occur along the length of the shear zone having an orientation parallel to the regional penetrative foliation.

51
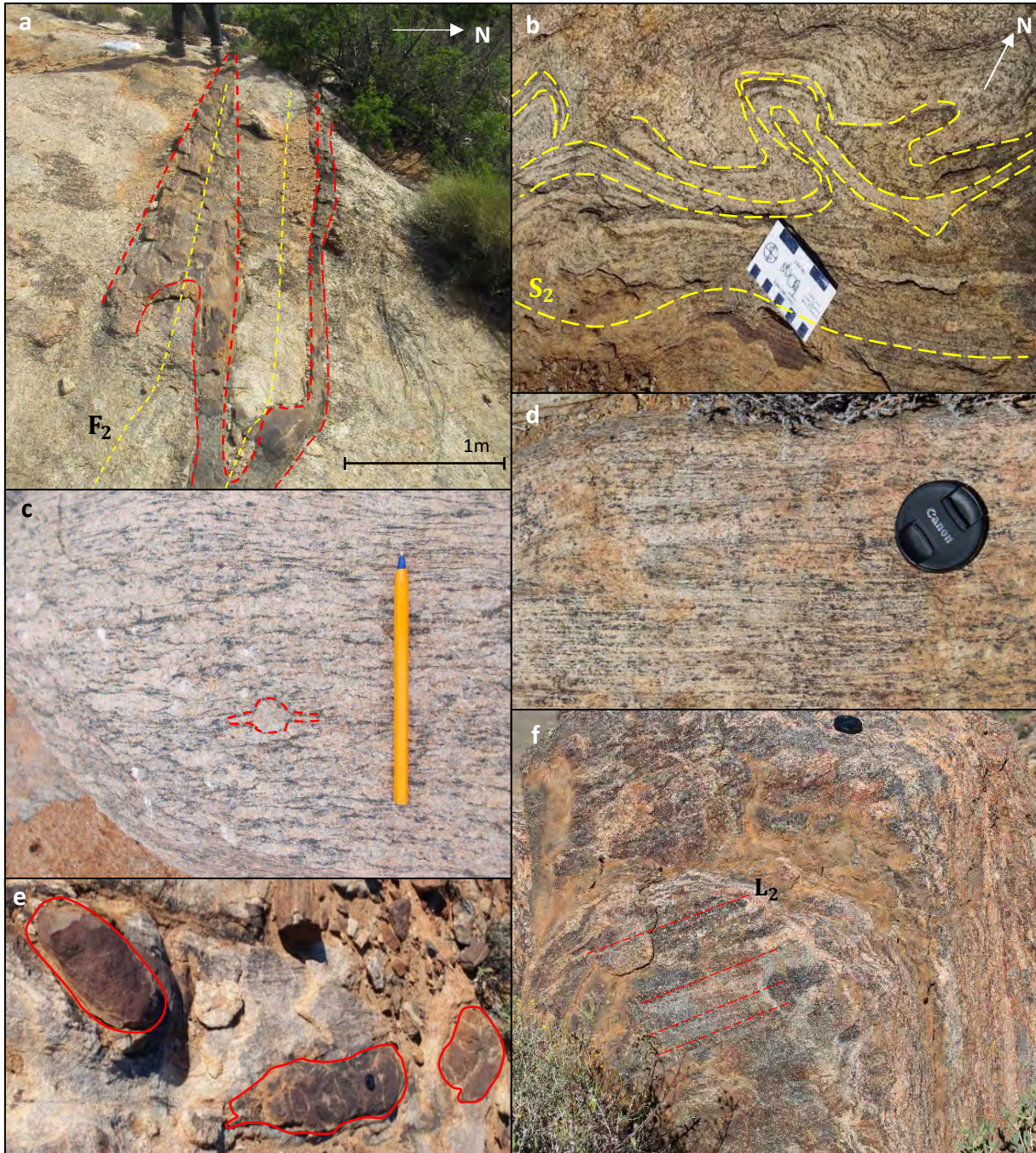
Figure 44 (a) A large isoclinal z-fold (red dashed line) of a raft of metapelitic material, with an axial plane (yellow dashed line) trending ENE-WSW; penetrative foliation of the surrounding Mesklip Gneiss is co-planar to the limbs of the F_2 fold. **(b)** Parasitic folding in the migmatitic grey gneisses/Hunboom Gneiss; **(c)** and **(d)** main penetrative S_2 foliation displayed by the K-feldspar augen (red dashed lines) which have symmetrical tails indicating pure shear flattening strain and well foliated appearance of the metapsammitic gneisses respectively; **(e)** Boudinaged amphibolite raft in the leucogneiss trending ENE-WSW (red outline) and **(f)** L_2 shallow-plunging elongation lineations in a metapsammitic gneiss with an orientation trending ENE (red line) looking at an S_2 plane.

Quartzofeldspathic pegmatites, with minor biotite, muscovite and tourmaline, are a common occurrence in the study area, trending between ENE-WSW and NE-SW. They commonly have a crosscutting to co-planar relationship with the main penetrative foliation where minerals in the pegmatite grow perpendicular to the wall rock. These pegmatites can range from 1 cm to 60 cm in thickness and are largely unfoliated indicating a possible intrusive relationship with the surrounding rocks post-D_3 and pre-D_4 as they have been observed being folded locally by D_4 which indicates their presence pre-D_4 (Fig. 45a & b).
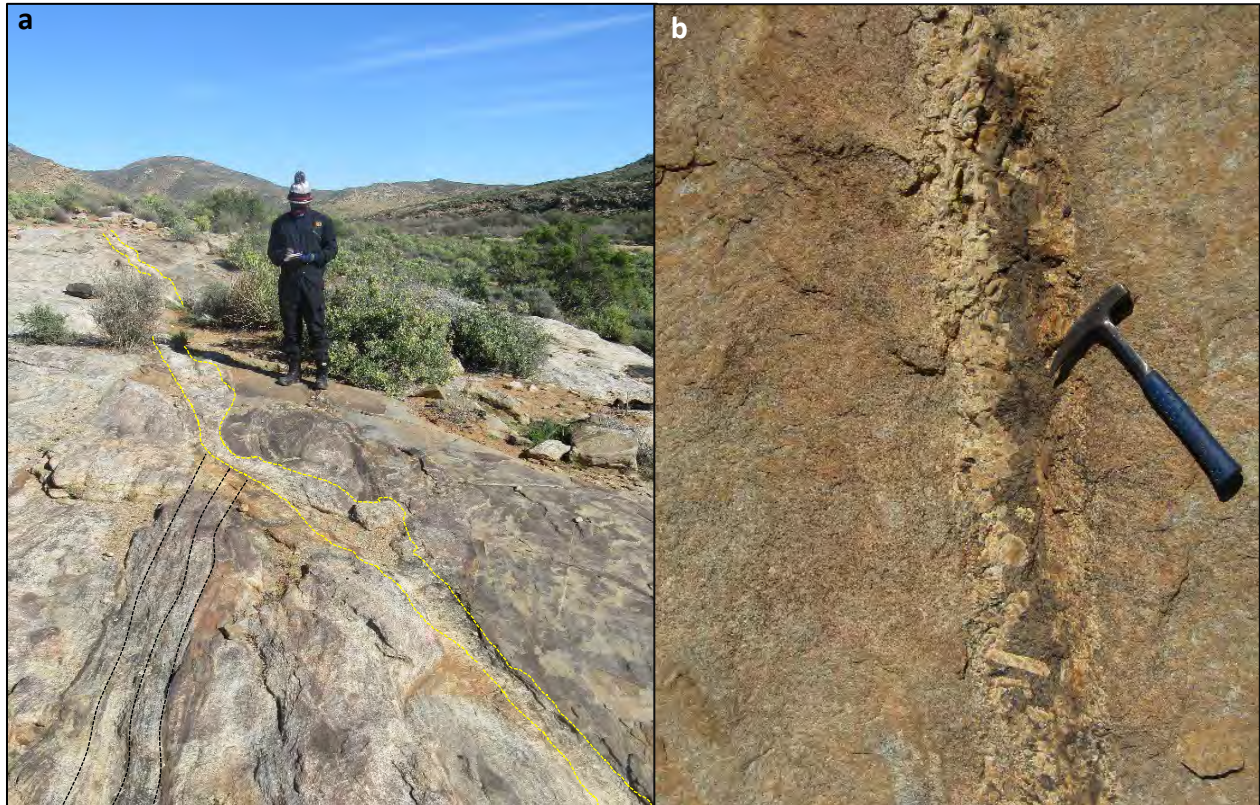
Figure 45 (a) Unfoliated NE-SW-trending quartz and K-feldspar-bearing pegmatite (yellow dashed lines) crosscutting the migmatitic gneiss (black dashed lines) and **(b)** an unfoliated, coarse-grained, quartz-K-feldspar pegmatite with minor biotite and tourmaline cross cutting the foliated Mesklip Gneiss.

7.2.3 Third deformation event- D_3

According to Joubert (1971), D_3 is characterised as large upright to inclined open folds with steeply north-west dipping axial planes and a SW-NE axial planar trend. Authors have noted an association between F_3 folds and the east-west-trending shear zones in the western Namaqua Metamorphic Province. In Figure 42 two megascale open antiformal (dome) and synformal (basin) structures occur north and south of the BRSZ, respectively, which represent F_3 structures formed through interference folding. Within the BRSZ F_3 has overprinted F_2, therefore folds within the BRSZ will be denoted as $F_{2/3}$ folds.

53

An S_3 fabric is also well developed throughout the shear zone and can be described as extensional shear bands with a crosscutting relationship with the regional penetrative S_2 foliation (Fig. 46). These S_3 fabrics formed obliquely to the main shear zone boundaries and have varying dip azimuths in relation to the shear plane. The oblique angle between the bulk shear plane trending ENE-WSW and the S_3 fabric varies between 17° and 90°. The S_3 fabric is considered to be non-penetrative and discrete ranging from sub-vertical to subparallel to S_2. According to Macey et al. (2011), S_3 shear planes developed along F_3 fold closures, and this shearing occurred along the limbs of the parasitic F_3 folds which tend to be dragged into parallelism with the S_2 foliations and crosscut at lower angles ranging between measured angles of 17° and 43° (Fig. 46a, b & c). Both sinistral and dextral shear sense can be found along S_3 structures throughout the study area. Along the hinge zones of these F_3 folds the S_3 fabrics tend to be orthogonal to the main S_2 foliation (Fig. 46d) and display little to no shearing or drag. Here the angle between the S_2 and S_3 fabrics ranges between 70° and 90° and S_3 shear zones are commonly filled with leucosomes of 2 cm to 10 cm thickness consisting of quartz ± feldspar ± biotite ± magnetite ± hornblende similar to what is documented by Macey et al. (2011) in the Kliprand area further to the south.

In conjunction with the overprinting of F_3 folds onto F_2 folds, shear zone development took place during D_3 and produced well-foliated streaky augen gneisses and supracrustal rocks found within the BRSZ in comparison to the rocks found adjacent to the approximately 4 km wide shear zone. This sheared fabric of the BRSZ is co-planar to the main penetrative S_2 foliation. Therefore, the main ENE-WSW-trending shear zone, that is closely associated with the contacts of the supracrustals and the intrusive suite, represents the re-activation of early D_2 structures according to Moore (1989). The augen textures of the Mesklip Gneiss found within the BRSZ display a reduction in grain size and consist of lenticular eye-shaped porphyroclasts of aggregates of K-feldspar and quartz minerals (Fig. 44c) which show symmetrical tails indicating a strong component of non-rotational pure shear flattening strain during the main $D_{2/3}$ deformational event. S_2 foliations constrained within the BRSZ are moderately to steeply dipping (~ 60° – 86°) to the south but north-dipping foliations with similar dip angles were also recorded. This high strain zone is largely positioned between the mega-scale dome and basin structures situated on either side of the BRSZ (Fig. 42) and no clear sense of shear along the length of the BRSZ can be identified or observed from satellite imagery as there is no visible drag recognised on either side of the shear zone (Fig. 42).

7.2.4 Fourth deformation event- D_4

In the study area the D_4 deformation phase is associated with very large-scale NW-trending open folds (F_4) that are monoclinal in places and can be observed locally at 1:250 000 scale (Fig. 42). F_4 folds are identifiable in the field through the reorientation of S_2 and S_3 foliations (Fig. 44b) as well as the slight reorientation of minor F_3 fold axes from NE-SW to NNE-SSW trending axes. This phase of deformation did not produce a new penetrative fabric and also varies in intensity and style throughout the study area. The various folding generations produced during the

known phases of deformation, namely D_2 and D_3, resulted in complex interference patterns forming dome and basin structures (Fig. 42) where discrete shear zones like the BRSZ are thought to be associated with the margins of these structures (Macey et al., 2011).

Also associated with the final phase of deformation are faults and fracturing with two main prominent joint systems identified, namely the widely occurring and commonly displaced N-S-trending joints and the less occurring displaced E-W-trending joints respectively. The N-S-trending joint and fault systems displace the older E-W-trending joints and are commonly filled with thin veins of epidote (Fig. 47).
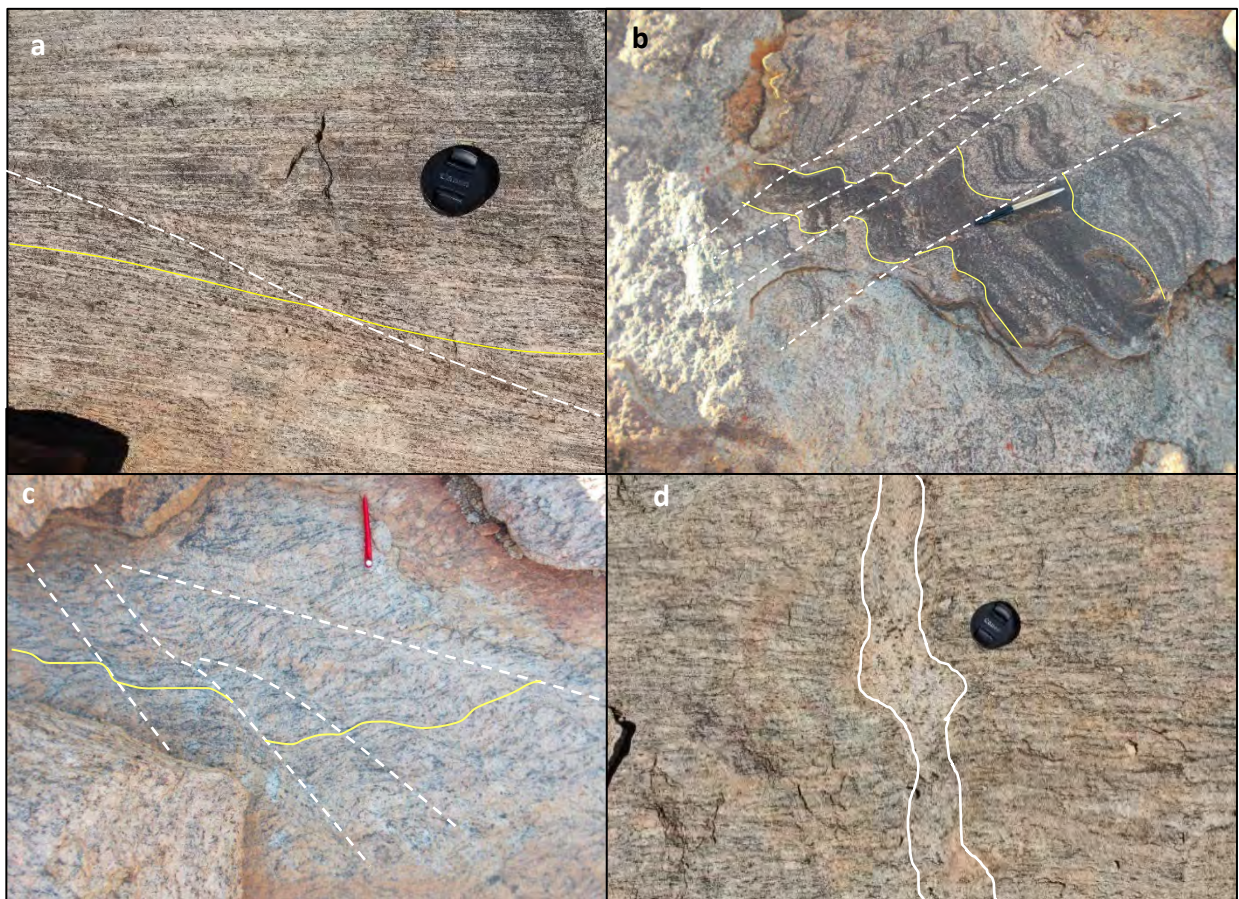
Figure 46 S_3 non-penetrative, discrete shear bands which show both sinistral and dextral sense of shear and can be either **(a)** sub-parallel or **(b & c)** sub-vertical to the S_2 penetrative ENE-WSW foliation respectively. **(d)** S_3 fabrics which are sub-vertical (~70° – 90°) to S_2 tend to show little to no shearing and are commonly filled with leucosomes of 2cm to 5 cm thickness. (white dashed lines – S_3; white solid line – outlines feature; yellow solid line – S_2)
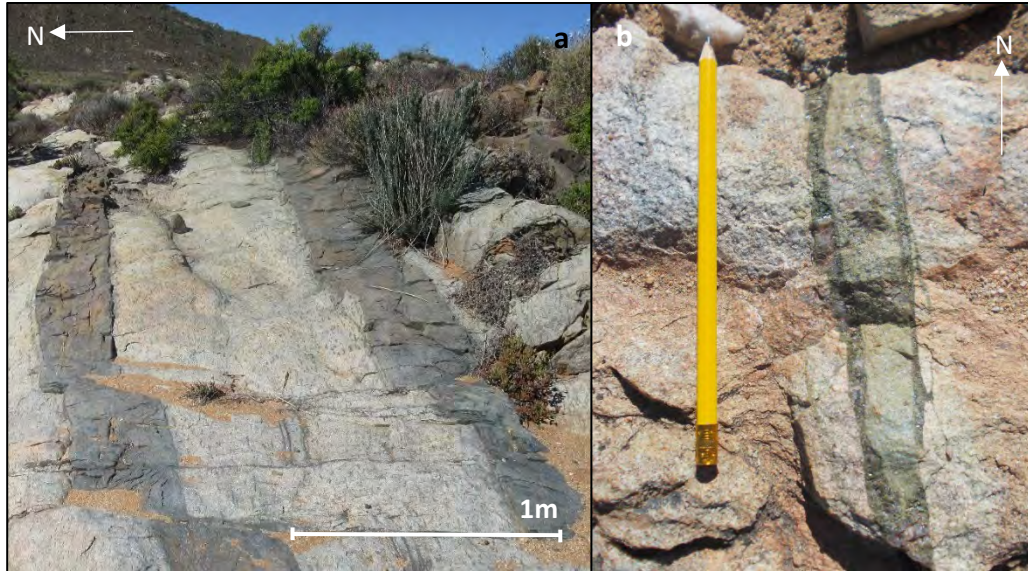
Figure 47 (a) The N-S-trending joints with various distances in displacement ranging from 5cm to 30cm. **b)** Epidote commonly fills the N-S-trending joints.

7.3 Description of subareas

7.3.1   Subarea 1

One thousand three hundred and sixty-seven data points were obtained for Subarea 1, through data collected by this project and historical data collected by previous authors who worked in this area (Marais et al., 2001; De Beer, 2010; Macey et al., 2011, Abrahams et al., 2020; Groenewald and Macey, 2020; Thomas, 2020). In Subarea 1 the antiformal structure named the Springbok Antiform (red dashed area) is situated north of the BRSZ (subarea 2) and the northernmost boundary of this dome extends to just north of the town of Concordia in the Northern Cape (legend in Figure 51). The Springbok Antiform is a doubly plunging antiformal structure with fold axes plunging ENE and WSW respectively. The structure is approximately 138 kilometres long (measured from southwest to northeast) with a maximum width of approximately 56 kilometres. Here the $S_{2/3}$ foliation is fairly shallowly dipping with the limbs having an average dip of 24° towards 341° and 24° towards 164°, respectively, and has an interlimb angle of 132° making it a gentle fold.

The Mesklip Gneiss dominates exposures along the perimeter and interior portion of the dome with lenses of supracrustal rocks from the Springbok Formation and Wortel Formation present predominantly along the hinge zones in the southwest and northeast of the dome respectively (Fig. 48a). The Concordia Granite is exposed in the central portion of the dome outlining its contact with the central Mesklip Gneiss exposures. Furthermore, minor exposures of the Brandewynsbank Gneiss and Steinkopf Gneiss occur as lenses within the Mesklip Gneiss both having a similar orientation.

A lower hemisphere equal area stereogram was constructed in order to classify the structure (Fig. 48d). The interlimb angle, as determined from Figure 48a, is 131° and the $D_{2/3}$ structure is best

56

described as a gentle fold with a fold axis plunging 5° towards 072° and an axial plane dipping 89° towards 163° and is an upright horizontal fold. Mineral lineations (L_2), which are shallow-plunging elongation lineations in the pelitic gneisses , are not oriented parallel to the fold axis but rather girdled between 40° and 80° (Fig. 48d). This is not a convincing great circle and is rather a poorly defined cluster that has shifted approximately 20° from the axial plane. Cross section A-A' was drawn through Subarea 1 and it could be categorised as an upright open fold (Fig. 48b).

7.3.2   Subarea 2

Subarea 2 represents the main study area (Fig. 49) and is a high-strain zone which has an overall trend of ENE-WSW with $S_{2/3}$ foliation moderate to steeply dipping to both the north and south with angles ranging between 60° and 88°. The Hunboom Gneiss as well as the garnet-biotite semi-pelitic gneisses dominates exposures along this subarea of the supracrustal belt with the well-foliated Mesklip Gneiss in the central portion of the BRSZ thinning out to the ENE. Lenses of the Hunboom Gneiss are largely present throughout its extent. The Rooiplatklip Gneiss in this subarea largely intrudes all rock types and has its largest exposure in the western portion of the subarea.

Two hundred and ninety-seven data points were obtained along the BRSZ (De Beer, 2010; Macey et al., 2011, Abrahams et al., 2020; Groenewald and Macey, 2020; Thomas, 2020). The lower hemisphere equal area stereogram shows that the interlimb angle is 25° (Fig. 49c) and the $D_{2/3}$ structure is best described as a tight fold with a fold axis plunging 3° towards 082° and an axial plane dipping 89° towards 352° and is an upright horizontal fold. In comparison to Subarea 1, the mineral lineations (L_2) in Subarea 2 are coaxial with the hinge of F_2 and plot close to π, and, although they represent a poorly defined cluster and not a clear girdle, the data represented could still be an indication that they formed synchronous to the F_2 fold generation (Fig. 49d). Cross section B-B' was drawn through Subarea 2 and it could be categorised as an upright tight fold (Fig. 49b).

7.3.3   Subarea 3

Subarea 3 is characterised by a structure here named the Rooifontein Basin which is situated south of the BRSZ (Subarea 2) with the southernmost boundary of this dome extending to the town of Kamieskroon (Fig. 50). The Rooifontein Basin is a synformal structure with an ENE-WSW-trending axial surface trace with fold closures to the southwest and northeast respectively. The structure is approximately 122 kilometres long (measured from southwest to northeast) with a width of approximately 26 kilometres. Here the $S_{2/3}$ foliation is moderately to steeply dipping with the limbs having an average dip of 65° towards 359° and 71° towards 160°, respectively.

The Mesklip Gneiss dominates exposures within Subarea 3 where the perimeter of the synform is wrapped in supracrustal rocks from the Kamiesberg Subgroup (Fig. 50a). The Lekkerdrink Gneiss is well exposed in the southeast and central portion of the subarea. There are minor exposures of the well-foliated Oorkraal Suite wrapped around the Rooifontein Synform in the south of the subarea.
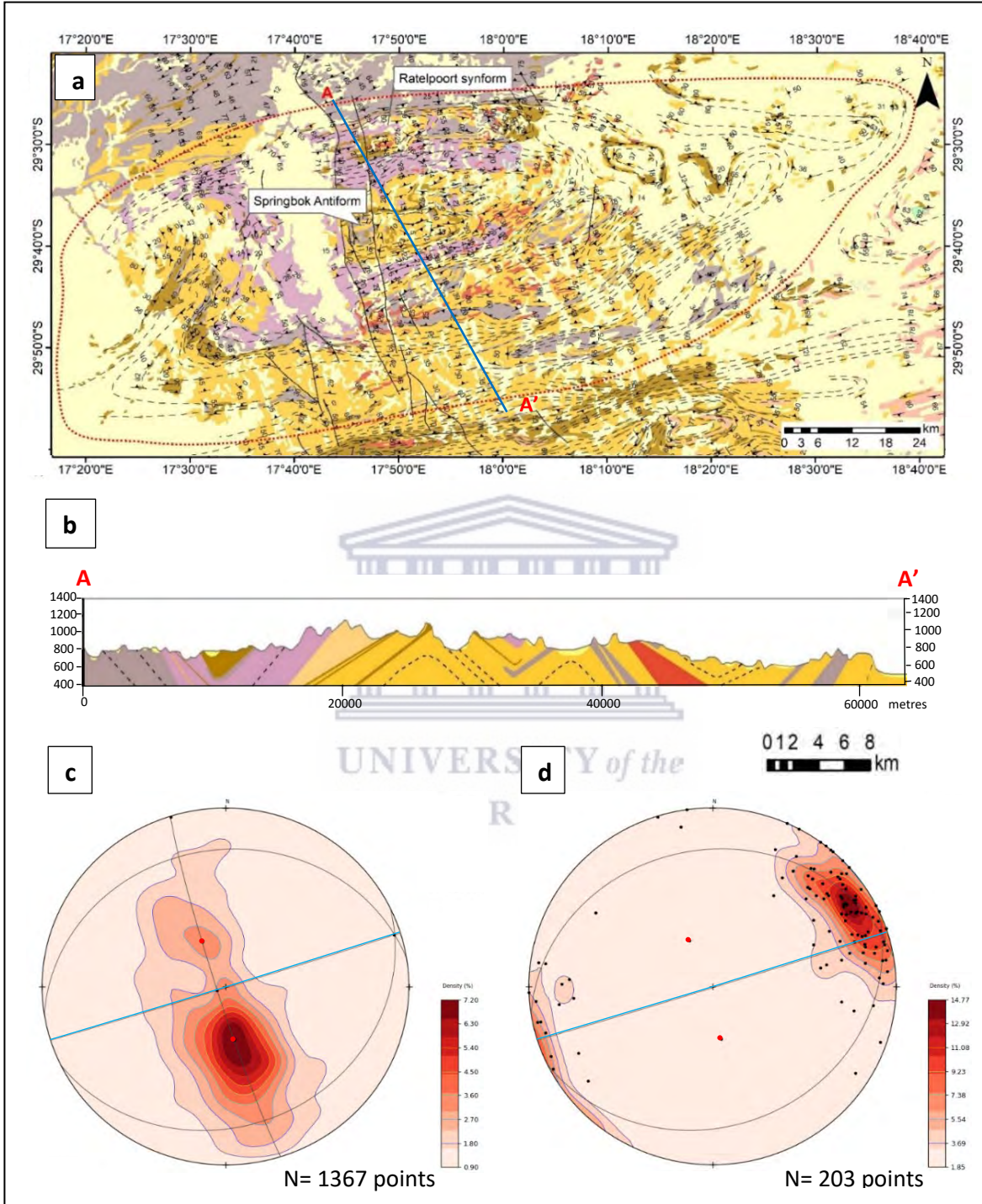
Figure 48 (a) Geological map of Subarea 1 with cross section line A-A' indicated. **(b)** Cross section A-A' of Subarea 1. **(c)** π diagram of S_2 for Subarea 1 and **(d)** a lower hemisphere stereographic projection of the two limbs (black great circles) displaying L_2 lineations (black dots). Red dots are pole maxima and the blue line is the axial plane. N = 203 points
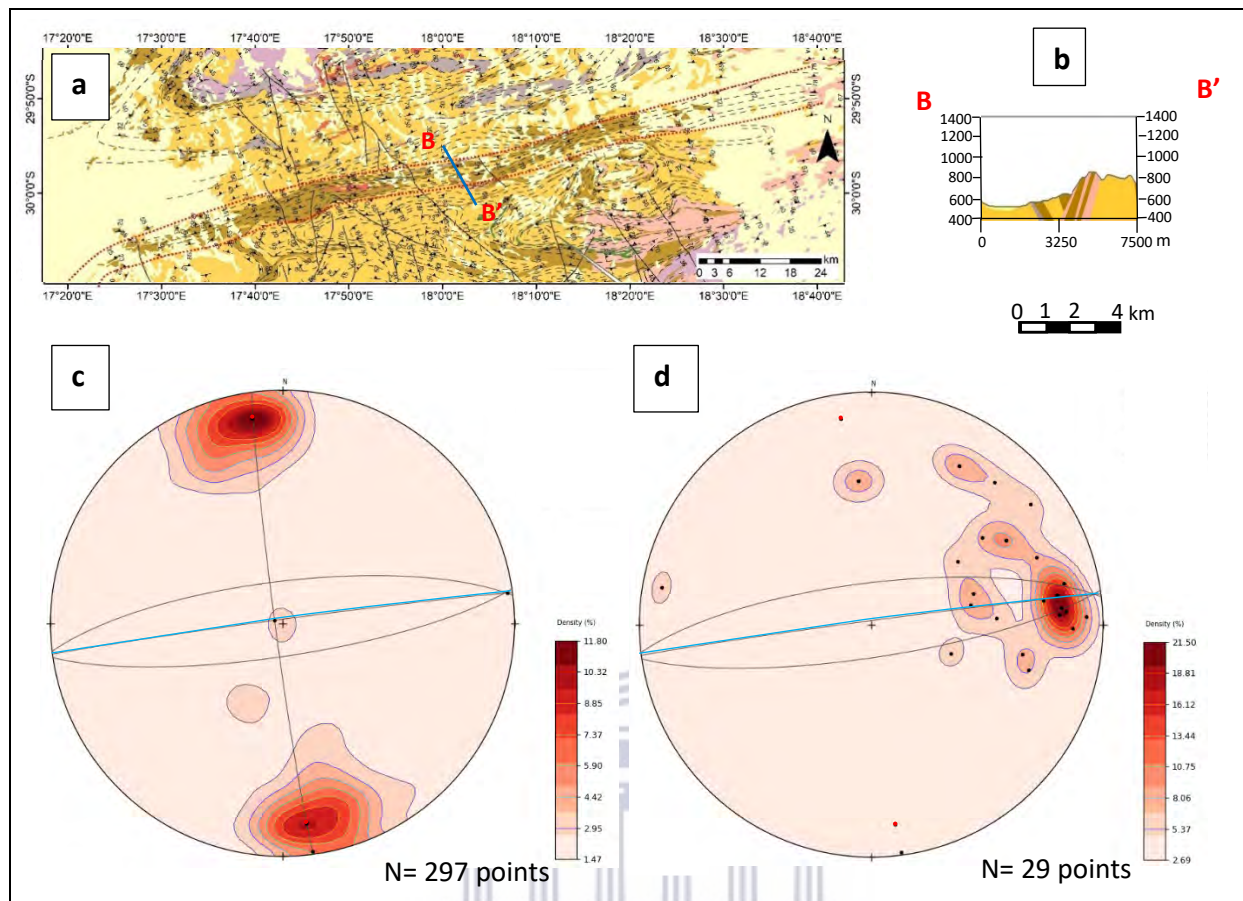
Figure 49 (a) Geological map of Subarea 2 with cross section line B-B' indicated. **(b)** Cross section B-B' of Subarea 2. **(c)** π diagram of S_2 for Subarea 2 and **(d)** a lower hemisphere stereographic projection of the two limbs (black great circles) displaying L_2 lineations (black dots). Red dots are pole maxima and the blue line is the axial plane. N = 29 points

Five hundred and nine data points were obtained through data collected by this project and historical collated data collected by previous authors who worked in this area (De Beer, 2010; Macey et al., 2011, Abrahams et al., 2020; Groenewald and Macey, 2020; Thomas, 2020). A lower hemisphere equal area stereogram was constructed in order to classify the structure (Fig. 50c). The interlimb angle, as determined from Figure 50c, is 132° and the $D_{2/3}$ structure is best described as a gentle fold with a fold axis plunging 23° towards 079° and an axial plane dipping 89° towards 169° and is an upright gently plunging fold. Similarly, to Subarea 1 the mineral lineations (L_2) are not oriented parallel to the fold axis but rather are girdled between 45° and 89°, an indication of a rather diffuse cluster (Fig. 50d). Cross section C-C' was drawn through Subarea 3 and it could be categorised as an upright gentle fold (Fig. 50b).

7.4 Lineation analysis

Well-developed mineral lineations in the study area are formed by the preferential orientation of minerals that are recognized on the S_2 plane (Fig. 44f), in particular that of the alignment of biotite in pelitic and psammitic supracrustal rocks as well as elongate quartz and alkali feldspar porphyroblasts in the streakier augen gneisses found in the BRSZ which were harder to measure

due to the whale back pavement weathering of the granitic gneisses. As a general overview, the lineation orientations from each subarea have similar plunging directions. They all broadly plunge ENE. In Figure 51, lineations are interpreted as a D_2 generation due to their alignment with the S_2 foliation and therefore are considered to be L_2 lineations that have dominant orientations which plunge shallowly towards 60° to 85° with a few lineations trending southwest. The L_2 lineations that are restricted to the BRSZ (Subarea 2), in particular, tend to trend more easterly than the typical ENE trend of the northern (Subarea 1) and southern (Subarea 3) structures outlined in Figure 51. Stereographic projection of these lineations represent a diffuse cluster with a large spread which could be interpreted to be due to folding about the F_3 axis and not necessarily defining a girdle. Therefore, the best description of lineations found along Subarea 2 is that their more easterly trend in comparison to the overall ENE-WSW trend is due to folding and increase in strain along the shear zone.
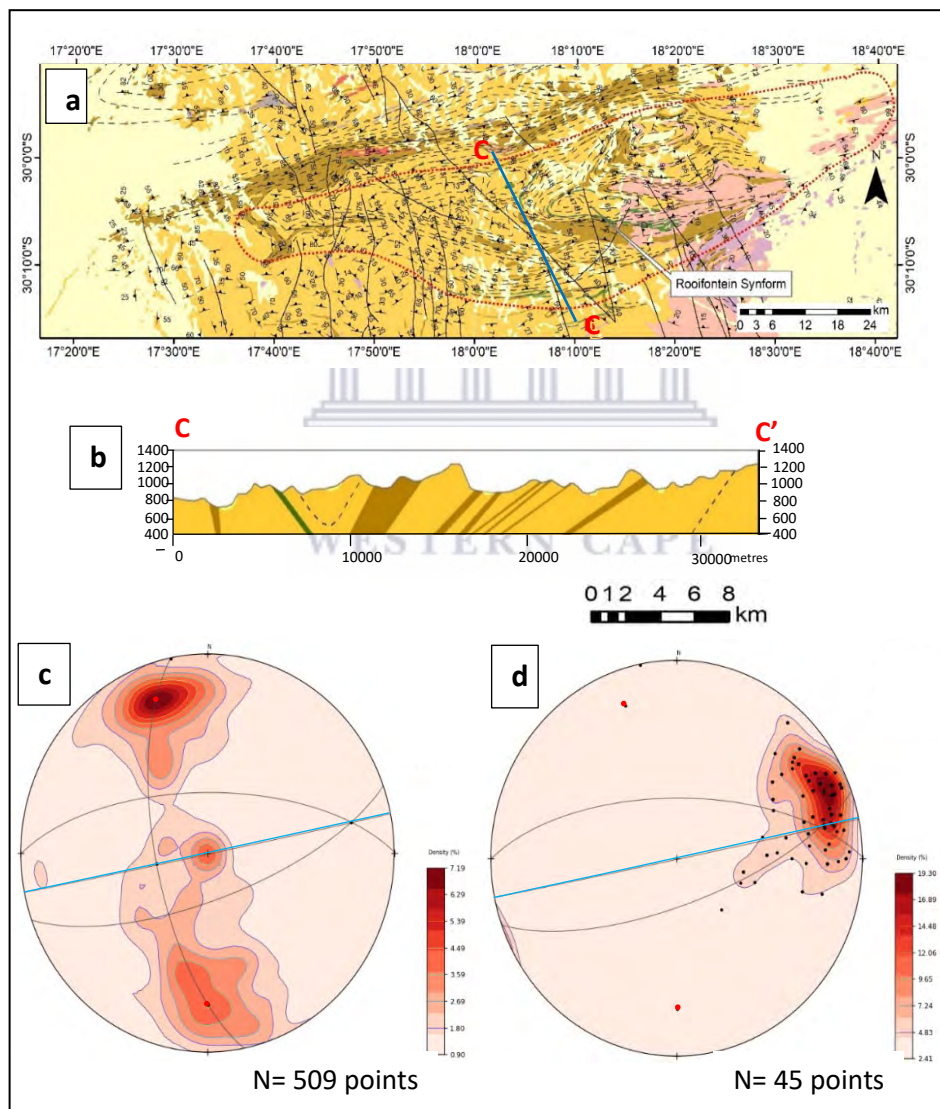
Figure 50 (a) Geological map of Subarea 3 with cross section line C-C' indicated. **(b)** Cross section C-C' of Subarea 3. **(c)** π diagram of S_2 for Subarea 3 and **(d)** a lower hemisphere stereographic projection of the two limbs (black great circles) displaying L_2 lineations (black dots). Red dots are pole maxima and the blue line is the axial plane. N = 45 points
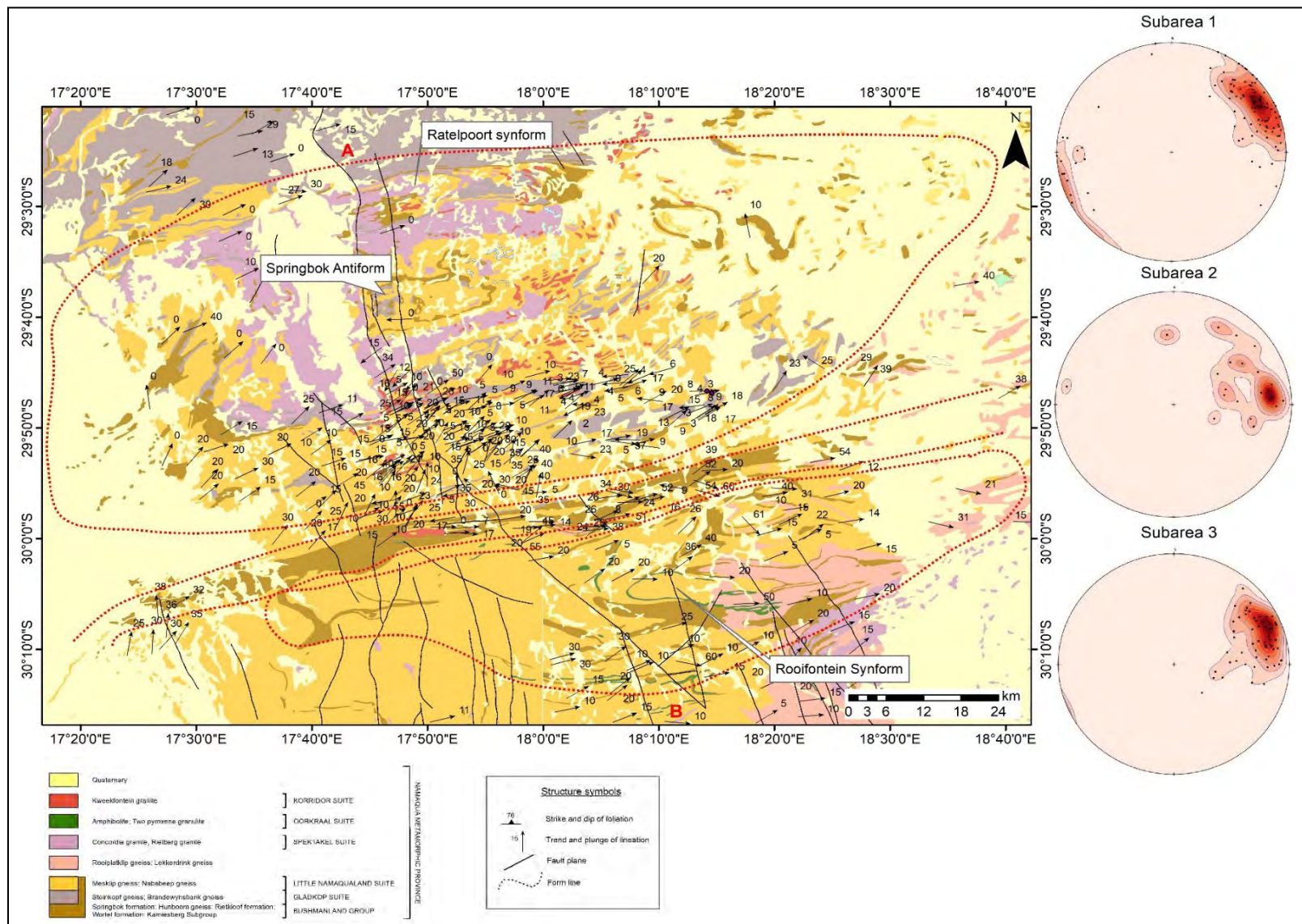
Figure 51 Regional lineation map of the study area (BRSZ) including the northern and southern dome and basin structures respectively. The red dashed lines enclose the subareas from north to south namely Subareas 1, 2 and 3. Lower hemisphere stereographic projection diagrams displaying L_2 lineations for each subarea displayed to the right of the map.

61

Chapter 8: Discussion

8.1 Characterisation of rock types occurring in the BRSZ

8.1.1   Felsic magmatic rocks

a)   Mesklip Gneiss

The Mesklip Gneiss can be characterised as a felsic alkali-granitic to granitic rock, rich in Na_2O and K_2O, plotting in the monzogranite field in the QAPF ternary diagram (Fig. 14b). This rock type can be described as metaluminous to weakly peraluminous with an FeO + MgO total that dictates that this felsic magmatic rock is magnesian. According to the MALI index the Mesklip Gneiss displays a range in composition ranging from alkali-calcic to calc-alkalic (Fig. 15c) with the majority of the samples dominating the calc-alkalic field. The Mesklip Gneiss also classifies as highly potassic plotting into the high-K alkaline series to shoshonite series (Fig. 15d). With SiO_2 having a strong negative relationship with all major oxides, except K_2O, it suggests the fractionation of mafic minerals such as clinopyroxene, orthopyroxene and amphibole along with plagioclase in the early stages of magmatic differentiation (Appendix A, Fig. A2). Since the extraction or crystallization of mafic minerals that are not rich in K gave rise to an increase in K in the magma, it indicates that the positive correlation of SiO_2 with K_2O in the Mesklip Gneiss indicates that K-feldspar likely crystallised later. According to the maficity plots in Appendix A (Fig. A4 & A5) the positive correlation of P with maficity suggests the entrainment of apatite. The strong positive correlations between Zr and Hf as well as REE-bearing accessory phase minerals suggests possible entrainment of zircon. The moderately negatively sloping pattern of the REE plot indicates a presence of a crustal component or derivation from a crustal source (Fig. 16a). The negative Eu anomaly suggests that there was a retention of plagioclase in the source area or that plagioclase was removed from the parental melt. The negative Ba, Sr, Nb and Ti anomalies with corresponding prominent positive Rb, Pb, Th and K anomalies once again indicate they are strongly related to a crustal influence or derivation from a crustal source. The negative Sr and Eu anomalies also indicate the fractionation or retention of plagioclase. The strong negative Nb anomaly is an indication of its retention in the source and depletion in the melt and thus strongly indicates that the Mesklip Gneiss is of crustal derivation. The negative Ti anomaly also indicates the retention of some Ti-bearing phase such as magnetite or ilmenite in the source.

The Mesklip Gneiss is Mesoproterozoic in age and three samples have been dated in this study at 1224 ± 5 Ma, 1205 ± 9 Ma and 1204 ± 8 Ma respectively (Figs. 35, 37 & 39). An average of ~1211 Ma is taken as the crystallization age of the Mesklip Gneiss. The U-Pb zircon age is believed to be magmatic because the zircons range from euhedral to subhedral, with unzoned cores with bright CL surrounded by dark rims. The geochronology results show that the three Mesklip Gneiss samples which were dated are related geochemically and geochronologically. Two samples taken, one along the BRSZ and the other just south of the BRSZ, with ages 1205 ± 9 Ma and 1204 ± 8 Ma respectively are similar in age and fall within error of each other and may indicate a separate felsic magmatic event to that of the 1224 ± 5 Ma age of sample 034D sampled further north of the BRSZ. Alternatively, this age could be taken as the maximum age of the Mesklip Gneiss in this study area. Various authors have dated what is termed the Mesklip Gneiss at ~1200 Ma (Joubert, 1986; Raith et al., 2003; Eglington, 2006). Sample 019A with a crystallisation age of 1204 ± 8 Ma occurs just south of the BRSZ as compared to sample 034D, with a crystallization age of 1224 ± 5 Ma, which occurs further north of the BRSZ. This

62

indicates that there may have been more than one magmatic phase of the Mesklip Gneiss from north to south. Both samples ages indicate that the ages of the Mesklip Gneiss on either side of the shear zone are within error and are certainly related.

The Mesklip Gneiss is the only magmatic rock that plots above the upper crustal curve (Fig. 58). Having a high initial $^{87}Sr/^{86}Sr$ ratio of 0.7391 is characteristic of a strong crustal influence (Rollinson, 1993). The negative $\varepsilon Nd_{(t)}$ values of -5.70 and -6.78 respectively suggests a significant crustal-type component. In Appendix A, Figure A14, where the initial $\varepsilon Nd_{(t)}$ values are plotted against their crystallization ages, the Mesklip Gneiss plots below the CHUR line. The three Mesklip Gneiss samples have corresponding T_{DM} ages of 2140 Ma, 2150 Ma and 1940 Ma respectively. Sample 019A also has a negative $\varepsilon Nd(t)$ value of -3.23 suggesting the presence of a significant depleted component.
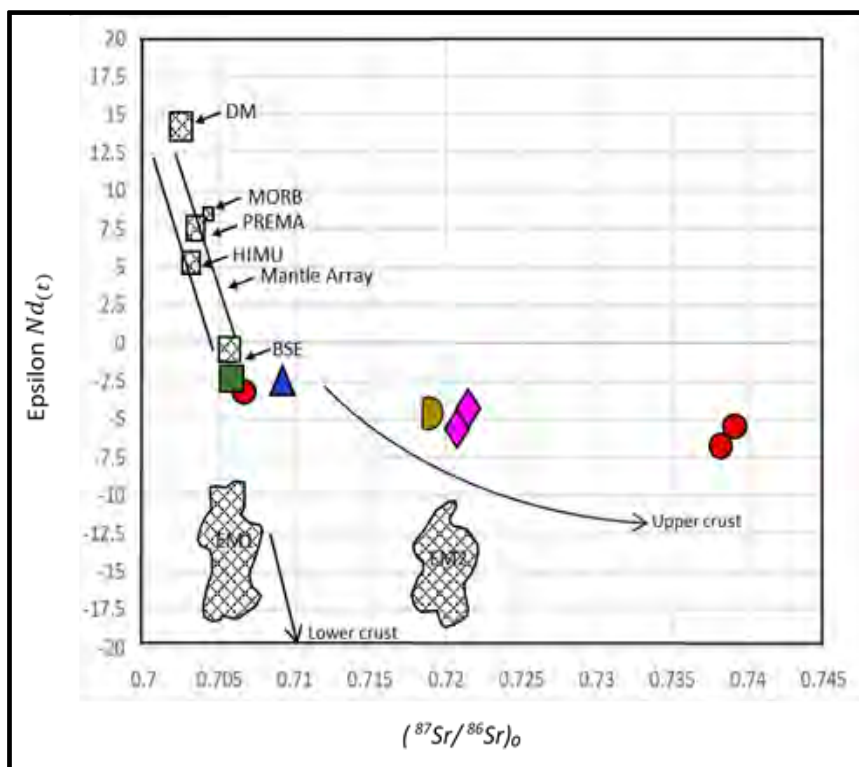
Figure 58 ($^{87}Sr/^{86}Sr)_i$ vs. $\varepsilon Nd(t)$ isotope correlation diagram displaying the samples taken from the Buffels River shear zone. The upper crustal curve (after Harris et al., 1986) and a theoretical lower crustal curve (from Ben Othman et al., 1984) are indicated for reference. The positions of the main oceanic mantle reservoirs identified by Zindler and Hart (1986) are shown: DM = depleted mantle, BSE = bulk silicate earth, EMI and EMII = enriched mantle I and II, HIMU = high mantle U/Pb ratio, PREMA = frequently observed prevalent mantle composition. The mantle sources of MORB and OIB and the mantle end-members DM, PREMA, HIMU, BSE, EMI and EMII are from Zindler & Hart (1986). (Red circle –Mesklip Gneiss, Brown half circle – garnet-biotite-quartz-sillimanite semi-pelitic gneiss, blue triangle- leucogranitic gneiss, pink diamond- Hunboom Gneiss and green square – amphibolite).

Although the $\varepsilon Nd_{(t)}$ value is negative it still does suggest a degree of enrichment. According to the fSm/Nd ratios of all three Mesklip Gneiss samples (-0.4717, -0.5009 and -0.4834 respectively) it is an indication of derivation from a relatively fractionated source (Appendix B, Table B4). This suggests that the Mesklip Gneiss is likely derived from a slightly enriched crustal source or a metasomatised enriched mantle.

b) Rooiplatklip Gneiss

The Rooiplatklip Gneiss can be characterised as an alkali-granitic to leucogranitic rock (Fig. 17a), plotting within the monzogranite field in the QAPF ternary diagram (Fig. 17b). This rock type can be described as peraluminous in nature with an $FeO_{TOT}/(FeO_{TOT} + MgO)$ composition plotting within the magnesian field (Fig. 18c). The MALI index displays the leucogneiss having a range in composition from alkali-calcic to calc-alkalic (Fig. 18b). The Rooiplatklip Gneiss classifies as highly potassic and falls within the high-K calc-alkaline to shoshonite series (Fig. 18d). In Appendix A, Figure A6, the negative correlation of MgO, TiO_2, FeO and CaO with increasing SiO_2 suggests the fractionation of mafic minerals such as clinopyroxene and amphibole along with calcic plagioclase during the early stages of magmatic differentiation. The positive correlation between Fe+Mg and P in the maficity plots (Appendix A, Figure A8) suggests entrainment of apatite into the melt which formed the granite. A crustal component or the derivation from a crustal source for the Rooiplatklip Gneiss is indicated by the trends seen in both the REE plot and the spider diagram (Fig. 19a & b). The average value for $[Gd/Lu]_{PM}$ is 3.51 suggesting a greater degree of fractionation between the HREE's. The negative Eu anomaly suggests retention of plagioclase in the source area or crystal fractionation of plagioclase in the magma system. Enrichment in Pb and Rb in the spider diagram also suggest that there is an influence of a crustal component due to the composition of the source area. Depletions in Ba and Sr suggest a plagioclase depletion in the source area or retention of plagioclase in the source during partial melting which gave rise to the partial melts of these magmatic rocks (Rollinson, 1993). The enrichment in Th relative to the primitive mantle values suggests a crustal influence. The strong depletion in P and Ti suggest the presence and retention of apatite as well as magnetite/ilmenite in the source area from which the magma forming the leucogneiss was generated. The emplacement age of the Rooiplatklip Gneiss is considered to be 1204 ± 4 Ma.

The Rooiplatklip Gneiss plots just below the Bulk Silicate Earth field (Fig. 58) with an initial $^{87}Sr/^{86}Sr$ ratio of 0.7108 and initial $^{143}Nd/^{144}Nd$ ratio of 0.51174 (Appendix B, Table B4). It has a negative $\epsilon Nd_{(t)}$ value of –2.76 suggesting the presence of a slightly depleted component in the source. The negative fSm/Nd ratio of -0.4838 suggests the source was relatively fractionated (Appendix B, Table B4). In the Goldstein et al. (1984) plot (Appendix A, Fig. A13) the leucogneiss has a T_{DM} age of 1900 Ma suggesting an influence of Paleoproterozoic basement which was reworked extensively.

8.1.2 Mafic magmatic rocks

a) Mafic rocks

The mafic rocks can be characterised as gabbroic, plotting within the olivine gabbro and gabbro field in the IUGS mafic rock classification ternary diagram (Appendix A, Figure A12-a, A12-b & A12-c)). In Figure 21a the REE plot shows an enrichment of LREE over HREE with a negatively sloping trend with an average $[La/Yb]_{PM}$ value of 25.17. All the samples have a negative Eu anomaly suggesting the retention of plagioclase in the source area or crystal fractionation of the plagioclase prior to emplacement. Enrichment in Pb suggests a crustal influence due to Pb being strongly partitioned into the crust relative to the mantle.

The mafic rocks were not dated in this study as they were previously dated by Bailie et al. (2019). The gabbro-norites of the Oorkraal Suite was dated by Bailie et al. (2019) and has a $^{207}Pb/^{206}Pb$ age of 1168 ± 9 Ma which is considered the emplacement age of the protolith.

The gabbroic rocks plot just below Bulk Silicate Earth (Fig. 58) with an initial $^{87}Sr/^{86}Sr$ ratio of 0.7060 and an initial $^{143}Nd/^{144}Nd$ ratio of 0.512002 (Appendix B, Table B4). The negative $\varepsilon Nd_{(t)}$ value of -2.38 suggest the gabbro was derived from a mildly enriched source and the negative fSm/Nd ratio of -0.3413 suggesting that the source was also relatively fractionated. In the Goldstein et al. (1984) plot (Appendix A, Figure A14) the amphibolite has a T_{DM} age of 2070 Ma and this suggests the reworking of Paleoproterozoic material and possible crustal contamination.

8.1.3   Metasedimentary rocks

a)   Hunboom Gneiss

The Hunboom Gneiss protolith is historically difficult to discriminate as to whether it is of volcanic or sedimentary origin. According to data collected the geochemistry discrimination indicate a felsic volcanic provenance but in contrast the zircon morphology shows zircons associated with being transported and therefore as a detrital pattern. This therefore suggests a possible volcaniclastic protolith where volcanic material was subsequently reworked in rivers and streams by Aeolian and/or fluvial processes. In the Herron (1988) diagram the Hunboom Gneiss samples are mostly classified as wacke (Fig. 22b). This is supported by geochemical evidence with the Biotite Gneisses having quite uniform compositions with relatively narrow ranges of $SiO_2:Al_2O_3$ ratios of between 4.44 and 5.56 (Fig. 22b). Both the REE plot and spider diagram (Fig. 23a & b) have a moderately negatively sloping trend and the gradual decrease in elemental concentration indicating the enrichment of LILE over HFSE indicates the derivation from a crustal source. The low value for $[Gd/Lu]_{PM}$ values (average = 1.91) suggests a low degree of fractionation between the HREE. Four samples of the Hunboom Gneiss display a negative Eu anomaly indicating the retention of plagioclase in the source area or crystal fractionation of plagioclase prior to emplacement of the provenance, with three samples having flat to positive Eu anomalies suggesting these samples have the same amount of plagioclase as the average crust. Enrichment in Pb suggests a crustal influence due to it being strongly partitioned into the crust relative to the mantle. The depletion in P and Ti suggests the presence and retention of apatite as well as magnetite/ilmenite in the source area from which the magma forming this rock was generated. The prominent Nb-Ta trough exhibits the possibility of a crustal influence for the provenance from which the sedimentary rocks were derived as well as subduction-related magmas generated in typical arc environments.

The Hunboom Gneiss is Mesoproterozoic in age and two samples have been dated in this study at 1138 ± 22 Ma and 1113 ± 22 Ma respectively. An average of ~1126 Ma is taken as the maximum age of deposition of the Biotite Gneiss protolith with an average metamorphic age of 1096 Ma as the minimum age of deposition (Table 2, 3a & b). The Hunboom Gneiss has a moderate initial $^{143}Nd/^{144}Nd$ value of 0.5117-0.5119 and a fairly high initial Sr ($^{87}Sr/^{86}Sr_{(i)}$) ratio of 0.7151-0.7108 (Appendix B, Table B4) which suggest the derivation from radiogenic reworked crust and/or influenced by the partial melting of rocks. The biotite gneiss plots close to the garnet-biotite-quartz-sillimanite semi-pelitic gneiss and the fairly high $^{87}Sr/^{86}Sr_{(i)}$ ratios for both the Hunboom Gneisses and garnet-biotite-quartz-sillimanite semi-pelitic gneiss suggests that either weathering or hydrothermal fluids have influenced the ($^{87}Sr/^{86}Sr_{(i)}$) ratio. Both biotite gneiss samples have relatively strongly negative epsilon $\varepsilon Nd_{(t)}$ value of -4.69 and -4.20 which once again indicates a provenance(s) with a relatively enriched signature, suggests a crustal source carrying a somewhat enriched signature and that these rocks were therefore potentially derived from a fairly enriched provenance. In the Goldstein et al. (1984) plot

65

(Appendix A, Figure A14) the Hunboom Gneisses have T_{DM} ages of 2210 Ma and 2160 Ma respectively and suggesting it was potentially derived from a source that underwent the reworking of Paleoproterozoic material and possible crustal contamination.

b) Metapelitic gneiss, metapsammitic gneiss and garnetiferous quartzofeldspathic biotite-sillimanite gneiss

The metapelitic and metapsammitic gneisses in the BRSZ are intermediate in nature and are considered to be the product of metamorphosed dirty sandstone as displayed in the Herron (1988) classification diagram (Fig. 24a & b). The REE plot trend for two samples (metapsammitic gneiss) are relatively flat to slightly negatively sloping (average $[La/Yb]_{PM}$ =1.28) with a negative Eu anomaly $((Eu/Eu*)_N$ between 0.76 and 1.13) which suggests the retention of plagioclase in the source area (Fig. 25a) or that plagioclase broke down during weathering and transport to the site of deposition, as compared to the three samples (one metapsammitic gneiss and two metapelitic gneisses) which have a strong negatively sloping trend as well as a flat to positive Eu anomaly which is an indication of a plagioclase-rich rock. This suggests a different provenance and mineralogical composition for these three samples. In the spider diagram (Fig. 25b) depletions in Na and Ca indicate that the precursors were derived from a plagioclase-poor provenance, with Al plotting around 1 and depletions in Sr also suggesting that the protolith was plagioclase-poor. An enrichment in Sc and Ni suggest the presence of a mafic component to the provenance.

The garnet-biotite-quartz-sillimanite semi-pelitic gneiss is Mesoproterozoic in age and one sample has been dated in this study at 1222 ± 25 Ma which is taken as the maximum age of deposition–with a metamorphic age of 1171 ± 21 Ma as the minimum age of deposition (Fig. 33). The garnet-biotite-quartz-sillimanite semi-pelitic gneiss has fairly high $^{87}Sr/^{86}Sr_{(i)}$ ratios (Appendix B, Table B4) and suggest that it was derived from a radiogenic reworked crust and possibly influenced by partial melting. The garnet-biotite-quartz-sillimanite semi-pelitic gneiss has a relatively strongly negative epsilon $\varepsilon Nd_{(t)}$ value of -4.90 which indicates an enriched source signature for the provenance and the negative fSm/Nd ratio of -0.3066 suggests it is derived from a highly fractionated source. In the Goldstein et al. (1984) plot (Appendix A, Figure A14) the garnet-biotite-quartz-sillimanite semi-pelitic gneiss has a T_{DM} age of 2400 Ma and likely suggests the derivation from a source of reworked Paleoproterozoic material and possible crustal contamination.

8.2 Defining the tectonic history

8.2.1 Constraining the age of the deformation

The first deformational phase (D_1) is not observed in the BRSZ due to the largely regional overprint of the second deformational event (D_2). A very strong D_2 tectonic fabric exists, known as the compressional phase during which a strong tectonic fabric was produced that terminates at approximately 1100 Ma as granites which intruded after this time are undeformed.

The Mesklip Gneiss, which is dated at ~1.21 Ga, is strongly deformed by the D_2 (Namaqua phase) deformation event (1180 - 1210 Ma; Robb et al., 1999; Clifford et al., 2004). The timing and characteristics of the Mesklip Gneiss correlate with magmatic events in the larger Namaqua Sector correlating with the overall ~1.2 Ga D_2 tectonic event (Thomas et al., 1994; Clifford et al., 2004; Eglington, 2006; Macey et al., 2018). The Mesklip Gneiss has inheritance ages from

~1811 Ma to ~1741 Ma indicative of an inheritance of Gladkop Suite-type material found in the northern portion of the Okiep Copper District (OCD).

The regional penetrative E-W-striking moderate to shallow-dipping S_2 fabric imposed on the Mesklip Gneisses is present both north and south of the BRSZ indicating the intense subvertical zone of steeply dipping fabric and complex strain along the BRSZ occurred post the Namaqua Orogeny during D_3. According to Macey et al. (2018) this indicates that the shared tectonic histories across the Namaqua Sector (excluding the Vioolsdrif Domain) points to the possibility that pre-existing tectonic domains were already juxtaposed by ~1.2 Ga. If the BRSZ were to represent a pre-existing terrane boundary it is thought that the Okiep and Garies terranes were accreted prior to the ~1.2 Ga magmatism and the present day BRSZ formed during D_3 is representative of a reactivated shear zone along this pre-existing terrane boundary.

According to Yuhara et al. (2002) the Sm-Nd isotopic ages differ across the shear zone which agrees with the data presented by Robb et al. (1999). According to Yuhara et al. (2002) they have inferred the BRSZ to be the boundary between the Okiep and Garies terranes because this high strain zone is positioned between two known differing isotopic age domains of the Okiep and Garies terranes respectively. The differing radiogenic ages suggest that prior to the Mesklip Gneisses emplacement older crust was reworked and produced a younger product in the south and older in the north.

The youngest detrital zircon ages for the Hunboom Gneisses are between ~1138 Ma and ~1113 Ma indicating possible extension associated with the deposition of its possible volcaniclastic protolith during this time. The garnet-biotite semi-pelitic gneiss has detrital zircons around 1222 Ma which is synchronous with the crystallisation of the Mesklip Gneiss. Therefore, the approximate age of the BRSZ can be constrained between ~1138 Ma and the age of the D_3 deformation event (between ~1138 and ~1005 Ma; Lambert, 2003). Inheritance ages of ~1300 Ma present in these supracrustal rocks (as well as the leucocratic gneisses) have no associated magmatic event to correlate to, but according to Cornell et al. (1990), initial Mesoproterozoic magmatism occurred at ~1.3 Ga which is coeval with igneous activity which occurred in the Areachap and Kakamas terranes of the Gordonia Subprovince to the east. Further investigation needs to be made in order to clearly identify the source of these inherited ages. Eglington (2006) also states that supracrustal gneisses from the Gordonia and Natal Subprovinces are around ~1.3 Ga in age and infers that the metasediments from the Garies terrane in the Bushmanland Subprovince are similar or younger in age. The Koperberg Suite rocks subsequently intruded between 1057 Ma and 1037 Ma during a major granulite facies metamorphic event (Robb et al., 1999). The mafic rocks were not dated in this study as they were previously dated by Robb et al. (1999) and Bailie et al. (2019). The two-pyroxene granulites dated by Robb et al (1999) have two zircon domains with $^{207}Pb/^{206}Pb$ ages of 1168 ± 9 Ma age of emplacement and 1063 ± 16 Ma age of metamorphic overprint respectively. The gabbro-norites of the Oorkraal Suite that were dated by Bailie et al. (2019) has a $^{207}Pb/^{206}Pb$ age of 1168 ± 9 Ma.

Metamorphic events seen in the zircon age data of this study indicates there are three main pulses of metamorphism along the BRSZ. The intrusion of the Little Namaqualand Suite granitoids corresponds to the first known event at ~1200 Ma followed by events at ~1148 Ma and ~1053 Ma, seen on a regional scale. The second metamorphic age is interpreted to be the age of emplacement of the Spektakel Suite (Macey et al, 2018) and the third and final

metamorphic event was a high-temperature, low pressure overprint accompanied by intrusions of the Koperberg Suite gabbro-norite that produced poorly structured zircon overgrowths (Robb et al., 1999). These ages are coeval with those of Robb et al. (1999), Raith et al. (2003) and Clifford et al. (1981, 2004).

8.2.2 Dome and basin structure

Subarea 1 represents a gentle fold with a fold axis plunging 5° towards 072° and an axial plane dipping 89° towards 163° and is determined to be an upright horizontal fold. It is clear from the overall geology that the Springbok antiform represents the core of this larger dome consisting of various smaller interference fold patterns likely due to the F_3 refolding of F_2 folds during D_3 deformation. Subarea 3 represents a gentle fold with a fold axis plunging 23° towards 079° and an axial plane dipping 89° towards 169° and is determined to be an upright gently plunging fold. The Rooifontein basin (Appendix A, Fig. A15) represents the core of this basin structure and once again consists of smaller domes and basins within this larger structure alluding to fold interference formation during D_3 deformation. Subarea 2 consists of the BRSZ itself and is described as a tight fold with a fold axis plunging 3° towards 082° and an axial plane dipping 89° towards 352° and is determined to be an upright horizontal fold.

8.3 Significance of the Buffels River shear zone as a terrane boundary

This will be discussed in two parts, firstly: (1) shear zone development vs. "steep structures" model, and (2) the characteristics of a terrane boundary and whether the BRSZ fits the typical model for one.

8.3.1 Shear zone development vs. "steep structures" model

Shear zones, by definition, are described as strongly deformed zones in relation to the surrounding rocks and are recognised as a planar zone which accommodates local strain (Ramsay & Huber, 1988). According to Ramsay & Huber (1988), shear zones can be divided into three types, namely brittle shear zones, brittle-ductile shear zones, and ductile shear zones. There will be particular focus placed on ductile shear zones since the BRSZ was formed under ductile deformation processes during high-grade metamorphic conditions and there is evidence of grain size reduction, strong stretching lineation and boudinage, all indicators of ductile deformation. It is said that ductile shear zones form in the lower crust and upper mantle and thus forms the base of the lithosphere (Ramsay & Huber, 1988). There are two types of shear strain that can take place either through compression or extension, which is termed pure shear (also referred to as coaxial deformation) or through tangential displacement, which is termed simple shear (also referred to as non-coaxial deformation). Usually the sense of rotation of the foliation from the margins of the shear is a safe kinematic indicator of simple shear but the BRSZ has no deflected marker beds on either side of the shear zone. As seen in the porphyroclasts of the Mesklip Gneiss their recrystallized tails are symmetric about the reference line and therefore indicate that they were likely produced due to coaxial deformation (Fig. 59). Another factor which indicates that the BRSZ formed through a pure shear regime is that the BRSZ is co-planar to the main penetrative S_2 foliation indicating that the principal axes before and after strain coincide and are non-rotational (Fig. 60). In particular, grain size reduction of the rocks within the shear zone are of importance in recognising the change in strain across the shear zone. Evidence of grain size reduction is clear when the sheared Mesklip Gneiss found within the BRSZ is compared to the medium to coarse grained Mesklip Gneiss found both north and south of the BRSZ (Fig. 59). The Flinn diagram (Fig. 61) generated using

68

OpenStereo software (Grohmann et al., 2017), indicates that the BRSZ plots between the prolate and plane strain field and the strain ellipsoid indicate constrictional strain, with the XY-plane of the ellipsoid being approximately parallel to the easterly trending, subvertical S_2/S_3 foliation of the core of the structure. This may all be indicative of the BRSZ undergoing NNW-SSE directed largely coaxial shortening strain where the foliations within the shear zone is much steeper when compared to the surrounding rocks. Its boundary with weaker foliated but nonetheless foliated rocks is gradational and in the same orientation as the shear zone itself. This indicates possible reactivation of an existing shear zone as well as the fact that D_2 and D_3 have fairly similar trending deformational histories.
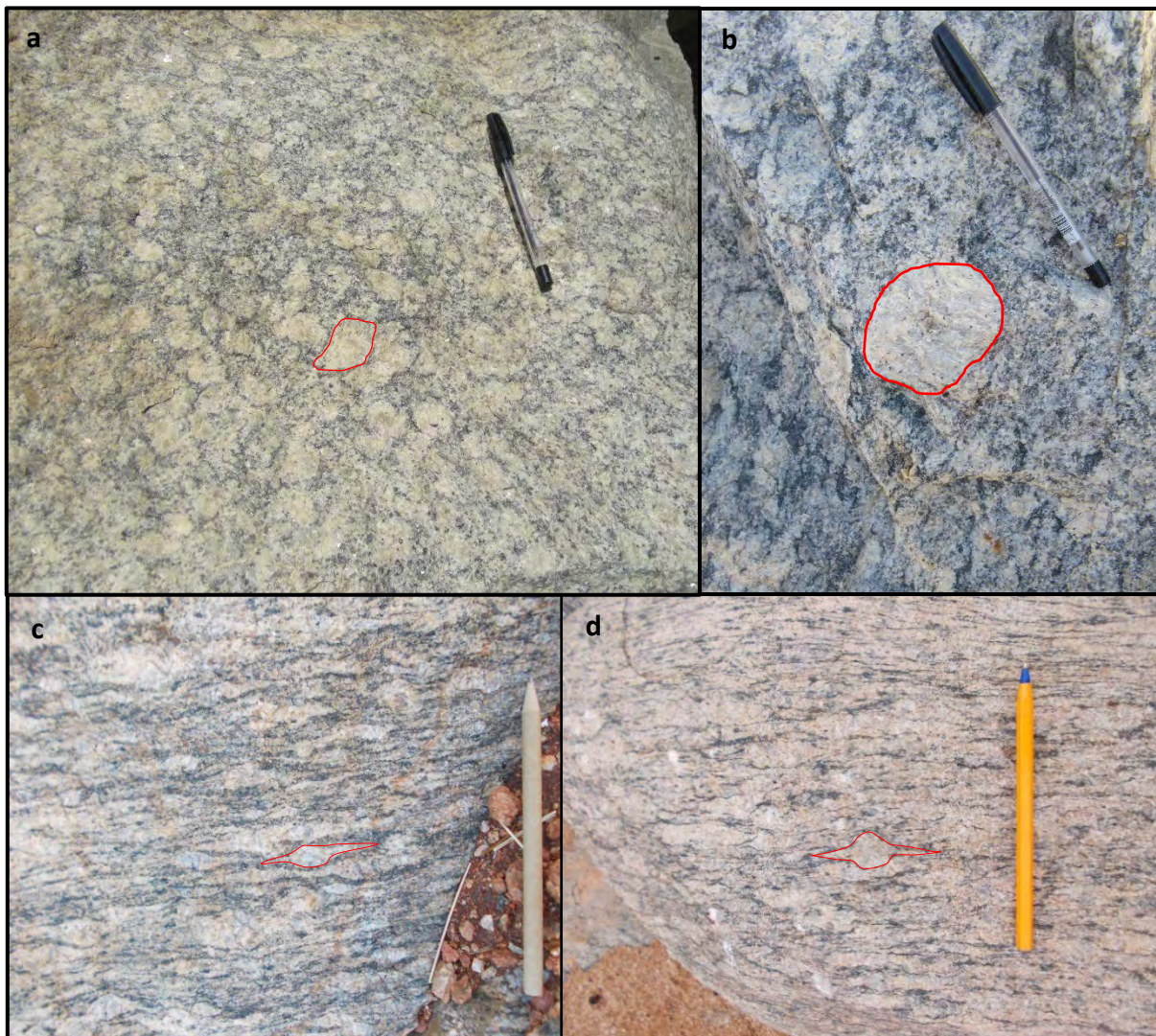
Figure 59 (a) and **(b)** Medium to coarse grained porphyritic Mesklip Gneiss which is moderately foliated and occurs adjacent to the BRSZ **(c)** and **(d)** Quartzofeldspathic porphyroblasts of the Mesklip Gneiss with symmetrical tails about the reference

Figure 60 A diagram displaying the various modes of shear strain (after Ramsay and Huber 1988).

Figure 61 Flinn diagram indicatess that the BRSZ plots between the prolate and plane strain field.

70

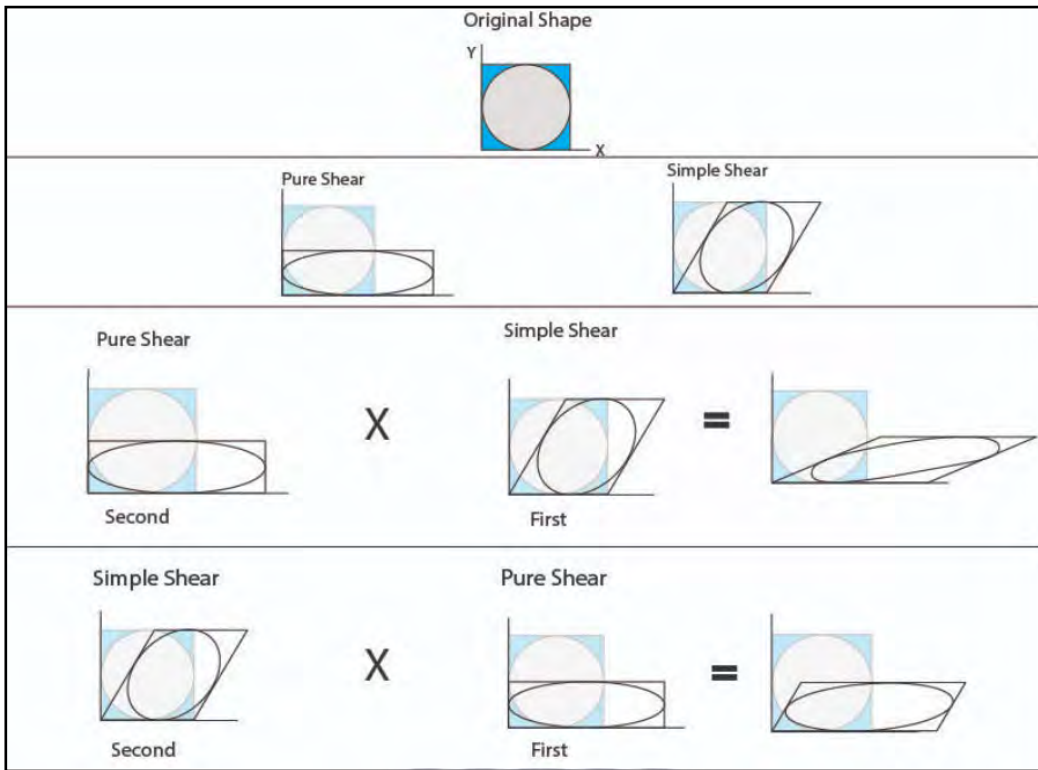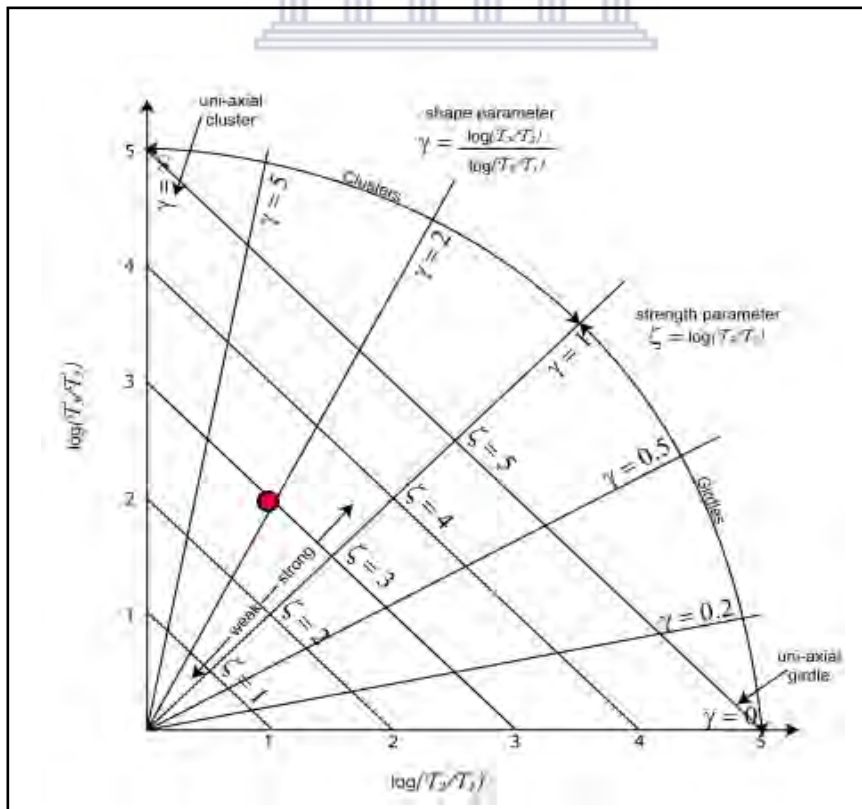Now to compare this to a "steep structures" model introduced by Kisters et al. (1996) which appears to be a unique structure limited to the Okiep Copper District and likely similar structures developed further south around the Kliprand area. These "steep structures" are thought to have an intimate structural relationship with antiformal and monoclinal warps of the known regional gneissosity. These "steep structures" are east-northeasterly-trending zones and formed when folding occurs parallel to the known regional D_3 folding resulting in a N-S-directed shortening strain where an S_2/S_3 fabric develops axial planar to the regional D_3 fabric (Kisters et al., 1996).

For the development of a "steep structure" in the Namaqua Sector there are a few criteria that need to be met: (1) the steep structure has an east-northeasterly trend which parallels the axial plane of open upright D_3 folds; (2) it has an intensely developed gneissic foliation and consists of complex migmatitic bodies, and (3) it is bounded by antiformal and monoclinal structures to the north and south respectively (Kisters et al., 1996). The BRSZ satisfies the criteria of a "steep structure" as it, in itself, is an east-northeasterly-trending, high-strain zone of intense gneissosity which parallels the axial plane of an open upright D_3 fold to the north (Subarea 1) and a gently upright plunging fold to the south (Subarea 3). No large-scale fold closures are observed in the central portion of the BRSZ (Subarea 2); instead the central portion of the structure is dominated by pervasive subvertical mylonitic fabrics. This would indicate a large increase in strain when approaching the inner parts of the structure (cf. Kisters et al., 1996). Therefore, a regional scale strain inhomogeneity exists, whereby the localized high strain is counterbalanced by low-strain zones in lateral alignment along the strike. The fabric development of the structure is also accompanied by a marked grain size reduction. Another indication of the presence of a "steep structure" is the easterly trending dykes of the Oorkraal Suite displaying boudinaged features parallel to the regional fabric which indicate a subhorizontal east-west direction of extension. All of these features are an indication of a D_3 origin for the development of the "steep structure". "Steep structures" range in size from metres to a few kilometres but larger structures have been observed (Lombard & Schreuder, 1978).

8.3.2 Definition of a terrane boundary

In understanding terrane boundaries, we need to understand how to classify a terrane boundary and investigate the stratigraphy and the structural controls of the study area in comparison to these characteristics. Investigating the stratigraphy provides information regarding the ages and paleogeographic relationships with the surrounding stratigraphy whereas the structural data will describe the configuration of the strata. These two aspects provide a tectonic analysis that offers solutions and an explanation for the kinematics and dynamic history of the BRSZ.

The requirements for the classification of a terrane boundary, according to Howell (1993), are:

1. Preservation of a distinctive geologic history which differs from that of the crustal material it is sutured to.
2. Terranes are usually fault-bounded.
3. They represent spatial relations that are not compatible with the inferred geologic histories.
4. They do not possess the same age as the surrounding strata.
5. Lithofacies are incompatible with the surrounding rocks, therefore genetically unrelated to the adjoining geology.

The preservation of geologic histories to the north in comparison to the south of the BRSZ, through geological mapping and lithological descriptions, indicate that the geologic history on either side of the BRSZ is preserved but is also identical. The Mesklip Gneiss occurs to the north, south and within the shear zone and has the same age throughout. Spatially, the geologic histories on either side of the BRSZ are consistent with each other and have lithofacies, geochemical and geochronological properties that are identical in nature. This indicates that the BRSZ does not, in fact, represent a terrane boundary between the Okiep and Garies terranes and that the terrane boundary, if there are, in fact, two different terranes, is likely situated further to the south of the BRSZ.

Based on the kinematics of the entire area (including Subareas 1 and 3) characteristics such as:

1. A marked grain size reduction of rocks found within the BRSZ
2. Boudinage of easterly trending Koperberg Suite amphibolites
3. Shear strain indicators classifying the BRSZ to have been formed through coaxial strain
4. The lack of large-scale fold closures within the BRSZ
5. The lack of the typical characteristics of a terrane boundary
6. The upright easterly-trending orientation of the BRSZ, which is parallel to the regional-scale D_3 folds

The BRSZ can be described as a "steep structure" or "accommodation/transfer zone" located between the dome and basin structures both north and south, respectively, based on the Kisters et al. (1996) description of "steep structures". The zone along the BRSZ was preferentially sheared due to the competency of the supracrustal rocks found in this zone. Shear zones commonly formed along these supracrustal belts in the Namaqua Metamorphic Province are present across approximately 240 kilometres occurring between Bitterfontein in the south to Geselskapbank in the north (Moore, 1989).

Chapter 9

9.1 Conclusion

This study evaluated, in detail, the characteristics of the BRSZ with the use of geological mapping, geochemical analysis of lithologies along the BRSZ, U-Pb zircon age determinations and isotopic analysis. There are three scenarios that likely best describe the evolution of the BRSZ: (1) the BRSZ represents a pre-existing terrane boundary where it is thought that the two tectonic domains were formed (accreted) prior to the ~1.2 Ga magmatism, and that the present day BRSZ formed during D_3 deformation is representative of a reactivated shear zone along this pre-existing terrane boundary, or (2) the BRSZ formed during D_3 deformation with age constraints between ~1138 Ma and ~1005 Ma and no terrane boundary exists at the BRSZ itself but is rather located further south of the shear zone, or (3) that both of these statements are true and that the BRSZ represents a reactivated shear zone located at the terrane boundary of the Okiep and Garies terranes which was reactivated between ~1138 Ma and ~1005 Ma and the differing radiogenic ages suggest that prior to the Mesklip Gneisses emplacement older crust was reworked and produced a younger product in the south and older in the north.

Based on the findings of this study the most likely scenario to represent the evolution of the Buffels River shear zone is that the development of the Buffels River shear zone initiated

preferentially along a supracrustal belt between ~1138 Ma and ~1005 Ma, during the D_3 deformational phase, forming what is known as a "steep structure" and it does not represent a terrane boundary between the Okiep and Garies terranes.

References

Abrahams, Y., Macey, P.H., & Groenewald, C., 2020. Revision of 2917DD Mesklip. 1:50 000 scale geological map field sheet, Council for Geoscience, Bellville, South Africa.

Agenbacht, A.L.D., 2007. The geology of the Pofadder area. Explanation of 1: 250 000 geology sheet 2918. Council for Geoscience, Pretoria, 89 pp.

Andreoli, A.G., Hart, R.J, Ashwal, L.D., & Coetzee, H., 2006. REE, Correlations between U, Th Content and Metamorphic Grade in the Western Namaqualand Belt, South Africa, with Implications for Radioactive Heating of the Crust, Journal of Petrology, Volume 47, Issue 6, June 2006, pp. 1095–1118

Barton, E., 1983. The geochronology of the frontal zones of the Namaqua-Natal mobile belt, University of Witwatersrand, Johanneburg: Unpublished Doctoral thesis.

Barton, M., & Young, S., 2002. Non-pegmatitic Deposits of Beryllium: Mineralogy, Geology, Phase Equilibria and Origin, Reviews in Mineralogy & Geochemistry, Volume 50, pp. 591-691.

Ben Othman, D., Polve, M. & Allerge, C.J., 1984. Nd-Sr isotopic composition of granulites and constraints on the evolution of the lower continental crust. Nature, 307, 510-515.

Clifford, T.N. & Barton, E.S., 2012. The O'okiep Copper District, Namaqualand, South Africa: a review of the geology with emphasis on the petrogenesis of the cupriferous Koperberg Suite. Miner Deposita, Volume 47, pp. 837-857.

Clifford, T.N., Barton, E.S., Stern, R.A. & Duchesne, J.C., 2004. U-Pb zircon calender for Namaquan (Grenville) crustal events in the granulite-facies terrain of the O'Okiep copper district of South Africa. Journal of Petrology, Volume 45, pp. 669-691.

Colliston, W.P. & Schoch, A.E., 2002. The structural development of the Aggeneys Hills, Namaqua Metamorphic Complex. South African Journal of Geology, Volume 105, pp. 301-324.

Cornell, D.H., Kroner, A., Humphreys, H. & Griffin, G., 1990. Age of origin of the polymetamorphosed Copperton Formation, Namaqua-Natal Province, determined by single grain zircon Pb-Pb dating. South African Journal of Geology, Volume 93, pp. 709-716.

Cornell, D. H., Thomas, R.J., Moen, H.F.G., Reid, D.L., Moore, J.M., & Gibson, R.L., 2006. The Namaqua-Natal Province. In: The Geology of South Africa. Johannesburg: The Geological Society of South Africa and the Council for Geoscience, pp. 325-380.

Cox, K.G., Bell, J.D. & Pankhurst, R.J., 1979. The Interpretation of Igneous Rocks. George Allen & Unwin.

De Beer, C.H., 2010. The geology of the Garies area. Explanation to Sheet 3017 Garies, Scale 1:250 000. Council for Geoscience.

Eglington, B. M., 2006. Evolution of the Namaqua-Natal Belt, southern Africa - A geochronological and isotope geochemical review. Journal of African Earth Sciences 46, pp. 93-111.

Frei, D. & Gerdes, A., 2009. Precise and accurate in situ U-Pb dating of zircon with high sample throughput by automated LA-SF-ICP-MS.. Chemical Geology, Volume 261, pp. 261-270.

Frost, B.R., Barnes, C.G., Collins, W.J., Arculus, R.J., Ellis, D.J. & Frost, C.D., 2001. A geochemical classification for granitic rocks. Journal of Petrology, 42, 2033-2048.

Gerringer, G.J., 1979. The origin and tectonic setting of amphibolites in part of the Namaqua Metaorphic Belt, South Africa. Transactions f the Geological Society of South Africa, Volume 82, pp. 287-303.

Goldstein, S.L., O'Nions, R.K. & Hamilton, P.J., 1984. A SmNd isotopic study of atmospheric dusts and particulates from major river systems. Earth and Planetary Science Letters, 70, 221–236.

Groenewald, C., & Macey, P.H., 2020. Revision of 2918CC Silwerfontein. 1:50 000 scale geological map field sheet, Council for Geoscience, Bellville, South Africa.

Grohmann, C.H., Campanha, G.A.C., & Correia, A.E. 2017. OpenStereo 2.0b Software.

Harlov, D. E., 2012. The potential role of fluids during regional granulite-facies dehydration in the lower crust. Geoscience Frontiers, 3(6), 813-827.

Harris, N.B.W., Pearce, J.A. & Tindle, A.G., 1986. Geochemical characteristics of collision-zone magmatism. In: Coward M.P. and Reis A.C. (eds.), Collision tectonics. Special publication geological society. 19, 67-81.

Hartnady, C., Joubert, P., & Stowe, C., 1985. Proterozoic crustal evolution in southwestern Africa: Episodes, v. 8, p. 236-244.

Herron, M.M., 1988. Geochemical classification of terrigenous sands and shales from core or log data. Journal of Sedimentary Research, 58, 820–829.

Hoffmann, D., 1993. Aspects of geology, geochemistry and metamorphism of the Lower Orebody, Broken Hill deposit, Aggeneys: unpublished Masters thesis, Cape Town: University of Cape Town.

Holcombe, R., 2017. GEOrient 9.5.1 Software. School of Earth Sciences, The University of Queensland, Australia, www.holcombe.net.au/software.

Jack, A.M., 1980. The geology of western Namaqualand. Bulletin Precambrian Research Unit, University of Cape Town 29, 173.

Joubert, P., 1971. The regional tectonism of the gneisses of part of the Namaqualand Metamorphic Complex. Bulletin of the Precambrian Research Unit, University of Cape Town, 10, 220 pp.

Joubert, P., 1984. The tectonic subdivision of the Richtersveld and Bushmanland Subprovinces and the evolution of the western Namaqua Province. Cape Town, Precambrian Research Unit, University of Cape Town, pp. 33-34.

Joubert, P. 1986a. The Namaqualand Metamorphic Complex — A summary. In: (C.R. Anhaeusser and S. Maske, Eds). Mineral Deposits of Southern Africa: Vol. II. pp. 1395– 1420.

Joubert, P., 1986b. Namaqualand- a model of Proterozoic accretion?. Transactions of the Geological Society of South Africa, Volume 89, pp. 79-96.

Kisters, A.F.M., Charlesworth, E.G., Gibson, R.L., & Anhaeusser, C.R., 1996. The relationship between antiformal and monoclinal steep structures in the Okiep Copper District, Namaqualand: A case study, South African Journal of Geology, 99(2), 185-195.

Kroner, A., 1968. The gneiss-sediment relationships north-west of Vanrhynsdorp, Cape Province. Bulletin Precambrian Research Unit, University of Cape Town, 3.

Lipson, R.D., 1978. Some aspects of the geology of part of the Aggeneysberg and surroundings gneisses, Namaqualand: unublished Masters thesis, Johannesburg: University of Witwatersrand.

Lipson, R.D., 1990. Lithogeochemistry and origin of metasediments hosting the Broken Hill deposit, Aggeneys, South Africa, and implications for ore genesis: unpublished Doctoral thesis, Cape Town: University of Cape Town.

Lombaard, A.P. & Schreuder, F.J.G., 1978. Distribution pattern and general geological features of steep structures, megabreccias and basic rocks in the Okiep Copper District. ln: Verwoerd, W.J. (Ed.), Mineralization in Metamorphic Terranes. Spec. Publ. geol. Soc. S. Aft, 4, 269-295.

Ludwig, K., 2003. Isoplot/Ex version 3.0: Geochronological toolkit for Microsoft Excel., Berkley: Geochonology Center.

Macey, P.H., Siegfried, H.P., Minnaar, H., & Almond, J., 2011. The Geology of the Loeriesfontein Area. Explanation to Sheet 3018, Scale: 1:250 000. Council for Geoscience.

Macey, P.H., Bailie, R.H., Miller, J.A., Thomas, R.J., De Beer, C., Frei, D., & Le Roux, P.J., 2018. Implications of the distribution, age and origins of the granites of the Mesoproterozoic Spektakel Suite for the timing of the Namaqua Orogeny in the Bushmanland Subprovince of the Namaqua-Natal Metamorphic Province, South Africa. Precambrian Research. 312, 68–98.

Marais, J.A.H., Agenbacht, A.L.D., Prinsloo, M., & Basson, W.A., 2001. The geology of the Springbok area. Explanation to sheet 2916 Springbok, Scale 1:250 000, 103 pp.

Mattison, J. M., 2010. Analysis of the relative decay constants of ^{235}U and ^{238}U by multi-step CA-TIMS measurements of closed-system natural zircon samples. Chemical Geology, Volume 275, pp. 186-198.

McCarthy, T.S., 1976. Chemical interrelationships in a low-pressure granulitic terrain in Namaqualand, South Africa, and their bearing on granitic genesis and the composition of the lower crust. Geochimica et Cosmochimica Acta 40, 1057–1068.

McClung, C., 2006. Basin Analysis of the Mesoproterozoic Bushmanland Group of the Namaqua Metamorphic Province, South Africa. Ph.D. Thesis, University of Johannesburg, Johannesburg, South Africa.

McDonough, W. F. & Sun, S., 1995. The composition of the Earth. Chemical Geology 120, 223-253.

McLennan S. M., 1989. Rare earth elements in sedimentary rocks: Influence of provenance and sedimentary processes. Review of Mineralogy, 21, 169-200.

McStay, J.H., 1991. Granulite-facies metamorphism, fluid buffering and partial melting in the Buffels River area of the Namaqualand Metamorphic Complex, South Africa, Cape Town: Ph.D. Thesis, Department of Geology and Mineralogy, University of Cape Town.

Moen, H.F., 1999. The Kheis Tectonic Subprovince, South Africa: a lithostratigraphic perspective. South African Journal of Geology, Volume 102, pp. 27-42.

Moen and Toogood, 2007

Moore, J.M., 1989. A comparative study of metamorphosed supracrustal rocks from Western Namaqualand Metamorphic Complex. Bulletin of the Precambrian Research Unit, University of Cape Town, 37, 370 pp.

Nasdala, L., Hofmeister, W., Norberg, N., Martinson, J. M., Corfu, F., Dörr, W., Kamo, S. L., Kennedy, A. K., Kronz, A., Reiners, P. W., Frei, D., Kosler, J., Wan, Y., Götze, J., Häger, T., Kröner, A., & Valley, J. W., 2008. Zircon M257 - A homogeneous natural reference material for the ion microprobe U-Pb analysis of zircon. Geostandards and Geoanalytical Research, 32(3), 247-265.

Nicolaysen, L.O. & Burger, A.J., 1965. Note on an extensive zone of 1000 million-year old metamorphic and igneous rocks in Southern Africa. Sciences de la Terre, 10, pp. 497-518.

Nowicki, T.E., Frimmel, H.E. & Waters, D.J., 1995. The occurence of osumilite in pelitic granulites of the Namaqualamd Metamorphic Complex, South Africa. South African Journal of Geology, Volume 98, pp. 191-201.

Paizes. P. E., 1975. The geology of an area between Vaalkop and Aggeneys in the vicinity of Pofadder, north-western Cape Province. M.Sc. thesis (unpublished), University of Witwatersrand.

Peccerillo, A. & Taylor S.R., 1976. Geochemistry of Eoscene calc-alkaline volcanic rocks from the Kastamonu area, northern Turkey. Contributions to Mineralogy and Petrology, 58, 63-81.

Petterson, A., 2008. Mesoproterozoic crustal evolution of Southern Africa, Sweden: University of Gothenburg.

Pin , C., Briot, D., Bassin, C. & Poitrasson, F., 1994. Concomittant separation of strontium and samarium-neodymium for isotopic analysis in silicate samples, based on specific extraction chromatography. Analytica Chimica Acta, Volume 298, pp. 209-217.

Pin, C. & Zalduegui, J. F. S., 1997. Sequential separation of light rare-earth elements, thorium and uranium by miniaturized extraction chromatography: Application to isotopic analyses of silicate rocks. Analytica Chimica Acta, 339(1-2), pp. 79-89.

Raith, J.G. & Harley, S.L., 1998. Low-P/high-T metamorphism in the Okiep copper district, western Namaqualand, South Africa. Journal of Metamorphic Geoloy, Volume 16, pp. 281-305.

Raith, J.G. & Meisel, T., 2001. Metabasites along the amphibolite-granulite facies transition in the Okiep Copper district, South Africa. South African Journal of Geology, Volume 104, pp. 77-100.

Raith, J.G., Cornell, D.H., Frimmel, H.E. & De Beer, C.H., 2003. New Insights into the Geology of the Namaqua Tectonic Province, South Africa, from Ion Probe Dating of Detrital and Metamorphic Zircon. The Journal of Geology, Volume 11, pp. 347-366.

Ramsay, J.G. & Huber, M.I., 1988. The Techniques of Modern Structural Geology. Volume 2: Folds and Fractures.

Reid, D.L., 1977. Geochemistry of Precambrian igneous rocks in the lower Orange River region. Precambrian Research Unit Bulletin, University of Cape Town, Volume 22, p. 397.

Robb, L.J., Armstrong, R.A., & Waters, D.J., 1999. The history of granulite facies metamorphism and crustal growth from single zircon U–Pb geochronology: Namaqualand, South Africa. Journal of Petrology, 40, 1747– 1770.

Rozendaal, A., 1975. The geology of Gamsberg, Namaqualand, South Africa: unpublished Masters thesis, Stellenbosch: University of Stellenbosch.

Ryan, P.H.J., Lawrence, A.L., Lipson, R.D., Moore, J.M., Patterson, A., Stedman, D.P. & Van Zyl, D., 1986. The Aggeneys base metal sulphide deposits, Namaqualand District. In: Anhaeusser, C.R. & Maske, S., (eds) Mineral deposits of southern Africa. Geological Society of South Africa II, pp 1447-1474.

SACS, 1980. Stratigraphy of South Africa. Pretoria: South African Committee for Stratigraphy.

Schmitz, Mark., 2004. Lower crustal granulite formation during Mesoproterozoic Namaqua-Natal collisional orogenesis, southern Africa. South African Journal of Geology. 107. 261-284.

Slama, J., Kosler, J., Condon, D.J., Crowley, J.L., Gerdes, A., Hanchar, J.M., Horstwood, M.S.A., Morris, G.A., Nasdala, L., Norberg, N., Schaltegger, U., Schoene, B., Tubrett, M.N., & Whitehouse, M.J., 2008. Plesovice zircon-a new natural reference material for U-Pb and Hf isotopic microanaylisis.. Chemical Geology, Volume 249, pp. 1-35.

Stacey, J.S. & Kramers, J.D., 1975. Approximation of terrestrial lead isotope evolution by a two stage model. Earth and Planetary Science Letters. 26, 207–221.

Steiger, R.H. & Jager, E., 1977. Subcommission on geochronology: Convention on the use of decay constants in geo- and cosmochronology. Earth and Planetary Sciencce Letters, 36(3), pp. 359-362.

Streckeisen, A., 1974. Classification and Nomenclature of Plutonic Rocks. Geologische Rundschau, 63, 773-786.

Sun, S.S., & McDonough, W.F., 1989. Chemical and isotopic systematics of oceanic basalts: Implications for mantle composition and processes. In: Saunders, AD. & Norry, M.J. (eds). Magmatism in ocean basins. Geological Society of London, Special Publication, 42, 313-345.

Taylor, S.R. & McLennan, S.M., 1995. The geochemical evolution of the continental crust. Reviews in Geophysics, 33: 241-265.

Thomas, C., 2001. 2916A Springbok Map sheet, Pretoria: Precambrian Research Unit.

Thomas, R.J., Cornell, D.H., Moore, J.M. & Jacobs, J., 1994. Crustal evolution of the Namaqua-Natal metamorphic prvince, Southern Africa. South African Journal of Geology, Volume 97, pp. 8-14.

Thomas, R., 2020. Revision of 2918CD Gamoep. 1:50 000 scale geological map field sheet, Council for Geoscience, Bellville, South Africa.

Van Niekerk, H.S., 2006. The origin of the Kheis Terrain and its relationship with the Grenvillian Namaqua Province in southern Africa, Johannesburg: unpublished Doctoral thesis, University of Johannesburg.

Von Backström, J., 1964. The Geology of an Area around Keimoes, Cape Province, with Special Reference to Phacoliths of Charnockitic Adamellite- Porphyry; Memoir of the Geological Survey of South Africa 53: Pretoria, South Africa, p. 218.

Waters, D.J., 1986. Metamorphic zonation and thermal history of pelitic gneisses from western Namaqualand, South Africa. South African Journal of Geology, Volume 89, pp. 97-102.

Waters, D.J., 1989. Metamorphic evidence for the heating and cooling path of Namaqualand granulites, in : Daly, J.S., Cliff, R.A., and Yardley, B.W.D., eds., Evolution of metamorphic belts. Geological Society Special Publications, Volume 43, pp. 357-363.

Waters, D. J. (1990) Thermal history and tectonic setting of the Namaqualand granulites, southern Africa: clues to Proterozoic crustal development. In: Vielzeuf, D. and Vidal, P. (eds.), Granulites and crustal evolution. Kluwer Academic Publishers, Netherlands, pp. 243-256.

Waters, D.J., 1991. Hercynite-quartz granulite: phase relations, and implications for crustal processes. European Journal of Mineralogy, Volume 3, pp. 367-386.

Wiedenbeck, M., Allé, P., Corfu, F., Griffin, W.L., Meier, M., Oberli, F., Von Quadt, A., Roddick J.C., & Spiegel, W., 1995. Three natural zircon standards for U-Th-Pb, Lu-Hf, trace-element and REE analyses. Geostandards Newsletter, Volume 19, pp. 1-23.

Wilson, M., 1989. Igneous Petrogenesis: A Global Tectonic Approach. Unwin Hyman, London, 466 p.

Yuhara, M., Kagami, H., & Tsuchiya, N., 2001. Rb-Sr and Sm-Nd systematics of granitic and metamorphic rocks in the Namaqualand Metamorphic Complex, South Africa: Implications for evolution of marginal part of Kaapvaal craton. Mem. Natl Inst. Polar Res., Spec. Issue, 55, 127-144, 2001.

Yuhara, M., Miyazaki, T., Ishioka, J., Suzuki, S., Kagami, H., & Tsuchiya, N., 2002. Rb-Sr and Sm-Nd Mineral Isochron Ages of the Metamorphic Rocks in the Namaqualand Metamorphic Complex, South Africa. Gondwana Research, Volume 5, pp. 771-779.

Zelt, G.A., 1980. Granulite-facies metamorphism in Namaqualand, South Africa. Precambrian Research, Volume 13, pp. 253-274.

Zindler, A. & Hart, S.R., 1986. Chemical Geodynamics. Annual Review of Earth and Planetary Sciences, 14, 493–571.

UNIVERSITY *of the*

WESTERN CAPE
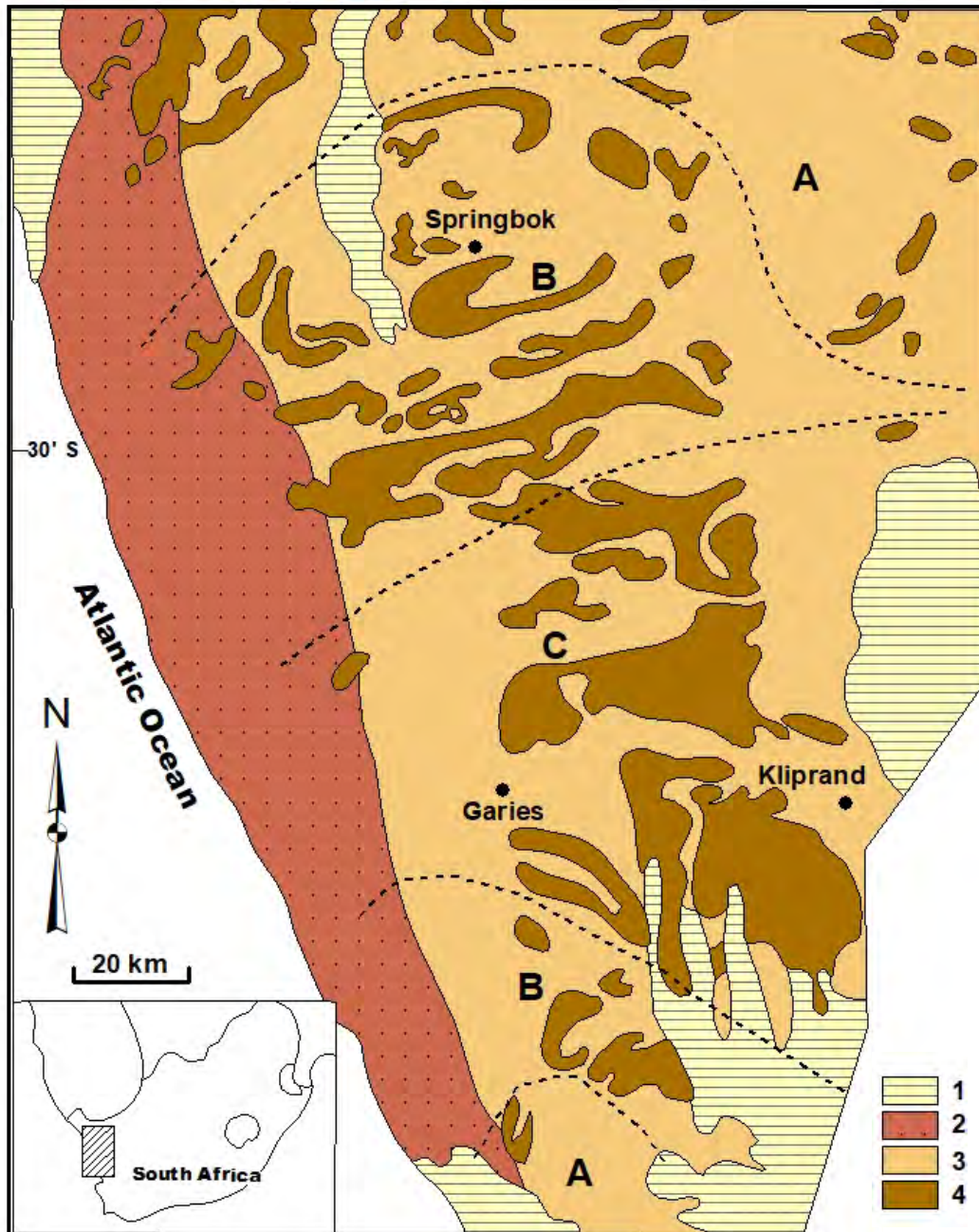
Appendices

Appendix A

Figure A1 A geological map of the western Namaqualand Metamorphic Province (modified after Waters (1986) and Yuhara et al. (2002)). 1: Late Precambrian to early Palaeozoic Nama Group, 2: reworked Namaqua Metamorphic Province during the Pan African event, 3: the intrusive rocks of granitic composition of the Namaqua Metamorphic Province, 4: supracrustal enclaves of the Namaqua Metamorphic Province. A: upper amphibolite facies zone, B: lower granulite facies zone, C: upper granulite facies zone.
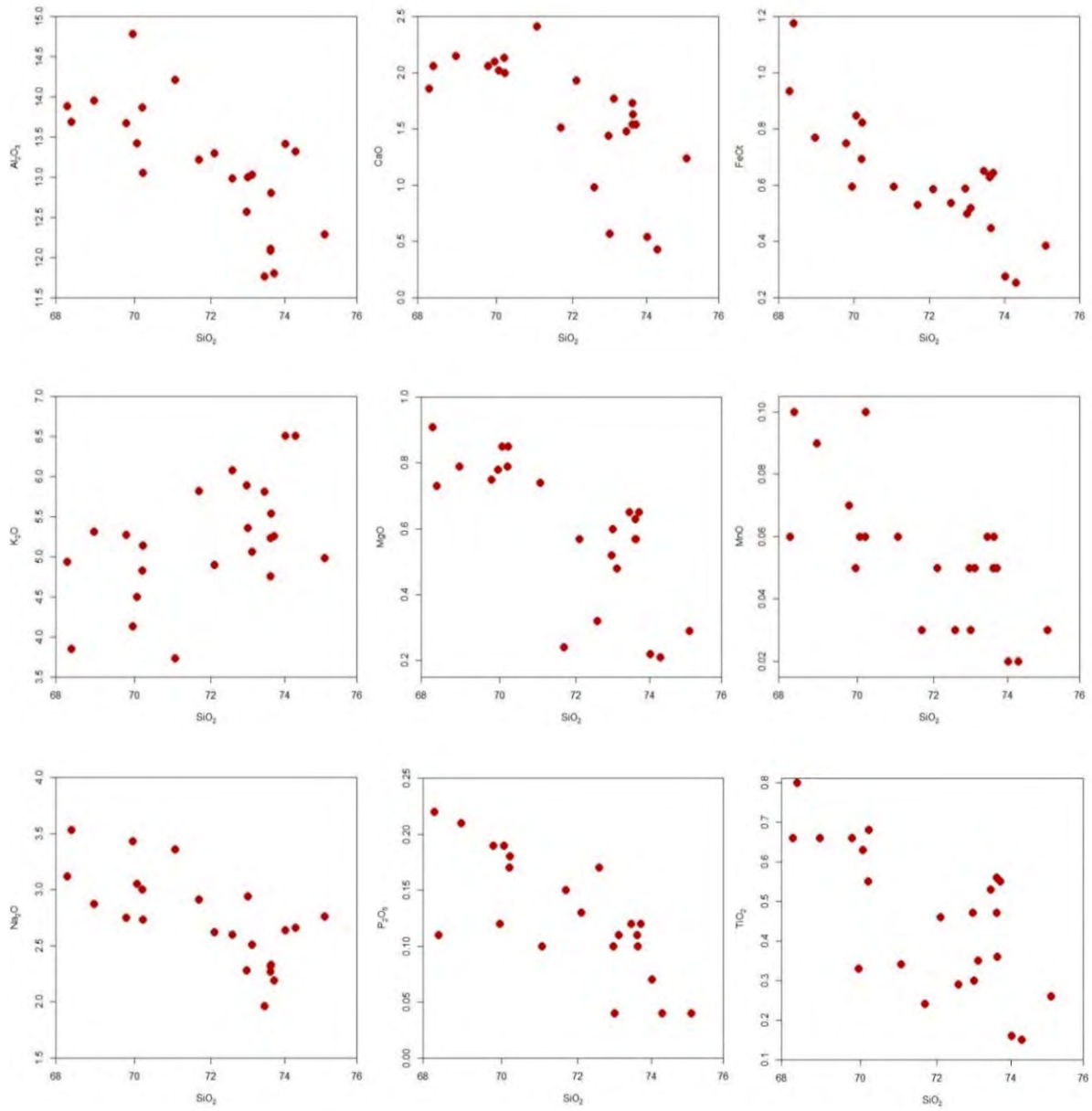
Figure A2 Harker diagram of major elements vs. SiO_2 for the Biotite and Leucocratic augen gneisses of the Buffels River shear zone.
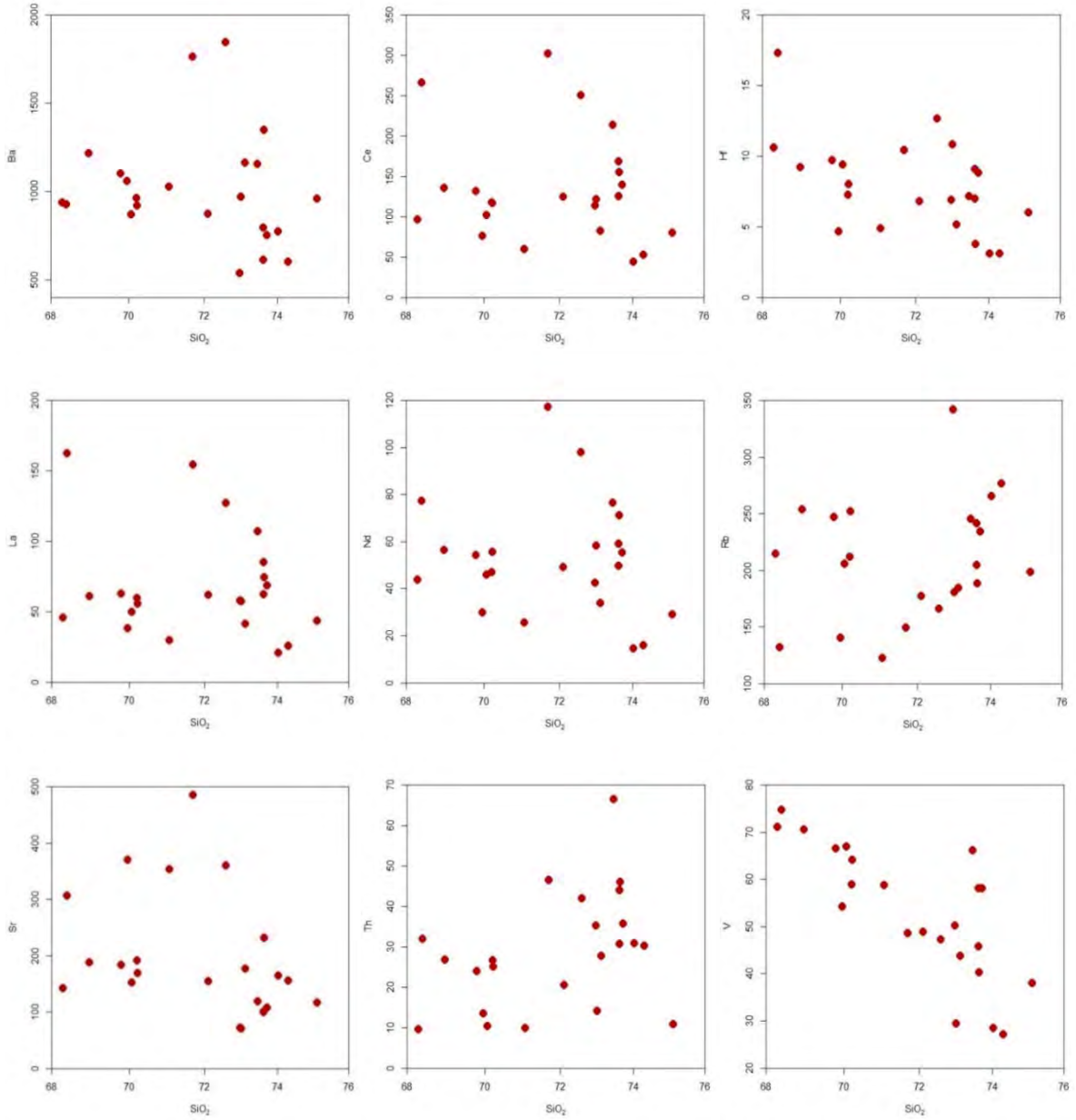
Figure A3 Harker diagram of trace elements vs. SiO_2 for the Biotite and Leucocratic augen gneisses of the Buffels River shear zone.
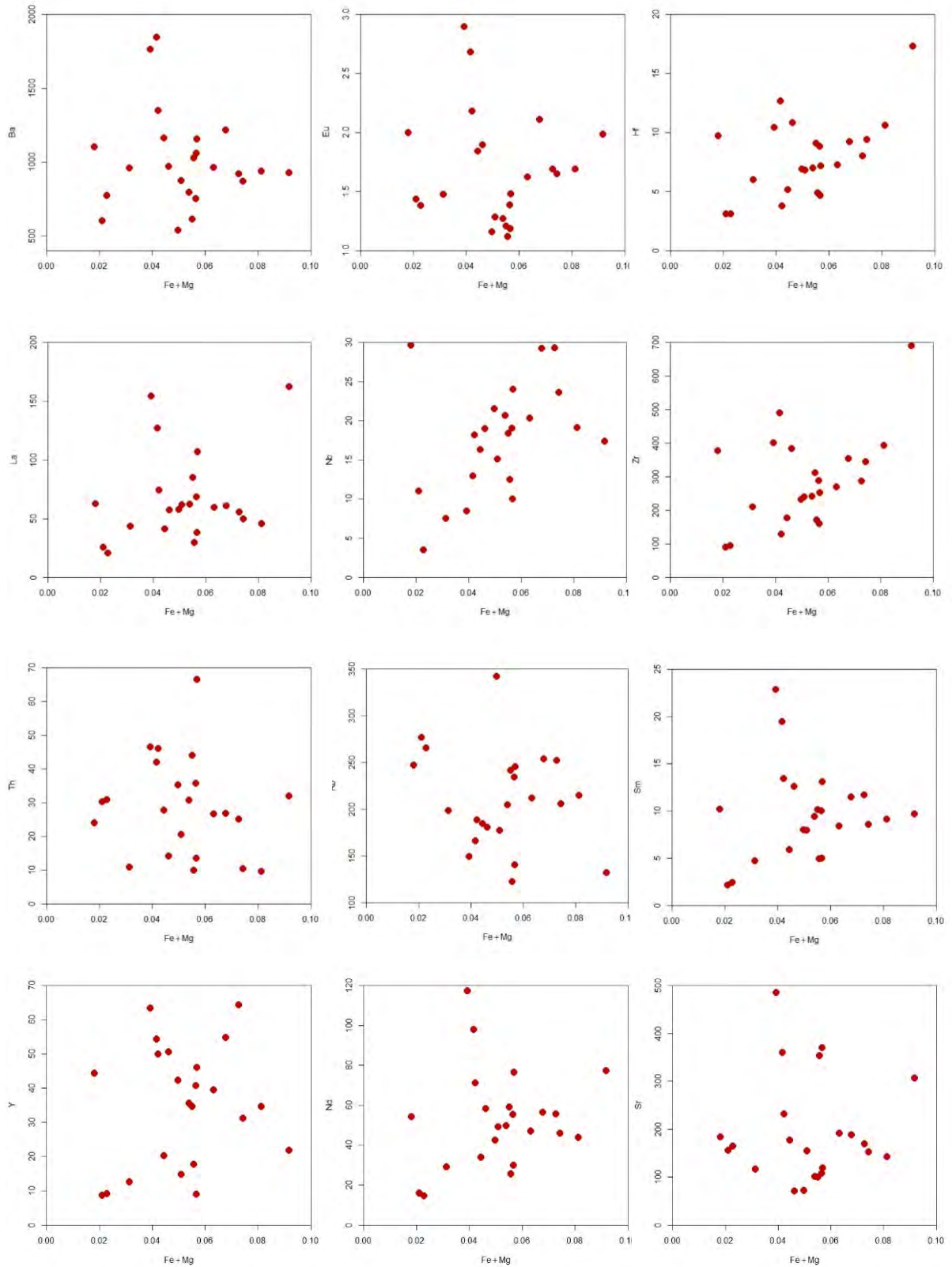
83

Figure A4 Maficity plots of trace elements vs. Fe+Mg for the Biotite and Leucocratic augen gneisses of the Buffels River shear zone.
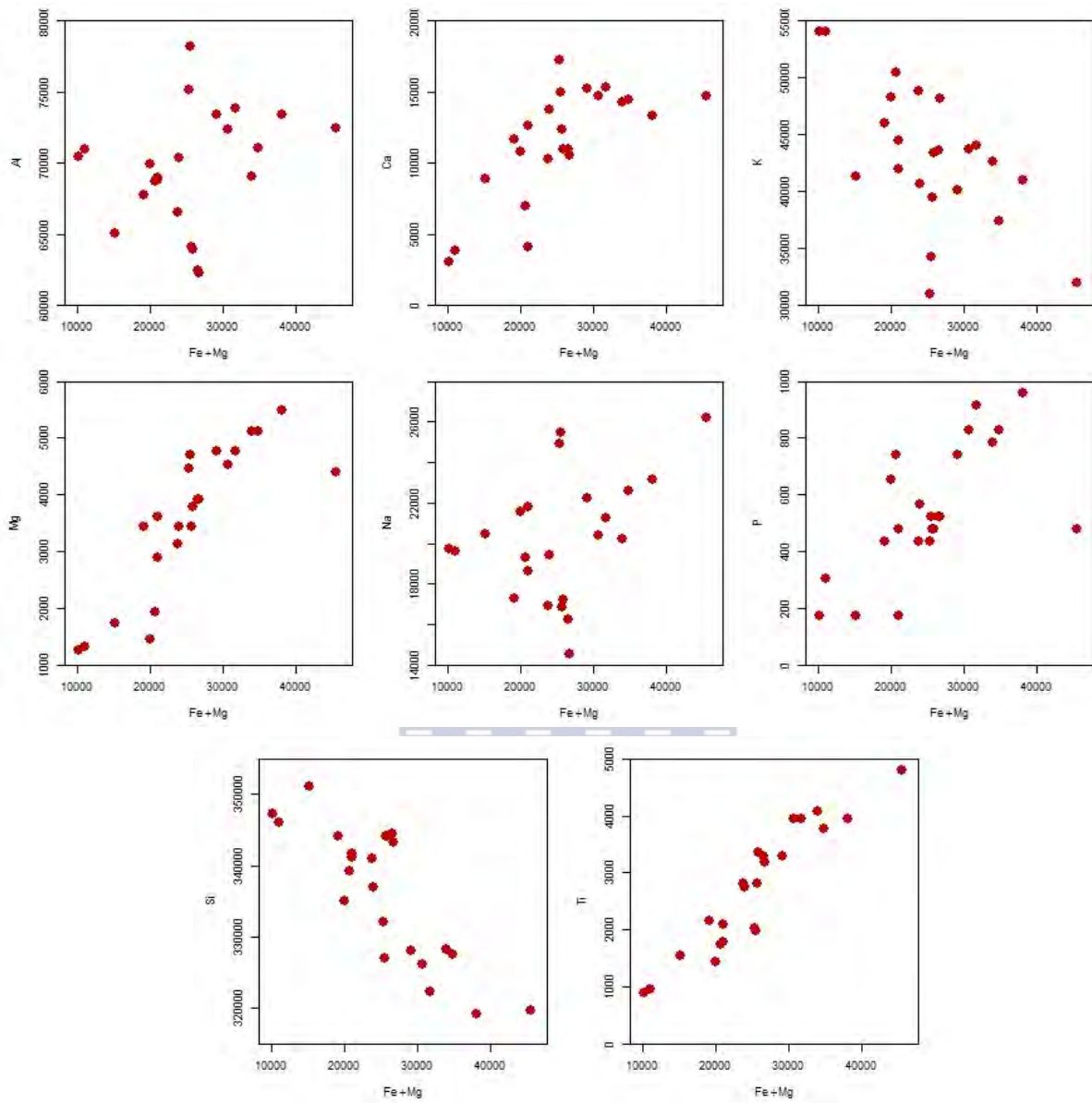
84

Figure A5 Maficity plots of ppm concentrations of the major and minor elements vs. Fe+Mg for the Biotite and Leucocratic augen gneisses of the Buffels River shear zone.
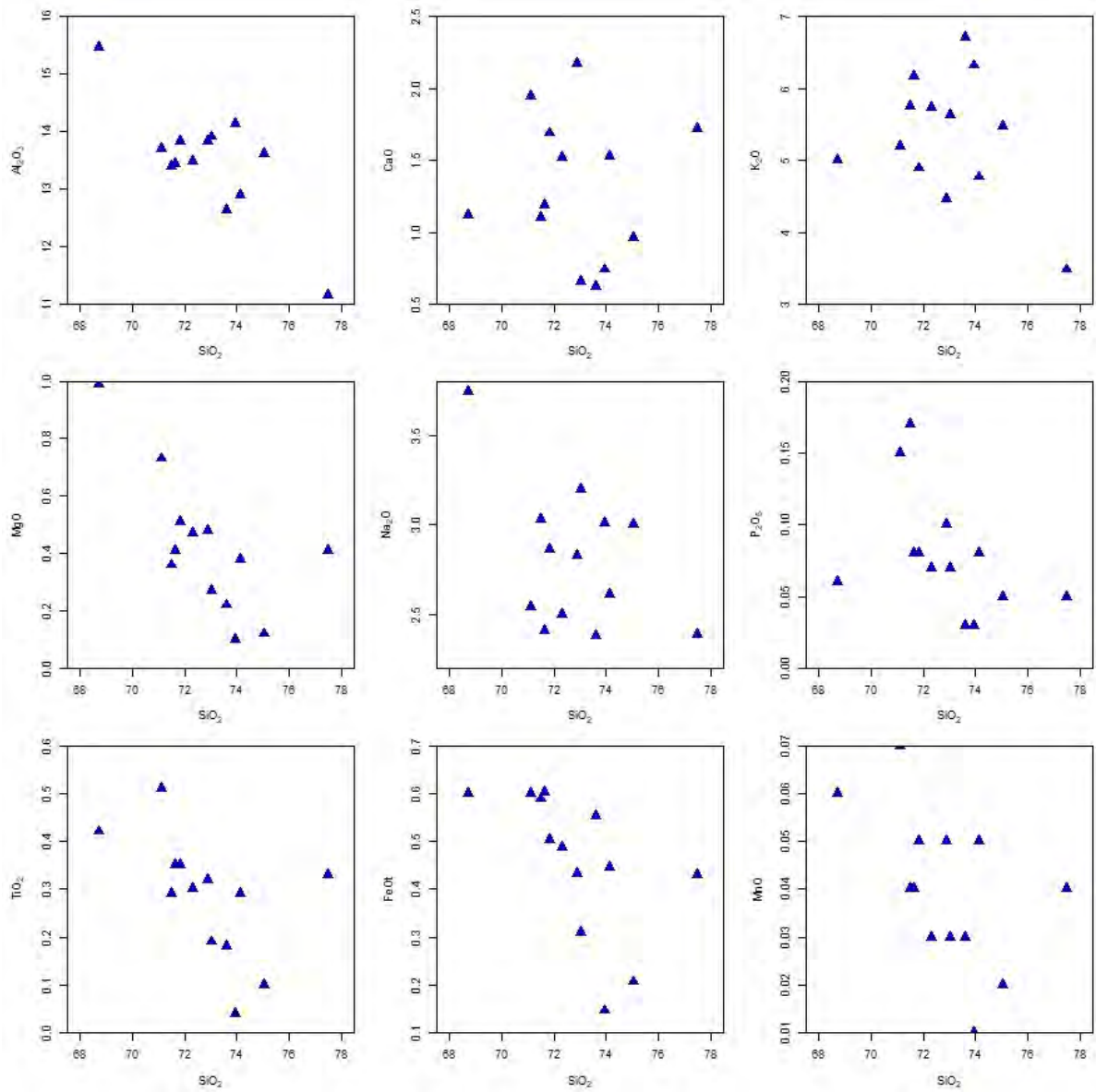
Figure A6 Harker diagram of major elements vs. SiO_2 for the Rooiplatklip Gneiss of the Buffels River shear zone.
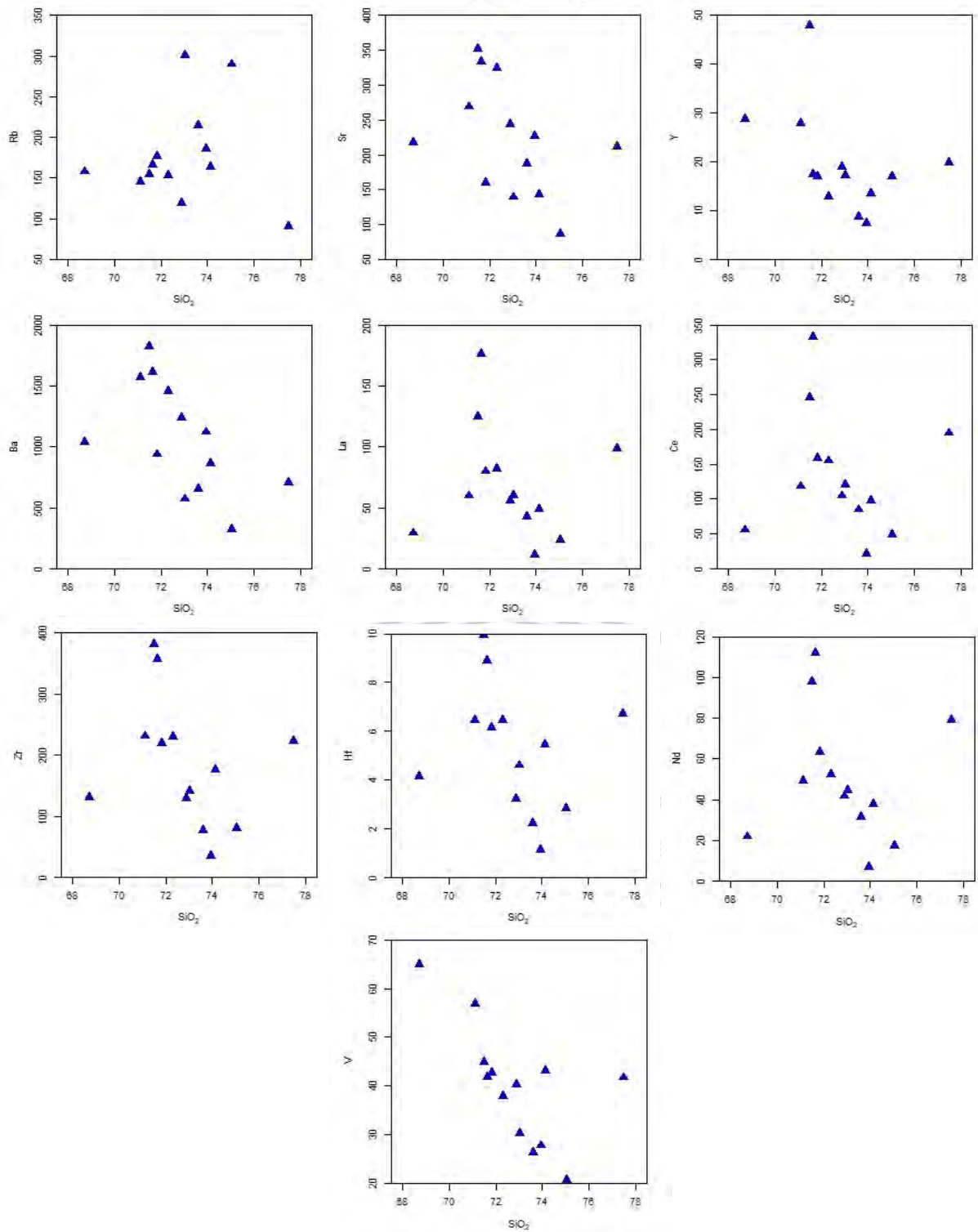
Figure A7 Harker diagram of trace elements vs. SiO_2 for the Rooiplatklip Gneiss of the Buffels River shear zone.
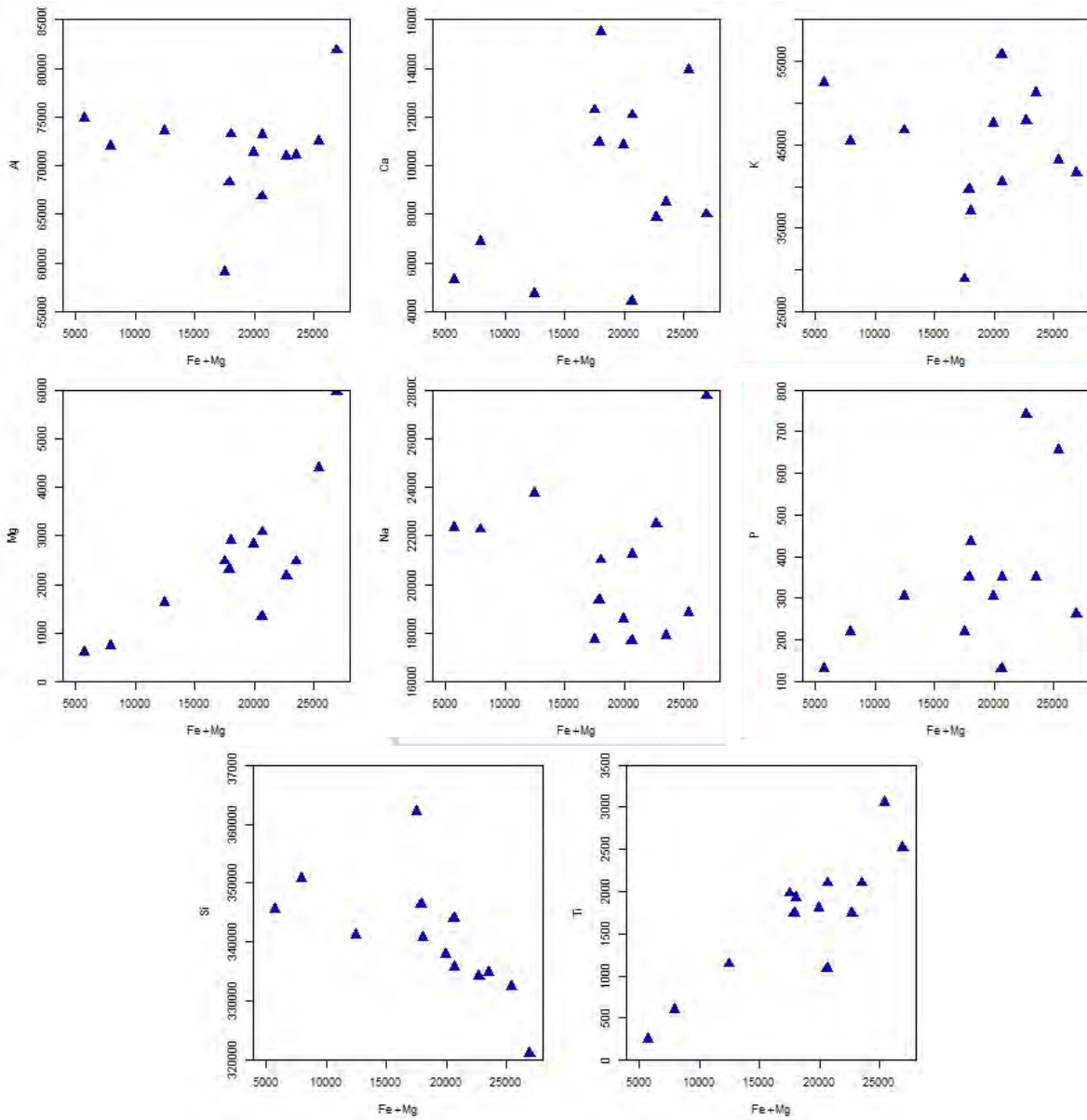
Figure A8 Maficity plots of ppm concentrations of major and minor elements vs. Fe+Mg for the Rooiplatklip Gneiss of the Buffels River shear zone.
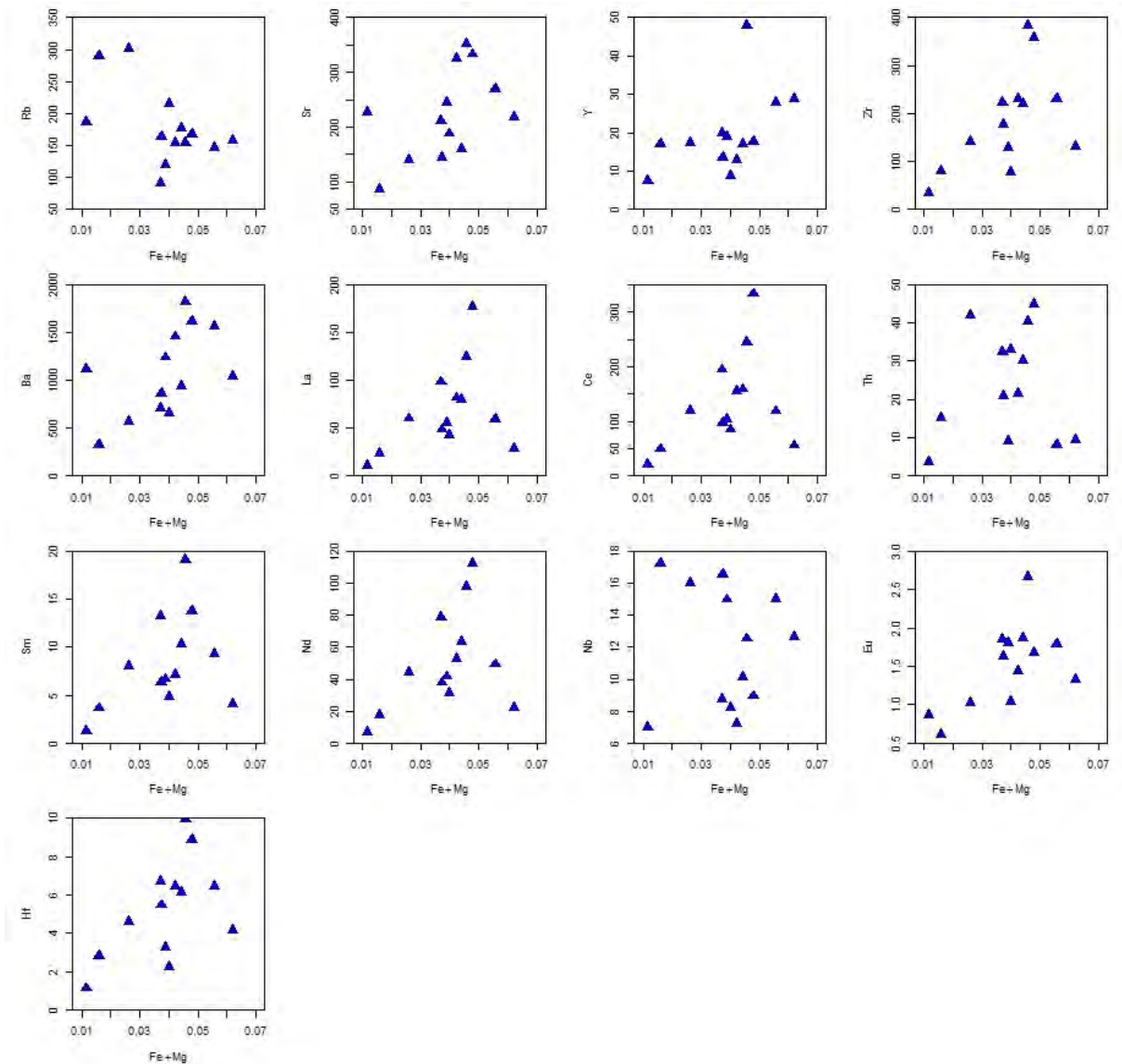
Figure A9 Maficity plots of trace elements vs. Fe+Mg for the Rooiplatklip Gneiss of the Buffels River shear zone.

89
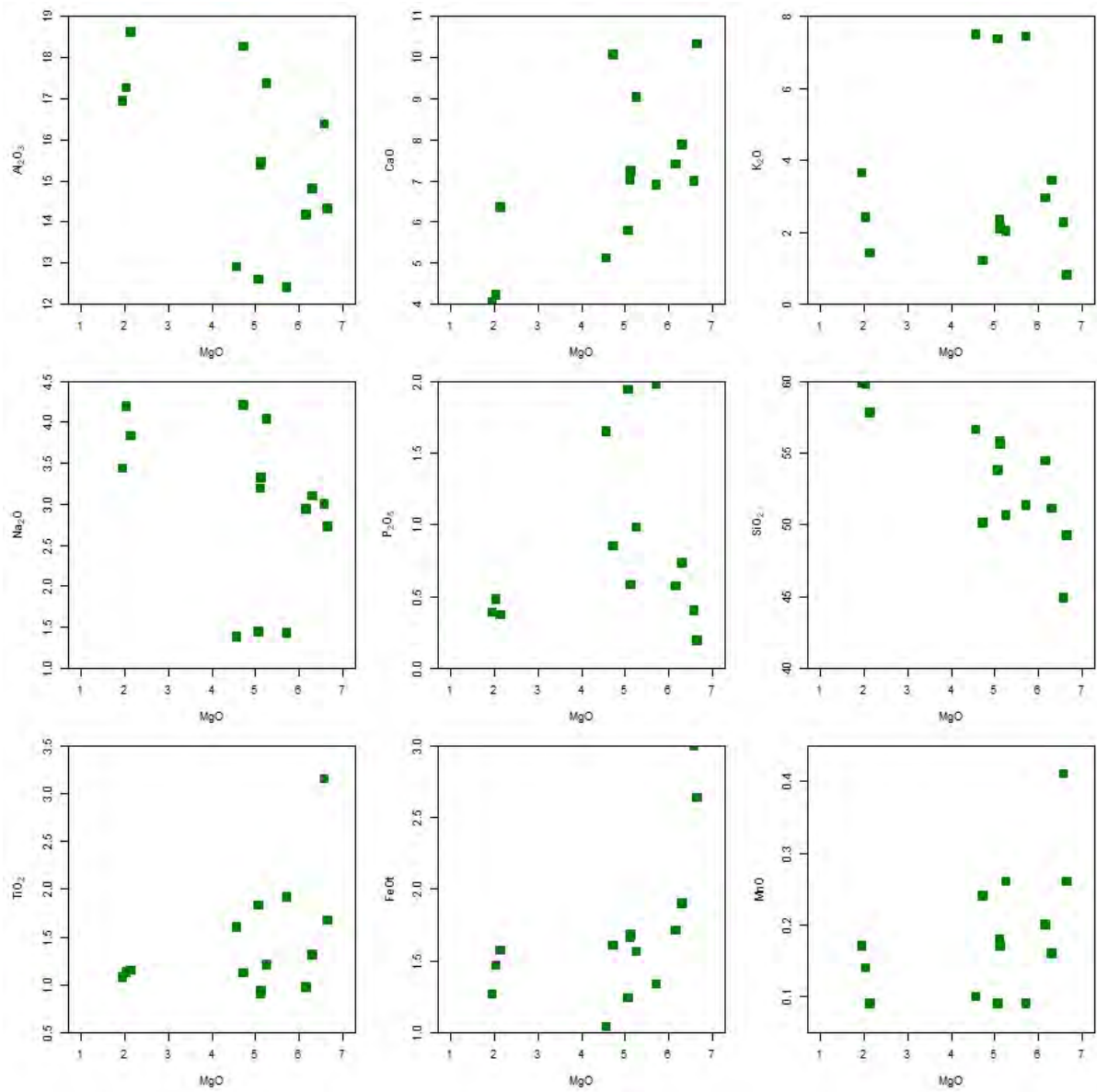
Figure A10 Binary plots of major elements vs. MgO for the mafic rocks of the Buffels River shear zone.
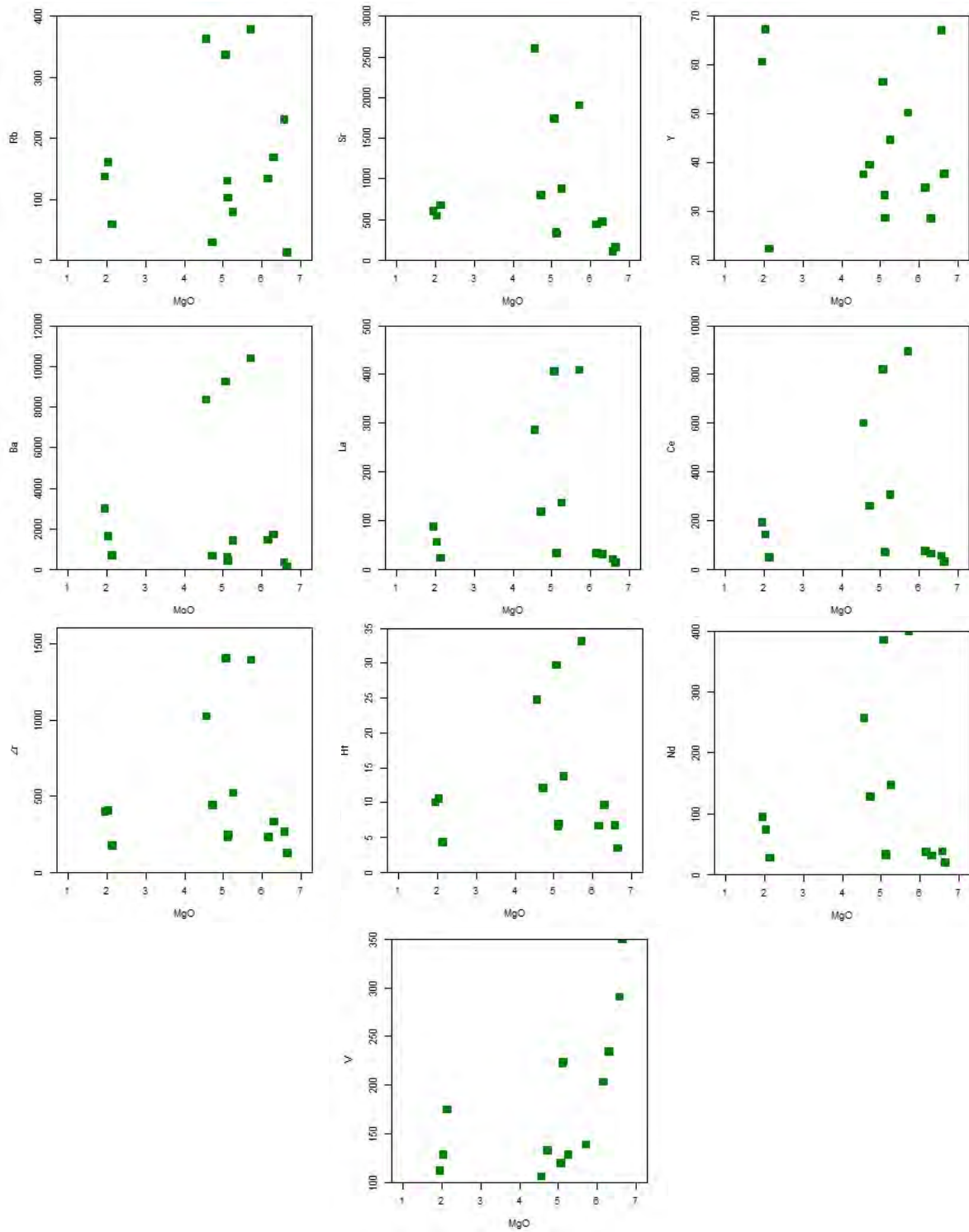
Figure A11 Binary plots of trace elements vs. MgO for the mafic rocks of the Buffels River shear zone.
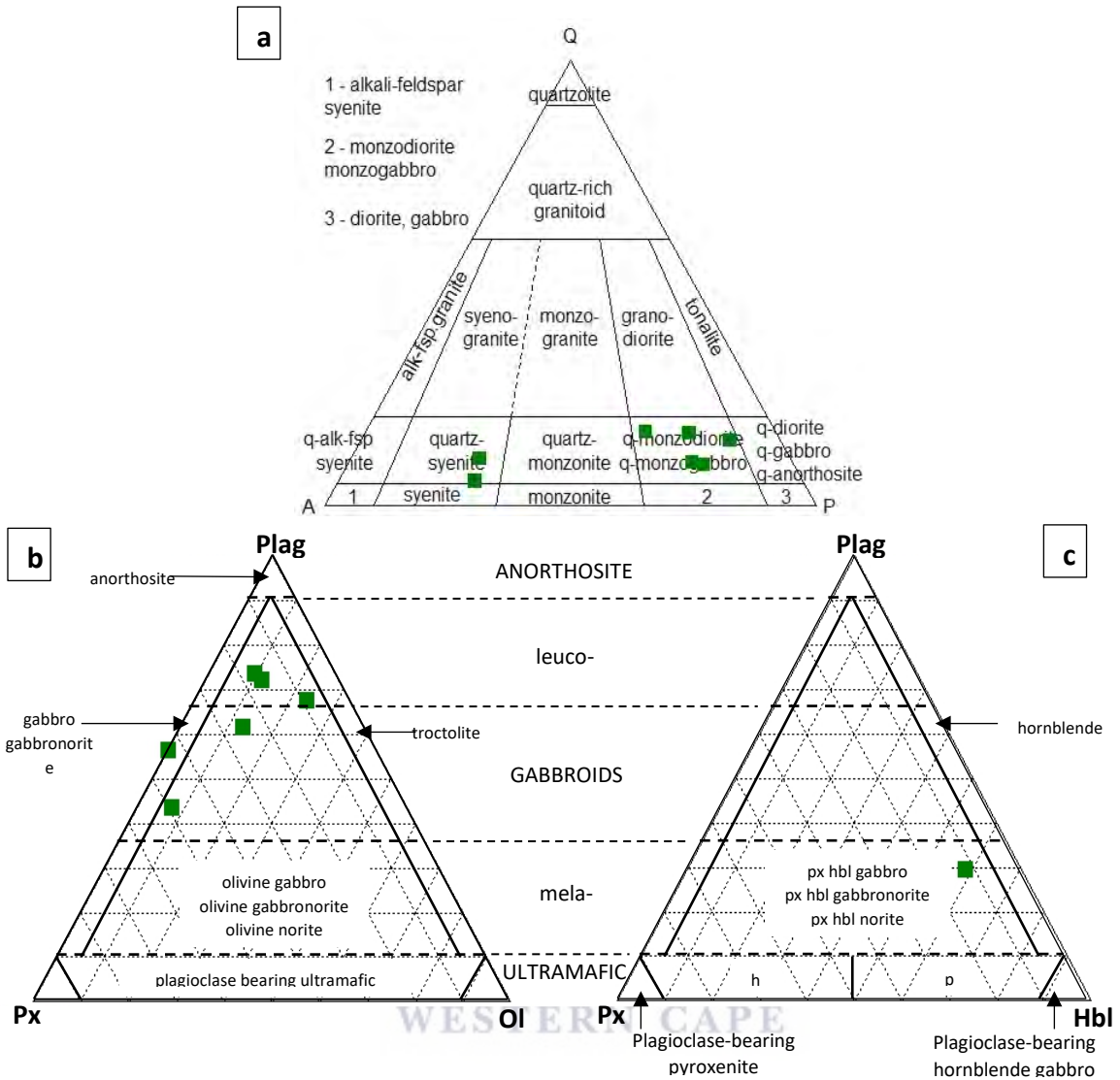
Figure A12 (a) The monzodiorite/monzogabbro and quartz syenite classification of the mafic magmatic rocks are represented in the QAPF diagram utilizing the CIPW norm (Streckeisen, 1974). The mafic granulites are further subdivided using the IUGS mafic rock classification ternary diagram seen in **(b)** and **(c)**.
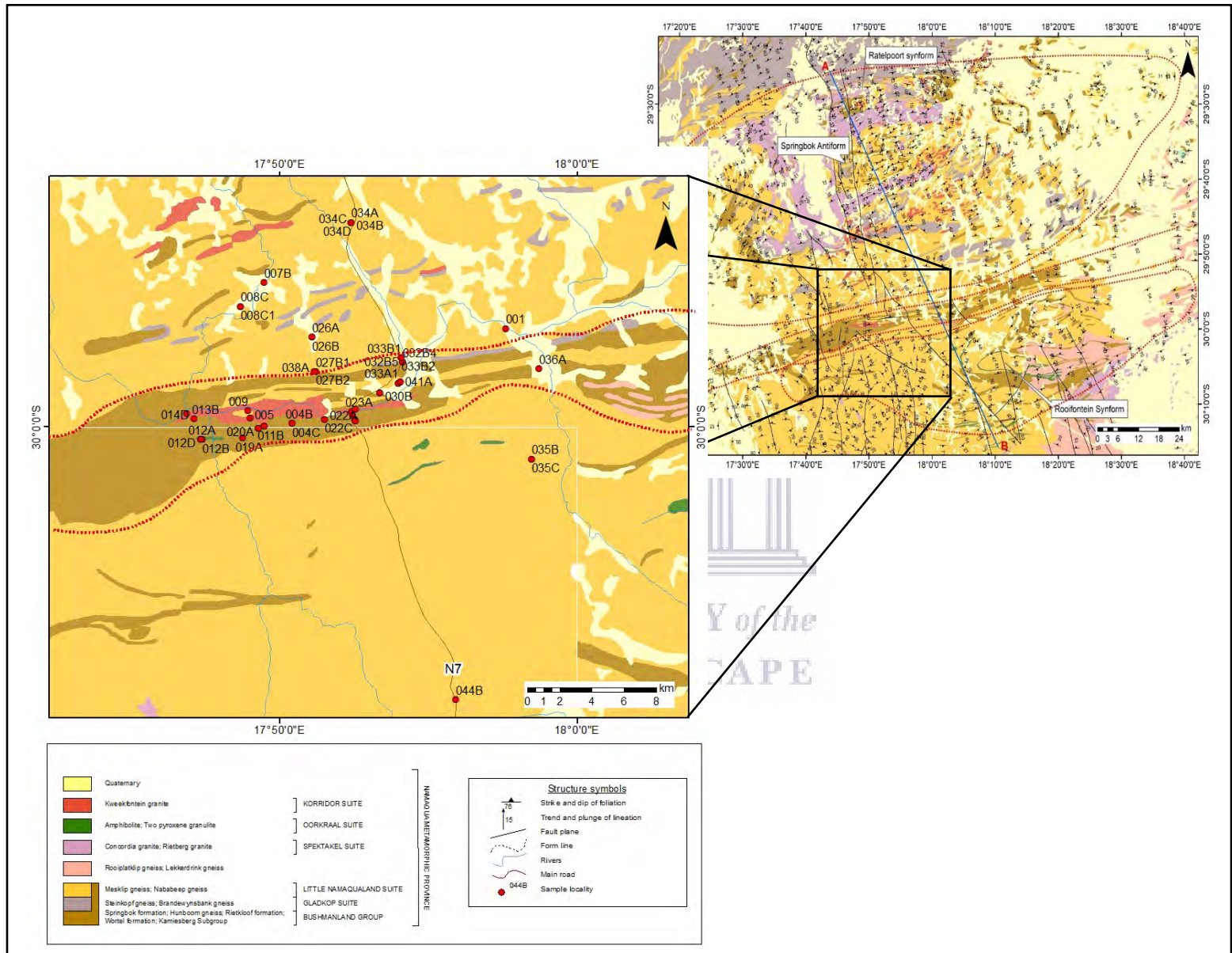
Figure A13 Sample location map along the Buffels River shear zone.
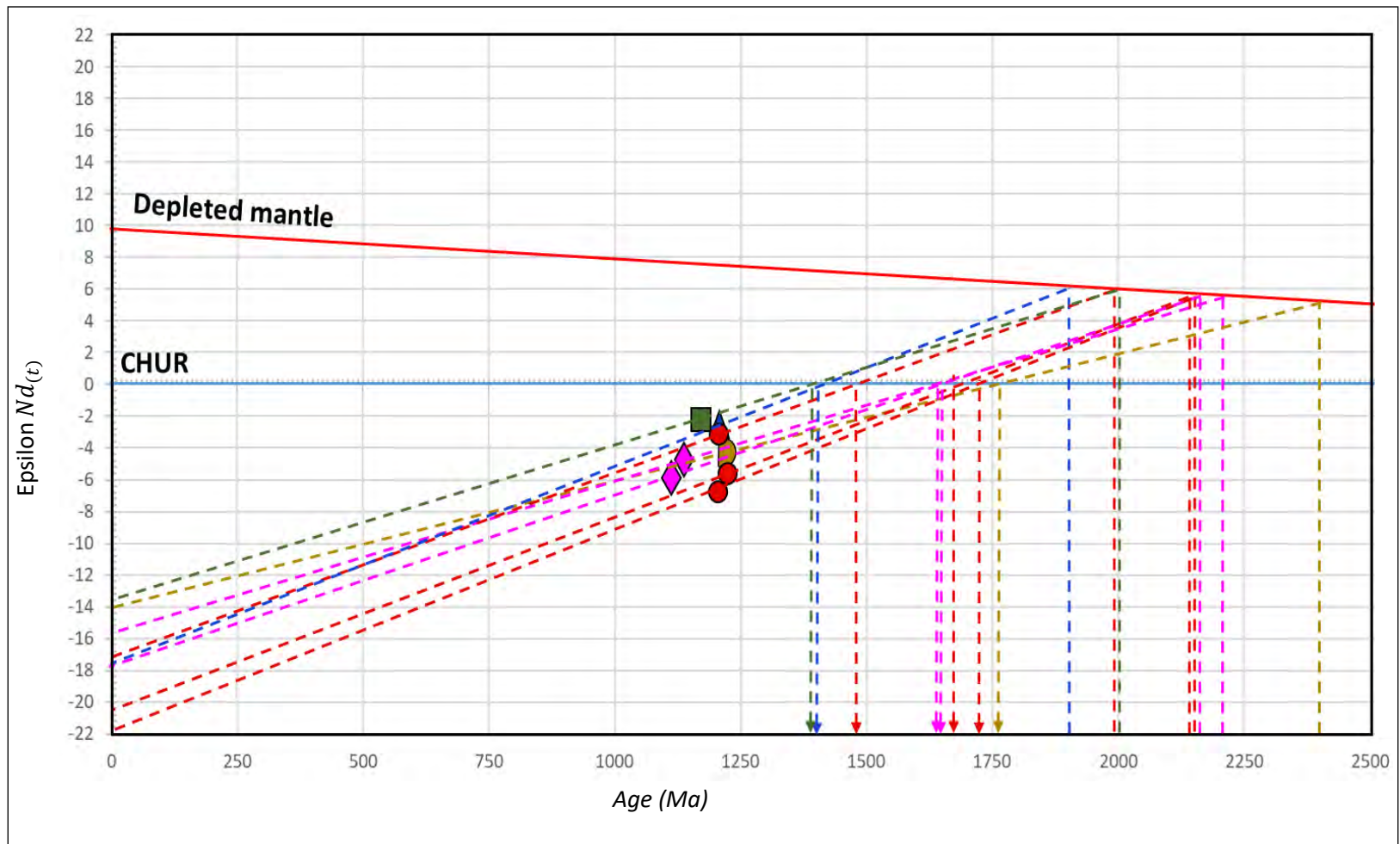
Figure A14 Initial ƐNd(t) vs. age plot for all of samples collected from the BRSZ area. Symbols become obscured by the dashed growth lines running through them. Red circle – Mesklip gneiss, Brown half circle – garnet-biotite-quartz-sillimanite semi-pelitic gneiss, blue triangle- leucogranitic gneiss, pink diamond- Hunboom gneiss and green square – amphibolite.

94
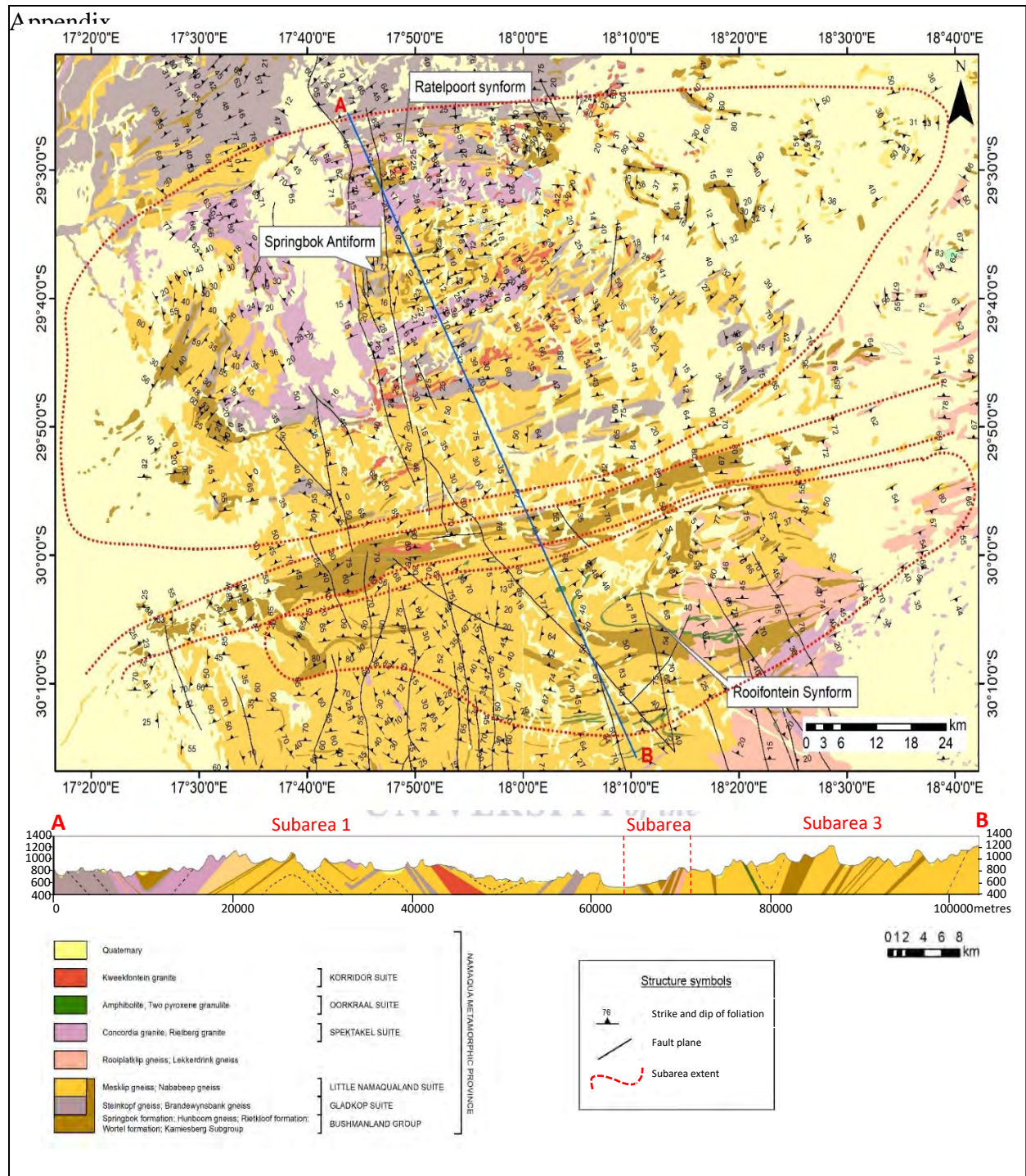
Figure A15 Regional geological map of the study area (BRSB) including the northern and southern dome and basin structures respectively. The red dashed lines enclose the subareas from north to south namely Subareas 1, 2 and 3. The cross section is drawn from north to south and is indicated on the geological map by a blue line labelled A – B.

95

Appendix B

Table B1 Whole-rock geochemistry analysis for 56 samples along and around the BRSZ.

| Sample number	Lithology	Stratigraphic Unit	Latitutde	Longitude	SiO2	Al2O3	CaO	K2O	Cr2O3	Fe2O3	MgO	MnO	Na2O	P2O5	TiO2
													MAJOR ELEMENTS		
001	Augen Gneiss	Mesklip Gneiss	-29,94500	17,95978	70,22	13,05	2,00	5,14	0,01	4,11	0,85	0,10	2,73	0,18	0,68
004B	Quartz monzodiorite	Oorkraal suite	-29,99800	17,84025	57,76	18,62	6,34	1,41	0,02	7,86	2,14	0,09	3,83	0,37	1,15
004C	Leucogranititc Gneiss	Rooiplatklip Gneiss	-29,99800	17,84025	77,47	11,16	1,72	3,48	0,02	2,15	0,41	0,04	2,39	0,05	0,33
005	Leucogranititc Gneiss	Rooiplatklip Gneiss	-29,99508	17,81661	73,00	13,91	0,66	5,63	0,01	1,55	0,27	0,03	3,20	0,07	0,19
007B	Augen Gneiss	Mesklip Gneiss	-29,91920	17,82447	72,10	13,30	1,93	4,90	0,01	2,93	0,57	0,05	2,62	0,13	0,46
008C	Olivine gabbronorite	Oorkraal suite	-29,93261	17,81117	51,32	12,39	6,90	7,44	0,03	6,69	5,72	0,09	1,43	1,98	1,91
008C1	Olivine gabbronorite	Oorkraal suite	-29,93261	17,81117	53,79	12,60	5,78	7,38	0,03	6,21	5,08	0,09	1,44	1,94	1,83
009	Biotite Gneiss	Hunboom Gneiss	-29,99106	17,81542	71,12	14,47	2,22	3,69	0,01	2,37	0,56	0,06	3,42	0,09	0,31
011A	Leucogranititc Gneiss	Rooiplatklip Gneiss	-29,99975	17,82458	74,12	12,90	1,53	4,77	0,01	2,23	0,38	0,05	2,61	0,08	0,29
011B	Leucogranititc Gneiss	Rooiplatklip Gneiss	-29,99975	17,82458	71,82	13,83	1,69	4,89	0,01	2,52	0,51	0,05	2,86	0,08	0,35
011C	Leuco-gabbro	Oorkraal suite	-29,99975	17,82458	44,86	16,37	6,99	2,26	0,04	14,99	6,58	0,41	3,00	0,40	3,15
012A	Grey Biotite Gneiss	Hunboom Gneiss	-30,00717	17,78972	67,72	14,84	2,67	2,14	0,02	6,06	2,00	0,06	3,08	0,06	0,81
012B	Grey Biotite Gneiss	Hunboom Gneiss	-30,00717	17,78972	66,16	14,87	2,64	2,65	0,02	6,93	2,40	0,06	2,82	0,05	0,85
012D	Leucogranititc Gneiss	Rooiplatklip Gneiss	-30,00703	17,78900	71,11	13,70	1,95	5,20	0,01	3,00	0,73	0,07	2,54	0,15	0,51
012E	Augen Gneiss	Mesklip Gneiss	-30,00703	17,78900	72,88	13,84	2,17	4,46	0,01	2,16	0,48	0,05	2,83	0,10	0,32
013B	Quartz monzodiorite	Oorkraal suite	-29,99236	17,78139	59,82	16,94	4,05	3,64	0,01	6,34	1,95	0,17	3,43	0,39	1,08
013C	Quartz monzodiorite	Oorkraal suite	-29,99233	17,78183	54,42	14,16	7,40	2,95	0,07	8,55	6,17	0,20	2,94	0,57	0,97
014D	Plagioclase bearing hornblende norite	Oorkraal suite	-29,99526	17,78520	59,77	17,26	4,22	2,40	0,02	7,33	2,04	0,14	4,19	0,48	1,13
019A	Augen Gneiss	Mesklip Gneiss	-30,00633	17,81258	69,95	14,78	2,10	4,13	0,01	2,97	0,78	0,05	3,43	0,12	0,33
020A	Augen Gneiss	Mesklip Gneiss	-30,00092	17,82125	73,63	12,80	1,63	5,54	0,01	2,24	0,57	0,06	2,33	0,10	0,36
020B	Augen Gneiss	Mesklip Gneiss	-30,00092	17,82125	73,10	13,03	1,77	5,06	0,01	2,59	0,48	0,05	2,51	0,11	0,35
020C	Gabbronorite	Oorkraal suite	-30,00092	17,82125	49,24	14,32	10,33	0,81	0,04	13,18	6,65	0,26	2,72	0,19	1,67
022A	Biotite Gneiss	Hunboom Gneiss	-29,99581	17,85853	68,70	15,47	1,12	5,01	0,01	3,00	0,99	0,06	3,74	0,06	0,42
022C	Biotite Gneiss	Hunboom Gneiss	-29,99581	17,85853	68,40	14,62	2,81	3,14	0,01	3,73	1,44	0,10	3,68	0,28	0,73
023A	Biotite Gneiss	Hunboom Gneiss	-29,99147	17,87381	68,92	15,41	2,24	3,18	0,01	2,94	0,74	0,09	4,80	0,16	0,38
023B	Biotite Gneiss	Hunboom Gneiss	-29,99147	17,87381	69,70	14,97	2,23	3,19	0,01	3,14	0,90	0,09	4,42	0,17	0,42
024C	Grey Biotite Gneiss	Hunboom Gneiss	-29,92731	17,81389	71,50	13,40	1,10	5,76	0,01	2,94	0,36	0,04	3,03	0,17	0,29
026A	Augen Gneiss	Mesklip Gneiss	-29,94981	17,85133	70,20	13,87	2,13	4,83	0,01	3,47	0,79	0,06	3,00	0,17	0,55
026B	Quartz syenite	Oorkraal suite	-29,94981	17,85133	56,61	12,90	5,11	7,50	0,03	5,20	4,57	0,10	1,38	1,65	1,60
027B1	Leucogranititc Gneiss	Rooiplatklip Gneiss	-29,96908	17,85339	74,30	13,32	0,43	6,51	0,01	1,26	0,21	0,02	2,66	0,04	0,15
027B2	Leucogranititc Gneiss	Rooiplatklip Gneiss	-29,96908	17,85339	74,02	13,41	0,54	6,51	0,01	1,38	0,22	0,02	2,64	0,07	0,16
028C1	Biotite Gneiss	Hunboom Gneiss	-29,99597	17,87550	73,64	13,25	2,38	3,04	0,02	2,52	0,63	0,04	3,25	0,09	0,27
028C2	Augen Gneiss	Mesklip Gneiss	-29,99597	17,87550	71,06	14,21	2,41	3,73	0,01	2,97	0,74	0,06	3,36	0,10	0,34

Table B1 continued. Whole-rock geochemistry analysis for 56 samples along and around the BRSZ.

															MAJOR ELEMENTS

Sample number	Lithology	Stratigraphic Unit	Latitutde	Longitude	SiO2	Al2O3	CaO	K2O	Cr2O3	Fe2O3	MgO	MnO	Na2O	P2O5	TiO2
028D	Leucogranititc Gneiss	Rooiplatklip Gneiss	-29,99656	17,87553	73,60	12,63	0,62	6,72	0,01	2,76	0,22	0,03	2,38	0,03	0,18
029	Leucogranititc Gneiss	Rooiplatklip Gneiss	-29,99022	17,87586	73,93	14,14	0,74	6,32	0,01	0,73	0,10	0,01	3,01	0,03	0,04
030A	Leucogranititc Gneiss	Rooiplatklip Gneiss	-29,98103	17,88942	72,29	13,49	1,52	5,73	0,01	2,44	0,47	0,03	2,50	0,07	0,30
030B	Leucogranititc Gneiss	Rooiplatklip Gneiss	-29,98103	17,88942	71,63	13,44	1,19	6,17	0,01	3,01	0,41	0,04	2,41	0,08	0,35
031A	Biotite Gneiss	Hunboom Gneiss	-29,97550	17,89947	67,82	15,17	3,70	3,81	0,01	3,23	1,56	0,07	3,43	0,11	0,37
032B4	Garnet-biotite semi-pelitic Gneiss	Kamiesberg Group	-29,96378	17,90228	58,48	17,11	2,28	4,42	0,04	8,96	2,72	0,13	3,50	0,05	1,22
032B5	Garnet-biotite semi-pelitic Gneiss	Kamiesberg Group	-29,96378	17,90228	61,78	17,09	2,13	4,57	0,01	6,61	1,89	0,11	3,64	0,07	0,86
033A1	Augen Gneiss	Mesklip Gneiss	-29,97550	17,89947	75,10	12,29	1,24	4,98	0,01	1,92	0,29	0,03	2,76	0,04	0,26
033B1	Augen Gneiss	Mesklip Gneiss	-29,96125	17,90108	68,28	13,88	1,86	4,94	0,01	4,67	0,91	0,06	3,12	0,22	0,66
033B2	Augen Gneiss	Mesklip Gneiss	-29,96125	17,90108	70,06	13,42	2,02	4,50	0,01	4,24	0,85	0,06	3,05	0,19	0,63
034A	Augen Gneiss	Mesklip Gneiss	-29,88556	17,87333	72,96	12,57	1,44	5,89	0,01	2,94	0,52	0,05	2,28	0,10	0,47
034B	Augen Gneiss	Mesklip Gneiss	-29,88556	17,87333	73,45	11,76	1,48	5,81	0,01	3,25	0,65	0,06	1,96	0,12	0,53
034C	Augen Gneiss	Mesklip Gneiss	-29,88556	17,87333	73,70	11,80	1,54	5,26	0,01	3,22	0,65	0,05	2,19	0,12	0,55
034D	Augen Gneiss	Mesklip Gneiss	-29,88556	17,87333	73,61	12,08	1,54	5,23	0,01	3,14	0,63	0,05	2,32	0,11	0,56
035B	Leuco-gabbro	Oorkraal suite	-30,01803	17,97417	50,11	18,27	10,07	1,20	0,04	8,04	4,73	0,24	4,20	0,85	1,12
035C	Leuco-gabbro	Oorkraal suite	-30,01803	17,97417	50,65	17,37	9,04	2,02	0,04	7,81	5,26	0,26	4,04	0,98	1,21
036A	Garnet-biotite semi-pelitic Gneiss	Kamiesberg Group	-29,96758	17,97853	64,08	16,18	0,83	3,07	0,02	8,51	4,29	0,08	0,79	0,15	1,19
037	Leucogranititc Gneiss	Rooiplatklip Gneiss	-29,99339	17,87406	75,02	13,61	0,96	5,47	0,01	1,03	0,12	0,02	3,00	0,05	0,10
038A	Augen Gneiss	Mesklip Gneiss	-29,96897	17,85242	69,79	13,67	2,06	5,27	0,01	3,74	0,75	0,07	2,75	0,19	0,66
041A	Quartz monzodiorite	Oorkraal suite	-29,97467	17,90067	55,61	15,45	7,23	2,09	0,04	8,40	5,14	0,17	3,32	0,58	0,93
041B	Quartz monzodiorite	Oorkraal suite	-29,97467	17,90067	55,83	15,38	7,00	2,35	0,04	8,30	5,12	0,18	3,19	0,58	0,91
043B	Augen Gneiss	Mesklip Gneiss	-29,83867	17,09358	73,61	12,11	1,73	4,76	0,02	3,17	0,57	0,05	2,27	0,11	0,47
044B	Augen Gneiss	Mesklip Gneiss	-30,15277	17,93170	73,00	13,00	0,57	5,36	0,01	2,49	0,60	0,03	2,94	0,04	0,30

97

Table B1 continued. Whole-rock geochemistry analysis for 56 samples along and around the BRSZ.

Sample number	Lithology	Stratigraphic Unit	Latitutde	Longitude	Sc	V	Cr	Co	Ni	Cu	Zn	Rb
											TRACE ELEMENTS	
001	Augen Gneiss	Mesklip Gneiss	-29,94500	17,95978	18,37	64,17	207,24	7,31	14,96	11,90	70,92	252,12
004B	Quartz monzodiorite	Oorkraal suite	-29,99800	17,84025	17,49	174,77	190,75	20,17	25,79	43,12	100,65	58,60
004C	Leucogranititc Gneiss	Rooiplatklip Gneiss	-29,99800	17,84025	7,75	41,70	256,16	2,80	10,69	8,29	41,63	90,62
005	Leucogranititc Gneiss	Rooiplatklip Gneiss	-29,99508	17,81661	6,01	30,26	195,24	1,86	11,02	6,30	30,48	300,93
007B	Augen Gneiss	Mesklip Gneiss	-29,91920	17,82447	7,29	48,92	148,60	5,29	13,38	10,25	53,26	177,46
008C	Olivine gabbronorite	Oorkraal suite	-29,93261	17,81117	23,01	138,74	250,74	25,88	147,33	11,73	127,43	378,35
008C1	Olivine gabbronorite	Oorkraal suite	-29,93261	17,81117	19,51	119,82	222,54	22,99	122,53	8,83	110,43	336,51
009	Biotite Gneiss	Hunboom Gneiss	-29,99106	17,81542	8,80	51,03	231,89	4,20	12,02	13,62	57,29	160,30
011A	Leucogranititc Gneiss	Rooiplatklip Gneiss	-29,99975	17,82458	9,22	43,07	214,57	2,87	9,10	7,22	37,15	163,76
011B	Leucogranititc Gneiss	Rooiplatklip Gneiss	-29,99975	17,82458	10,54	42,62	210,84	4,12	10,98	13,16	47,41	177,34
011C	Leuco-gabbro	Oorkraal suite	-29,99975	17,82458	42,40	290,24	271,38	45,30	110,25	34,14	218,68	230,42
012A	Grey Biotite Gneiss	Hunboom Gneiss	-30,00717	17,78972	13,32	129,05	282,72	16,08	48,04	30,47	89,45	109,27
012B	Grey Biotite Gneiss	Hunboom Gneiss	-30,00717	17,78972	14,37	153,71	342,28	20,09	52,83	33,51	106,22	121,30
012D	Leucogranititc Gneiss	Rooiplatklip Gneiss	-30,00703	17,78900	9,11	56,78	188,05	5,56	8,35	8,51	66,23	145,45
012E	Augen Gneiss	Mesklip Gneiss	-30,00703	17,78900	6,56	40,30	161,82	4,38	12,01	9,91	45,98	118,82
013B	Quartz monzodiorite	Oorkraal suite	-29,99236	17,78139	19,86	112,32	148,32	10,80	13,07	18,02	111,70	136,91
013C	Quartz monzodiorite	Oorkraal suite	-29,99233	17,78183	31,47	203,08	479,85	28,95	78,67	30,33	119,38	133,62
014D	Plagioclase bearing hornblende norite	Oorkraal suite	-29,99526	17,78520	23,69	128,38	133,59	12,48	16,27	33,59	145,47	160,63
019A	Augen Gneiss	Mesklip Gneiss	-30,00633	17,81258	10,61	54,24	187,59	5,71	16,18	9,32	54,21	140,31
020A	Augen Gneiss	Mesklip Gneiss	-30,00092	17,82125	13,05	40,28	194,84	4,16	11,68	25,46	39,69	188,37
020B	Augen Gneiss	Mesklip Gneiss	-30,00092	17,82125	10,71	43,86	168,14	2,91	10,09	5,95	44,58	184,69
020C	Gabbronorite	Oorkraal suite	-30,00092	17,82125	45,46	349,50	285,10	42,04	94,71	40,50	129,06	12,41
022A	Biotite Gneiss	Hunboom Gneiss	-29,99581	17,85853	10,58	64,87	182,96	7,67	37,41	10,90	42,84	157,84
022C	Biotite Gneiss	Hunboom Gneiss	-29,99581	17,85853	11,73	75,57	232,89	9,07	24,91	8,29	80,34	151,44
023A	Biotite Gneiss	Hunboom Gneiss	-29,99147	17,87381	9,68	37,58	166,61	3,71	9,22	8,09	77,22	120,69
023B	Biotite Gneiss	Hunboom Gneiss	-29,99147	17,87381	10,80	43,07	167,14	4,52	10,13	10,76	84,48	131,25
024C	Grey Biotite Gneiss	Hunboom Gneiss	-29,92731	17,81389	8,24	44,94	205,90	4,69	10,64	18,73	29,12	154,60
026A	Augen Gneiss	Mesklip Gneiss	-29,94981	17,85133	11,54	58,93	189,08	6,66	11,67	10,30	64,27	211,83
026B	Quartz syenite	Oorkraal suite	-29,94981	17,85133	15,22	106,11	241,93	20,96	114,21	11,26	118,92	362,50
027B1	Leucogranititc Gneiss	Rooiplatklip Gneiss	-29,96908	17,85339	4,09	27,12	181,25	2,67	9,79	6,69	31,61	277,06
027B2	Leucogranititc Gneiss	Rooiplatklip Gneiss	-29,96908	17,85339	4,09	28,57	187,29	2,59	8,72	8,33	29,09	266,00
028C1	Biotite Gneiss	Hunboom Gneiss	-29,99597	17,87550	8,14	53,54	254,78	4,20	12,10	14,43	39,35	93,69
028C2	Augen Gneiss	Mesklip Gneiss	-29,99597	17,87550	9,33	58,83	243,44	5,18	12,73	8,56	51,46	122,73

Table B1 continued. Whole-rock geochemistry analysis for 56 samples along and around the BRSZ.

| | | | | | TRACE ELEMENTS | | | | | | | |
| | | | | | Sr | Y | Zr | Nb | Mo | Cs | Ba | La |
Sample number	Lithology	Stratigraphic Unit	Latitutde	Longitude								
001	Augen Gneiss	Mesklip Gneiss	-29,94500	17,95978	169,31	64,42	287,78	29,38	13,16	2,50	922,42	55,74
004B	Quartz monzodiorite	Oorkraal suite	-29,99800	17,84025	670,58	22,33	172,65	12,61	10,53	1,05	689,50	22,69
004C	Leucogranititc Gneiss	Rooiplatklip Gneiss	-29,99800	17,84025	212,13	19,82	223,51	8,76	15,82	0,58	706,30	98,30
005	Leucogranititc Gneiss	Rooiplatklip Gneiss	-29,99508	17,81661	139,35	17,27	140,93	16,00	12,44	1,63	571,11	59,97
007B	Augen Gneiss	Mesklip Gneiss	-29,91920	17,82447	154,36	14,77	240,32	15,10	8,08	0,92	873,30	61,92
008C	Olivine gabbronorite	Oorkraal suite	-29,93261	17,81117	1904,02	50,21	1390,08	32,69	6,02	5,56	10386,05	408,32
008C1	Olivine gabbronorite	Oorkraal suite	-29,93261	17,81117	1739,96	56,52	1402,30	28,04	5,69	4,41	9233,02	404,98
009	Biotite Gneiss	Hunboom Gneiss	-29,99106	17,81542	300,62	20,23	138,12	11,86	14,42	1,19	873,72	39,59
011A	Leucogranititc Gneiss	Rooiplatklip Gneiss	-29,99975	17,82458	143,57	13,52	176,04	16,58	12,53	1,10	866,75	48,53
011B	Leucogranititc Gneiss	Rooiplatklip Gneiss	-29,99975	17,82458	159,74	16,99	219,55	10,13	13,58	1,28	937,19	79,76
011C	Leuco-gabbro	Oorkraal suite	-29,99975	17,82458	104,13	67,08	263,33	49,05	4,96	7,93	338,18	20,73
012A	Grey Biotite Gneiss	Hunboom Gneiss	-30,00717	17,78972	298,47	23,84	208,19	15,45	12,23	1,61	541,78	91,43
012B	Grey Biotite Gneiss	Hunboom Gneiss	-30,00717	17,78972	306,87	17,96	253,26	17,14	14,91	1,64	719,94	65,84
012D	Leucogranititc Gneiss	Rooiplatklip Gneiss	-30,00703	17,78900	268,88	27,91	230,99	15,03	11,37	0,91	1565,97	59,75
012E	Augen Gneiss	Mesklip Gneiss	-30,00703	17,78900	244,23	19,00	128,36	14,99	9,85	0,60	1237,77	55,59
013B	Quartz monzodiorite	Oorkraal suite	-29,99236	17,78139	601,15	60,65	397,78	28,95	8,40	2,27	2990,59	87,63
013C	Quartz monzodiorite	Oorkraal suite	-29,99233	17,78183	434,81	34,81	228,92	14,69	6,28	2,81	1447,50	32,90
014D	Plagioclase bearing hornblende norite	Oorkraal suite	-29,99526	17,78520	541,34	67,31	404,07	33,50	8,80	3,00	1632,53	55,67
019A	Augen Gneiss	Mesklip Gneiss	-30,00633	17,81258	370,10	9,08	160,92	10,03	11,42	2,13	1059,73	38,24
020A	Augen Gneiss	Mesklip Gneiss	-30,00092	17,82125	231,68	49,93	128,84	18,23	11,41	0,96	1351,31	74,29
020B	Augen Gneiss	Mesklip Gneiss	-30,00092	17,82125	177,13	20,34	178,06	16,33	9,91	1,06	1163,44	41,21
020C	Gabbronorite	Oorkraal suite	-30,00092	17,82125	157,64	37,59	125,75	17,50	4,75	0,37	108,27	13,66
022A	Biotite Gneiss	Hunboom Gneiss	-29,99581	17,85853	217,16	28,78	131,19	12,63	9,36	0,84	1036,78	29,23
022C	Biotite Gneiss	Hunboom Gneiss	-29,99581	17,85853	485,31	38,58	164,30	25,99	13,18	1,36	799,90	74,92
023A	Biotite Gneiss	Hunboom Gneiss	-29,99147	17,87381	181,22	47,25	275,71	18,44	10,30	0,90	363,93	51,70
023B	Biotite Gneiss	Hunboom Gneiss	-29,99147	17,87381	203,20	43,56	254,49	22,10	9,45	1,15	485,98	55,10
024C	Grey Biotite Gneiss	Hunboom Gneiss	-29,92731	17,81389	351,40	47,85	382,46	12,54	12,42	0,40	1823,19	124,87
026A	Augen Gneiss	Mesklip Gneiss	-29,94981	17,85133	192,19	39,54	269,90	20,33	11,66	1,60	962,30	59,79
026B	Quartz syenite	Oorkraal suite	-29,94981	17,85133	2604,30	37,51	1022,26	27,54	8,57	6,87	8342,52	285,38
027B1	Leucogranititc Gneiss	Rooiplatklip Gneiss	-29,96908	17,85339	155,47	8,70	89,72	11,03	11,67	1,25	603,79	25,87
027B2	Leucogranititc Gneiss	Rooiplatklip Gneiss	-29,96908	17,85339	164,91	9,20	94,37	3,52	11,48	1,11	774,83	20,92
028C1	Biotite Gneiss	Hunboom Gneiss	-29,99597	17,87550	342,12	14,12	136,29	15,17	15,47	0,60	842,69	27,39
028C2	Augen Gneiss	Mesklip Gneiss	-29,99597	17,87550	353,51	17,72	172,12	12,50	14,94	0,84	1028,23	29,94

99

Table B1 continued. Whole-rock geochemistry analysis for 56 samples along and around the BRSZ.

					TRACE ELEMENTS							
Sample number	Lithology	Stratigraphic Unit	Latitutde	Longitude	Ce	Pr	Nd	Sm	Eu	Gd	Tb	Dy
001	Augen Gneiss	Mesklip Gneiss	-29,94500	17,95978	117,17	13,89	55,79	11,73	1,69	10,84	1,75	10,85
004B	Quartz monzodiorite	Oorkraal suite	-29,99800	17,84025	48,51	6,25	27,54	5,74	1,64	5,38	0,76	4,52
004C	Leucogranititc Gneiss	Rooiplatklip Gneiss	-29,99800	17,84025	194,45	21,85	78,97	13,26	1,86	9,04	1,14	5,46
005	Leucogranititc Gneiss	Rooiplatklip Gneiss	-29,99508	17,81661	120,27	12,99	44,49	8,07	1,03	5,54	0,71	3,52
007B	Augen Gneiss	Mesklip Gneiss	-29,91920	17,82447	124,60	13,57	49,27	7,95	1,29	5,84	0,69	3,63
008C	Olivine gabbronorite	Oorkraal suite	-29,93261	17,81117	892,89	106,74	399,76	58,85	12,65	31,85	2,99	12,39
008C1	Olivine gabbronorite	Oorkraal suite	-29,93261	17,81117	820,15	102,20	384,31	54,23	12,20	29,54	2,83	12,16
009	Biotite Gneiss	Hunboom Gneiss	-29,99106	17,81542	82,33	9,66	36,82	7,10	1,37	5,75	0,73	4,17
011A	Leucogranititc Gneiss	Rooiplatklip Gneiss	-29,99975	17,82458	97,53	10,70	37,84	6,40	1,62	4,50	0,61	2,76
011B	Leucogranititc Gneiss	Rooiplatklip Gneiss	-29,99975	17,82458	158,80	17,49	63,25	10,31	1,87	7,40	0,86	4,16
011C	Leuco-gabbro	Oorkraal suite	-29,99975	17,82458	55,27	8,07	37,50	10,85	2,83	11,52	1,85	12,23
012A	Grey Biotite Gneiss	Hunboom Gneiss	-30,00717	17,78972	187,34	21,42	79,34	13,61	2,04	9,56	1,21	5,84
012B	Grey Biotite Gneiss	Hunboom Gneiss	-30,00717	17,78972	134,00	15,29	56,08	10,15	1,83	7,37	0,91	4,37
012D	Leucogranititc Gneiss	Rooiplatklip Gneiss	-30,00703	17,78900	118,36	13,33	49,27	9,27	1,79	6,97	1,02	5,63
012E	Augen Gneiss	Mesklip Gneiss	-30,00703	17,78900	104,50	11,36	41,64	6,69	1,80	5,55	0,73	4,13
013B	Quartz monzodiorite	Oorkraal suite	-29,99236	17,78139	190,75	23,30	94,76	17,68	3,95	14,33	1,89	11,44
013C	Quartz monzodiorite	Oorkraal suite	-29,99233	17,78183	73,57	9,16	37,02	8,13	2,04	6,90	1,05	6,71
014D	Plagioclase bearing hornblende norite	Oorkraal suite	-29,99526	17,78520	142,06	17,46	73,58	15,13	3,37	13,06	1,95	11,43
019A	Augen Gneiss	Mesklip Gneiss	-30,00633	17,81258	76,04	8,18	29,95	5,03	1,19	2,71	0,30	1,86
020A	Augen Gneiss	Mesklip Gneiss	-30,00092	17,82125	155,68	18,42	71,11	13,47	2,19	11,28	1,62	9,52
020B	Augen Gneiss	Mesklip Gneiss	-30,00092	17,82125	82,23	9,06	34,03	5,93	1,84	4,62	0,69	3,88
020C	Gabbronorite	Oorkraal suite	-30,00092	17,82125	31,47	4,13	18,89	5,06	1,46	5,66	0,99	6,55
022A	Biotite Gneiss	Hunboom Gneiss	-29,99581	17,85853	55,73	6,09	21,77	4,06	1,33	3,65	0,62	4,47
022C	Biotite Gneiss	Hunboom Gneiss	-29,99581	17,85853	143,46	15,01	53,75	9,22	1,58	7,41	1,00	6,53
023A	Biotite Gneiss	Hunboom Gneiss	-29,99147	17,87381	107,47	12,66	47,96	9,00	1,81	8,59	1,30	8,61
023B	Biotite Gneiss	Hunboom Gneiss	-29,99147	17,87381	118,11	13,95	52,17	10,93	1,91	8,37	1,32	8,15
024C	Grey Biotite Gneiss	Hunboom Gneiss	-29,92731	17,81389	245,37	27,41	97,95	19,08	2,67	15,62	2,22	11,74
026A	Augen Gneiss	Mesklip Gneiss	-29,94981	17,85133	117,82	12,85	47,07	8,41	1,63	7,78	1,16	7,22
026B	Quartz syenite	Oorkraal suite	-29,94981	17,85133	599,90	69,09	256,62	36,08	8,77	19,48	1,82	8,15
027B1	Leucogranititc Gneiss	Rooiplatklip Gneiss	-29,96908	17,85339	52,49	4,76	16,08	2,18	1,44	1,82	0,26	1,66
027B2	Leucogranititc Gneiss	Rooiplatklip Gneiss	-29,96908	17,85339	43,91	4,10	14,64	2,41	1,38	1,78	0,26	1,69
028C1	Biotite Gneiss	Hunboom Gneiss	-29,99597	17,87550	53,49	6,13	21,53	3,85	1,08	3,27	0,46	2,55
028C2	Augen Gneiss	Mesklip Gneiss	-29,99597	17,87550	60,07	6,63	25,71	4,94	1,12	3,67	0,51	3,17

Table B1 continued. Whole-rock geochemistry analysis for 56 samples along and around the BRSZ.

					TRACE ELEMENTS				
Sample number	Lithology	Stratigraphic Unit	Latitutde	Longitude	Hf	Ta	Pb	Th	U
001	Augen Gneiss	Mesklip Gneiss	-29,94500	17,95978	8,04	2,15	33,47	25,16	2,38
004B	Quartz monzodiorite	Oorkraal suite	-29,99800	17,84025	4,28	0,48	12,06	1,21	0,47
004C	Leucogranititc Gneiss	Rooiplatklip Gneiss	-29,99800	17,84025	6,70	0,26	21,95	32,48	1,71
005	Leucogranititc Gneiss	Rooiplatklip Gneiss	-29,99508	17,81661	4,60	0,42	43,02	42,07	2,59
007B	Augen Gneiss	Mesklip Gneiss	-29,91920	17,82447	6,81	0,36	30,90	20,56	0,63
008C	Olivine gabbronorite	Oorkraal suite	-29,93261	17,81117	33,10	1,61	86,29	111,76	18,01
008C1	Olivine gabbronorite	Oorkraal suite	-29,93261	17,81117	29,68	1,52	75,67	92,16	15,06
009	Biotite Gneiss	Hunboom Gneiss	-29,99106	17,81542	4,21	0,42	35,86	19,96	1,46
011A	Leucogranititc Gneiss	Rooiplatklip Gneiss	-29,99975	17,82458	5,47	0,36	30,09	20,79	1,26
011B	Leucogranititc Gneiss	Rooiplatklip Gneiss	-29,99975	17,82458	6,15	0,45	32,61	30,23	1,40
011C	Leuco-gabbro	Oorkraal suite	-29,99975	17,82458	6,69	3,04	10,55	2,04	2,64
012A	Grey Biotite Gneiss	Hunboom Gneiss	-30,00717	17,78972	5,93	0,96	26,03	44,94	1,74
012B	Grey Biotite Gneiss	Hunboom Gneiss	-30,00717	17,78972	7,05	1,03	27,73	32,18	1,16
012D	Leucogranititc Gneiss	Rooiplatklip Gneiss	-30,00703	17,78900	6,46	0,95	24,58	8,13	0,65
012E	Augen Gneiss	Mesklip Gneiss	-30,00703	17,78900	3,25	0,43	22,19	9,23	0,27
013B	Quartz monzodiorite	Oorkraal suite	-29,99236	17,78139	10,02	1,33	19,82	13,94	1,07
013C	Quartz monzodiorite	Oorkraal suite	-29,99233	17,78183	6,63	1,06	17,56	7,54	1,79
014D	Plagioclase bearing hornblende norite	Oorkraal suite	-29,99526	17,78520	10,52	4,32	21,25	12,28	3,66
019A	Augen Gneiss	Mesklip Gneiss	-30,00633	17,81258	4,68	0,92	29,01	13,55	1,91
020A	Augen Gneiss	Mesklip Gneiss	-30,00092	17,82125	3,78	1,88	34,97	46,13	2,97
020B	Augen Gneiss	Mesklip Gneiss	-30,00092	17,82125	5,15	0,37	33,39	27,80	2,35
020C	Gabbronorite	Oorkraal suite	-30,00092	17,82125	3,43	1,21	7,67	4,03	0,80
022A	Biotite Gneiss	Hunboom Gneiss	-29,99581	17,85853	4,14	0,57	44,98	9,49	0,77
022C	Biotite Gneiss	Hunboom Gneiss	-29,99581	17,85853	4,51	1,68	25,63	29,48	1,89
023A	Biotite Gneiss	Hunboom Gneiss	-29,99147	17,87381	7,72	0,82	24,12	10,30	1,93
023B	Biotite Gneiss	Hunboom Gneiss	-29,99147	17,87381	7,21	1,03	23,49	14,08	2,41
024C	Grey Biotite Gneiss	Hunboom Gneiss	-29,92731	17,81389	9,95	0,88	21,74	40,27	1,20
026A	Augen Gneiss	Mesklip Gneiss	-29,94981	17,85133	7,27	1,50	35,41	26,77	2,37
026B	Quartz syenite	Oorkraal suite	-29,94981	17,85133	24,75	1,20	44,43	49,15	12,63
027B1	Leucogranititc Gneiss	Rooiplatklip Gneiss	-29,96908	17,85339	3,12	0,12	36,02	30,29	4,53
027B2	Leucogranititc Gneiss	Rooiplatklip Gneiss	-29,96908	17,85339	3,13	0,10	38,39	30,96	5,62
028C1	Biotite Gneiss	Hunboom Gneiss	-29,99597	17,87550	3,93	0,46	23,40	8,25	1,01
028C2	Augen Gneiss	Mesklip Gneiss	-29,99597	17,87550	4,89	0,58	27,25	10,01	1,30

101

Table B1 continued. Whole-rock geochemistry analysis for 56 samples along and around the BRSZ.

TRACE ELEMENTS

Sample number	Lithology	Stratigraphic Unit	Latitutde	Longitude	Sc	V	Cr	Co	Ni	Cu	Zn	Rb
028D	Leucogranititc Gneiss	Rooiplatklip Gneiss	-29,99656	17,87553	5,74	26,31	189,79	2,17	12,93	7,30	41,46	215,26
029	Leucogranititc Gneiss	Rooiplatklip Gneiss	-29,99022	17,87586	3,87	27,76	175,59	1,71	10,82	9,02	14,94	186,33
030A	Leucogranititc Gneiss	Rooiplatklip Gneiss	-29,98103	17,88942	8,29	37,85	120,86	3,94	10,43	7,27	35,00	153,61
030B	Leucogranititc Gneiss	Rooiplatklip Gneiss	-29,98103	17,88942	12,50	41,86	164,64	3,85	9,93	15,07	40,54	166,85
031A	Biotite Gneiss	Hunboom Gneiss	-29,97550	17,89947	13,98	70,98	161,88	10,39	32,47	15,48	48,46	117,86
032B4	Garnet-biotite semi-pelitic Gneiss	Kamiesberg Group	-29,96378	17,90228	27,94	167,90	289,07	24,83	63,85	11,57	101,43	210,09
032B5	Garnet-biotite semi-pelitic Gneiss	Kamiesberg Group	-29,96378	17,90228	22,15	121,47	261,58	16,61	48,12	11,22	80,51	160,72
033A1	Augen Gneiss	Mesklip Gneiss	-29,97550	17,89947	7,40	38,00	234,32	2,55	9,70	6,12	36,16	198,89
033B1	Augen Gneiss	Mesklip Gneiss	-29,96125	17,90108	11,41	71,12	240,90	7,59	15,60	23,04	92,35	214,91
033B2	Augen Gneiss	Mesklip Gneiss	-29,96125	17,90108	10,76	66,97	210,38	6,98	15,72	17,62	83,80	205,79
034A	Augen Gneiss	Mesklip Gneiss	-29,88556	17,87333	10,82	50,28	197,73	4,72	11,61	10,37	45,41	342,49
034B	Augen Gneiss	Mesklip Gneiss	-29,88556	17,87333	11,89	66,28	206,31	6,00	12,02	22,60	51,40	245,72
034C	Augen Gneiss	Mesklip Gneiss	-29,88556	17,87333	12,70	58,17	226,14	5,22	10,95	11,08	50,57	234,54
034D	Augen Gneiss	Mesklip Gneiss	-29,88556	17,87333	10,02	45,89	100,47	5,23	10,70	10,00	50,90	241,89
035B	Leuco-gabbro	Oorkraal suite	-30,01803	17,97417	21,36	133,02	287,72	29,86	145,08	22,67	240,97	28,64
035C	Leuco-gabbro	Oorkraal suite	-30,01803	17,97417	20,89	128,64	291,85	29,21	148,47	18,64	317,40	78,43
036A	Garnet-biotite semi-pelitic Gneiss	Kamiesberg Group	-29,96758	17,97853	12,45	143,86	267,15	22,09	77,36	9,62	127,44	150,61
037	Leucogranititc Gneiss	Rooiplatklip Gneiss	-29,99339	17,87406	5,01	20,64	101,25	1,73	7,98	5,63	32,08	289,93
038A	Augen Gneiss	Mesklip Gneiss	-29,96897	17,85242	12,57	66,57	214,55	7,31	12,61	12,09	59,49	247,10
041A	Quartz monzodiorite	Oorkraal suite	-29,97467	17,90067	29,66	223,98	304,82	28,12	59,22	32,45	101,42	102,06
041B	Quartz monzodiorite	Oorkraal suite	-29,97467	17,90067	29,29	221,43	293,88	26,77	53,90	30,69	98,77	130,17
043B	Augen Gneiss	Mesklip Gneiss	-29,83867	17,09358	11,55	58,21	255,71	5,22	13,76	10,14	46,65	205,07
044B	Augen Gneiss	Mesklip Gneiss	-30,15277	17,93170	9,94	29,52	184,41	1,98	9,01	8,13	55,52	180,98

Table B1 continued. Whole-rock geochemistry analysis for 56 samples along and around the BRSZ.

					TRACE ELEMENTS							
Sample number	Lithology	Stratigraphic Unit	Latitutde	Longitude	Sr	Y	Zr	Nb	Mo	Cs	Ba	La
028D	Leucogranititc Gneiss	Rooiplatklip Gneiss	-29,99656	17,87553	187,88	8,69	76,14	8,20	11,76	1,55	653,30	42,67
029	Leucogranititc Gneiss	Rooiplatklip Gneiss	-29,99022	17,87586	227,08	7,49	34,40	6,98	9,95	0,75	1120,03	11,21
030A	Leucogranititc Gneiss	Rooiplatklip Gneiss	-29,98103	17,88942	324,50	12,91	229,72	7,19	6,67	0,78	1456,38	81,69
030B	Leucogranititc Gneiss	Rooiplatklip Gneiss	-29,98103	17,88942	333,12	17,52	357,66	8,94	10,05	0,65	1610,70	176,46
031A	Biotite Gneiss	Hunboom Gneiss	-29,97550	17,89947	376,02	21,94	113,32	7,89	9,81	0,57	851,42	19,23
032B4	Garnet-biotite semi-pelitic Gneiss	Kamiesberg Group	-29,96378	17,90228	365,70	48,77	399,74	25,94	8,66	3,06	1514,26	77,87
032B5	Garnet-biotite semi-pelitic Gneiss	Kamiesberg Group	-29,96378	17,90228	277,83	42,23	269,13	22,40	10,19	1,86	1273,28	59,55
033A1	Augen Gneiss	Mesklip Gneiss	-29,97550	17,89947	116,97	12,67	211,08	7,53	15,34	1,43	961,36	43,77
033B1	Augen Gneiss	Mesklip Gneiss	-29,96125	17,90108	142,81	34,69	394,27	19,12	15,87	2,00	937,58	46,01
033B2	Augen Gneiss	Mesklip Gneiss	-29,96125	17,90108	152,91	31,19	344,38	23,67	12,53	1,96	868,84	49,76
034A	Augen Gneiss	Mesklip Gneiss	-29,88556	17,87333	72,37	42,34	232,15	21,57	14,64	4,45	538,55	57,86
034B	Augen Gneiss	Mesklip Gneiss	-29,88556	17,87333	119,39	46,02	253,35	24,02	13,68	2,33	1156,70	107,28
034C	Augen Gneiss	Mesklip Gneiss	-29,88556	17,87333	108,28	40,70	288,73	19,12	14,60	2,46	752,57	68,64
034D	Augen Gneiss	Mesklip Gneiss	-29,88556	17,87333	99,79	34,68	312,35	18,41	7,08	2,71	614,15	85,25
035B	Leuco-gabbro	Oorkraal suite	-30,01803	17,97417	797,78	39,49	437,68	16,38	4,38	0,72	665,09	117,26
035C	Leuco-gabbro	Oorkraal suite	-30,01803	17,97417	873,04	44,61	519,88	19,33	4,31	1,87	1426,92	136,27
036A	Garnet-biotite semi-pelitic Gneiss	Kamiesberg Group	-29,96758	17,97853	92,30	29,70	198,27	29,33	7,92	2,55	799,32	38,04
037	Leucogranititc Gneiss	Rooiplatklip Gneiss	-29,99339	17,87406	86,01	16,94	80,69	17,23	6,31	1,22	325,40	23,40
038A	Augen Gneiss	Mesklip Gneiss	-29,96897	17,85242	183,61	44,33	378,33	29,68	13,93	2,27	1103,89	62,76
041A	Quartz monzodiorite	Oorkraal suite	-29,97467	17,90067	319,35	28,63	244,72	15,29	6,61	1,41	428,34	32,41
041B	Quartz monzodiorite	Oorkraal suite	-29,97467	17,90067	343,46	33,27	226,99	14,41	4,90	1,76	578,26	33,49
043B	Augen Gneiss	Mesklip Gneiss	-29,83867	17,09358	101,36	35,64	241,95	20,73	16,80	3,72	794,44	62,26
044B	Augen Gneiss	Mesklip Gneiss	-30,15277	17,93170	70,54	50,62	383,66	19,05	11,18	0,86	972,25	57,64

Table B1 continued. Whole-rock geochemistry analysis for 56 samples along and around the BRSZ.

<div align="right">TRACE ELEMENTS</div>

Sample number	Lithology	Stratigraphic Unit	Latitutde	Longitude	Ce	Pr	Nd	Sm	Eu	Gd	Tb	Dy
028D	Leucogranititc Gneiss	Rooiplatklip Gneiss	-29,99656	17,87553	84,84	9,08	31,57	4,88	1,04	2,76	0,40	1,88
029	Leucogranititc Gneiss	Rooiplatklip Gneiss	-29,99022	17,87586	20,91	2,07	6,78	1,25	0,86	1,18	0,17	1,03
030A	Leucogranititc Gneiss	Rooiplatklip Gneiss	-29,98103	17,88942	155,05	16,13	52,50	7,17	1,44	4,80	0,57	2,84
030B	Leucogranititc Gneiss	Rooiplatklip Gneiss	-29,98103	17,88942	332,85	33,80	112,14	13,78	1,68	8,14	0,92	4,37
031A	Biotite Gneiss	Hunboom Gneiss	-29,97550	17,89947	42,00	5,37	21,42	4,99	1,49	4,43	0,71	4,39
032B4	Garnet-biotite semi-pelitic Gneiss	Kamiesberg Group	-29,96378	17,90228	154,94	17,15	64,32	11,60	2,36	9,89	1,45	8,72
032B5	Garnet-biotite semi-pelitic Gneiss	Kamiesberg Group	-29,96378	17,90228	118,70	13,18	50,15	8,81	1,98	7,65	1,13	7,52
033A1	Augen Gneiss	Mesklip Gneiss	-29,97550	17,89947	80,58	8,40	29,09	4,72	1,48	3,29	0,44	2,60
033B1	Augen Gneiss	Mesklip Gneiss	-29,96125	17,90108	96,39	11,22	43,82	9,12	1,69	8,26	1,13	6,76
033B2	Augen Gneiss	Mesklip Gneiss	-29,96125	17,90108	102,38	11,76	45,96	8,56	1,65	7,35	1,05	6,01
034A	Augen Gneiss	Mesklip Gneiss	-29,88556	17,87333	113,69	12,23	42,52	8,03	1,16	7,01	1,09	7,00
034B	Augen Gneiss	Mesklip Gneiss	-29,88556	17,87333	214,15	22,78	76,58	13,12	1,48	9,62	1,42	8,61
034C	Augen Gneiss	Mesklip Gneiss	-29,88556	17,87333	139,86	15,50	55,32	10,06	1,39	8,15	1,21	7,59
034D	Augen Gneiss	Mesklip Gneiss	-29,88556	17,87333	168,38	17,56	59,17	10,17	1,21	8,11	1,18	7,05
035B	Leuco-gabbro	Oorkraal suite	-30,01803	17,97417	260,11	32,43	127,69	19,98	4,35	12,98	1,42	7,32
035C	Leuco-gabbro	Oorkraal suite	-30,01803	17,97417	305,73	38,16	147,05	23,47	4,99	14,33	1,66	8,51
036A	Garnet-biotite semi-pelitic Gneiss	Kamiesberg Group	-29,96758	17,97853	79,17	9,36	35,99	8,12	1,25	7,37	1,12	6,72
037	Leucogranititc Gneiss	Rooiplatklip Gneiss	-29,99339	17,87406	49,33	5,24	17,52	3,62	0,61	2,99	0,46	2,85
038A	Augen Gneiss	Mesklip Gneiss	-29,96897	17,85242	131,70	14,66	54,21	10,23	2,00	8,27	1,29	8,09
041A	Quartz monzodiorite	Oorkraal suite	-29,97467	17,90067	67,41	8,07	31,78	7,11	1,77	6,39	0,95	5,71
041B	Quartz monzodiorite	Oorkraal suite	-29,97467	17,90067	70,41	8,41	34,18	7,63	1,70	6,53	1,02	6,26
043B	Augen Gneiss	Mesklip Gneiss	-29,83867	17,09358	125,95	13,93	49,70	9,40	1,27	8,23	1,22	6,75
044B	Augen Gneiss	Mesklip Gneiss	-30,15277	17,93170	121,51	14,82	58,48	12,61	1,90	11,29	1,72	10,40

Table B1 continued. Whole-rock geochemistry analysis for 56 samples along and around the BRSZ.

Sample number	Lithology	Stratigraphic Unit	Latitutde	Longitude	Hf	Ta	Pb	Th	U
							TRACE ELEMENTS		
028D	Leucogranititc Gneiss	Rooiplatklip Gneiss	-29,99656	17,87553	2,22	0,86	48,09	33,15	1,99
029	Leucogranititc Gneiss	Rooiplatklip Gneiss	-29,99022	17,87586	1,13	0,05	44,64	3,64	0,36
030A	Leucogranititc Gneiss	Rooiplatklip Gneiss	-29,98103	17,88942	6,47	0,33	29,68	21,61	0,48
030B	Leucogranititc Gneiss	Rooiplatklip Gneiss	-29,98103	17,88942	8,90	0,38	32,99	44,88	0,89
031A	Biotite Gneiss	Hunboom Gneiss	-29,97550	17,89947	3,33	0,43	24,11	3,98	1,36
032B4	Garnet-biotite semi-pelitic Gneiss	Kamiesberg Group	-29,96378	17,90228	11,37	1,19	29,78	30,50	1,97
032B5	Garnet-biotite semi-pelitic Gneiss	Kamiesberg Group	-29,96378	17,90228	7,71	0,78	30,35	29,36	1,41
033A1	Augen Gneiss	Mesklip Gneiss	-29,97550	17,89947	6,01	0,43	26,92	10,95	0,76
033B1	Augen Gneiss	Mesklip Gneiss	-29,96125	17,90108	10,63	0,84	25,28	9,60	1,64
033B2	Augen Gneiss	Mesklip Gneiss	-29,96125	17,90108	9,41	0,71	23,57	10,44	2,56
034A	Augen Gneiss	Mesklip Gneiss	-29,88556	17,87333	6,90	1,74	29,30	35,32	4,34
034B	Augen Gneiss	Mesklip Gneiss	-29,88556	17,87333	7,18	1,37	34,95	66,61	3,55
034C	Augen Gneiss	Mesklip Gneiss	-29,88556	17,87333	8,84	1,32	30,49	35,79	2,20
034D	Augen Gneiss	Mesklip Gneiss	-29,88556	17,87333	9,11	1,10	31,32	44,03	2,35
035B	Leuco-gabbro	Oorkraal suite	-30,01803	17,97417	12,03	0,81	27,22	18,23	7,24
035C	Leuco-gabbro	Oorkraal suite	-30,01803	17,97417	13,75	0,93	27,08	21,76	6,53
036A	Garnet-biotite semi-pelitic Gneiss	Kamiesberg Group	-29,96758	17,97853	5,59	1,01	11,95	15,50	1,40
037	Leucogranititc Gneiss	Rooiplatklip Gneiss	-29,99339	17,87406	2,84	0,37	49,01	15,08	2,29
038A	Augen Gneiss	Mesklip Gneiss	-29,96897	17,85242	9,74	1,46	33,63	24,05	3,46
041A	Quartz monzodiorite	Oorkraal suite	-29,97467	17,90067	6,95	1,06	17,14	11,21	4,49
041B	Quartz monzodiorite	Oorkraal suite	-29,97467	17,90067	6,48	1,12	17,31	12,45	4,08
043B	Augen Gneiss	Mesklip Gneiss	-29,83867	17,09358	6,99	1,11	25,88	30,77	4,12
044B	Augen Gneiss	Mesklip Gneiss	-30,15277	17,93170	10,83	0,87	32,56	14,14	1,57

Table B2 Location of geochronology samples with brief lithological descriptions.

Sample number	Rock Name	Lithology	Subprovince/Terrane	Latitude	Longitude
034D	Mesklip gneiss	Magmatic; Medium- to coarse-grained streaky augen gneiss	Bushmanland/Garies	-29,88556	17,87333
033A1	Mesklip gneiss	Magmatic; Medium-grained biotite augen gneiss	Bushmanland/Garies	-29,97550	17,89947
019A	Mesklip gneiss	Magmatic; Medium-grained leucocratic augen gneiss	Bushmanland/Garies	-30,00633	17,81258
004C	Rooiplatklip gneiss	Magmatic; Fine-grained leucogranitic gneiss	Bushmanland/Garies	-29,99800	17,84025
037	Hunboom gneiss	Metasedimentary; Medium-grained migmatitic grey gneiss,	Bushmanland/Garies	-29,99339	17,87406
038A	Hunboom gneiss	Metasedimentary; Medium-grained migmatitic grey gneiss,	Bushmanland/Garies	-29,96897	17,85242
036A	Garnet-biotite semi-pelitic gneiss	Metasedimentary; Garnet-biotite-feldspathic schist	Bushmanland/Garies	-29,96758	17,97853

Table B3 Whole−rock Sr−Nd isotopic data for the rocks of the Buffels River shear zone.

Sample name	Rock type	Age (Ma)	Rb (ppm)	Sr (ppm)	Rb/Sr	$^{87}Rb/^{86}Sr$	$(^{87}Sr/^{86}Sr)_o$	±2σ	Sr_I	epsilon Sr(t)	Sm	Nd	Sm/Nd	$^{147}Sm/^{144}Nd$	$(^{143}Nd/^{144}Nd)_o$	±2σ	epsilon Nd(0)	$f^{Sm/Nd}$	epsilon Nd(t)	T_{CHUR}	T_{DM}
037	Grey biotite gneiss	1201	289.93	86.01	3.3708	8.9538	0.8649	17	0.7108	222.8385	3.6	17.5	0.2063	0.1248	0.511857	8	-15.24	-0.3655	-4.20	1.65	2.21
038A	Grey biotite gneiss	1223	247.10	183.61	1.3458	3.5748	0.7777	14	0.7151	247.8346	10.2	54.2	0.1886	0.1141	0.511735	9	-17.62	-0.4200	-4.69	1.66	2.16
036A	Gt-qtz-bt-sil schist	1162	150.61	92.30	1.6318	4.3346	0.7972	9	0.7251	258.0131	8.1	36.0	0.2255	0.1364	0.511927	10	-13.86	-0.3066	-4.90	1.79	2.40
034D	Streaky augen gneiss	1224	241.89	99.79	2.4241	6.4390	0.8520	14	0.7391	509.9677	10.2	59.2	0.1718	0.1039	0.511601	11	-20.22	-0.4717	-5.70	1.70	2.14
033A1	Biotite augen gneiss	1205	198.89	116.97	1.7004	4.5166	0.8163	14	0.7383	498.7601	4.7	29.1	0.1623	0.0982	0.511512	11	-21.97	-0.5009	-6.78	1.74	2.15
019A	Leucocratic augen gneiss	1204	140.31	370.10	0.3791	1.0070	0.7239	9	0.7065	46.7069	5.0	29.9	0.1680	0.1016	0.511721	9	-17.89	-0.4834	-3.23	1.47	1.94
004C	Leucogranitic gneiss	1204	90.62	212.13	0.4272	1.1347	0.7287	10	0.7092	84.5127	13.3	79.0	0.1678	0.1015	0.511745	11	-17.42	-0.4838	-2.76	1.43	1.90
013F	Amphibolite gneiss	1168	168.45	470.16	0.3583	0.9517	0.7219	10	0.7060	38.3690	6.6	30.6	0.2142	0.1296	0.512002	13	-12.41	-0.3413	-2.38	1.44	2.07

ɛNd = [($^{144}Nd/^{143}Nd$)sample/($^{144}Nd/^{143}Nd$)CHUR-1] x 10 000; ƒSm/Nd = [(147Sm/144Sm)sample/(147Sm/144Nd)CHUR] − 1.

TDM = 1/(λ)× ln(1+($^{144}Nd/^{143}Nd$(sample, t) - $^{144}Nd/^{143}Nd$(DM, t)))/ ($^{147}SM/^{144}Nd$(sample, t) - $^{147}SM/^{144}Nd$(DM, t))) × 0,000000001 (after DePaolo, 1981)

TCHUR = 1/(λ) × ln(1+($^{144}Nd/^{143}Nd$(sample, t) - $^{144}Nd/^{143}Nd$(CHUR, t))/($^{147}SM/^{144}Nd$(sample, t) - $^{147}SM/^{144}Nd$(CHUR, t))) × 10^9 (after DePaolo, 1981)

Calculated using $^{144}Nd/^{143}Nd$ today = 0.512638 and $^{147}SM/^{144}Nd$ today = 0.1967